University of Nottingham
UK | CHINA | MALAYSIA

EPSRC
Engineering and Physical Sciences Research Council

POLYOXOMETALATES AND PEPTIDES:

hybridisation and disulfide detection

Heather Anne Damian

4311269

Supervised by Dr Nicholas Mitchell and Dr Graham Newton

School of Chemistry

University of Nottingham

I hereby declare that this thesis is all my own work, expect as indicated in the text:

Signature: H. A. Damian

Date: 28/12/2021

A thesis submitted to the University of Nottingham in 2021 for the degree of Doctor of Philosophy

ACKNOWLEDGEMENTS

Over the course of my PhD I have grown in several different ways, the challenged encountered in my research not only challenged me academically but mentally. I have shown strength and determination when sometimes I felt like walking away.

I would like to thank my two supervisors for showing their endless support and determination to see me through my PhD. I appreciate the opportunity they have given me and without your encouragement to apply in my master's year I would not have done a PhD so thank you Nick! Additionally, I'd like to thank the staff in the CDT, for first giving me a place and then supporting me throughout, being on the CDT allowed me to make the most of my PhD.

Both my research groups were full of supportive individuals, and I have made some great friends. Sharad, Rory, Alex, Andrea, Rhys and Jamie thank you for all your help in my projects, I would not have gotten as far as I did without each of you giving me support and guidance.

Thank you to my lovely friends for their mental support and endless encouragement, Cath I love our mix of runs and chemistry and I am so happy we both ended up in the Newton Group. Claire, there are not enough words for the tough love and support we have both given each other. You continuously challenge me and have become one of my closest friends and allies.

Anna, I am amazed at the friendship that we have managed to form from standing opposite each other in the first ever conference we attended. I look forward to more holidays and less stressful times ahead. Thank you for being my writing buddy and being the loveliest person, I know.

To Adele, Iris and Maja for making my last year so much better and helping me get through every day. I have had the best experience with our puppies and it has made my final year easier and motivated me to finish.

Farah, habibti, I miss you and I would not have gotten through my first few years without you being there. My family away from home.

To my worse half, you have managed to challenge me continuously outside of my PhD and have kept me level-headed. Having you has helped me have perspective and to see what I

work towards. Thank you for sitting through all my presentations without understanding a word, continuously encouraging me to take every opportunity and make fun of my to not let me head grow too big. Danke Mat! And Tyler for keeping me young but also making me feel so old.

Meine Familie, ohne euch haette ich alles nicht geschaft und ich waere nicht hier. Oma ich habe dich ueber alles lieb und du hast immer an mich geglaubt und weisst wie schwerr alles fuer mich war. Meine lieben eltern, ich hoffe das ihr heute stolz seit und wisst das ohne eurem example waere ich nicht so weit gekommen.

And a special thank you to my examiners (Prof. Neil Thomas and Dr. Scott Mitchell) for their help in corrections and identifying errors I had missed.

Table of Contents

ABBREVIATION LIST…… vi

NOTATION……ix

COLOUR SCHEME……x

ABSTRACT…… xi

CHAPTER ONE: INTRODUCTION ……..

1.1 Polyoxometalates……1

1.2 Structure, Bonding and Synthesis…… 1

1.3 Archetypal Polyoxometalate Structures…….. 6

1.4 Hybridisation of POMs…… 13

1.5 Electronic Characteristics of POMs…… 15

1.6 Accessing the Electronic Properties of POMs……..17

1.7 Biological Activity of POMs……..21

1.8 Disulfide Bonds in Nature…….. 29

1.9 Research Directions…… 43

1.10 References…… 4

CHAPTER TWO: DEVELOPMENT OF POM REDUCTION TECHNIQUES……

2.1 Introduction…… 53

2.2 Aims…….. 55

2.3 Results and Discussion…… 56

2.4 Conclusion…… 92

2.5 Experimental……93

2.6 References……97

CHAPTER 3: EMPLOYING TWO REDUCED POM SPECIES FOR DISULFIDE BOND REDUCTION

3.1 Introduction…… 98

3.2 Aims……100

3.3 Results and Discussion……101

3.4 Conclusion……117

3.5 Experimental……119

3.6 References……120

CHAPTER FOUR: DEVELOPMENT OF BISPHOSPHONATE HYBRID POMS……..…

4.1 Introduction……..122

4.2 Aim……..126

4.3 Results and Discussion……127

4.4 Conclusion……..140

4.5 Experimental……141

4.6 References……..144

CHAPTER FIVE: DEVELOPMENT OF BISPHOSPHONATE PEPTIDE HYBRID POMS – CHAIN GROWTH AND CHARACTERISATION ……

5.1 Introduction……..146

5.2 Aim……..150

5.3 Results and Discussion……..151

5.4 Conclusion……..161

5.5 Experimental……162

5.6 References……..167

ABBREVIATION LIST

AA	Amino acid
ACE	Angiotensin converting enzyme
AD	Alzheimer's disease
AGT	Angiotensinogen
ATR-IR	Attenuated total reflectance infra-red
BBB	Blood brain barrier
CE	Counter electrode
CJD	Creutzfeldt-Jakob disease
CT	Charge transfer
CV	Cyclic voltammetry
DCM	Dichloromethane
DFT	Density functional theory
DMF	*N,N*-dimethylformamide
DMSO	Dimethyl sulfoxide
DSC	Differential scanning calorimetry
DTNB	(Ellman's Reagent) (5,5-dithio-*bis*-(2-nitrobenzoic acid)
ESIPT	Excited-state intramolecular proton transfer
ESI-MS	Electrospray ionisation mass spectrometry
ER	endoplasmic reticulum
Fmoc-SPPs	Fmoc-Solid Phase Peptide Synthesis

HAT	Hydrogen atom transfer
HD	Huntington's disease
HOMO	Highest occupied molecular orbital
IVCT	Intervalence charge transfer
LMCT	Ligand to metal charge transfer
LUMO	Lowest unoccupied molecular orbital
MOF	Metal organic framework
NMR	Nuclear magnetic resonance
POM	Polyoxometalate
PA	Photoacoustic imaging
PCET	Proton coupled electron transfer
PD	Parkinson's disease
PDI	Protein disulfide isomerase
PTT	Photothermal therapy
SCE	Standard calomel electrode
SET	Single electron transfer
TBA	Tetra-*n*-butylammonium
TEA	Tetra-*n*-ethylammonium
TGA	Thermogravimetric analysis
TPVD	Tetra-*iso*-propyl vinylidene
UV	Ultraviolet

UV-vis	Ultraviolet visible
WE	Working electrode

NOTATION

In line with standard notation, the formulae of anion cluster compounds will be noted in square brackets, such as $[PW_{12}O_{40}]^{3-}$ and $[H_2W_{12}O_{40}]^{7-}$. This example illustrates that such notation can result in long and awkward formulae which do not necessarily add to the clarity in the text. Therefore, for each structure use, an abbreviated notation will be introduced where the number and type of addenda and heteroatoms as well as the number of substituted metal centres of the cluster are indicated in curly brackets, thereby representing the complete cluster unit. For example, the formula of the cluster units above, $[PW_{12}O_{40}]^{3-}$ and $[H_2W_{12}O_{40}]^{7-}$ may be reduced to $\{PW_{12}\}$ and $\{W_{12}\}$ respectively.

In addition, when referring to the geometric coordination motifs found within a cluster, these will be indicated using a square bracket notation. For example, an octahedral building unit where six oxygen ligands (O) coordinate to a central transition metal (M) will be noted as $[MO_6]$. As this description refers to an purely formal structural building unit, no charge will be assigned to it.

COLOUR SCHEME

All figures that have not been reproduced or taken from literature refer to specific structures adhere to the following colour scheme:

Tungsten: Light blue

Phosphorus: Pink

Vanadium: Blue/grey

Silicon: Orange

Molybdenum: Teal

Sulfur: Yellow

Carbon: Dark/grey

Hydrogen: Light/grey

Oxygen: Red

Nitrogen: Blue

ABSTRACT

The structure of proteins and peptides determines their ability to perform their proper biological function. A key factor contributing to the tertiary structure formation are disulfide bridges. These bonds can increase a proteins resistance to extreme environments and have shown to protect protein-based therapeutics from rapid proteolytic degradation. Due to the importance of disulfide bonds in nature and therapeutics their detection and characterisation is significant.

Herein a novel colorimetric approach to investigate the redox state of biological disulfide bonds is explored, utilizing supramolecular metal-oxide nanoclusters (polyoxometalates) as soluble, redox-tunable probes. The ability to fine-tune the physicochemical properties of these clusters provides an exciting opportunity to create bespoke reducing agents which can be targeted to a specific substrate. The strong colorimetric response arising from the difference between the colourless oxidized (d^0) state and the blue reduced (d^1) states, provides a convenient and sensitive spectroscopic handle for ease-of-analysis. These states are attributed to the molecular poms addenda (M) atoms being found in either the (d^1) or (d^0) states. The technique development and experimental set up will be investigated and clarified.

As a proof of concept for this approach, two distinct polyoxoanions, $[PW_{12}O_{40}]^{3-}$ and $[H_3W_{12}O_{40}]^{5-}$, have been explored for use as redox probes by a combination of detailed theoretical, electrochemical, and spectroscopic analyses. Unlike existing analytical methods such as the classical Ellman's test, the approach discussed herein is shown to be suitable for the direct interrogation of oxidised disulfide bonds. This is demonstrated for a range of model substrates. Herein is demonstrated the difference in reduction potential presented by the two POMs and their effects on commercial disulfides as well as two model peptides. These were synthesised through Fmoc-SPPS and then oxidised to form the disulfide bond. Characterisation of all the synthesised molecules was undertaken through NMR, CV, MS and HPLC.

Over the last decades polyoxometalates have demonstrated promising biological activities due to their diversity in structures and properties. The focus in the field of biologically active polyoxometalates lies on polyoxometalate-based nanocomposite structures and organically

functionalised hybrids. These show enhanced antitumour activity and significantly reduced toxicity towards normal cell tissue in comparison to the parent polyoxometalates.

In this is explored the development of a novel linker system to attach to organic functional groups to a Wells-Dawson polyoxometalate. These linkers are based on bisphosphonate structures which are prevalent in a range of therapeutics, additionally there has been prior work done to show the synergistic effect of bisphosphonates couples to metal-oxide clusters. Three novel polyoxometalate-bisphosphonate linker molecular are formed and characterised using NMR and MS as well as identifying their absorption profiles under UV-vis light. Furthermore, the work progresses to demonstrate the use of the bisphosphonates as a handle for the attachment of amino acids to the hybrid structures. A selection of amino acids is explored, and then subsequent attachment of peptides is investigated. The peptides were synthesised *via* Fmoc-SPPS, purified *via* preparative HPLC, and characterised through MS and HPLC prior to addition to the linker systems.

CHAPTER ONE: INTRODUCTION

1.1 Polyoxometalates

Polyoxometalates (POMs) are a class of discrete supramolecular anionic metal oxide clusters; composed of transition metals (typically M = W, Mo, V, Nb, Ta or Cr) in their highest oxidation states ligated by bridging and terminal oxo ligands. The clusters are assembled through condensation reactions of pseudo-octahedral [MOx] units. Due to these species displaying a myriad of desirable properties through impressive structural diversity, such as photoactivity, cytotoxicity, high thermal and chemical stability, and in particular their rich and reversible redox activities, they have found application in a wide range of fields such as electro- and photo-catalysis,[1,2,3] medicine,[4] sensing,[5] battery technology[6] and magnetism.[7]

In addition, to the large library of available POM clusters with unique, characterised properties, various avenues exist to allow for fine-tuning of the electronic properties of POMs through the modification of the POMs immediate surroundings (solvent or counter-cations) or direct manipulation of the structure itself.[8,9] This 'designer' aspect of these species through simple late-stage modification ensures that both POM and non-POM chemists alike continue to be amazed by this ever-evolving field.

1.2 Structure, Bonding and Synthesis

The principles of POM formation and bonding is extensive due to the variety of shapes, sizes and compositions possible; the majority of structures can be described by a set of simple rules and concepts. Firstly, looking at the smallest unit of a POM, the [MO_x] polyhedron (where x = 4-7, usually 6) the central metal atom in this unit is typically referred to as the addenda atom, coordinated to between 4 and 7 oxo-ligands which are formally O^{2-} anions, Figure 1. In order to form discrete clusters each individual addenda atom must possess certain properties to be able to poly-condense, namely: 1) the ability to change coordination number from 4 to 6 upon acidification in solution; 2) be among the smaller of metal ions capable of forming octahedral packing arrangements with oxygen and possess high positive charges; 3) ability to form double bonds with unshared (terminal) oxygen atoms *via* pπ-dπ

orbital interactions.[10–12] Therefore, obeying these rules, the majority of POM species are comprised of addenda atoms from group V and VI transition metals such V, Nb, Ta, Mo, W in their highest oxidation states (usually d^0 or d^1 configuration).

The structurally versatile components of the POM are the oxo-ligands comprising the vertices of the polyhedron. These bridging oxo-ligands can link anywhere between two and six addenda atoms, represented by the notation μ_n (where n = number of bridged metal atoms). The stability of the POM cluster is due to the presence of terminal M=O groups, exhibiting a strong thermodynamic trans-effect by weakening the opposite bridging oxo-M bond that shares the same orbital. The result of this trans-effect displaces the metal centre towards the terminal oxo-ligand and distorts the octahedral geometry.

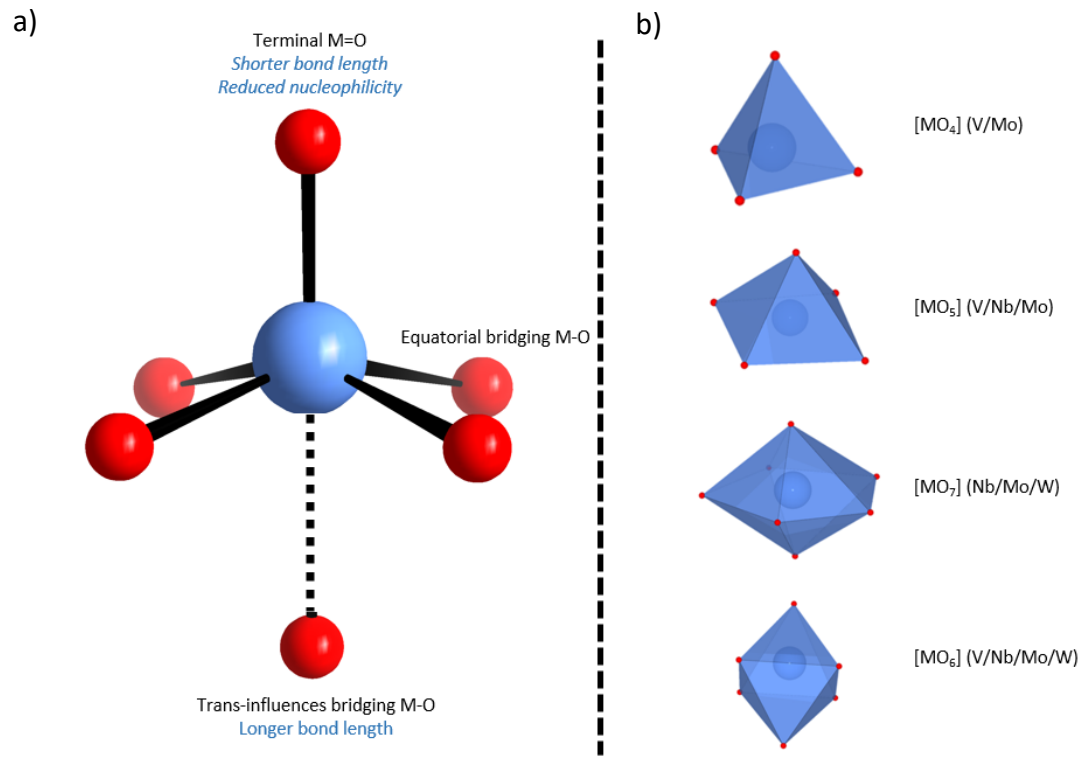

Figure 1: a) Visual representation of the trans-effect upon the coordination environment of the metal in polyoxometalates. b) Polyhedral units that are commonly encountered as building blocks in POM structures.

This reduced the basicity of the terminal oxo-ligand and the probability of acid mediated protonation. Therefore, the ability to further poly-condense into larger species is inhibited. This is the main reason why POMs exist as discrete molecular clusters.

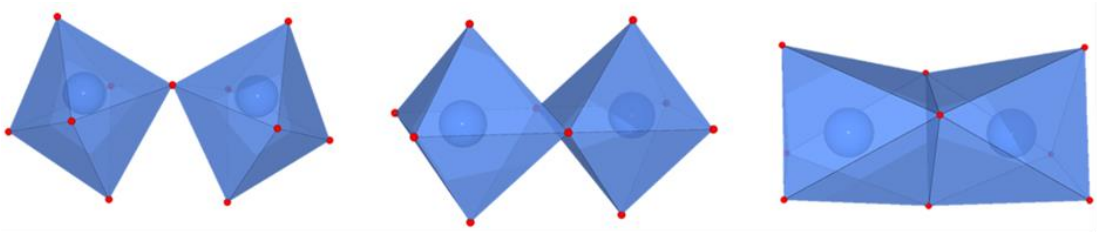

Figure 2: Connectivity modes between polyhedral units upon oligomerisation based on the sharing of one (corner), two (edge) or three (face) oxygen atoms between two metal centres.

Another factor that causes variation is the way the polyhedral [MO_x] units polymerise, each unit can be connected in three different ways: corner sharing, edge sharing and face sharing, corresponding to the sharing of one, two and three oxo-bridged ligands between two octahedral units. A single POM is composed of a mixture of these three structural condensation products. The POM architecture is limited only by the restraint that each single polyhedron must contain either one or two terminal oxo-ligands, this is known as the 'Lipscombe Principle',[13] this has both structural and electronic implications on the clusters.[14] The classification system of POMs is also based on this principle, whereby the number of terminal M=O bonds dictates which group the POM exists in. There are three types of POM classifications: type I POMs possess one terminal M=O bond, type II possesses two terminal M=O (cis-oxo) and type III possess a combination of the two. The number of terminal M=O bonds has a strong effect on the electronic properties of the POMs. Type I POMs are known to observe rich and reversible redox behaviour. Such POMs can be mixed valence and their reduced species have been heavily investigated, formally known as "heteropoly blues".[15–18] Conversely, type II POMs cannot be easily reduced without decomposition. This is due to the non-bonding LUMO octahedra in type I *vs* the anti-bonding LUMO exhibited by Type II octahedra.[19]

Another feature to consider with respect to the *trans-effect* mentioned above, is a distortion of the uniform M-O bonding nature of the octahedra. This results in the shortening of the M=O bond and lengthening of the opposite internal M-O bond. The weakening of this bond results in a lower bonding rigidity, allowing for the incorporation of hetero atoms. Heteroatoms are non-addenda atoms integral to the POMs formation (sometimes referred to as 'templating atoms') and typically sits within its core. These templating atoms can be either metallic or non-metallic in nature but must be able to bond at least three oxygen atoms. This limits the selection of heteroatoms to d- or p-block elements in high oxidation states which can form 4-coordinate or 6-coordinate oxyanions. This distinguishing feature leads to the separation of the POM species into two families: iso-polyoxometalates $\{[M_xO_y]^{n-}\}$ where no hetero-elements are present in the POM structure and hetero-polyoxometalates $\{[A_zM_xO_y]^{n-}\}$ (with $z \leq x$ and = overall oxidation state) when there are one or more heteroatoms present, Figure 3.[18]

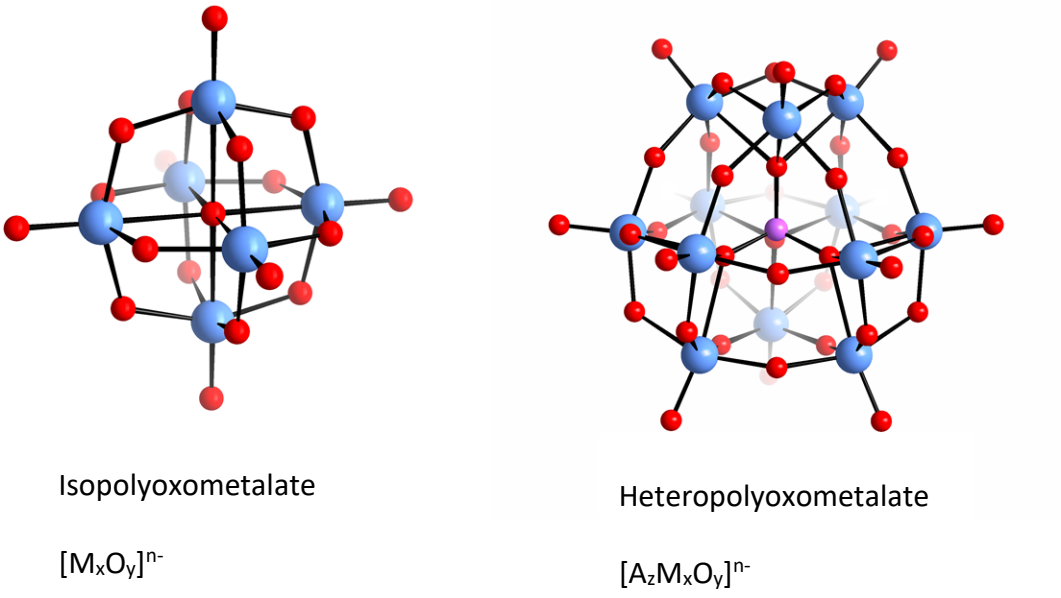

Figure 3: Ball and stick representation of an isopolyoxometalate $[M_xO_y]^{n-}$ and a heteropolyoxometalate $[A_zM_xO_y]^{n-}$.

Polyoxometalate synthesis occurs *via* pH mediated self-assembly of individual $[MO_x]$ building blocks, introduced via water soluble oxometallate salt such as Na_2WO_4, $NaMoO_4$ or $NaHVO_3$. For the synthesis of hetero-polyoxometalates a source of heteroatom is also added

either before or during a reaction, these typically are mineral acids or alkali metal derivatives. Individual [MO_x] blocks are protonated in the presence of acid and undergo polycondensation reactions to form discrete anionic clusters. Slight modification of the reaction conditions allows for a specific POM synthesis, here factors such as pH, solvent temperature, heteroatom reagents and cations play a large role in the assembly of the POM. Due to the complex nature of the self-assembly process, isomeric and structural purity of the product can be difficult to achieve. To isolate pure products, workups include the precipitation of POMs from solution with cations, or for more complex situations purity can be achieved through crystallisation.

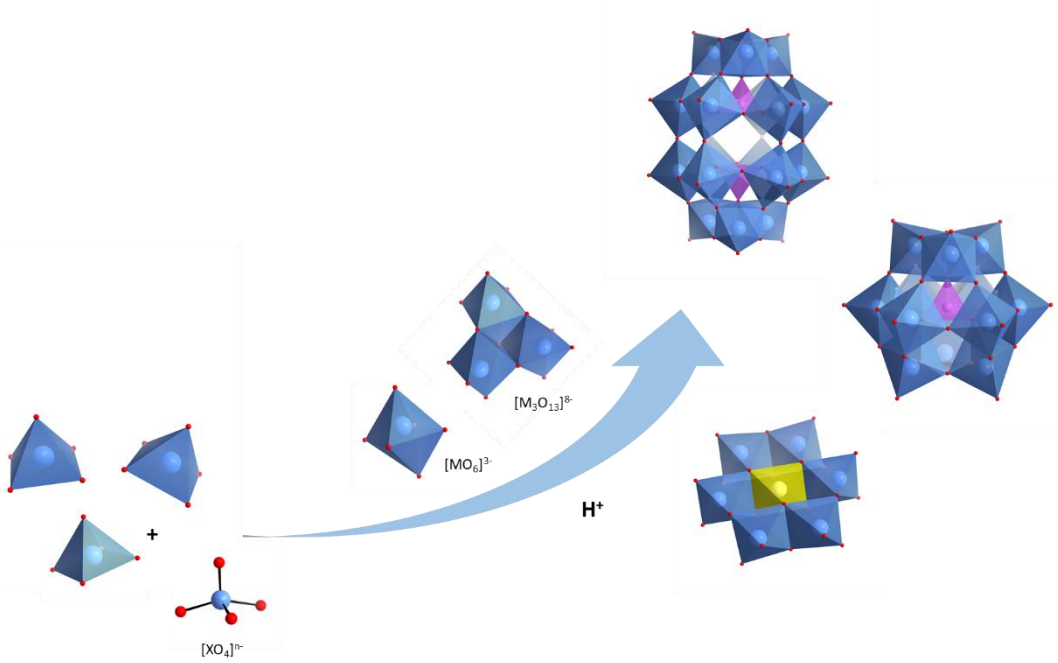

Figure 4: A simplified illustration of the general polycondensation pathway of metal-oxo fragments to polyoxometalates.

1.3 Archetypal Polyoxometalate Structures

Despite the large library of POMs present and the conceptually limitless structures that octahedral and tetrahedral units could form through the sharing of oxide ligands, most POMs can be identified as derivatives of one of four distinct structural groups: Lindqvist, Keggin, Well-Dawson or Anderson clusters. Each of these structures have demonstrated function as discrete clusters are commonly used due to their reproducibility and stability, also making them excellent candidates as the basis of the construction of larger clusters.[20]

1.3.1 Lindqvist Anion

The hexametalate Lindqvist POM is one of the simplest and smallest iso-polyoxometalates, and was discovered in 1950.[21] The cluster possesses the general formula $[Mo_6O_{19}]^{n-}$ and can be isolated using the early transition metals such as Nb,[21] Ta,[22] Mo,[23] and W.[22] The structure is composed of six octahedra edge-sharing $[MO_6]$ units, to form a super-octahedron (Oh symmetry), where the six addenda are coordinated to a μ_6-oxo ligand.

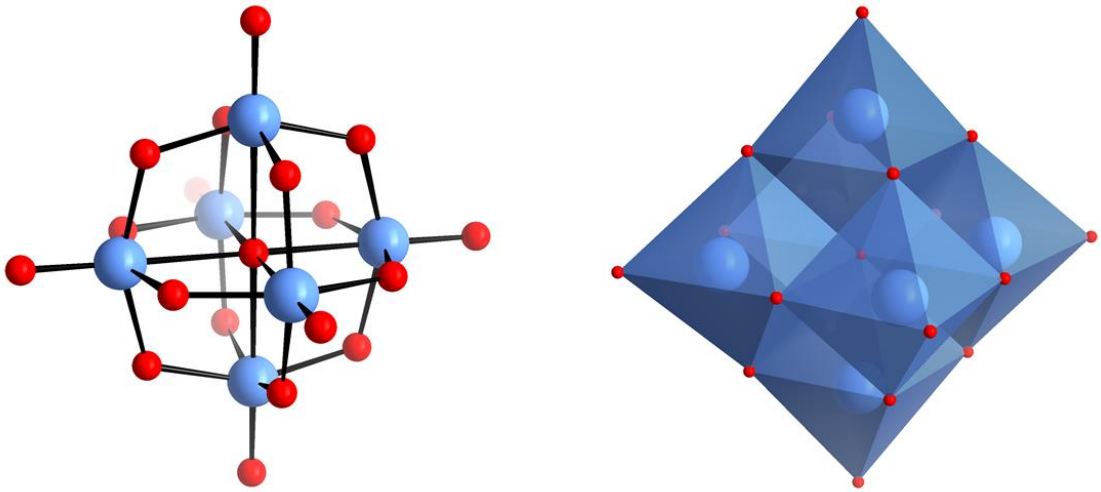

Figure 5: Ball and stick structure (left) and polyhedral representation (right) of the Lindqvist polyoxometalate $[M_9O_{19}]^{n-}$.

1.3.2 Anderson-Evans Anion

Commonly referred to as the Anderson cluster, the Anderson-Evans POM species was predicted by Anderson in 1937 and solved by Evans in 1948.[24,25] This cluster is comprised of a central octahedral heteroatom surrounded by a hexagonal planar ring of equivalent edge-sharing [MO_6] octahedra which yields a heptametalate D_{3h} species; the POM has a general formula of $[H_yXM_6O_{24}]^{n-}$. The addenda atoms are usually molybdenum, tungsten or vanadium. There are three oxygen environments present in the structure; six μ3 oxygen atoms connecting the heteroatom to each pair of adjacent addenda atoms; six μ2 oxygen atoms which connect each pair of adjacent addenda atoms to each other on the periphery of the ring; and 12 terminal M=O bonds, located in pairs on each of the six addenda atoms. Unlike the vast majority of POMs, the Anderson-Evans structure has limited redox chemistry associated with the d_0 addenda metal centres. The main diversity in the cluster is installed by the variation of the heteroatom which can be a wide variety of transition metals and p-block elements, therefore, the nature of the properties of the cluster are heavily dictated by the heteroatom. This cluster is a good example of a type II POM.[26]

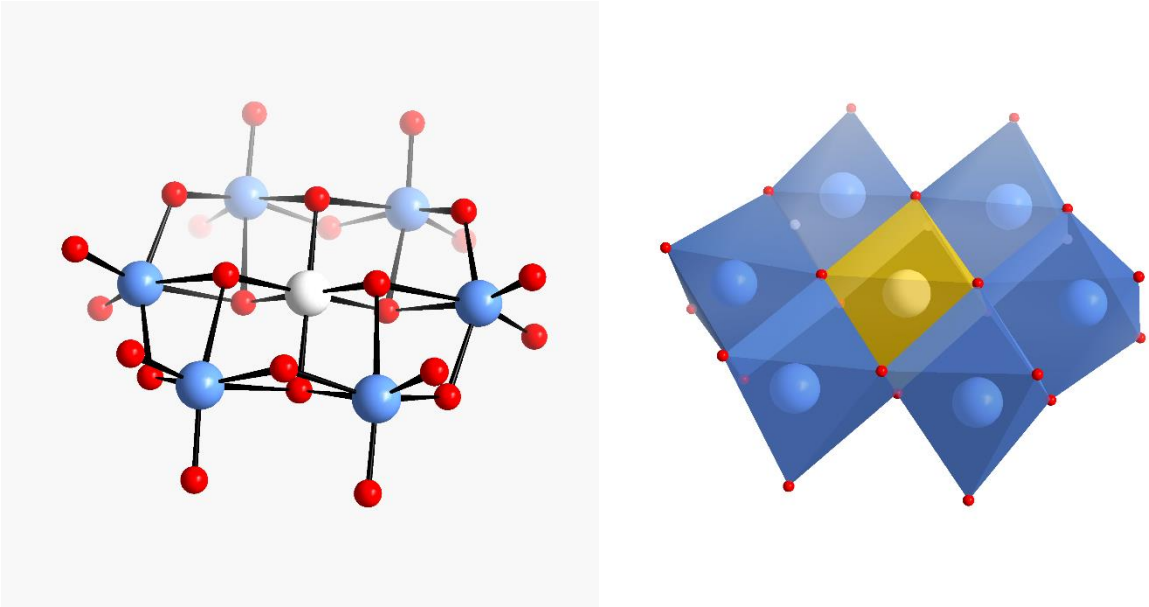

Figure 6: Ball and stick structure (left) and polyhedral representation (right) of the Anderson polyoxometalate $[HyXM_6O_{24}]^{n-}$.

1.3.3 Keggin Anion

The Keggin structure represents the simplest of the hetero-polyoxometalates and was the first polyoxometalate structure to be crystallographically elucidated with the characterisation of 12-phosphotungstic acid in 1933, although reported in 1826.[27] The structure has the general formula of $[XM_{12}O_{40}]^{n-}$ (where X = P, Si, As, etc., M = V, Mo, W, etc.). The anion has an overall tetrahedral symmetry and is based around a central $[XO_4]$ tetrahedron, this is surrounded by four $[M_3O_{13}]$ triads also with Td symmetry. The $[MO_6]$ units within each triad are edge-sharing and the triads are connected to each other through a corner-sharing oxygen atom. There are four oxygen environments within the structure; four bridging oxygens link the addenda atom to the central heteroatom, 24 oxygen atoms bridge each addenda atom by either corner or edge-sharing, and 12 terminal M=O bonds exist each on one addendum. This results in the species being classed as a type I POM with high stability and rich redox chemistry. Common heteroatoms for the Keggin are p-block elements such as B, Si, Ge, P and S.[28,29]

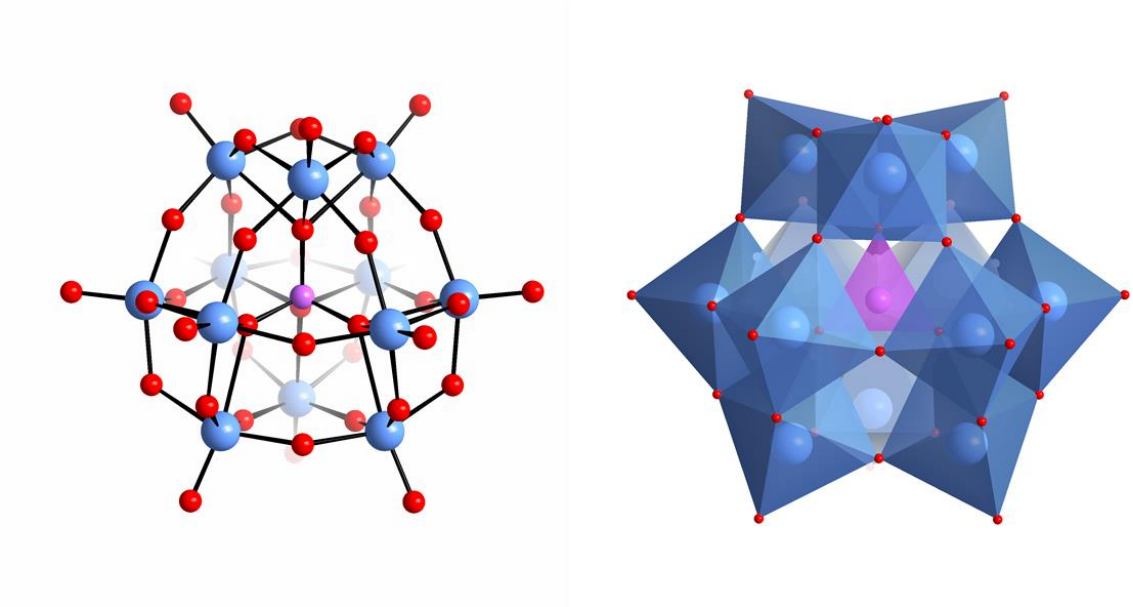

Figure 7: Ball and stick structure (left) and polyhedral representation (right) of the Keggin polyoxometalate $[XM_{12}O_{40}]^{n-}$.

Unlike the Lindqvist anion, the Keggin anions have a degree of rotational isomerism associated with the $[M_3O_{13}]$ triads, each can exist in one of two possible orientations. Starting from the α-isomer (T_d symmetry), successively rotating each of the triad units through 60° gives the other four possible isomers (β: C_{3v}, γ: C_{2v}, δ: C_{3v}, ε: T_d).[30] Within the α-

and β-isomers, the four triad units are linked via corner-sharing as mentioned, however for γ, δ and ε, the corner-shared linkages are replaced by one, three and six edge-sharing linkages, respectively. The most stable, symmetrical and ubiquitous throughout literature is the α-isomer, although the β-isomer is also stable it is less common with fewer fully characterised structures.[31] Due to the higher relevant abundance of these two isomers research has focused on investigating their properties. Comparatively, fewer examples exist of the γ,[32] δ,[33] and ε,[34] isomers.

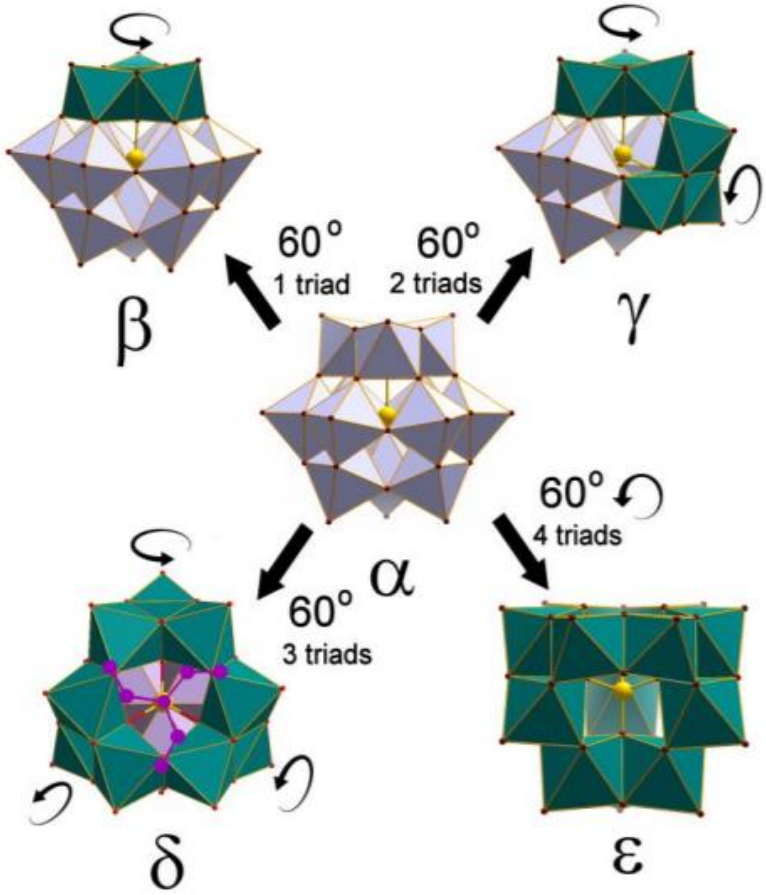

Figure 8: Polyhedral representation of the crystal structures of all the isomers of the Keggin anion: β, γ (top from the left), δ and ε (bottom from the left). The green polyhedra show the {M3O13} units which have been rotated the 60o with respect to the α-isomer shown in the centre. The yellow spheres are the heteroatom templates, the small red spheres are the oxo-ligands. The purple ball and stick show the coordinating ligand which allows the δ isomer to form. Image taken from H. Sartzi, H. N. Miras, L. Vila-Nadal, D. L. Long and L. Cronin, Angew, Chem. Int. Ed., 2015, 54, 15488-15492.[173]

1.3.4 Wells-Dawson Anion

The Wells-Dawson anion, commonly referred to as the Dawson cluster, was first identified in 1954 through the characterisation of potassium 9(18)-tungstophosphate.[35] This cluster has a general formula $[X_2M_{18}O_{62}]^{n-}$ (where X = P, Si, As etc., M = Mo, W). The structure of this hetero-polyoxometalate can be viewed as the connection of two α-type trilacunary Keggin clusters, $[XMo_9O_{34}]^{n-}$, via corner-sharing; this results in a structure which can simply be described as two 'belts' of six $[MO_6]$ units with a 'cap' on each end made up of $[M_3O_{13}]$ groups.[36] The chemical properties of the cluster are strongly influenced by these two sites within the structure, this is due to the electron transfer properties differing within the 'cap' and 'belt' positions. Lastly the tetrahedral hetero-anion, $[XO_4]_n$ links to the three addenda of a $[M_3O_{13}]$ cap through μ_3-oxo coordination and to six of the addenda atoms within the

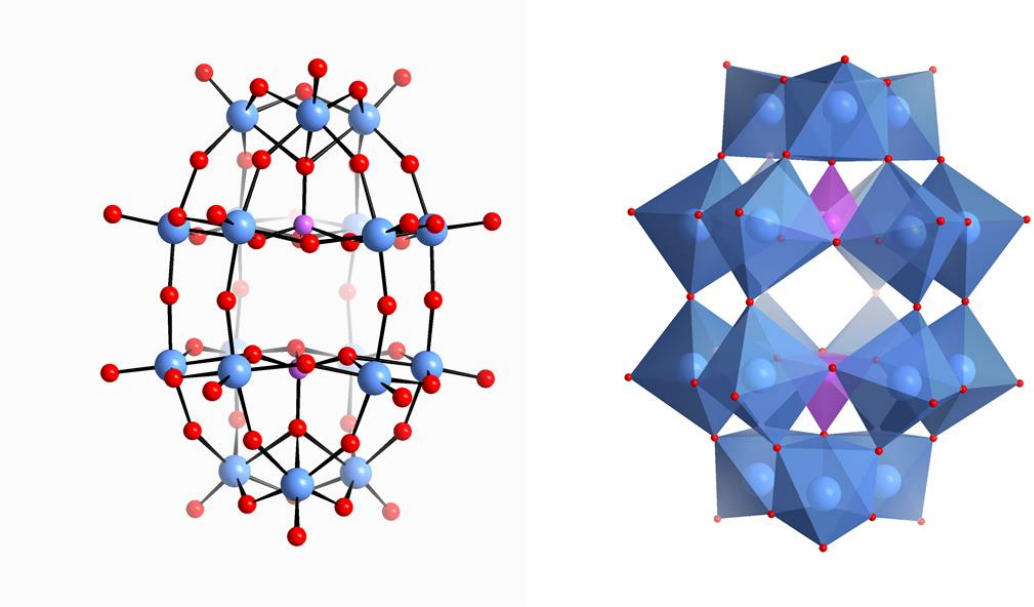

Figure 9: Ball and stick structure (left) and polyhedral representation (right) of the Wells-Dawson polyoxometalate $[X_2M_{18}O_{62}]^{n-}$.

octahedral belt.

Similarly, to the Keggin cluster, the different orientation of the triad caps of the Dawson cluster leads to the formation of six different isomers (α, α*, β, β*, γ and γ*). The α, β, and γ isomers are produced through successive 60° rotations of the end caps (displaying D_{3h}, C_{3v} and D_{3h} symmetry respectively), Figure 10. The rotation of the caps in the staggered form (where the pyramidal heteroatoms are staggered by 180°) results in the α*, β*, and γ*

isomers (D_{3d}, C_{3v} and D_{3d} symmetry respectively).[37,38] The stability of the isomers follows the general trend α, β, γ, γ*, β*, α*, with only the first four having been isolated to date.[39]

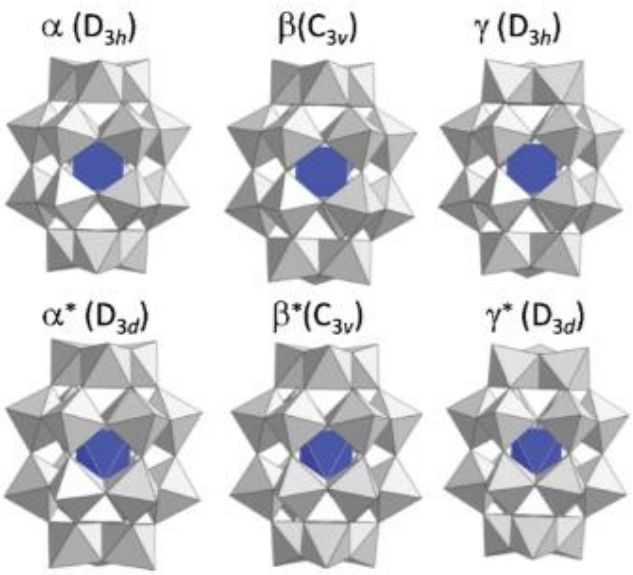

Figure 10: Six isomers of the Wells-Dawson anion, the top series is accessed through rotation of the two caps by 60°C with the core tetrahedral heteroatoms aligned whereas the bottom series is accessed through rotation of the caps by 60°C with the core tetrahedral heteroatoms misaligned by 60°C. Reproduced from L. Vila-Nadal, S. G. Mitchell, D.-L. Long, A. Rodriguez-Fortea, X. Lopez, J. M. Poblet and L. Cronin, Dalton Trans., 2012, 41, 2264-2271.37

1.3.5 Lacunary Anion

The pH-controlled hydrolysis of a number of addenda units can be accomplished with some POM clusters, mainly the Keggin and Dawson anions. The resulting species are referred to as '*lacunary*' anions – lacuna meaning unfilled space or gap, the parent polyoxometalates are referred to as '*plenary*' POMs. The removal of one or more addenda atoms results in the exposure of anionic oxo-ligands and an increase in the overall charge of the POM. The polyoxotungstates result in stable and isolable lacunary species, whereas for polyoxomolybdates these species tend to be highly reactive and often difficult to isolate and handle without degradation. Lacunary species are extremely important in the functionalisation of POMs as the exposed oxo-anions are capable of either coordinating a variety of metals,[40] or undergoing covalent organo-functionalisation with oxo-philic p-block elemments.[41]

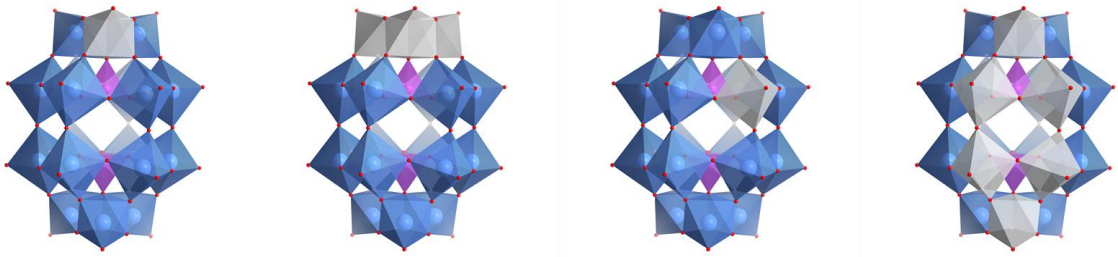

Figure 11: Polyhedral representation of the four possible lacunary species of the Wells-Dawson cluster.

There are three known types of lacunary structures for the Keggin anion, these are achieved through the removal of one to three metal centres, generating the mono-lacunary $[XM_{11}O_{39}]^{n-4}$, dilacunary $[XM_{10}O_{36}]^{n-4}$ and trilacunary $[XM_9O_{34}]^{n-6}$ derivatives (where n = the charge of the parent anion). The increase in negative charge of the POM corresponds directly to the number of oxo-anions that are formed through the removal of the metal centre(s). additionally successive hydrolysis occurs at the same site on the POM, resulting in an increasingly large lacuna, not isolated sites. Due to the removal of addenda atoms destabilizing the POM, isomerisation can occur to stabilise the structure.

The formation of lacunary structures from the Wells-Dawson cluster are also common. Conversely to the Keggin structure, the formation of lacuna in the Wells-Dawson structure does not proceed in a sequential fashion. Instead, lacunary species are formed from the

removal of; a single metal (monolacunary, $[X_2M_{17}O_{61}]^{n-4}$); a single cap (trilacunary, $[X_2M_{15}O_{56}]^{n-6}$); or a single "*face*" (hexalacunary, $[X_2M_{12}O_{48}]^{n-8}$) of the structure. Due to the plenary POMs high thermodynamic stability the formation of lacunary structures can only be isolated by base driven hydrolysis. There is far less positional isomerism present in these structures, as only the α-Dawson anion leads to stable lacunary structures.

1.4 Hybridisation of POMs

As alluded to above, POMs are well-known to exhibit an extensive library of structures that can be accessed through the slight manipulation of synthetic conditions. Further hybridisation of POMs can be achieved through the coupling of new species to the already assembled clusters, this can impart POMs with additional functionality and used to tune their intermolecular properties. Hybridisation can occur through the grafting of inorganic or organic moieties.

Hybrid POMs can be separated into inorganic hybrid POMs and organic-inorganic hybrid POMs. Inorganic functionalisation refers to the addition of hetero transition metals or f-block elements, either through a one-pot synthesis where the POM is synthesised in the presence of the cationic species (e.g. transition metals) or through the coupling with a vacant site in a lacunary POM where metal species can bind. The inorganic hybrid species are usually highly stable due to the POMs ability to stabilise co-ordinately and electrostatically the highly charged cationic centres. This hybridisation technique has been shown particularly effective for the modulation of the POM's properties.[42] For example, the incorporation of a molybdenum atom into a polyoxotungstate to form a tungstomolybdate POM species possesses the stability of polyoxotungstates and also the lower LUMO energies and positive redox potentials associated with polyoxomolybdates.[43] An even greater degree of structural diversity is accessible owing to the broad range of cationic species available and their differing coordination geometries, also allowing for ample choice in the alteration of POM properties. Due to this flexibility in inorganic-hybrid POM formation the species have demonstrated promising properties in catalysis, [1,2,3] magnetism[7] and medicine. [4]

Organic hybridisation involves the association of organic moieties with POMs, forming organic-inorganic hybrid species. There are two distinct groups of these hybrids,

distinguished by the nature of the interaction with the POM. Class I hybrids defines the systems where the POM and the organic components are associated through electrostatic interactions (i.e. ionic, Van der Waal or hydrogen bonding).[44] The synthesis of the Class I hybrids is relatively simple and generally involves the ion exchange reaction (salt metathesis) through the mixing of the two precursor salts in solution with molar ratios based on the desired product. Although this method is relatively rapid and simplistic, the weak interactions between the POM and organic moieties also provides the hybrids with lower stability and leaves them susceptible to further salt exchange reactions. Additionally, the synergistic benefits of the two components in proximity are often lost in solution phase.[45,46]

Class II hybrids are the product of the covalent bonding between organic components and the inorganic POM species. The synthesis of these is more specific depending on the POM structure and the identity of the addenda atoms, Figure 12. For example, the sole strategy used for hybridisation of Lindqvist hexamolybdates is imido-functionalisation; this works by the direct reaction of the POM with primary amines through diimide catalysed nucleophilic addition-substitution.[47] This results in the substitution of terminal oxo-groups with primary amines, forming formal molybdenum-nitrogen triple and double bonds. Tripodal alcohols (triols) are another commonly used group, these can be used to functionalise the Anderson

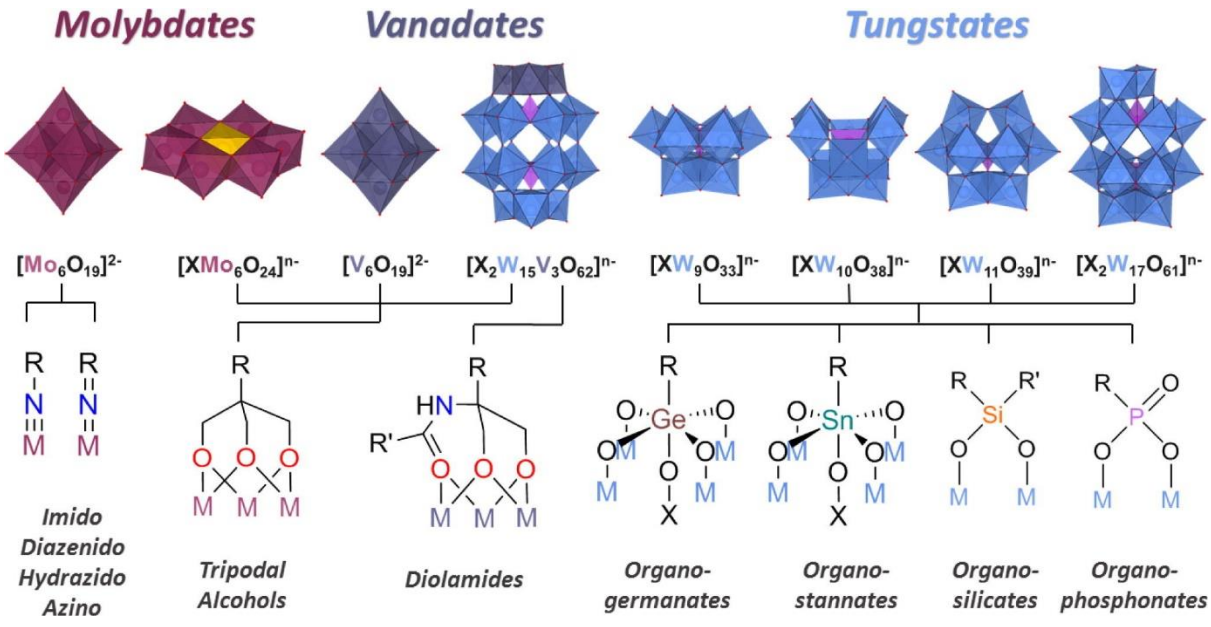

Figure 12: A schematic showing covalent organo-functionalisation routes for a variety of archetypal and lacunary structures. Reproduced from A. J. Kibler and G. N. Newton, Polyhedron, 2018, 154, 1-20.[41]

molybdate, Lindqvist hexavanadate and the vanadate caps of mixed addenda Wells-Dawson POMs ($[X_2W_{15}V_3O_{62}]^{n-}$, X = the templating atom).

The reaction of this linker proceeds *via* a formal esterification of the protonated bridging oxo-ligands. Similarly, diolamide linkers haven been used on the vanadate capped tungsten Dawson anion successfully.

The above methods work well for polyoxovanadates and polyoxomolybdates due to their lower stability and higher reactivity,[48] allowing for the hybridisation reactions to occur between the surface of these clusters and organic ligands displaying certain functionalities, however the grafting of organic groups to polyoxotungstates cannot proceed so easily. Covalent hybridisation of the Keggin and Dawson polyoxotungstate anions can proceed using lacunary species. The removal of one or more tungsten atom forms a lacuna containing negatively charge exposed oxygen atoms. these reactive oxygen sites can undergo condensation reactions with oxophillic components such as organogermanium, organotin, organosilicon and organophosphorus compounds.[41,49]

The addition of these linker molecules to the POMs not only provide a structural tool onto which to graft further organic ligands but can also install some electronic effect which can impact the POMs HOMO-LUMO energy levels. This can be further modulated when considering the electronic effects imposed by organic ligands themselves.[50]

1.5 Electronic Characteristics of POMs

POMs are synthesised from transition metals in their highest oxidation state (W^{VI}, Mo^{VI}, V^{V}, Nb^{V}). Therefore, these centres can undergo reduction which allows POMs to act as electron reservoirs. Above was discussed the characterisation of most POM clusters into two groups depending on the metal atoms possessing either one (mono-oxo) or two (cis-dioxo) terminal M=O, forming Type I and Type II respectively. Additionally Type III exists and is a mixture of the two, most common in some lacunary structures. Molecular orbital theory tells us that the octahedral metal-oxo units displayed in Type I and III (M=O terminal bonds) have one vacant non-bonding t_{2g} orbital that can be populated on reduction. Type II POMs on the other hand lack a non-bonding t_{2g} orbital as the orbitals are involved in π-bonding.[51] Therefore structures such as the Anderson type POM can only undergo irreversible

reductions under highly forcing conditions, while structures such as the Lindqvist, Keggin and Dawson can undergo several reversible reductions of their metal centres. When Type I/III POMs accept electrons onto the structure it is accompanied with little structural changes, this is because of the non-bonding nature of the orbital where the electrons are placed, this results in the clusters displaying highly reversible electron loading and unloading properties. As the redox properties of POMs are highly interesting to us only Type I and III POMs will be discussed.

Pope *et al.* first described the relationship between the structure of POMs and their ability to accept electrons. [18] The ability of an addenda atom of a POM to accept electrons is related to the size and charge of the POMs, q/m (where q = the overall negative charge and m = the number of metal ions in the structure), this can also be viewed as a simplified version of the charge density.[18] Basically this means that highly charged, small polyoxometalates accept electrons less easily than large POMs with low negative charge, which are very easily reduced. Considering POMs of the same structure but with different addenda, a trend can be seen in which the LUMO energies of the POMs decreases with the increase in electronegativity of the d_0 metal addenda (W < Mo < V).[52] Additionally the ability of a hetero-polyoxometalate to accept electrons can be impacted by the nature of the templating anion. This was verified by Nadjo *et al.* who performed density functional theory calculations on the Keggin cluster while modulating the hetero-atom.[53] The group reported that the size of the internal [XO_4] units affected the POMs reduction potential, due to different X atoms (within the same group) exhibiting slight variations in properties. Smaller X atoms possess lower atomic numbers, resulting in the net effect of a more negative potential in the surroundings this causes a smaller capacity to accept electrons. Therefore, the POM cluster can in turn accept less electrons.

Upon reduction a selection of POMs exhibit a strong blue colour transition, referred to as '*heteropolyblue*'. This colour is observed due a phenomenon known as the intervalence charge transfer (IVCT) of electrons.[11,15,16] It is the rapid, thermally assisted, electron transfer between metal centres in the POM core and gives rise to a strong absorption profile in the low energy visible and near infra-red absorption regions. Within very symmetrical POMs such as the Keggin and Lindqvist structures, a higher degree of electron *'hopping'* is observed over the entire molecule due to the equivalence of the metal centres.

Consequently, in structures presenting different metal centres, such as the '*cap*' and '*belt*' of the Dawson anion, delocalisation occurs within regions of equivalent metal centres. These absorption bands correlate with the degree of reduction of the POM and further addition of electrons results in the development of new IVCT bands at well-defined wavelengths. Subsequently, this makes the IVCT bands powerful diagnostic aids for monitoring the reduced states of POMs within solution. For example due to the redox properties and the corresponding colour change some POMs have been applied to the sensitive spectrochemical determination of phosphorus (molybdenum blue method)[54–56] and the evaluation of antioxidant capacities of food and beverages (Fouline-Ciolato method).[57]

1.6 Accessing the Electronic Properties of POMs

1.6.1 Photoactivity of POMs

The rich electronic properties displayed by POMs can be accessed through several pathways, such as through their interaction with light. Mainly Type I and Type III POMs are inherently photoactive due to their ability to excite the ligand to metal charge transfer (LMCT) bands of the terminal metal-oxygen bonds. Mechanistically this process involves the transfer of an electron from a doubly occupied 2p orbital of the oxygen (HOMO) to a d orbital of the metal (LUMO). Hence the charge transfer interaction essentially represents the HOMO-LUMO gap of the POM. These absorption bands normally are found in the UV region of the spectrum with some overlap into the visible, however, the LUMO energy of POMs can be lowered by using more electronegative metal ions. Therefore polyoxotungstate displays high energy LMCT bands with minimal tailing into the visible region whereas polyoxomolybdates and vanadates exhibit lower energy bands with some tailing into the visible region.[52]

The excitation of the LMCT band results in a localised d^1 electron on the metal centre and an oxo-centred radical cation with a short-lived triplet state. This triplet state is rapidly quenched either by hydrogen atom transfer (HAT) or single electron transfer (SET) depending on the POM and substrate/solution. This results in a trapped d^1 electron on the metal.[58] This trapped d^1 electron undergoes IVCT, resulting in the '*heteropolyblue*' colour previously described. It is important to observe however that while the IVCT process does

increase the absorption profile of the POM into the visible region, it doesn't not result in photosensitisation of the POM due to IVCT not generating the oxo-centred radical cations and hence is photochemically inactive. Continued irradiation can however yield multiple photoreductions of the POM, and the formation of more than one IVCT band. This can also be achieved by electrochemical methods.

Several nanoagents have been explored as exogenous agents for photoacoustic (PA) imaging and photothermal therapy (PTT), more recently the spotlight has shifted to POMs, mainly the Keggin structure, due to their photo-active electronic properties. [59–61] A recent study by Cai *et al.* demonstrated the development of a theranostic agent based on POM clusters with the highest oxidation state of Mo(VI) for pH-responsive assembly and redox-activated PA imaging-guided PTT.[60] These POMs showed no near-infrared absorption in their original chemical form however upon addition to the tumour redox microenvironment a strong near infrared absorption was exhibited due to the Mo(VI) reduction to Mo(V).[59] The in vitro toxicity of these oxidised POMs was tested by a standard MTT assay after incubation with human embryonic kidney 293 (HEK293) and murine breast cancer 4T1 cells. Initially the oxidised POMs showed negligible toxicity for both cell lines. Upon reduction of the clusters, adding to the 4T1 cell lines and then NIR laser irradiation an increase in activity was identified.[59]

Additionally, Zhang *et al.* had a similar approach in using the acidic tumour microenvironment to induce protonation of their Keggin anions ($[PMo_{12}O_{40}]^{3-}$), leading to the formation of larger vesicles.[61] Due to the POMs initial small dimensions, they were able to circulate in the blood before accumulating within the tumour tissue to form aggregates. The accumulation is believed to be due to acidity and reducibility in the tumour microenvironment. The distinct approach was that irradiation of this area would result in eradicating tumour cells.[62]

1.6.2 Electrochemical Reduction of POMs: Cyclic Voltammetry

The structure of POMs, especially ones based on the Keggin and Dawson-type structures, allow for multiple reversible electron transfer processes. Due to the importance of the redox processes in POMs extensive investigations have been undertaken on the

electrochemistry of POMs in various electrolyte solutions and electrodes by using standard electrochemical techniques such as cyclic voltammetry (**CV**) which will also be described herein. The typical voltametric behaviours of POMs have been described in several books and review articles.[53,63]

1.6.2.1 Cyclic Voltammetry Explained

The investigation of the reduction and oxidation processes of POMs is commonly done through the popular electrochemical technique known as cyclic voltammetry. In a voltammogram the x-axis is represented by the applied potential (*E*), while the y-axis is the response i.e., the resulting current (*I*) passed. The CV measurements taken herein are taken from right to left (positive to negative potential), see Figure 13. Another crucial parameter to consider is the scan rate (v) (e.g. v = 100 mV/s), this indicates that during a run the potential was varied linearly at the speed of 100 mV per second. The reduction processes are displayed by sweeping the potential negatively from a starting potential E_1 to a switching potential E_2, displayed for the Keggin ($H_3[PW_{12}O_{40}].xH_2O$) POM in Figure 13. This is referred to as the anodic trace, reversing the scan direction (negative to positive potentials) and sweeping the potential back to E_1, is referred to as the cathodic trace. When the solution is scanned to negative potentials the POM is reduced indicated by the first peak, scanning to a more negative potential allows for a second-electron reduction to be accessed and so forth.

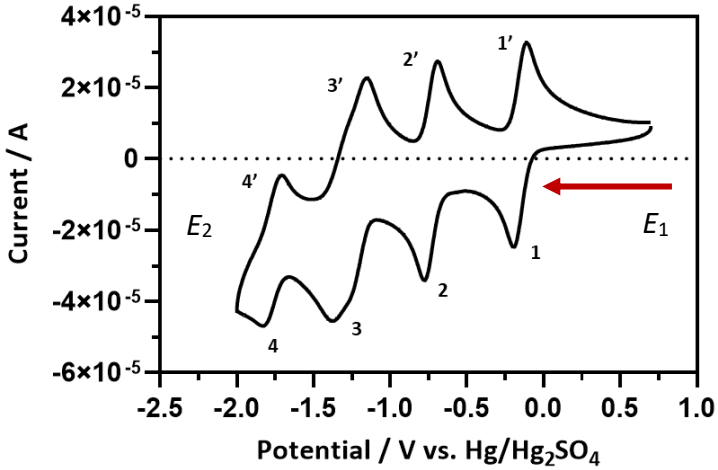

Figure 13: shows the CV scan taken of 2 mM Keggin dissolved in dry DMF with 0.1 M [TBA][PF_6]. The scan was swept from 0.7 V to -2.0 V and back at a scan rate of 100 mV, 2 cycles; displayed above is the second cycle.

The vessel used for a cyclic voltammetry experiment is referred to as an electrochemical cell, Figure 14. During a CV experiment electron transfer occurs, the electrical neutrality is maintained *via* the migration of ions in solution. Electrons move from the electrode to the analyte; the ions move in solution to compensate the charge and close the electrical circuit. Dissolved within the solution is a salt forming the supporting electrolyte, this aids in reducing the solution resistance. High supporting electrolyte concentrations are used to increase solution conductivity. As the electron transfer occurs at the electrodes, the supporting electrolyte will migrate to balance the charge and complete the circuit. The electrochemical event of interest occurs at the working electrode. A potentiostat is used to control the applied potential of the working electrode as a function of the reference electrode potential. The most important aspect of the working electrode is that it is composed of redox inert material in the potential range of interest. A reference electrode is used as a reference point against which the potential of other electrodes can be measured in an electrochemical cell; it has a well-defined and stable equilibrium potential. The applied potential is thus typically reported as “vs” a specific reference. The counter electrode is present to complete the electrical circuit. As a potential is applied to the working electrode to reduce / oxidise the analyte, current begins to flow. The current recorded results from the flow of electrons between the WE and the CE. When studying a reduction at the WE, an oxidation occurs at the CE. As such, the CE should be chosen to be as inert as possible. Counter electrodes can generate by-products depending on the experiment; therefore, these electrodes may sometimes be isolated from the rest of the system by a fritted compartment.

1.6.2.2 Brief Analysis of Observed Reduction Waves of Keggin and Wells Dawson POMs

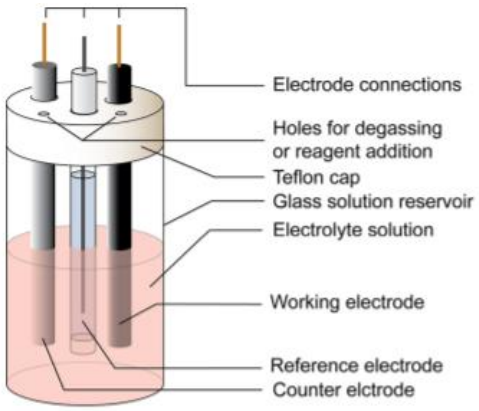

Figure 14: Schematic showing the set up of an electrochemical cell for CV experiments.

Certain slight environmental changes cause a shift in the redox potentials of the Keggin-type POMs ($[SiW_{12}O_{40}]^{4-}$, $[PW_{12}O_{40}]^{3-}$, $[PMo_{12}O_{40}]^{3-}$ and $[GeMo_{12}O_{40}]^{4-}$) and the Wells Dawson-type POM ($[P_2W_{18}O_{62}]^{6-}$) such as the acidity and basicity of the organic solvent. Redox waves of the β-form appear at more positive potentials than those of the corresponding α-form, e. g., β-$[PM_{12}O_{40}]^{3-}$ > α-$[PM_{12}O_{40}]^{3-}$ (M = Mo, W).[54] The pH of the solution can be linked with the potential of the reversible redox pairs. As described above when the heteropoly anions undergo rapid one and two-electron reductions they produce the '*heteropoly blue'* through the LMCT process and the delocalization of electrons on the addenda atoms. These reductions increase the negative charge density and hence the basicity of solution.[64] Both the Dawson and Keggin-type POMs undergo several one-electron reductions in neutral aqueous or organic solutions where no protonation occurs. The subsequent decrease in pH causes the two one-electron processes as more negative potentials to convert into a one two-electron wave, commonly accompanied by protonation.

1.7 Biological Activity of POMs

Polyoxometalates can establish multiple interactions with biological macromolecules (e.g., proteins, and peptides) due to their nano-scale dimensions, charge, and rigidity.[65–67] Additionally the proton coupled electron transfer (PCET) behaviour displayed lead to unique biological activity, with potential applications as anti -bacterials, -virals, and -tumorals.[68] However the biological applications of POMs is restrained due to the inadequate selectivity resulting in toxic side effects, low hydrolytic stability and poor cell penetration. The functionalisation of these structures shows promise for installing better bioavailability and higher stability to the structures, in addition to introducing other useful functionalities e.g. for tracking and delivery.[4]

The antiviral properties of POMs has been at the forefront in bio-active POM investigations.[69] in particular the anti-HIV activities displayed. Ammonium-21-tungsto-9-antimonate, known as HPA-23, was used in clinical trials which were discontinued as the drug showed high toxicity.[70,71] Subsequent studies have focused on the synthesis of less toxic antiviral POMs.[72] Additionally, POMs have shown activity on both Gram-positive and

Gram-negative bacteria. Their use has been tested directly as well as synergistically with conventional antibiotic agents. A series of structure-activity studies was undertaken between POMs against *Helicobacter pylori* and *Streptococcus pneumoniae*. Keggin-type POMs where used, indicating the polyoxotungstates, polyoxovanadotungstates and large highly negatively charged POMs were most effective against *H. pylori*. Polyoxovanadates, on the other hand, showed higher activities against *S. pneumoniae* and other bacteria.[73]

The first mention of the anticancer activity of POMs was by Mukherjee in 1965, where the *in vivo* application of a mixture of $H_3[PW_{12}O_{40}]$, $H_3[Mo_{12}O_{40}]$ and caffeine on gastrointestinal cancer patients was presented.[74] However, the interest in the biological activity of POMs only later developed after 1974 where Jasmin *et al.* demonstrated the inhibitory effect of $(NH_4)_{17}Na[NaSB_9W_{21}O_{86}]$ against sarcoma-virus induced tumours.[75] Following this, Yamase *et al.* pioneered progress in the field through the development of $[NH_3{}^iPr]_6[Mo_7O_{24}]$ known as PM-8.[76] The POM showed a high efficacy *in vivo* towards the suppression of tumour growth in mice, demonstrating increased activity over approved drugs such as 5-fluorouracil (5-FU) and nimustine.[77] Fujita *et al.* showed a study identifying the anticancer activity of 50 POMs including PM-8 and variants of it.[78] From this Yamase noticed that PM-8 seemed to reduce into a more toxic form (PM-17) and then be re-oxidized, reducing and killing the tumour cells.[79] This mechanism was accepted due to the ability of FMN (an electron carrier responsible for the electron transport from NADH to coenzyme Q) to biologically reduce PM-8.[79,80] as this process is coupled with the generation of ATP the proposed redox-cycle for the apoptosis of cells is based on the inhibition of ATP formation.

Despite this success current research focus is shifting from inorganic POMs to organic-inorganic hybrid POMs where the functionalisation and encapsulation of POMs with organic moieties can not only reduce toxicity but also increase the anti-tumoral activity.[4,59,61,81]

1.7.1 Electrostatic Interactions of POMs and Proteins

Due to the increased interest in the biological activity of POMs many research groups have focused on the interaction between POMs and proteins. A number of studies have indicated that POMs bind to specific sites on the protein surface.[82–84] The difference in the amino acid (AA) sequences of two proteins, of bovine and human serum albumin, resulted in a

difference in interaction strength, affecting the folding and surface charge.[85] Whilst a thermodynamic study showed that the binding stoichiometry of the POM-protein complex was affected by the temperature and ionic strength of the solution.[86] The electrostatic interactions and hydrogen bonding between the basic oxygen atoms of POM clusters and of the side chains of positively charged AAs (arginine and lysine) and of polar uncharged AAs (tyrosine, serine and asparagine) were observed using molecular dynamic simulations. Several AAs may interact simultaneously with the POM depending on its shape and size, resulting in a cooperative effect.[87]

1.7.1.1 POMs in Protein Crystallography

Protein crystallography is notoriously complex due to many proteins having intricate three-dimensional structures, recent work has focused on the beneficial effects of POMs on protein crystallization.[88] This potential was initially demonstrated through the addition of a hetero-polytungstate cluster to ribosome crystals resulting in the improved resolution of the structure determination. The POM showed a two-fold benefit: providing anomalous phasing power and importantly the stabilisation of selected functional conformations.[89]

Through the study of several POM structures Rompel *et al.* demonstrated that the Anderson-Evans type polyoxotungstate ($[TeW_6O_{24}]^{6-}$) was superior as a crystallization additive.[90,91] Through the group's method of using POM as additives they managed to crystallize previously unknown protein structures such as: mushroom tyrosinase[92,93] and aurone synthase[94], while hen egg white lysozyme (HEWL) was crystallized in a new crystal form.[91] Additionally, the advantages of these Anderson-type POMs were recently summarized and the promise of an extension through the modification of the inorganic core suggested.[90]

1.7.1.2 POMs as Enzyme Mimetics and Inhibitors

The ability of POMs to catalyse reactions and interact with bio-molecules motivated their use as enzyme mimetics, especially their use in proteomics. The hydrolysis of lysozyme was first reported by Stroobants *et al.* by a Ce-substituted Keggin type POM ($[Ce(\alpha\text{-}PW_{11}O_{39})_2]^{10-}$) under physiological conditions.[86] The electrostatic interactions between the POM and protein were shown to be detrimental for the hydrolysis to occur when the hydrolysis of α-

lactalbumin, a structurally highly homologous protein with a different surface potential, was attempted. It was proposed that the reactivity of the metal cation towards the protein surface, similar to the molecular recognition of an enzyme, was directed by the POM structure towards the positively charged areas on the protein surface.[95] Selective peptide bond hydrolysis was also achieved for human serum albumin, oxidized insulin chain B, myoglobin and cytochrome C with a range of Ce(IV)-substituted and Zr(IV)-substituted Lindqvist- type, Keggin-type and Wells–Dawson type POMs.[83,96,97]

Due to the ability to easily modify and isolate hetero-polyoxometalates they are preferred for the inhibition of enzymes. The hydrolytic stability is of great importance as this causes POMs to remain stable under experimental conditions allowing for the identification of active species.[66] This hydrolytic stability can be further increased through the incorporation of metal atoms or organic ligands, and grafting of bioactive compounds. Several different enzyme families have been shown inhibition by POMs with potencies ranging from micromolar to nano-molar concentrations. Stephan *et al.* compiled an overview of the inhibition of enzymes by POMs. The group indicated the interaction between POMs and the target proteins at the extracellular site dives the observed biological and *in vivo* effects of POMs.[98]

1.7.1.3 POMs as Anti-Amyloid Agents

A contributing factor to the development of amyloid diseases such as Alzheimer's disease (AD), Parkinson's disease (PD), Huntington's disease (HD) Creutzfeldt-Jakob disease (CJD) and type II diabetes is thought to be contributed by a disruption in the balance between the production and clearance of amyloid proteins. Hence accelerating the clearance of these proteins forms a promising treatment strategy.[99] Through multiple analysis techniques Zhou *et al.* showed that two POMs, the small Keggin-type metatungstate $[H_2W_{12}O_{40}]^{6-}$ and the larger wheel-shaped Preyssler anion $[NaP_5W_{30}O_{110}]^{14-}$, alter the amyloid aggregation behaviour.[100] A novel strategy developed by Li *et al.* reported the self-assembly of POM and the Ab15-20 peptide, forming colloidal spheres which inhibit amyloid aggregation. The group also developed a technique for the fluorescent monitoring of the aggregation process. Other efforts made to improve on POM-based amyloid aggregation inhibition include the combined use of POMs as inhibitors and photo degradation agents[101] and the

use of POM nanoclusters, transition-metal-substituted POMs[102]; and nanoparticle and nanorod-based POM compounds.[103,104]

1.7.2 Activity of Organic-Inorganic Hybrid POMs

As indicated due to their surface characteristics purely inorganic POMs usually exhibit toxic side effects and limited cell penetration, therefore the main focus of bioactive POMs is the functionalisation of POMs with organic groups. Depending on the biological moiety grafted to the POMs it can result in an increase in stability in aqueous solution, an enhanced and more specific interaction with the biological target and a change in surface, charge, polarity and redox properties. An indication of the work carried out towards these goals is described below.

1.7.2.1 Organo-metallo substituted POMs

Due to the biological activity exhibited by many organometallic molecules their use for hybridisation seems promising.[105] Several studies were carried out on Keggin-, sandwich Keggin- and Wells-Dawson-type structures containing organotin RSn (R = $C_4H_7O_2$, $C_5H_9O_2$, and NC_3H_4) or metal-cyclopentadienyl CpM^{n+} groups (Cp = η_5-C_5H_5, M = Ti^{IV}, Zr^{IV}, V^{IV}, Fe^{II}) against human cervical (HeLa) and liver (SSMC-7721) cancer cells.[106,107] The studies concluded that sandwich-Keggin clusters showed superior activity over Keggin structures and structures with attached cyanoethyltin groups (NC_3H_4Sn) were more active than ester-tin groups ($C_4H_7O_2Sn$ and $C_5H_9O_2Sn$), increasing the RSn content showed enhanced antitumour activity. Additionally, the studies revealed that the antitumour activity correlated with their redox potential, the stronger the oxidation ability of the POM, the higher the cytotoxicity.[108] Some of these clusters were seen to have superior activity over the clinically approved drug cyclophosphamide (CP) against SMMC-7721 (inhibitory rate = 37.2 % at 36.4 mg kg^{-1}) but less active than 5-FU against other cell lines (56-57.4 % at 15-30 $mgkg^{-1}$), and it was shown to be the least toxic compound.[109]

1.7.2.2 POM-Drug Hybrids

Due to the synergistic properties that can be displayed by POM-drug hybrids capable of interacting with multiple targets, these hybrids are likely to have less drug resistance and

exhibit improved activity and selectivity. This was demonstrated by the functionalisation of Keggin polyoxotungstates ($[PW_{12}O_{40}]^{3-}$, $[SiW_{12}O_{40}]^{4-}$, and $[BW_{12}O_{40}]^{5-}$) with the anticancer drug 5-FU, these hybrids showed a higher activity against the tumour cell lines HeLa, Hep-G2, and SMMC-7721 than 5-FU alone.[110,111]

The Dolbecq group investigated the antitumour activity of a series of POM-bisphosphonate complexes.[112–115] These will be elaborated upon in Chapter 5.

POM-quinolone complexes have also been shown to display anti-tumoural properties.[108,116–118] Quinolone antibiotics such as pipemidic acid (PPA) inhibit the growth of Gram-negative bacteria via preventing DNA from unwinding and duplicating. Quinolones make good multidentate ligands for POM hybridisation due to them containing abundant *O* and *N* donors. Several Keggin-type polyoxotungstates and an octamolybdate were decorated with several quinolone antibiotics such as PPA, enrofloxacin (enro), norfloxacin (norf), and enoxacin (eno); as well as some transition metals (Cu^{II}, Zn^{II}, Ni^{II}, Co^{II}) being incorporated into the structures.

The quinolones acted as organic ligands for the transition metals. The complexes exhibited mixed results against cancer cell lines as only several of them showed good antitumor activity, the vast majority showed no to moderate activity. Some of the reduced activity was attributed to the steric hindrance between the POM and tumour cells.[108]

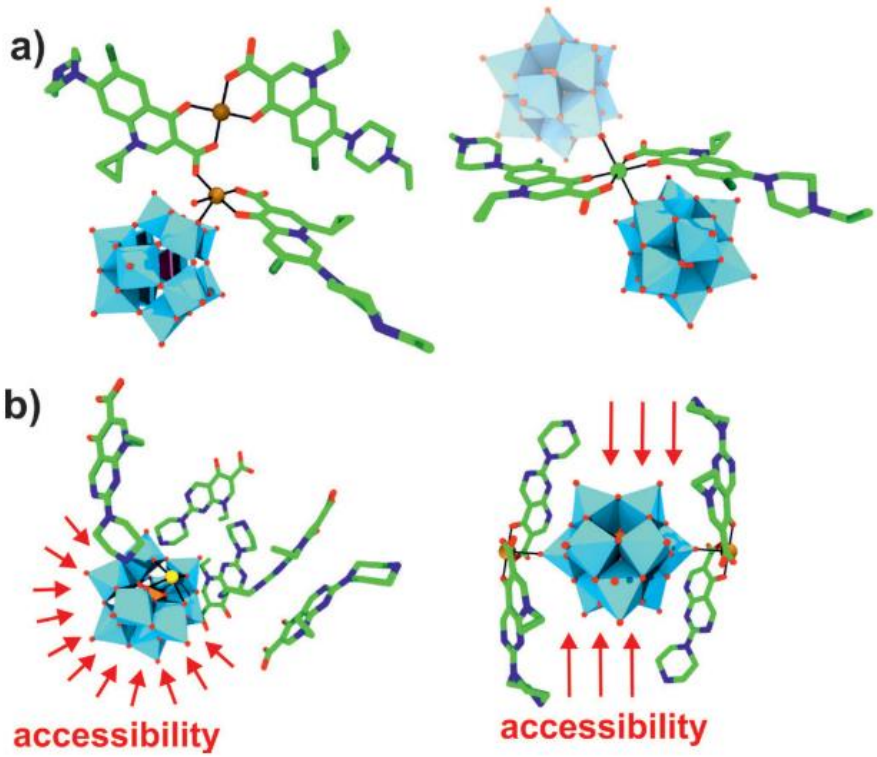

Figure 15: structures of POM-quinolone hybrids. POMs are decorated with different quinolone antibiotics such as pipemidic acid (PPA), enrofloxacin (enro), norfloxacin (norf), and enoxacin (eno). A) $[Cu_2(Enro)_3H_2O][SiW_{12}O_{40}]$ (left) and $H_2[Ni\ (Enro)_2][SiW_{12}O_{40}]$ is indicated by a transparent molecule; however, in solution this site is most probably occupied by a solvent molecule. B) $[HPPA]_5[PW_{11}CdO_{39}]$ (left) and $[Cu\ (PPA)_2]_2[PW_{12}O_{40}]$ (right). Red arrows indicate the accessible inter-action sites. Light blue polyhedral are $\{WO_6\}$, orange polyhedral $\{PO_4\}$, green sticks carbon, dark blue sticks nitrogen, dark green sticks fluorine, brown sphered copper, green sphere nickel, yellow sphere cadmium, red sticks, and spheres oxygen. Image reproduced from A. Bijelic, M. Aureliano and A. Rompel, Angew. Chemie, 2019, 58, 2980–2999.[4]

1.7.2.3 Anderson POM-Biomolecule Hybrids

The Anderson structure is at the forefront of structures studied due to the ease of its tris-functionalisation (tris =tris(hydroxymethyl)amino- methane) which can be further modified through simple amidation.[9,119–121] Yang *et al.* studied several Anderson-type structures grafted with bioactive receptor ligands, with the aim to increase the selectivity and antitumour activity of the POM.[122] The molybdate Anderson was symmetrically functionalised with five groups, cholic acid (CA), dehydrocholic acid (DHCA), *O*-succinyl-choles- terol (CHOL), 6-O-(3-carboxypropanoyl)-1,2:3,4-di-*O*-iso-propylidene-b-d-galactopyranose (GAL) and adipic acid (AA), Figure 16.

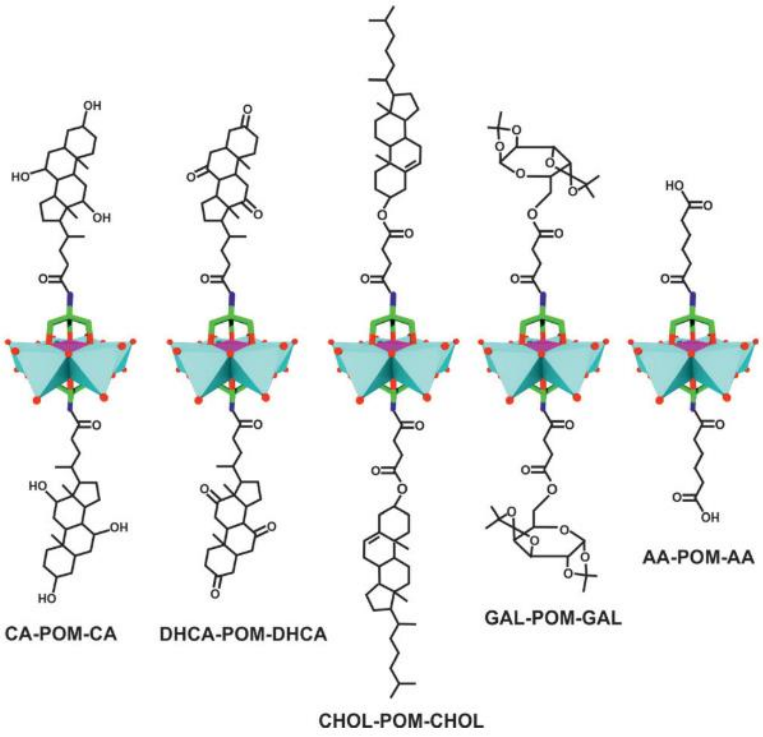

Figure 16: Biomolecule-functionalized Anderson structures. Cyan polyhedra are {MoO6}, magenta polyhedral {MnO6 }, green sticks carbon, dark blue sticks nitrogen, red spheres oxygen. Abbreviations stand for cholic acid (CA), dehydrocholic acid (DHCA), O-succinyl-choles- terol (CHOL), 6-O-(3-carboxypropanoyl)-1,2:3,4-di-O-iso-propylidene-b-d-galactopyranose (GAL) and adipic acid (AA). Image taken from A. Bijelic, M. Aureliano and A. Rompel, Angew. Chemie, 2019, 58, 2980–2999.[4]

The cytotoxicity of these hybrids was tested against breast cell lines MCF-7 and MDA-MB-231 as well as a noncancerous breast cell line MCF-10A. Two POMs stood out exerting the highest selectivity and antitumour activity; the CA-POM-CA (IC50 = 55.9, 37.9 and 278.2 µM) and DHCA-POM-DHCA (IC50 = 112.7, 149.0 and > 400 µM).[123] Of note is that in a biological context these alone are rather poor anti-cancer agents as their IC50 values are much higher than the 10 µM cut off required for NCI-60 screening tests.

1.7.2.4 POM-Amino acid Hybrids

The 21 canonical amino acids are the basic building blocks of the proteome. Their specific combination forms peptides and proteins with specific structures. They show diversity due to their unique functional side chains. This structural and chemical variety and biocompatibility makes them promising organic units for POM biofunctionalization.

Several POM-AA hybrids have been synthesised, displaying anticancer activity. Kamenar *et al.* functionalised a γ-isomer of the octamolybdate, γ-$[Mo_8O_{26}]^{4-}$, with different amino acids

to form four hybrid structures: $Na_4[Mo_8O_{26}(ala)_2]$, $Na_4[Mo_8O_{26}(glygly)_2]$, $[Hmorph]_4[Mo_8O_{24}(OH)_2(met)_2]$, and $[Hmorph]_4[Mo_8O_{24}(OH)_2(ala)_2]$ (Ala = alanine, glygly = glycylglycine, morph = morpholine, Met = methionine). These demonstrated the selective inhibition of the cell growth of human liver and breast cancer cells (Hep-G2 and MCF-7) with no significant effect on other cancer cell lines.[124] it was determined that the antiproliferative properties displayed by these hybrids did not induce apoptosis as the activity was not cell-cycle related. Later a proposal made by Cartuyvels *et al.* suggested that the antitumour activity of octamolybdates and such hybrids could be connected to the hydrolysis of ATP. This is due to the group observing the ATP hydrolysis in the presence of $Na_4[Mo_8O_{26}(pro)_2]$ (pro = proline) at acidic pH (< 5.8).[125] However, other research on the role of ATP hydrolysis during cancer progression is tenuous, as ATP has been seen to exhibit biphasic actions; as in it has both tumour promoting and inhibitory effects.[126]

Other studies concentrating on the hexamolybdate Anderson-type structures decorated with glycine: $K_2Na[AsMo_6O_{21}(Gly)_3]$ (Gly = glycine). This hybrid showed weak to moderate inhibitory effects against human lung carcinoma cells (A-549, IC50 = 330.2 μM), however still superior to that of 5-FU (ca. 40 % inhibition at 1 mM).[127] Later the arsenomolybdate was found to have higher activity than all-*trans* retinoic acid, which is a clinical anticancer drug, but less active than the antileukemic agent As_2O_3.[128] The disadvantage of As_2O_3 is its high cytotoxicity towards normal cells e.g. human umbilical vein endothelial cells (HUVECs), comparing the arsenomolybdate hybrid which showed no significant activity on HUVECs. It was suggested that the selective anti-leukemic activity displayed by the hybrid could be sue to the As^{III}, making it a promising alternative in leukemia treatment.[4,129]

1.8 Disulfide Bonds in Nature

The interest in sulfhydryl compounds and their redox processes in chemistry and biochemistry is easily understood due to their diversity in functions. Notably, they play a vital role in normal cell biology and in defence of cells against oxidants, free radicals and electrophiles.[130] A linkage between two cysteine (Cys) molecules within a protein is referred to as a disulfide-bond/ bridge/ cystine. Native disulfide bond formation is critical for the correct folding of many proteins; these bonds can be found in nearly one-third (7000) of the proteins in the eukaryotic proteome.[131] Disulfide bond formation commonly starts with the

formation of sulfenic acid (-SOH), which rapidly condenses. Alternatively to the formation of this cystine, the formation of sulfinic acid (RSO(OH)) and sulfoxides (R−S(=O)−R') are not particularly common, being readily oxidized to the sulfonic acids and sulfones, respectively.[132]

1.8.1 The Formation of Disulfide Bonds

An integral function of the disulfide bond it to stabilize the tertiary and quaternary structures of proteins. There is evidence that certain proteins contain some labile disulfide bonds, resulting in functional changes. However, bonds found to be structurally important are not exposed at the protein surface.[133] These structural disulfides are critically important for the stability of secreted and plasma-membrane proteins destined to function in the harsh oxidizing extracellular environment,[134] outside of the cytosol. This presents a challenge in terms of folding and assembly of complex hetero-oligomeric proteins from extended polypeptide chains by eukaryotic cells under cellular conditions whilst monitoring the outcome and ensuring the protein function in its requisite location[135]. Nature's solution to this was the endoplasmic reticulum (ER); a vast reticular organelle present in all nucleated eukaryotic cells containing oxidoreductases and members of the protein disulfide isomerase (PDI) family[134,135]. Hence the biosynthesis of these proteins is primarily in the ER which has a chemical environment similar to the outside of the cell in terms of ion concentrations and oxidizing capabilities. These structural disulfide bonds exist as intra-molecular (i.e. stabilizing the folding of a single polypeptide chain) and inter-molecular disulfide bonds (i.e. multi-subunit proteins such as antibodies or the A and B chains of insulin),[136] generated in a highly controlled fashion predominately by the oxidoreductases[137,138] family, recent studies have identified several other mechanisms for the controlled disulfide bond formation[139]. In addition to the importance in the folding and structure of a protein, thiol redox reactions are an essential part of catalytic activity of several metabolic enzymes. The reactivity of proteins can be altered by changing the redox state of the Cys residues; under specific cellular conditions several transcription factors, including the bacterial OxyR and Hsp33,[140] also become activated by the oxidation of Cys residues that form disulfide bonds[141,142].

The first protein folding catalyst studied and reported was protein disulfide isomerase (PDI) and despite many advances in the past five decades of study there is still a lot unknown. However, many other pathways have since been observed; additionally, many similarities have been established at a mechanistic level of function between the prokaryotic and eukaryotic pathways of disulfide bond formation.

Due to the large interest in disulfide bonds the chemistry of their formation is well established. The formation of a disulfide bond from two Cys thiols (-SH) is a two-electron oxidation often coupled to the reduction of oxygen, flavin cofactors, oxidized glutathione and other electron acceptors. The spontaneous formations of a disulfide bond *in vitro* simply involve the loss of electrons from the two thiols coupled with the gain of electrons by an available acceptor, such as oxygen. Despite the association of oxygen with protein thiols being thermodynamically favorable it can be kinetically slow; this can be overcome through the use of an intermediary such as a transition metal or flavin[143].

In contrast, *in vivo* disulfide bonds are predominantly formed via thiol-disulfide exchange reaction of free thiols with a disulfide-bonded species, shown in Figure 17. This reaction can occur between a cysteine and any sulfhydryl-containing compound e.g, glutathione (GSH). Thiol-disulfide exchange reactions provide the basis of catalyzed protein disulfide-bond formation from prokaryotes to eukaryotes. Such an exchange reaction as demonstrated in Figure 17 can also occur intramolecularly, leading to the rearrangement of disulfide bonds within a protein. After the completion of the thiol-disulfide exchange reaction, the redox state of the active-site Cys in either product can regenerate for another catalytic cycle by another protein, or by a redox molecule such as glutathione.

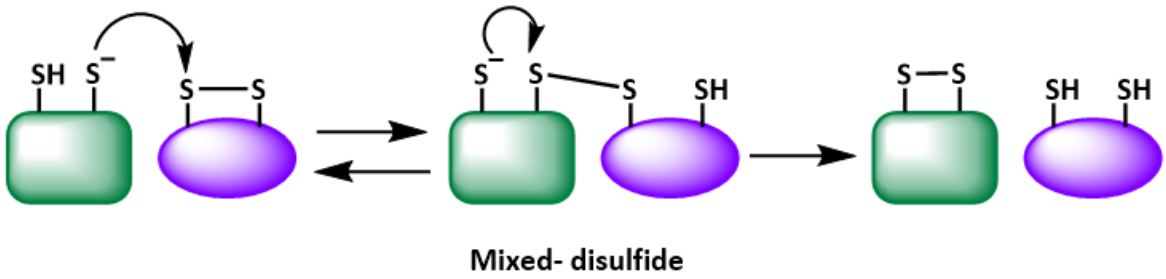

Figure 17: Thiol-disulfide exchange between proteins. The deprotonation of a free thiol forms the formation of a thiolate anion ($-S^-$), this displaces one sulfur of the disulfide bond in the oxidized species. This results in the formation of a transient mixed disulfide bond between the two proteins (or between a protein and a redox molecule). The second exchange reaction comprises of the thiolate anion attacking the mixed disulfide bond and resolving it. The net product of the reaction is the oxidation of the originally reduced protein and the subsequent reduction of the initially oxidized redox species.

1.8.2 Reactions of Thiol-Containing Biomolecules

Disulfide bonds play a vital role in normal cell biology due to their function in proteins for structure but also in defence of cells due to their reactivity against oxidants, free radicals, electrophiles[130] and their affinity for metals. This highlights the importance of the redox-active relationships between intramolecular protein disulfides and mixed disulfides with small-molecule thiols (eg, glutathione), in regulating protein activity and localization in response to cellular redox potentials. Hence redox-active disulfides are highly dynamic and are influenced by oxidative or reductive changes in the local environment, unlike static disulfides[144]. Making them versatile in the biological roles they play but also a potential downfall for modification and dysregulation to destabilize normal biology. This highlights the interest taken by researchers in the study and identification of the delicate balance of productive versus pathogenic reactions occurring among thiol groups in small molecules and proteins. These variations are attributed to several factors including pKa, redox potential, entropy, and bond-strain energy.

1.8.2.1 Redox Potential

A favourable pathway of disulfide-bond transfer can be determined by the comparison of the relative redox potentials of proteins and other redox active molecules. For example, consider the action of thioredoxin (Trx1), a powerful cytosolic reductase. This can be rationalized due to its active site having a more reducing redox potential relative to

cytoplasm. The redox potential specifies the propensity of a thiol-disulfide to be reduced and hence dictates the formation and stability of that species in a given redox environment[145], expressed in quantitative terms. Hence a short summary of the principles shall be provided here. A redox pair refers to a pair of molecules which can be interconverted by the addition or loss of electrons, these interconversions can be written in the form of a reductive or oxidative half-reaction.

The redox potential can be determined experimentally by measuring the relative amounts of oxidized and reduced protein species in a redox equilibrium with a compound of known redox potential. A full reaction involves the coordinated reduction (gain of electrons) of one species and the oxidation (loss of electrons) of another. Their energetics of simple biomolecular electron transfer reactions can be analyzed through forming two half - reactions, identifying the electron explicitly being gained or lost noted. For example Kaiser *et al.*[140] consider an oxidized protein P(SS) and the reduced protein species $P(SH)_2$ relative to glutathione, the reduced form GSH and the oxidized form GSSG; the half equations are shown in *equations X* and *X*.

$P(SH)_2 \leftrightarrow P(SS) + 2e^- + 2H^+$ Equation 1

$GSSG + 2e^- + 2H^+ \leftrightarrow 2GSH$ Equation 2

Forming the net reaction: $P(SH)_2 + GSSG \leftrightarrow P(SS) + 2GSH$

This can be used to find the equilibrium constant of the overall reaction, taking k_1 as the forward reaction and k_2 as the reverse:

$$K_{eq} = k_1 k_2 = \frac{[P(SS)][GSH]^2}{[P(SH)_2][GSSG]}$$ Equation 3

The redox potential of a protein is most often expressed as an electrochemical potential (E_p) in units of volts. A reaction is thermodynamically favorable (spontaneous) if $E^e > 0$, where E^e is the standard reduction potential associated with each half-equation[146]. This refers to the electrode potential of each half equation compared to the standard hydrogen electrode, under 'standard' conditions defined as 298.15 K, 1M concentration of each component and 1 atm; by convention, biochemical standard conditions use a pH value of 7, noted by the inclusion of a 'prime' symbol, hence E^e' entitles the biochemical standard reduction potential.

In order to calculate the reduction potential associated with a given redox couple under defined conditions the Nernst equation can be used:

$$E_p = \frac{RT}{nF} lnK_{eq} + E_G$$ Equation 4

In this equation T is the absolute temperature (in K), n is the number of electrons transferred in the reaction, and R and F are the universal gas and Faraday constants, respectively 8.314 $JK^{-1}mol^{-1}$ and 96,485 $JV^{-1}mol^{-1}$, E_G refers to the electrochemical potential of glutathione and K_{eq} is shown above in Equation 4.

For the net reaction the change in $E^{e'}$ ($\Delta E^{e'}$) is calculated from the difference between the standard biochemical reduction potentials of the component half reactions:

$\Delta E^{e'}$ = [$E^{e'}$ of the half-reaction containing the oxidizing agent] – [$E^{e'}$ of the half-reaction containing the reducing agent]

If the resulting value of $\Delta E^{e'}$ is positive the reaction under standard conditions and pH 7 is spontaneous. And hence, the standard free energy change associated with this reaction can also be calculated from $\Delta E^{e'}$ according to the following relationship:

$\Delta G^{e'} = -nF\Delta E^{e'}$ (or equivalently $\Delta G = -nF\Delta E$ under any conditions).

Usually, for cellular disulfides, redox potentials are measured relative to glutathione as a standard. Taking glutathione as an example due to the high (mM) concentrations of oxidized and reduced forms of glutathione found in cells (GSSG/GSH), the GSSG/GSH couple often controls the oxidation and reduction of disulfides through the thiol-disulfide exchange reaction. Hence, in these scenarios redox potentials are often measured against a glutathione standard. Disulfide bonds with more negative redox potentials are considered more stable and less likely to undergo the exchange reactions in the presence of glutathione. It has been noted that the redox potentials for protein disulfides varies by at least 375 mM[134]. For example, the intracellular half-cell potential of the GSSG/2GSH couple varies from E ~-240 mV to -170 mV.[147]

1.8.2.2 Thiol pKa

The pKa of both the nucleophilic cysteine thiol and the leaving-group thiol affects the kinetics of the exchange reaction. The chemical moieties normally referred to as thiol groups meaning the R-SH forms can be deprotonated (loss of H+) forming the charged thiolates (R-S-). The standard pKa for a thiol is 8.5 resulting in protonation at physiological pH; however, Cys pKa is known to range from much lower pKa of 3.5 to <12 depending on the local microenvironment[139,143] and H-bonding.

Considering the nucleophilic Cys thiol; electron withdrawing groups or nearby positive charges can stabilize the thiolate and hence decrease the pKa of the Cys, this results in an increase in rate of the thiol-disulfide exchange reaction. Therefore, the rate constant peaks when the thiol pKa is equivalent to the solution pH[148]. On the other hand, a decrease in the leaving group thiol pKa results in an increase in the rate of exchange, irrespective of the solution pH. When thiol addition reactions take place at asymmetrical disulfides (RSSR'), the thiol with the lowest pKa acts as the leaving group.

1.8.2.3 Entropy

Defining entropy to be the measure of disorder and randomness in a system, wherein a gain in entropy drives the rate of formation. The entropic barriers, including rotation and translation, affect stability of the formation of a disulfide bond. Firstly, consider a denatured protein, if there is a large distance between cysteine residues the entropic barriers are higher, this is due to the rotational and translational freedom characteristics of denatured proteins. However, if two cysteine residues are close together within the primary sequence the amount of conformational freedom decreases and the orientations allowing for the formation of the disulfide bond increases; this results in a decrease in the entropic cost of the disulfide bond formation. Conversely the tertiary structure of a folded protein has the potential to bring the Cys residues closer together making the bond formation more thermodynamically favorable and leading to faster disulfide bond formation relative to denatured proteins[134,148,149]. Secondly, the factors to consider differ between intermolecular or intramolecular disulfide bonds, overall intramolecular disulfide bond formation is associated with a decreased loss in entropy than intermolecular bond formation. This can be

largely linked to the thiols in intramolecular situations already being connected in the same molecule; whereas intermolecular bonds link two separate molecules together which in turn results in a loss in translational and rotational degrees of freedom. The effective concentration of thiols could be high where an intramolecular bond forms, any factors which place two cysteines in proximity with the correct geometry will lead to a decrease in spatial degrees of freedom and an increase in effective molarity. These factors together increase the rate of reaction and shift the equilibrium in favour of bond formation[145]. Therefore overall, the formation of an intramolecular disulfide bond is more efficient than the formation of an intermolecular bond.

1.8.2.4 Strain

The formation of new bonds can lead to strain which is directly connected to the stability of the bond. Only little to no strain introduced upon formation of the disulfide will lead to a stable bond, but some structural disulfides have very high equilibrium constants[145]. The formation of a bond could for example decrease the flexibility, imposing strain and in turn decreasing the stability of the bond. The ideal dihedral angle for a disulfide has been determined to be ± 90◦, studies have shown that distortion of the angle can lead to an increased redox potential of 10-100 mV[150].

It has been found using single molecule force-clamping spectroscopy that the thiol-disulfide exchange reaction is actually promoted by force, this means if strain is associated with the formation of a bond the kinetics are affected and the nucleophile is more reactive[145,151].

An interplay between the folding and disulfide bond formation has been identified in secretory disulfide-containing proteins. As explained above, bond formation in unfolded/denatured proteins leads to the loss of translational, rotational, and vibrational degrees of freedom. If a disulfide is formed which is incorrect the bond will remain unstable as it is not supported by the overall stabilization of the structure in the folding pathway.

Disulfide bond formation is made more favourable by the noncovalent interactions (in the secondary and tertiary structure of the protein) imposing organization on the unfolded protein because a decrease of entropy loss is then associated with the bond formation. The folding and formation of the protein overall structure will drive the correct formation of

disulfide bonds. It should be recognized that under reducing conditions the formation of the correct disulfide linkages may proceed more efficiently as isomerization is favoured and formation of correct disulfides are ultimately driven by the formation of the correct fold.[145]

1.8.2.5 Redox-Active Disulfides

Unlike static structural disulfides, redox-active disulfides are highly dynamic and are regulated by oxidative and reductive changes in the local environment. The formation and reduction of these bonds impacts their activity and cellular localization. Efficient and controlled formation of structural disulfide bonds is essential to maintaining protein integrity. The dysregulation of cellular redox potentials can result in aberrant oxidation or reduction of redox-active disulfides contributing to diseases such as Parkinson's, thrombosis and pre-eclampsia.[130,152–155] Dysregulated structural disulfide-bond formation is a characteristic of diseases such as Creutzfeldt-Jakob disease (CJD)[156], amyotrophic lateral sclerosis (ALS)[154] and oxidative stress[134].

1.8.3 Example Thiols of Interest

1.8.3.1 A Labile Disulfide: Angiotensinogen

Herein, our focus is on angiotensinogen (**AGT**); a non-inhibitory member of the serpin family of protease inhibitors.[157,158] AGT contains a labile disulphide bond which can form between Cys-18 and Cys-138, Figure 18. The oxidation of these thiols results in the formation of a disulfide bridge exposed at the proteins surface; subsequently changing the conformation of the protein. This alteration in shape results in the exposure of an angiotensin-containing tail. Renin cleavage yields the decapeptide, angiotensin I. Angiotensinogenase (Renin) is an enzyme that participates in the renin-angiotensin-aldosterone system (RAAS). This is the precursor to the vasopressor octapeptide, angiotensin II, by the angiotensin converting enzyme (**ACE**).[159] Angiotensin II is a major contributor to high blood pressure. Hence the presence of this disulphide bond, between Cys18-Cys138, is a clear indication to the imminent increase in blood pressure; leading to damage of the heart, kidneys, brain etc and contributing to over 62,000 unnecessary deaths per year in the UK alone.[160,161]

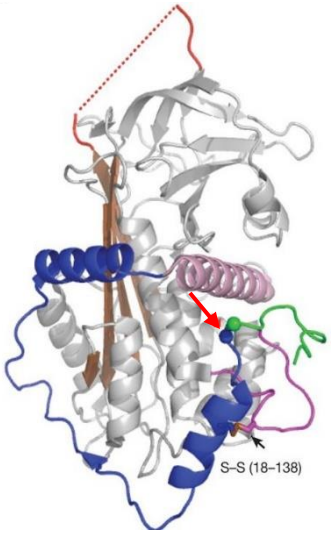

Figure 18: the protein angiotensinogen, a member of the serpin family. AGT displays a conformational change upon the oxidation of the disulphide bridge between Cys18 and Cys138, allowing for the green end N-terminus to stick out and be cleaved by renin at the point indicated with the red arrow. Figure from: Zhou, A., Carrell, R., Murphy, M. et al. A redox switch in angiotensinogen modulates angiotensin release. Nature 468, 2010, 108–111.[155]

The development of an analytical technique to probe the redox state of biologically significant S-S bonds and thus enable the quantitative measurement of AGTox (the oxidized form of AGT) would allow rapid diagnosis and more effective treatment of hypertension and diseases such as pre-eclampsia.

Despite a wide variety of literature precedent regarding the identification of free thiol concentration in biological medium and proteins,[162] there are few established analytical techniques for the determination of intact disulfides using rapid, operationally simple and cheap methods. In spite of applications such as chromatographic[163] or electrophoretic[164,165] separation providing high resolution and clear differentiation between oxidized and reduced thiols within proteins; sample preparation and calibration is not a trivial task.[166]

1.8.3.2 Immunoglobulin G3 (IgG3) Antibody

The primary peptide disulfide tested throughout chapter 2 and 3 is a peptide based upon a disulfide bond found within the immunoglobulin G3 (IgG3) antibody.

Antibodies are part of the adaptive immune system and play a major role in protection against infections by binding to and inactivating invading pathogens/ antigens.

Immunoglobulins are a group of closely related glycoproteins, comprised of 82 – 96 % protein and 4 – 18 % carbohydrate. They all have a basic 4-chain structure; 2 identical heavy chains and 2 identical light chains, figure 20, linked by intermolecular disulfide bonds. It was this symmetry that drew us to use them initially due to the simplicity of synthesis and oxidation.

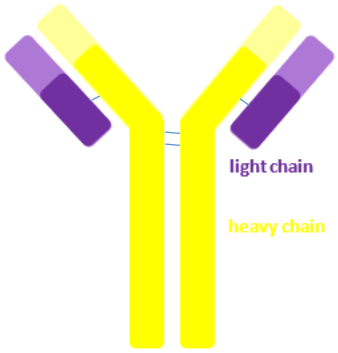

Figure 19: showing the basic structure of an antibody, merely to indicate where the chains would lie, this is not representative of any antibody in particular.

The glycoprotein IgG forms 75 % of immunoglobulins in the plasma of a healthy individual, making it the most abundant and a major effector molecule of the humoral immune response in man. The other 25 % is comprised of IgM, IgA, IgD and IgC. IgG has 4 subclasses: IgG1 (60-70% in plasma), IgG2 (20-30%), IgG3 (5-8%), and IgG4 (1-3%).[167] The amino acid sequences are >95% homologous in the constant domain of the heavy chains of the human IgG subclasses. The most obvious differences between the subclasses is the amino acid composition and structure of the 'hinge region'; which refers to the part of the molecule containing disulfide bonds between heavy chains). The flexibility within the hinge region decreases in the order IgG3 > IgG1 > IgG4 > IgG2. The superior stability in the IgG3 class is due to its unique extended hinge region consisting of 62 amino acids (with 21 prolines and 11 cysteines) forming an inflexible polyproline double helix consisting of 11 disulfide bridges (compared with two in the hinge region of IgG1 and IgG4, and four in the hinge region of IgG2). But, this forms a more accessible hinge region making IgG3 more susceptible to cleavage by proteolytic enzymes. In addition to the elongated hinge region and greater flexibility; IgG3 also displays extensive polymorphisms and additional glycosylation sites not presented on other subclasses. These physiochemical characteristics make IgG3 a uniquely potent immunoglobulin.[168]

Research on IgG3 alone is extensive and will not be covered further here however more information can be found in the referenced material. Our interest in IgG3 was due to the homology of the chains and the abundance of disulfides. The peptide used for most of the studies to be described in this report are based on the disulfide bond found in a heavy chain of an IgG3 glycoprotein, figure 20.

1.8.4 Established Techniques for Thiol and Disulfide Detection

Nature is well versed in these oxidation and reduction processes for specific functions. Due to the profound effects that can be induced through the action of these redox-active disulfides the detection of relevant bonds is of a great deal of interest.

The advancement in biochemical analysis methods has contributed to an increase in accuracy of detection techniques and manipulation of these protein redox states in various biological processes, allowing for alterations in protein thiol redox state to be monitored. Currently there are several methods for the detection of the redox bond between two cysteines in biological systems. These are applicable for inter- and intra-protein disulfides as well as reduced protein thiols[169].

1.8.4.1 Monitoring Reduced Protein Thiol Species

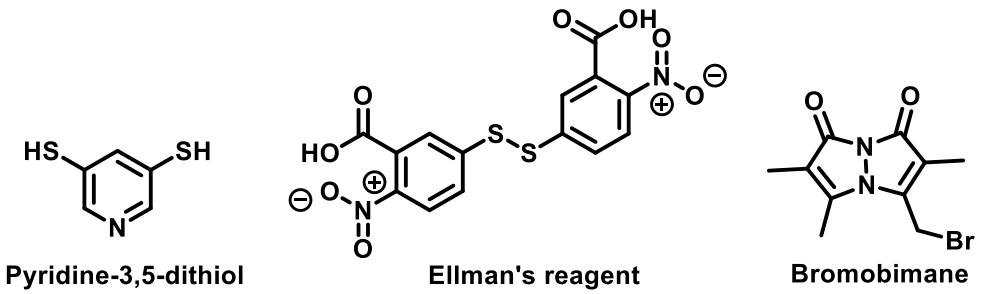

Figure 20: the structures of three popular thiol-disulfide exchange reagents are shown.

Generally established methods primarily cater to reduced protein thiols; these identify a system being in oxidative stress when lower levels of reduced thiols are identified. The most popular thiol-disulfide exchange reagents are pyridyl dithiol and 5-thio-2-nitrobenzoic acid-thiol derivatives (Ellman, 1959; King *et al.,* 1978), structures are shown in Figure 20. A classic example for free thiol detection is the Ellman's assay which provides a colorimetric readout of totally reduced thiols; a major issue with this technique is its inability to detect subtle

changes in thiol redox state, in addition to requiring the reduction of disulfide bonds. Conversely, it has been used in the pre-activation of the Cys residue for subsequent modification.[170] Bromobimanes[171,172] have proven to show more stability, fluorescence and sensitivity than DTNB; however, these still require the use of a generic tag-based reductive switch-labelling method (step 1: blocking free thiols with alkylating agents e.g. maleimide, step 2: reduction of the redox state e.g. dithiothreitol, step 3: labelling of nascent thiols e.g. biotin-maleimide, step 4: separation and identification of labelled nascent thiols e.g. SDS-PAGE, HPLC, MS/MS, immunoblotting)[169] which is a lengthy and time-consuming multi-step process, Figure 21.

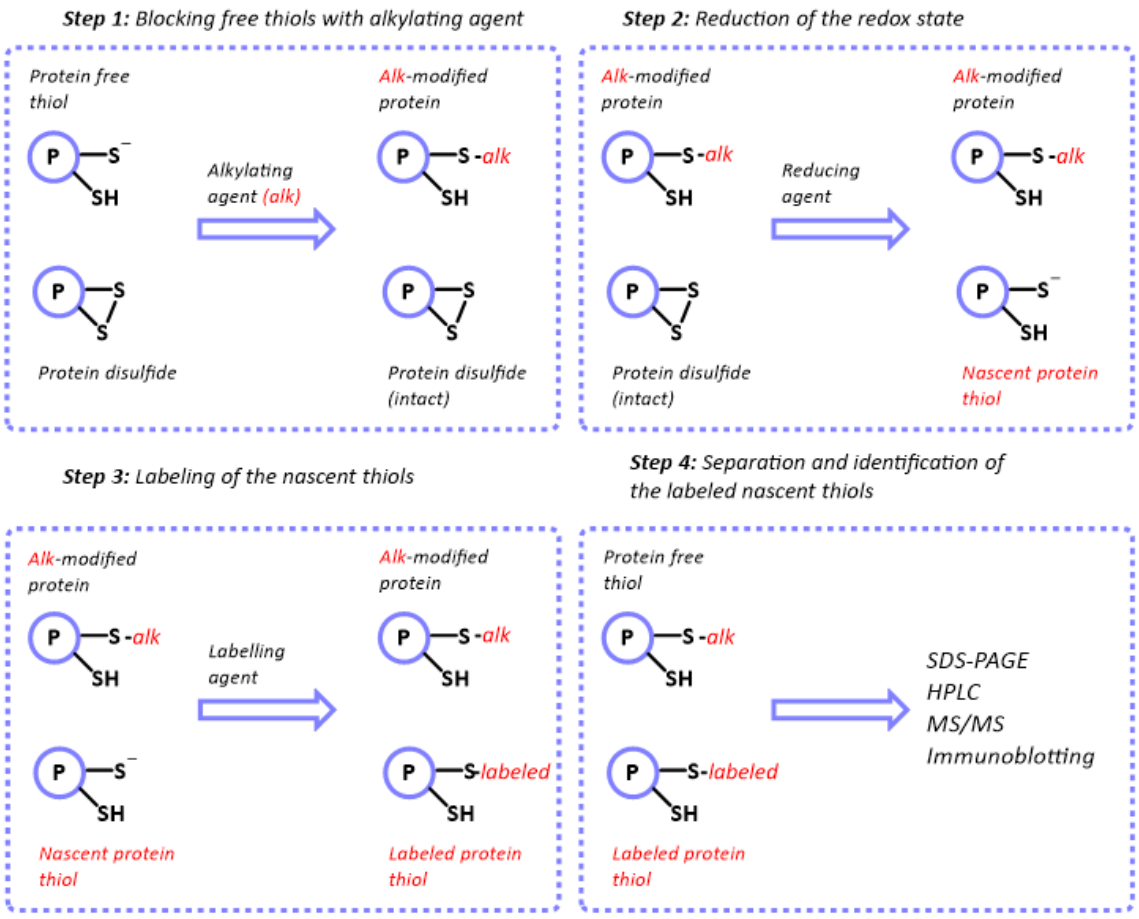

Figure 21: adapted from O. Rudyk, P. Eaton; Redox Biology 2 (2014) 803–813 [169]. Showing the 4 step method classically used to create and label free thiols.

1.8.4.2 Monitoring Inter-Protein Disulfides

There are far fewer sensitive approaches for monitoring intra- and inter-protein disulfides. Intra-protein disulfides refer to the bond between vicinal cysteine residues in a protein. It has been demonstrated that the presence of intra-disulfides induces a faster migration on non-reducing SDS-PAGE, however, band shifts can be small and not guaranteed in many proteins of interest. Additionally, the generic switch-labelling method mentioned above can be used. Inter-disulfide bonds are found between two cysteine thiols on two protein subunits generating either homo- or heterodimers; the presence of these interactions commonly leads to a significant increase in the protein molecular weight. Hence, the method used to monitor these bonds commonly is western immunoblotting analysis; specifically, diagonal electrophoresis techniques are used, and the sample identified through MS analysis. Despite this valuable library of techniques advancing the ability to monitor changes in protein redox state there is room for improvement, not only in sensitivity and accuracy but sample preparation and calibration, as currently this is not a trivial task[162]. Development of novel imaging methods or probes to detect and monitor the redox status of disulfides in vitro is highly desirable.

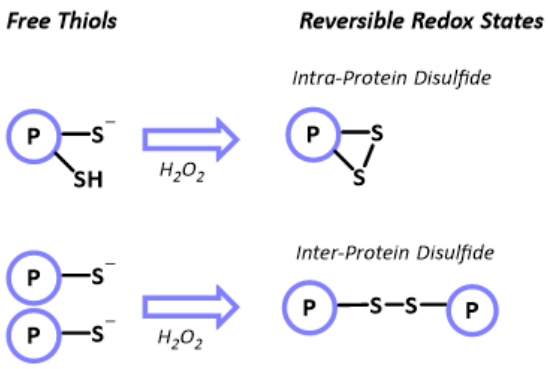

Figure 22: demonstrating the difference between inter and intra-protein disulfides.

The conventional sample preparation steps (including deproteinization and derivatization) alluded to above hinder the successful quantification of low-molecular mass thiols and disulfides involved in cellular redox processes by the oxidation or degradation of analytes throughout the process. Researchers therefore pursue techniques that minimize sample handling and permit direct detection of thiols and disulfides within a single chromatographic separation.

1.9 Research Directions

This thesis is comprised of two separate themes and approaches in polyoxometalate and peptide/protein chemistry. The first two chapters focus on electrostatic interactions and single electron transfer processes of reduced POM species on disulfide bonds, modifying the POMs through counter-cations and the structure to reach required reduction levels for the reduction of disulfides. While the latter two chapters focus on the covalent grafting of species onto a POM cluster for biological relevance.

Chapter 2 introduces the POM and disulfide structures to be used. The two Keggin-type POMs are analysed, and their reduction abilities characterised, these being novel analyses for one of the POMs. Additionally, several reduction techniques will be employed to attempt to achieve specific electron reduction levels of the POM which can then be employed to reduce the disulfide bonds of several compounds.

Chapter 3 will employ the technique found to be preferential for the analysis of the POMs to contrast the abilities of two types of POM to reduce disulfide bonds. This chapter focuses on the development of a colorimetric assay to enable the quantification of disulfide reduction using biologically relevant disulfide system. The Randles-Sevcik equation is used to verify the number of electrons in each reduction to give an accurate idea of the strength and number of electrons required to reduce the disulfides.

Chapters 4 and **5** focus on the development of new hybrid peptide-POM conjugates by exploring ligand-based diphosphonate linkers. The work was carried out in collaboration with Dr Sharad Amin; herein we found that the type of diphosphonate linker influences the photoactivity of the POM clusters. To graft amino acids and peptide sequences to the POMs, a diphosphonate linker was employed using robust thiol-addition chemistry to generate a new class of hybrid POMs. The successful optimisation of this conjugate approach led to the synthesis of a hexapeptide hybrid POM. The hexapeptide chosen displayed the starting sequence of the HIV-TAT peptide which has been commonly used for cell penetration and grafting onto other moieties.

1.10 References

1 C. M. Flynn and M. T. Pope, *Inorg. Chem.*, 1972, **11**, 1950–1952.

2 N. M. Mahmoodi, M. A. Rezvani, M. Oveisi, A. Valipour and M. A. Asli, *Mater. Res. Bull.*, 2016, **84**, 422–428.

3 S. Fujimoto, J. M. Cameron, R. J. Wei, K. Kastner, D. Robinson, V. Sans, G. N. Newton and H. Oshio, *Inorg. Chem.*, 2017, **56**, 12169–12177.

4 A. Bijelic, M. Aureliano and A. Rompel, *Angew. Chem. Int. Ed.*, 2019, **58**, 2980–2999.

5 C. G. Lin, J. Hu and Y. F. Song, *Adv. Inorg. Chem.* 2017, **69**, 181-212.

6 Q. Li, L. Zhang, J. Dai, H. Tang, Q. Li, H. Xue and H. Pang, *Chem. Eng. J.*, 2018, **351**, 441–461.

7 J. Friedl, F. L. Pfanschilling, M. V. Holland-Cunz, R. Fleck, B. Schricker, H. Wolfschmidt and U. Stimming, *Clean Energy*, 2019, **3**, 278–287.

8 H. Cameron, J. M. Fujimoto, S. Wei, R. Newton, G. N. Oshio, *Dalton. Trans.*, 2018, **47**, 10590–10594.

9 A. Blazevic and A. Rompel, *Coord. Chem. Rev.*, 2016, **307**, 42–64.

10 M. T. Pope, in *Polyoxometalate Molecular Science*, ed. J. J. Borrás-Almenar, E. Coronado, A. Müller, Pope, Springer Dordrecht, Netherlands, 2003, pp. 3–31.

11 G. Hervé, A. Tézé, R. Contant in *Polyoxometalate Molecular Science*, ed. J. J. Borrás-Almenar, E. Coronado, A. Müller, Pope, Springer Dordrecht, Netherlands, 2003, pp. 33–54.

12 L. C. W. Baker. and D. C. Glick, *Chem. Rev.*, 1998, **98**, 3–50.

13 W. N. Lipscomb, *Inorg. Chem.*, 1964, **4**, 132–134.

14 U. Kortz, M. G. Savelief, B. S. Bassil, M. H. Dickman, *Angew. Chem. Int. Ed.* 2001, **40**, 3384–3386.

15 G. M. Varga, E. Papaconstantinou and M. T. Pope, *Inorg. Chem.*, 1970, **9**, 662–667.

16 E. Papaconstantinou and M. T. Pope, *Inorg. Chem.*, 1967, **6**, 1147–1152.

17 D. Dimotikali and E. Papaconstantinou, *Inorganica Chim. Acta*, 1984, **87**, 177–180.

18 M. T. Pope, *Angew. Chem. Int. Ed.*, 1984, **96**, 730–732.

19 J. E. Molinari, L. Nakka, T. Kim and I. E. Wachs, *ACS Catal.*, 2011, **1**, 1536–1548.

20 D. L. Long, R. Tsunashima and L. Cronin, *Angew. Chem. Int. Ed.*, 2010, **49**, 1736–1758.

21 I. Lindqvist, *Ark. Kemi*, 1953, **5**, 247–250.

22 P. I. Molina, D. J. Sures, P. Miró, L. N. Zakharov and M. Nyman, *Dalton. Trans.*, 2015, **44**, 15813–15822.

23 T. M. A. Bakker, S. Mathew and J. N. H. Reek, *Sustain. Energy Fuels*, 2019, **3**, 96–100.

24 J. S. Anderson, *Nature*, 1937, **140**, 850.

25 H. T. Evans, *J. Am. Chem. Soc.*, 1948, **70**, 1291–1292.

26 G. H. and Y. J. F. Robert, A. Tézé, *Acta Crystallogr.*, 1980, **36**, 11–15.

27 J. F. Keggin and W. L. Bragg, *Proc. Math. Phy*, 1934, **144**, 75–100.

28 G. H. M. Abbessi, R. Contant, R. Thouvenot, *Inorg. Chem.*, 1991, **30**, 1695–1702.

29 R. Thouvenot, C. Rocchiccioli-Deltcheff, M. Fournier, R. Franck, *Inorg. Chem.*, 1983, **22**, 207–216.

30 L. Cronin, *Cheminform*, 2004, **35**, 1–56.

31 I. A. Weinstock, W. A. Neiwert, J. J. Cowan, K. I. Hardcastle, C. L. Hill, *Inorg. Chem. Commun.*, 2002, **4**, 6950–6952.

32 A. Tézé, E. Cadot, V. Béreau and G. Hervé, *Inorg. Chem.*, 2001, **40**, 2000–2004.

33 J. Rowsell and L. F. Nazar, *J. Am. Chem. Soc.*, 2000, **122**, 3777–3778.

34 R. Neumann, D. Sloboda-Rozner, K. Neimann, *J. Mol. Catal. A-chem.*, 2007, **262**, 109–113.

35 B. Dawson, *Acta Crystallogr.*, 1953, **6**, 113–126.

36 E. Coronado and C. J. Gómez-García, *Chem. Rev.*, 1998, **98**, 273–296.

37 L. Vilà-Nadal, S. G. Mitchell, D. L. Long, A. Rodríguez-Fortea, X. López, J. M. Poblet and L. Cronin, *Dalt. Trans.*, 2012, **41**, 2264–2271.

38 M. Yuan, Y. Li, E. Wang, C. Tian, L. Wang, C. Hu, N. Hu and H. Jia, *Inorg. Chem.*, 2003, **42**, 3670–3676.

39 F. Q. Zhang, W. Guan, L. K. Yan, Y. T. Zhang, M. T. Xu, E. Hayfron-Benjamin and Z. M. Su, *Inorg. Chem.*, 2011, **50**, 4967–4977.

40 J. Server-Carrió, J. Bas-Serra, M. E. González-Núñez, A. García-Gastaldi, G. B. Jameson, L. C. W. Baker and R. Acerete, *J. Am. Chem. Soc.*, 1999, **121**, 977–984.

41 A. J. Kibler and G. N. Newton, *Polyhedron*, 2018, **154**, 1–20.

42 E. N. Glass, J. Fielden, Z. Huang, X. Xiang, D. G. Musaev, T. Lian and C. L. Hill, *Inorg. Chem.*, 2016, **55**, 4308–4319.

43 L. Parent, P. A. Aparicio, P. De Oliveira, A. L. Teillout, J. M. Poblet, X. López and I. M. Mbomekallé, *Inorg. Chem.*, 2014, **53**, 5941–5949.

44 M. Stuckart and K. Y. Monakhov, *Chem. Sci.*, 2019, **10**, 4364–4376.

45 S. Greiner, M. H. Anjass, M. Fichtner and C. Streb, *Inorg. Chem. Front.*, 2019, **7**, 134–139.

46 M. Stuckart and K. Y. Monakhov, *J. Mater. Chem. A*, 2018, **6**, 17849–17853.

47 M. Cortés, M. Fuentealba, C. Manzur and D. Carrillo, *J. Chil. Chem. Soc.*, 2008, **53**, 6–9.

48 C. Li, A. Jimbo, K. Yamaguchi and K. Suzuki, *Chem. Sci.*, 2021, **12**, 1240–1244.

49 H. S. Booth, J. C. Bailar, M. Grennert, *Inorganic Syntheses*, ed. H. S. Booth, Part 6, McGraw-Hill Book Company, New York, 1939, vol. 1, pg. 132-133.

50 J. M. Cameron, S. Fujimoto, K. Kastner, R. J. Wei, D. Robinson, V. Sans, G. N. Newton and H. H. Oshio, *Chem. - A Eur. J.*, 2017, **23**, 47–50.

51 N. I. Gumerova and A. Rompel, *Nat. Rev. Chem.*, 2018, **2**, 0112.

52 X. López, C. Bo and J. M. Poblet, *J. Am. Chem. Soc.*, 2002, **124**, 12574–12582.

53 I. M. Mbomekallé, X. López, J. M. Poblet, F. Sécheresse, B. Keita and L. Nadjo, *Inorg. Chem.*, 2010, **49**, 7001–7006.

54 T. Ueda, *ChemElectroChem*, 2018, **5**, 823–838.

55 A. E. Greenberg, A. D. Eaton, L. S. Clesceri, *Standard Methods for the Examination of Water and Wastewater*, Washington DC, American Public Health Association, 20th edn., 1998.

56 H. C. K. Robards, I. D.M cKelvie, Ri L. Benson, P. J. Worsfold, N. J. Blundell, *Anal. Chim. Acta*, 1994, **287**, 147–190.

57 L. M. Magalhães, M. A. Segundo, S. Reis and J. L. F. C. Lima, *Anal. Chim. Acta*, 2008, **613**, 1–19.

58 V. De Waele, O. Poizat, M. Fagnoni, A. Bagno and D. Ravelli, *ACS Catal.*, 2016, **6**, 7174–7182.

59 D. Ni, D. Jiang, H. F. Valdovinos, E. B. Ehlerding, B. Yu, T. E. Barnhart, P. Huang and W. Cai, *Nano Lett.*, 2017, **17**, 3282–3289.

60 W. Tang, W. Fan, Z. Wang, W. Zhang, S. Zhou, Y. Liu, Z. Yang, E. Shao, G. Zhang, O. Jacobson, L. Shan, R. Tian, S. Cheng, L. Lin, Y. Dai, Z. Shen, G. Niu, J. Xie and X. Chen, *ACS Nano*, 2018, **12**, 12269–12283.

61 G. Guedes, S. Wang, H. A. Santos and F. L. Sousa, *Eur. J. Inorg. Chem.*, 2020, **2020**, 2121–2132.

62 C. Zhang, W. Bu, D. Ni, C. Zuo, C. Cheng, Q. Li, L. Zhang, Z. Wang and J. Shi, *J. Am. Chem. Soc.*, 2016, **138**, 8156–8164.

63 L. C. W. Baker and D. C. Glick, *Chem. Rev.*, 1998, **98**, 3–50.

64 M. Sadakane and E. Steckhan, *Chem. Rev.*, 1998, **98**, 219–237.

65 M. Zhao, X. Chen, G. Chi, D. Shuai, L. Wang, B. Chen and J. Li, *Inorg. Chem. Front.*, 2020, **7**, 4320–4332.

66 L. S. Van Rompuy and T. N. Parac-Vogt, *Curr. Opin. Biotechnol.*, 2019, **58**, 92–99.

67 M. Arefian, M. Mirzaei, H. Eshtiagh-Hosseini and A. Frontera, *Dalton. Trans.*, 2017, **46**, 6812–6829.

68 V. Tagliavini, C. Honisch, S. Serratì, A. Azzariti, M. Bonchio, P. Ruzza and M. Carraro, *RSC Adv.*, 2021, **11**, 4952–4957.

69 J. T. Rhule, C. L. Hill, D. A. Judd and R. F. Schinazi, *Chem. Rev.*, 2002, **98**, 327–358.

70 S. K. Moskovitz B., Lane H., Masur H., Lange M., Englard A., McKinley G., Volberding P., Abrams D., Mildvan D., Gottlieb M., Wolfe P., Polk B., Druckman D., Poiesz B., Smith C., Kusmierek J., *Antimicrob. Agents Chemother.*, 1988, **32**, 1300–1303.

71 C. Burgard, Marianne; Sansonetti, Philippe; Vittecoq, Daniel; Descamps, Philippe; Guetard, Denise; Herson, Serge; Rozenbaum, Willy; Rouzioux, *AIDS*, 1989, **3**, 665–668.

72 S. Wang, W. Sun, Q. Hu, H. Yan and Y. Zeng, *Bioorganic Med. Chem. Lett.*, 2017, **27**, 2357–2359.

73 A. Bijelic, M. Aureliano and A. Rompel, *Chem. Comm.*, 2018, **54**, 1153–1169.

74 H. N. Mukherjee, *J. Indian. Med. Assoc.*, 1965, **44**, 477–479.

75 M. R. C. Jasmin, J. Chermann, G. Herve, A.Teze, P. Souchay, C. Boy-Loustau, N. Raybaud, F. Sinoussi, *J. Natl. Cancer Inst.*, 1974, **53**, 469–474.

76 T. Yamase, *J. Mater. Chem.*, 2005, **15**, 4773–4782.

77 T. Yamase, H. Fujita, K. Fukushima, *Inorganica Chim. Acta*, 1988, **151**, 15–18.

78 H. Fujita, T. Fujita, T. Sakurai, *Chemotherapy*, 1992, **40**, 173–178.

79 T. Yamase, *Mol. Eng.*, 1993, **3**, 241–262.

80 K. Tomita, T. Yamase, *Inorganica Chim. Acta*, 1990, **169**, 147–150.

81 B. Hasenknopf, *Front. Biosci.*, 2005, **10**, 275–287.

82 G. Zhang, B. Keita, C. T. Craescu, S. Miron, P. De Oliveira and L. Nadjo, *J. Phys. Chem. B*, 2007, **111**, 11253–11259.

83 K. Stroobants, G. Absillis, E. Moelants, P. Proost and T. N. Parac-Vogt, *Chem. - A Eur. J.*, 2014, **20**, 3894–3897.

84 A. Sap, E. Dezitter, L. Vanmeervelt and T. N. Parac-Vogt, *Chem. - A Eur. J.*, 2015, **21**, 11692–11695.

85 V. Goovaerts, K. Stroobants, G. Absillis and T. N. Parac-Vogt, *Phys. Chem. Chem. Phys.*, 2013, **15**, 18378–18387.

86 K. Stroobants, D. Saadallah, G. Bruylants and T. N. Parac-Vogt, *Phys. Chem. Chem. Phys.*, 2014, **16**, 21778–21787.

87 A. Solé-Daura, V. Goovaerts, K. Stroobants, G. Absillis, P. Jiménez-Lozano, J. M. Poblet, J. D. Hirst, T. N. Parac-Vogt and J. J. Carbó, *Chem. - A Eur. J.*, 2016, **22**, 15280–15289.

88 A. Bijelic and A. Rompel, *Coord. Chem. Rev.*, 2015, **299**, 22–38.

89 A. Bashan and A. Yonath, *J. Mol. Struct.*, 2008, **890**, 289–294.

90 A. Bijelic and A. Rompel, *Acc. Chem. Res.*, 2017, **50**, 1441–1448.

91 S. G. Mauracher, A. Bijelic, C. Molitor and A. Rompel, R. Al-Oweini, U. Kortz, *ChemBioChem*, 2014, **16**, 233–241.

92 A. Rompel, S. G. Mauracher, C. Molitor, R. Al-Oweini, U. Kortz, *Acta Crystallogr.*, 2014, **70**, 2301–2315.

93 A. Rompel, S. G. Mauracher, C. Molitor, R. Al-Oweini, U. Kortz, *Acta Crystallogr. F Struct Biol Commun*, 2014, **70**, 262–266.

94 A. Rompel, C. Molitor, S. G. Mauracher, *Acta Crystallogr F Struct Biol Commun*, 2015, **71**, 746–751.

95 K. Stroobants, E. Moelants, H. G. T. Ly, P. Proost, K. Bartik and T. N. Parac-Vogt, *Chem. - A Eur. J.*, 2013, **19**, 2848–2858.

96 H. G. T. Ly, G. Absillis, R. Janssens, P. Proost and T. N. Parac-Vogt, *Angew. Chemie - Int. Ed.*, 2015, **54**, 7391–7394.

97 A. Sap, L. Van Tichelen, A. Mortier, P. Proost and T. N. Parac-Vogt, *Eur. J. Inorg. Chem.*, 2016, **2016**, 5098–5105.

98 H. Stephan, M. Kubeil, F. Emmerling and C. E. Müller, *Eur. J. Inorg. Chem.*, 2013, 1585–1594.

99 N. Gao, Y. X. Chen, Y. F. Zhao and Y. M. Li, *Molecules*, 2017, **22**, 1–9.

100 Y. Zhou, L. Zheng, F. Han, G. Zhang, Y. Ma, J. Yao, B. Keita, P. de Oliveira and L. Nadjo, *Colloids Surfaces A Physicochem. Eng. Asp.*, 2011, **375**, 97–101.

101 M. Li, C. Xu, J. Ren, E. Wang and X. Qu, *Chem. Commun.*, 2013, **49**, 11394–11396.

102 N. Gao, H. Sun, K. Dong, J. Ren, T. Duan, C. Xu and X. Qu, *Nat. Commun.*, 2014, **5**, 1–9.

103 Y. Guan, M. Li, K. Dong, N. Gao, J. Ren, Y. Zheng and X. Qu, *Biomaterials*, 2016, **98**, 92–102.

104 N. Gao, K. Dong, A. Zhao, H. Sun, Y. Wang, J. Ren and X. Qu, *Nano Res.*, 2016, **9**, 1079–1090.

105 G. Gasser, I. Ott and N. Metzler-Nolte, *J. Med. Chem.*, 2011, **54**, 3–25.

106 X. H. Wang, H. C. Dai and J. F. Liu, *Polyhedron*, 1999, **18**, 2293–2300.

107 J. H. and J. L. Xiaohong Wang, Jianxin Li, *Met. Based drugs*, 2001, **8**, 179–182.

108 J. Q. Sha, X. Li, Y. H. Zhou, P. F. Yan, G. M. Li and C. Wang, *Solid State Sci.*, 2011, **13**, 1972–1977.

109 X. Wang, J. Liu, J. Li, Y. Yang, J. Liu, B. Li and M. T. Pope, *J. Inorg. Biochem.*, 2003, **94**, 279–284.

110 X. Feng, C. G., Wang, S. S., Liu, *Pol. J. Chem.*, 2009, **83**, 2079–2087.

111 X. Liu, Q. Gan and C. Feng, *J. Rare Earths*, 2012, **30**, 604–608.

112 A. Boulmier, X. Feng, O. Oms, P. Mialane, E. Rivière, C. J. Shin, J. Yao, T. Kubo, T. Furuta, E. Oldfield and A. Dolbecq, *Inorg. Chem.*, 2017, **56**, 7558–7565.

113 A. Saad, W. Zhu, G. Rousseau, P. Mialane, J. Marrot, M. Haouas, F. Taulelle, R. Dessapt, H. Serier-Brault, E. Rivière, T. Kubo, E. Oldfield and A. Dolbecq, *Chem. - A Eur. J.*, 2015, **21**, 10537–10547.

114 H. El Moll, W. Zhu, E. Oldfield, L. M. Rodriguez-Albelo, P. Mialane, J. Marrot, N. Vila, I. M. Mbomekallé, E. Rivière, C. Duboc and A. Dolbecq, *Inorg. Chem.*, 2012, **51**, 7921–7931.

115 J. D. Compain, P. Mialane, J. Marrot, F. Sécheresse, W. Zhu, E. Oldfield and A. Dolbecq, *Chem. - A Eur. J.*, 2010, **16**, 13741–13748.

116 J. Q. Sha, L. Y. Liang, P. F. Yan, G. M. Li, C. Wang and D. Y. Ma, *Polyhedron*, 2012, **31**, 422–430.

117 C. Li, J. Lu, F. Tu, J. Chen and Y. Li, *Inorg. Chem. Commun.*, 2011, **14**, 1192–1195.

118 H. Z. Jingquan Sha, Taoye Zheng, Erlin Zhang, Hongbin Qiu , Mingyuan Liu, *J. Coord. Chem.*, 2013, **66**, 977–985.

119 E. Al-Sayed, A. Blazevic, A. Roller and A. Rompel, *Chem. - A Eur. J.*, 2015, **21**, 17800–17807.

120 N. I. Gumerova, A. Roller and A. Rompel, *Chem. Commun.*, 2016, **52**, 9263–9266.

121 N. I. Gumerova, A. Roller and A. Rompel, *Eur. J. Inorg. Chem.*, 2016, **2016**, 5507–5511.

122 N. Alasmael, R. Mohan, L. Meira, N. Plant, *Cancer Lett.*, 2016, **370**, 250–259.

123 M. H. Wu, T. M. Hong, H. W. Cheng, S. H. Pan, Y. R. Liang, H. C. Hong, W. F. Chiang, T. Y. Wong, D. Bin Shieh, A. L. Shiau, Y. T. Jin and Y. L. Chen, *Mol. Cancer Res.*, 2009, **7**, 311–318.

124 M. Cindric, T. Kajfez, S. Kraljevic, B. Kamenar, *Inorganica Chim. Acta*, 2006, **359**, 1673–1680.

125 E. Cartuyvels, K. Van Hecke, L. Van Meervelt, C. Görller-Walrand and T. N. Parac-Vogt, *J. Inorg. Biochem.*, 2008, **102**, 1589–1598.

126 J. X. Jiang, M. A. Riquelme and J. Z. Zhou, *Oncoscience*, 2015, **2**, 673–674.

127 C. Li, W. Qi, H. Cao, Y. Qi, S. Zhang, S. Xu, J. Sun and S. Guo, *Biomed. Pharmacother.*, 2016, **79**, 78–86.

128 C. Li, H. Cao, J. Sun, R. Tian, D. Li, Y. Qi, W. Yang and J. Li, *J. Inorg. Biochem.*, 2017, **168**, 67–75.

129 Y.-K. Sun, S.-J.Wang, *Acta Acad. Med. Sin.*, 2009, **31**, 538–541.

130 J. J. Mieyal, M. M. Gallogly, S. Qanungo, E. A. Sabens and M. D. Shelton, *Antioxidants Redox Signal.*, 2008, **10**, 1941–1988.

131 P. Arvan, G. Rajpal, *Handbook of Biologically Active Peptides (Second Edition)*, ed. A. J. Kastin, Academic Press, Elsevier, Boston, Chapter 236, 2013, pg. 1721-1729.

132 I. Dalle-Donne and R. Rossi, *J. Chromatogr. B Anal. Technol. Biomed. Life Sci.*, 2009, 877, 3271–3273.

133 P. Cresswell, L. Ciaccia, C. Metcalfe, A. N. Barclay and B. Thomas, *Open Biol.*, 2011, **1**, 110010–110010.

134 T. J. Bechtel and E. Weerapana, *Proteomics*, 2017, **17**, 139–148.

135 M. J. Feige and L. M. Hendershot, *Curr. Opin. Cell Biol.*, 2011, **23**, 167–175.

136 K. Kong, B. J. Smith, C. J. Watson, L. Žáková, E. Kletvíková, S. J. Chan, D. F. Steiner, G. G. Dodson, M. Andrzej, E. Hall and R. Parade, *Nature*, 2013, **493**, 241–245.

137 S. Parakh and J. D. Atkin, *Front. Cell Dev. Biol.*, 2015, **3**, 1–11.

138 M. Depuydt, J. Messens and J. F. Collet, *Antioxidants Redox Signal.*, 2011, **15**, 49–66.

139 T. J. Bechtel and E. Weerapana, *Proteomics*, 2017, **17**, 1–49.

140 C. S. Sevier and C. A. Kaiser, *Nat. Rev. Mol. Cell Biol.*, 2002, **3**, 836–847.

141 U. Jakob, W. Muse, M. Eser and J. C. A. Bardwell, *Cell*, 1999, **96**, 341–352.

142 F. Aslund, G. Storz, M. Zheng, *Science*, 1998, **279**, 11–14.

143 L. B. Poole, *Free Radic. Biol. Med.*, 2015, **80**, 148–157.

144 M. A. Wouters, S. W. Fan and N. L. Haworth, *Antioxidants Redox Signal.*, 2010, **12**, 53–91.

145 K. S. Jensen, R. E. Hansen and J. Winther, *Antioxidants Redox Signal.*, 2009, **11**, 1047–1058.

146 F. Armstrong, P. Atkins, T. Overton, J. Rourke, M. Weller, *Shriver & Atkins' Inorganic Chemistry 5th edition*, W H Freeman & Co, New York, 2009.

147 L. Flohé, *Biochim. Biophys. Acta - Gen. Subj.*, 2013, **1830**, 3139–3142.

148 Z. Shaked, R. P. Szajewski and G. M. Whitesides, *Biochemistry*, 1980, 4156–4166.

149 T. Intact, D. Bonds, C. N. Pace, G. R. Grimsley, J. A. Thomson and B. J. Barnett, *J. Bio.Chem.*, 1988, **263**, 11820–11825.

150 J. S. Richadrson, The Anatomy and Taxonomy of Protein Structure, http://kinemage.biochem.duke.edu/teaching/anatax/pdfs/AnaTax_II.pdf, (accessed 9 April 2020).

151 B. J. Berne, A. Holmgren, A. P. Wiita, R. Perez-jimenez, K. A. Walther, F. Gra, J. M. Sanchez-ruiz and J. M. Fernandez, *Nature*, 2007, **450**, 124–127.

152 D. Butera, K. M. Cook, J. Chiu, J. W. H. Wong and P. J. Hogg, *Blood,* 2014, **123**, 2000–2007.

153 D. F. D. Mahmood, A. Abderrazak, K. El Hadri, T. Simmet and M. Rouis, *Antioxidants Redox Signal.*, 2013, **19**, 1266–1303.

154 K. Dasuri, L. Zhang and J. N. Keller, *Free Radic. Biol. Med.*, 2013, **62**, 170–185.

155 A. Zhou, R. W. Carrell, M. P. Murphy, Z. Wei, Y. Yan, P. L. D. Stanley, P. E. Stein, F. B. Pipkin and R. J. Read, *Nature*, 2010, **468**, 108–111.

156 S. Xu, S. Sankar and N. Neamati, *Drug Discov. Today*, 2014, **19**, 222–240.

157 P. E. Stein, D. A. Tewkesbury and R. W. Carrell, *Biochem. J.*, 2015, **262**, 103–107.

158 R. Huber and R. W. Carrell, *Biochemistry*, 1989, **28**, 8951–8966.

159 A. Zhou, R. W. Carrell, M. P. Murphy, Z. Wei, Y. Yan, P. L. D. Stanley, P. E. Stein, F. B. Pipkin and R. J. Read, *Nature*, 2010, **468**, 108–111.

160 F. Forette, M. L. Seux, J. A. Staessen, L. Thijs, W. H. Birkenhäger, M. R. Babarskiene, S. Babeanu, A. Bossini, B. Gil-Extremera, X. Girerd, T. Laks, E. Lilov, V. Moisseyev, J. Tuomilehto, H. Vanhanen, J. Webster, Y. Yodfat and R. Fagard, *Lancet*, 1998, **352**, 1347–1351.

161 Cancer Research UK, http://www.cancerresearchuk.org/health-professional/cancer-statistics-for-the-uk, (accessed 22 January 2018).

162 M. Scampicchio, N. Lawrence, A. Arecchi and S. Mannino, *Electroanalysis*, 2007, **19**, 2437–2443.

163 G. S. Owens, W. R. Lacourse, *Anal. Chim. Acta*, 1995, **307**, 301.

164 G. S Owens and W. R Lacourse, *J. Chromatogr. B.*, 1997, **695**, 15-25.

165 M. Zhong and S. Lunte, *Anal. Chem.*, 1999, **71**, 251-255.

166 T. Nambara, M. Tanaka, K. Shimada, *J. Chromatogr. B*, 1994, **659**, 227–241.

167 T. Damelang, S. J. Rogerson, S. J. Kent and A. W. Chung, *Trends Immunol.*, 2019, **40**, 197–211.

168 P. W. Sanders, in *Molecular and Genetic Basis of Renal Disease*, ed. D. B. Mount, M. R. Pollak, Philadelphia: W. B. Saunders, Inc., an affiliate of Elsevier, 2008, pp. 435–440.

169 O. Rudyk and P. Eaton, *Redox Biol.*, 2014, **2**, 803–813.

170 O. Boutureira and G. J. L. Bernardes, *Chem. Rev.*, 2015, **115**, 2174–2195.

171 R. C. Fahey, G. L. Newton, R. Dorian and E. M. Kosower, *Anal. Biochem.*, 1980, **107**, 1–10.

172 J. R. Winther and C. Thorpe, *Biochim. Biophys. Acta - Gen. Subj.*, 2014, **1840**, 838–846.

173 H. Sartzi, H. N. Miras, L. Vilà-Nadal, D. L. Long and L. Cronin, *Angew. Chemie - Int. Ed.*, 2015, **54**, 15488–15492.

CHAPTER TWO: DEVELOPMENT OF POM REDUCTION TECHNIQUES

2.1 Introduction

Several POMs can undergo several reversible reductions at their metal centres. The reduction of POMs results in an LMCT; contributing to the '*heteropolyblue*' colour displayed by POMs.[1] To summarize the process: the reduction of the POM results in a LMCT of a terminal metal-oxygen bond (M=O). The resulting oxo-centred radical cation is rapidly quenched by the solvent, for example, subsequently leaving a trapped d^1 electron on the metal.[2] This delocalized d^1 electron undergoes IVCT, resulting in the '*heteropolyblue*' colour. Continued irradiation can however yield multiple photoreductions of the POM, and the formation of more than one IVCT band. This can also be achieved by electrochemical methods. Due to the unique absorption bands observed for each electron reduction, they can be observed and followed through UV-Vis spectroscopy. There are several techniques which can be used to reduce POMs.

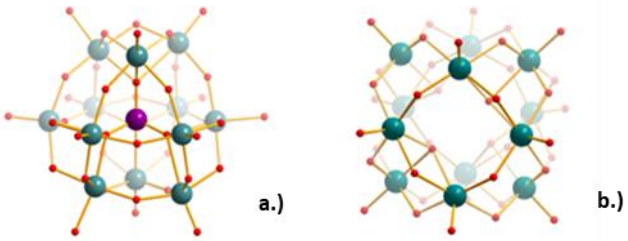

Figure 23: The structures of a) the Keggin-type, $[PW_{12}O_{40}]^{3-}$, $\{PW_{12}\}$, showing the central phosphorus template atom, and b) the Metatungstate -type, $[H_2W_{12}O_{40}]^{7-}$, $\{W_{12}\}$, shown with a hollow interior due to there being no heteroatom template. Each element is represented by a different colour: tungsten is turquoise, oxygen is red and phosphorous is purple.

In this chapter several reduction techniques will be explored on two Keggin-type POM structures. The two poly-tungstate structures differ by the presence of the phosphate templating ion; making one a heteropoly- and the other a isopoly-anion structure. Due to the twelve tungsten atoms being structurally equivalent within both POMs the addenda atoms are displaced towards the exterior of the anion.[3] The reduction of these POM species is most commonly undertaken through photo-,[4] electro-[5] and chemical-reduction methods.[6] The two POMs chosen for the work herein are due to their similarity in structure and yet

strikingly different electronic character. The choice of POMs is largely due to computational studies run by collaborators. The difference in structure is due to the central phosphorus template atom in the Keggin whilst the metatungstate constitutes of a hollow interior, where hydrogen can exchange within, Figure 23.

The importance of monitoring disulfide bond reduction within biological species is clear, outlined on pages 29 to 41. There are limited methods for the detection of these bonds. The objective of this project is to progress into utilizing redox-tunable supramolecular metal-oxide nanoclusters (polyoxometalates), for the reduction of oxidized disulfide bonds in peptides. The strong colorimetric response arising from the difference between the colourless oxidized (d^0) state and the blue reduced (d^1) state of the POMs, provides a convenient and sensitive spectroscopic handle for ease-of-analysis. Additionally, when compared to the existing colour switching materials used for disulfide detection, (i) the reduced and oxidized states of the POMs are stable and can retain the colour for a period of time under ambient conditions; (ii) the structure and configuration of the POMs are stable throughout;[7,8] (iii) reaction conditions for the reduction/ oxidation and hence colour switching are simple and convenient e.g. UV irradiation, (iv) POMs display biocompatibility; [9–19] (v) some POMs, such as certain Keggin typed phosphotungstic acid, are commercially available, hence do not require complex synthesis and are relatively cheap.[20]

2.2 Aims

This chapter specifically describes the steps taken towards the development of a technique to reliably reduce two POM species to a chosen reduction potential. Upon the correct degree of reduction, the system required the ability of the re-oxidation of the POM to be monitored through UV-vis spectroscopy. As this project contains many facets, initially the characterization of the POMs is undertaken. This allows for a full understanding of the two structures and their differences and similarities as well as their UV-Vis profiles and re-oxidation character. Most importantly a suitable reduction technique applicable to both POMs is explored and a reliable set up established.

As previously stated, disulfide bonds are important in the structure and activity of peptides and proteins.[21] Many disulfide bridges in nature are labile and can be found in reduced and oxidized forms. Due to the progression of this project and its future focus this chapter will include some characterization and reduction reactions of certain disulfides. Once reduced the POM species will be tested with several substrates with disulfide bonds to trace the re-oxidation of the POM and subsequent reduction of the disulfide.

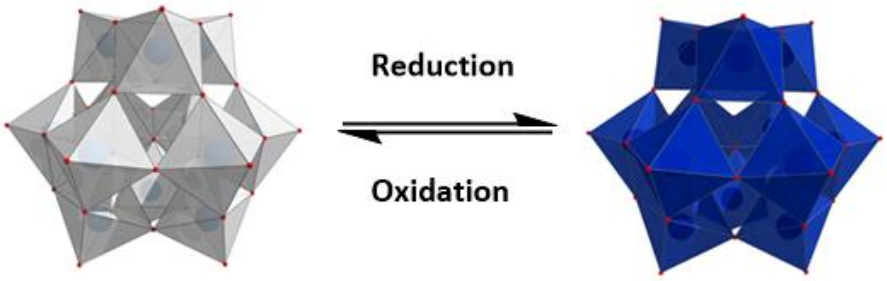

Figure 24: Representing the colour change associated with the reduced and oxidized forms of the Metatungstate-type POM.

2.3 Results and Discussion

In this section will be discussed the steps taken to develop a reliable and reproducible technique to reduce the two chosen polyoxometalates to specific reduction potentials. Once reduced the techniques are trialled through the addition of a selection of known, characterized disulfide bonds, and the re-oxidation process monitored through UV-Vis spectroscopy. Once the polyoxometalates were synthesized and characterized several reduction methods were investigated and compared through the addition of two commercial disulfides. Additionally, to testing different reduction methods, the polyoxometalates had counter cations, solvent and atmospheric environment varied.

2.3.1 Preliminary Computational Calculations

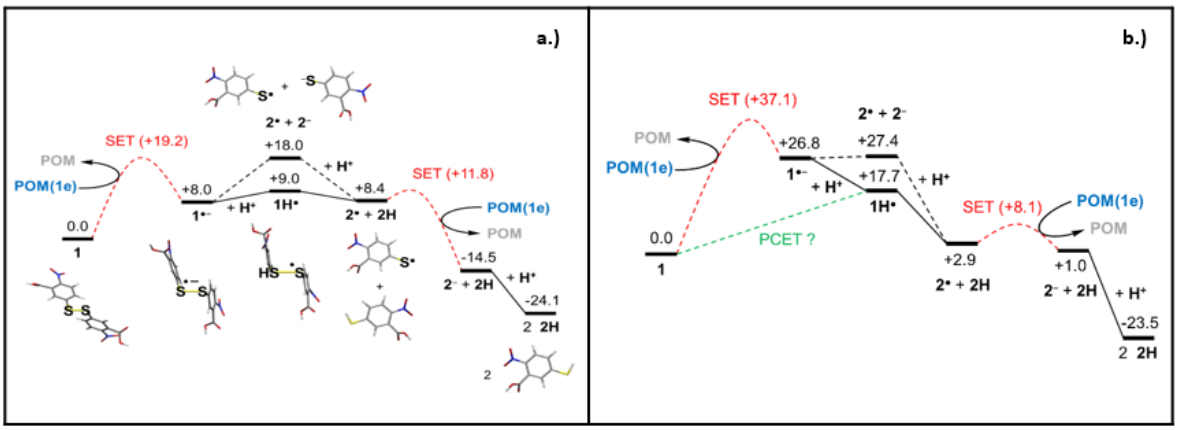

Figure 25: a) {PW_{12}}(1e) = POM(1e) Calculated Gibbs free energy profile (kcal mol^{-1}) for the reduction of DTNB (**1**) by 2 $[PW_{12}O_{40}]^{4-}$ anions, **POM(1e)**. The standard state correction of +1.9 kcal mol^{-1} (from ideal gas to 1 mol L^{-1} at 298.15 K) was applied to the free energy of all the species. Figure 26b) Calculated Gibbs free energy profile (kcal mol^{-1}) for the reduction of cystine (**2**) by 2 $[PW_{12}O_{40}]^{4-}$ anions, **POM(1e)**. The standard state correction of +1.9 kcal mol^{-1} (from ideal gas to 1 mol L^{-1} at 298.15 K) was applied to the free energy of all the specie

The end objective is to investigate the reduction of disulfides using reduced POMs to develop a colorimetric assay for disulfide quantification. Initial calculations to find the minimum energy requirements of a reduced POM to the disulfide inform of the most appropriate POM structure to use. Hence prior to any experimental work DFT models of the POMs and some disulfides were carried out and energy barriers identified.

Computational studies carried out by collaborators at Universitat Rovira i Virgli suggested that regarding interactions of POMs and disulfides (namely the electron donation from a POM cluster to the disulfide) a Gibbs Free activation energy below + 25 kcal mol^{-1} is necessary. The group looked at two forms of Keggin type tungsten-12 POMs, introduced above, and two disulfide substrates, 5,5-dithio-bis-(2-nitrobenzoic acid) (**DTNB**) (**1**) and a di-cysteine model (**3**),Figure 26. Looking more closely at the chosen substrates; the processes found that the reduction of the weaker S-S bond in DTNB could be broken using a 2:1 ratio of the mono-reduced Keggin-type POM {**PW_{12}**}(1e) to DTNB; as a value of + 19.2 kcal mol^{-1} was calculated. The studies then progressed to looking at a di-cysteine (**3**), model which was used to represent a model closer in similarity to a peptide S-S bond, i.e. aliphatic in nature. Looking at the same process as before with {PW_{12}}(1e) showed the reduction of the disulfide through the proposed mechanism, to be too energy demanding (ΔG > 37 kcal/mol) to occur, Figure 25. This is where the second POM was introduced, namely the Metatungstate-type POM, ({**W_{12}**}, $[H_2W_{12}O_{40}]^{7-}$}.

Further calculations for both POMs are shown in Table 1; these findings provided more detail to the reductive power of the singly reduced {PW_{12}} (4- charge), doubly reduced {PW_{12}} (5- charge) and the singly reduced {W_{12}} (7- charge). These workings demonstrated that the {W_{12}} has a greater reductive potential than either the singly or doubly reduced {PW_{12}} forms, neither of which has the potential to reduce the disulfide found in a cystine molecule. {W_{12}} on the other hand displays a Gibbs Free activation energy of + 24.9 kcal mol^{-1} indicating a theoretical potential to reduce the disulfide. Obviously, the value is very close to the calculated cut off of + 25 kcal mol^{-1} in which the reaction will not proceed hence the viability of reaction needs to be checked with experimentation. Overall, the calculations suggest that in order to reduce the more stable S-S bonds such as in proteins or peptides a stronger reductant is required; such as the doubly reduced $[PW_{12}O_{40}]^{5-}$, {PW_{12}}(2e) or the 1 electron reduced $[H_2W_{12}O_{40}]^{7-}$, {W_{12}}(1e). Hence, it was summarized that in these higher

charged systems, both the kinetics and the thermodynamics of the 1st reduction of the substrate are more favourable (but still difficult for the cystine). Experimentally a cystamine dihydrochloride (**2**) model was used prior to moving into peptide models as it was deemed a good bridging S-S molecule, as well as it being cheap and commercially available.

These higher charged systems can be obtained through several techniques: electrochemically, chemical or solar reduction of the POM.

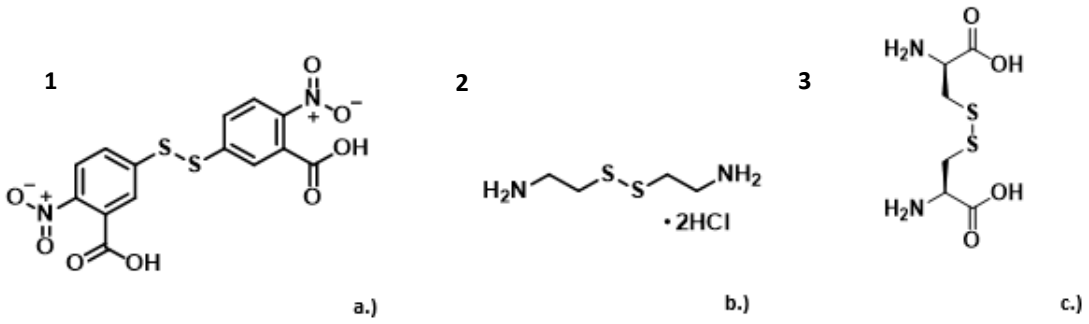

Figure 26. a) 5,5-dithio-bis-(2-nitrobenzoic acid), DTNB (1) the aromatic substrate, b) cystamine dihydrochloride, CD, (2) and c) the cystine model (3) used for computational calculations as a model substrate for aliphatic and peptidic molecules.

Disulphide	Reductant	$\Delta G^{\ddagger}$ (1st set) (kcal mol^{-1})	ΔG^{0} (1→1$^{\cdot-}$) (kcal mol^{-1})
DTNB	$[PW_{12}O_{40}]^{4-}$	+19.2	+8.0
	$[PW_{12}O_{40}]^{5-}$	+14.1	-3.3
	$[H_2W_{12}O_{40}]^{7-}$	+9.8	-16.0
Cystine	$[PW_{12}O_{40}]^{4-}$	+37.1	+26.8
	$[PW_{12}O_{40}]^{5-}$	+30.8	+15.5
	$[H_2W_{12}O_{40}]^{7-}$	+24.9	+2.8

Table 1: showing further calculations of the reductive powers of the singly (at overall charge of 4-) and doubly (overall charge of 5-) reduced Keggin and the Metatungstate, $Na_6[H_2W_{12}O_{40}]$; suggesting Metatungstate has a far greater reduction potential with just enough energy for the ability to break a cystine bond with +24.9 kcal

2.3.2 Electronic Characterisation

2.3.2.1 Polyoxometalates: Keggin - $H_3[PW_{12}O_{40}].xH_2O$ and Metatungstate - $Na_6W_{12}O_{39}$

The synthesis of both the Keggin $\{PW_{12}\}$ and Metatungstate $\{W_{12}\}$ POM was taken from the primary literature.[22,23] The difference in structure is due to the central phosphorus template atom in the Keggin whilst the Metatungstate constitutes of a hollow interior which allows the interchanged of protons inside, Figure 23.

Due to our interest in their electronic properties', cyclic voltammetry (**CV**) studies were undertaken to determine the reduction potentials of the POMs. This was carried out using a CHI600 potentiostat, in 0.1 M $[TBA][PF_6]$ supporting electrolyte solution. The cathode (working electrode) was glassy carbon. The anode was a platinum wire and the reference, mercury, containing a saturated aqueous solution of mercury chloride. Reference and anode electrodes were separated in the reaction mixture by a porous fritted glass. Prior to running a CV the dissolved dioxygen was eliminated by bubbling nitrogen into the solution. The substrates were dissolved in DMF for the $\{PW_{12}\}$ and a 1:4 water:DMF mixture for the $\{W_{12}\}$. The cell was continuously blanketed with nitrogen throughout the runs.

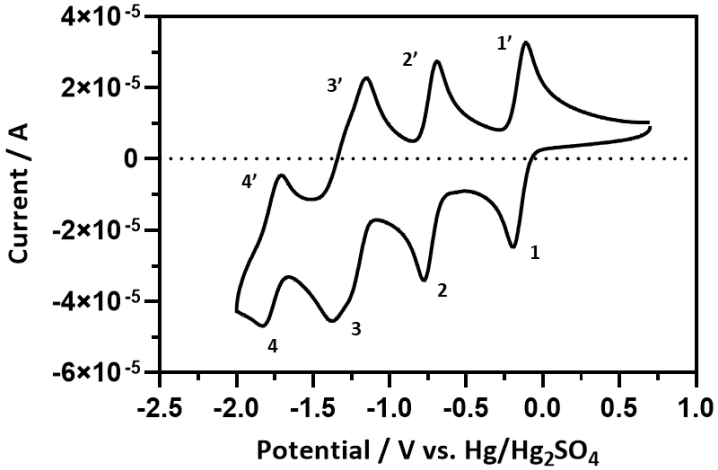

Figure 27: shows the CV scan taken of 2 mM Keggin dissolved in dry DMF with 0.1 M $[TBA][PF_6]$. The scan was swept from 0.7 V to -2.0 V and back at a scan rate of 100 mV, 2 cycles; displayed above is the second cycle.

The CV scan taken of Keggin $\{PW_{12}\}$ displayed in Figure 27, clearly indicates four reduction processes as the scan is swept negative, these events are observed at: -0.2 V, -0.75 V, -1.4 V

and -1.8 V respectively, all four processes are reversible. Each redox couple is a one electron process with the possible exception of reduction 3, deduced from the broadness of the reduction trough and the indication of a secondary underlying trough inside it. However, interest was centred on the first two reduction processes as these were explored by our computational collaborators and hence no further exploration of the later ones was undertaken.

Taking CV scans, Figure 28, of the $\{W_{12}\}$ species showed the first reduction as more negative than the first reduction observed for the $\{PW_{12}\}$, $\{PW_{12}\}(1e)$, Figure 27. Due to solubility issues a 1:4 water:DMF mixture was required, this was rather unconventional; however, this gave an adequate potential window of the electrolyte to work in whilst having all the substrates in solution.

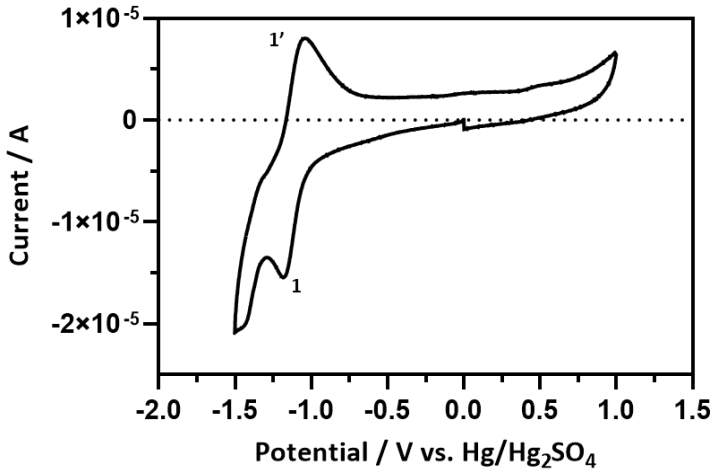

Figure 28: the CV scan taken of 1 mM Metatungstate-$\{W_{12}\}$ dissolved in a 1:4 water:DMF mixture with 0.1 M [TBA][PF_6]. The scan was swept from 1 V to -1.5 V and back, 2 cycles; displayed above is the second cycle.

The metatungstate-$\{W_{12}\}$ CV indicates one reversible reduction process at -1.25 V. The reduction was assumed to be a one electron process due to the sharp peak. The potential was not taken much lower as the shape of the scan post the reduction indicates the edge of the potential window of the water and hence any other reductions would lack clarity and would be inaccurate to use.

2.3.2.2 Cuvette Electro-Chemistry

Due to the nature of the project being the use of the POMs as colorimetric redox probes, monitored using UV-Vis techniques, the distinct absorption profiles of the POMs were of extreme importance.

After performing CV studies and identification of the reduction potential at which the electron reduction processes occur; theoretically it was possible to set up the electro-chemical reduction of a sample at a chosen potential. The primary objective was to identify the UV-Vis absorption profiles for the differing reductions possible in the POMs. This we did through spectro-electrochemical reactions. The first set up used can be seen in Figure 29, this allowed the use of minimal quantities of solvent, which was an important factor when moving to peptide systems due to the complexity of structure and the difficulty in synthesis, hence only small samples were produced at a time.

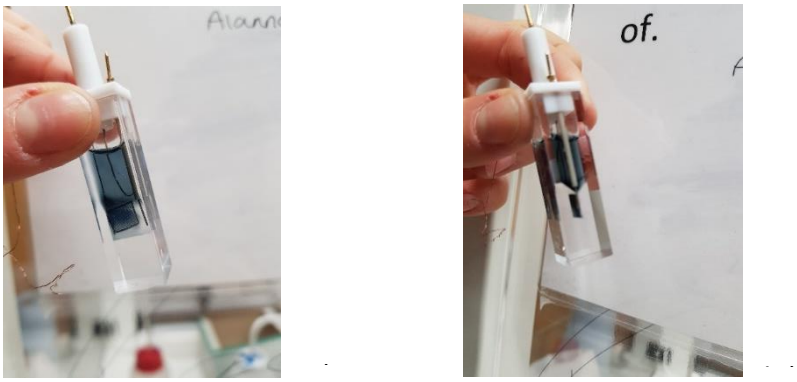

Figure 29: Demonstrates the first set up for the spectro-electrochemical reactions. using a platinum mesh for the working electrode, a silver wire as the reference and a platinum counter electrode. The pathlength is 1 mm within the cuvette and in the sample above roughly 1 mL solvent was used. The solution shown is the mono-reduced Keggin. 0.1 M [TBA][PF_6] electrolyte solution was used for all samples, the concentrations for Keggin were varied.

Although the characteristic UV-Vis absorption bands of the 1st electron reduction of the Keggin-{PW_{12}} was seen we were unable to reach a convergence point, which here is referred to as the point where the absorption profiles overlap and no further increase in absorbance can be observed, indicating saturation. This point is important to identify as it represents the point where 100 % of the {PW_{12}} is mono-reduced. This was tested over a variety of concentrations. Despite seeing a typical blue colour change indicating reduction of the POM, Figure 29, the current output never stabilized indicating that not all the {PW_{12}} sample was being reduced even when running the experiments over an 8-hour period. From

previous reactions undertaken in the solar reactor a rapid reduction rate was expected (within seconds); especially from the {PW_{12}} POM, therefore, it was concluded there was a fault in the set up. Additionally, the 2nd electron reduction was not seen when increasing the potential. These factors led to a re-evaluation of the technique used.

It was concluded that the problem was due to the electrode set up. Although reduction was occurring, seen through the colour change; due to the positioning of the electrodes all in such close proximity, oxidation was occurring at the counter electrode. This prevented the maximum UV-Vis convergence point from being reached. Furthermore, it was highlighted that the use of a silver wire was not an adequate reference, as it is present in the solution and therefore the values could shift depending on the solvent system and age of the wire. Therefore, the reaction set-up was changed.

2.3.2.3 Refined Spectro-Electrochemical Set-up

A set up mimicking that described to take the CV measurements, regarding the electrodes was used. This ensured consistency and the application of a reliable potential. Changing the working electrode from glassy carbon to platinum was necessary but it was anticipated that no negative effects from this alteration would occur. An inert atmosphere cuvette was used containing the counter and working electrodes with the reference electrodes connected through a porous fritted glass and in a saturated aqueous solution of mercury chloride as described before; images of the set up can be seen in Figure 30. The cathode (working electrode) was a platinum/ rhodium wire, and it was assumed that there was no change to the glassy carbon used for the CV scans. The anode was a platinum wire and the reference mercury, containing a saturated aqueous solution of mercury chloride. Reference and anode electrodes were separated in the reaction mixture by a porous fritted glass. Prior to running an experiment, the dissolved dioxygen was eliminated by bubbling nitrogen into the solution. The substrates were dissolved in DMF for Keggin and DTNB and a 1:4 water:DMF mixture for the Metatungstate; [TBA][PF_6] was used as a supporting electrolyte. The cell was continuously blanked with nitrogen throughout the runs.

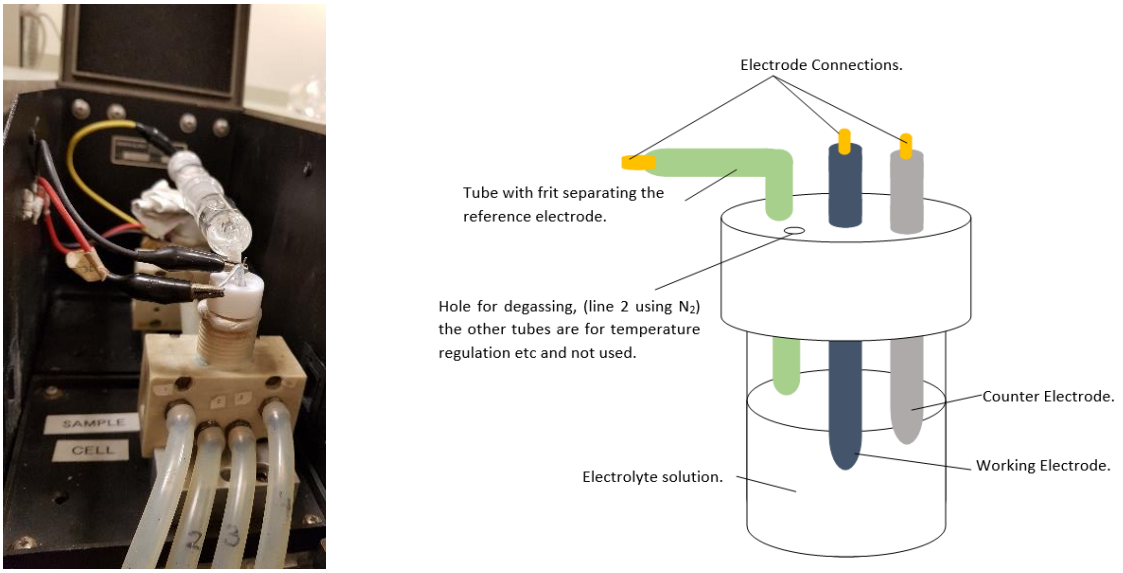

Figure 30: Images of the spectro-electrochemical set up for the reduction of certain substrates while recording UV-vis absorptions. a.) shows the side view while b.) depicts the top; lines 1, 2, 3 and 4 were responsible for flooding the spectrometer with nitrogen throughout the experiments and available for temperature control; temperature was never varied more than ±0.1.

The $\{PW_{12}\}$ species showed discrete absorption patterns for the different electron reductions. The $\{PW_{12}\}$ solution had a potential applied of -0.57 V, which was taken from the CV scans as a point past the 1st electron reduction process, Equation 5, but prior to going into the 2nd reduction process, Equation 6. UV-vis scans were taken every 10 minutes until a convergence point was observed, Figure 31; this indicated the complete reduction of the first reduction process in every POM molecule present in the solution. At this point the potential was reverted to 0 V to check the reversibility of the first reduction process. As the absorbance reverted again to zero and no more peaks were observed it indicated the full reversibility of the POM. Next a potential of -1.12 V was applied to reduce the second reduction process. Figure 32 depicts the scans taken for the reduction. Again, scans were taken every 10 minutes until a convergence point was observed. Subsequently the potential was decreased to -0.57 V again (the first reduction process) and then to 0 V to see whether the reduction process was completely reversible; the baseline reached subsequently to the appearance of the first reduction profile. From the figures it can be clearly seen that the 1st reduction is analogous with a band forming at 750 nm and a smaller one at ~500 nm; whereas upon reduction to the 2nd process a shift in the bands is observed to 650 nm and 450 nm respectively, the second peak also becomes much more distinct. This makes the two profiles at a lower wavelength characteristic to the doubly reduced $\{PW_{12}\}$ species. The studies showed measurement of the $\{PW_{12}\}$ species starting from 0 V and depicting the

progression from the first reduction process to the second reduction process. Close monitoring of these processes allowed for the identification of the absorption profiles and the shift in peaks between the two processes, making the recognition of the reduction process by the UV-vis band possible. The reversibility of the POM was encouraging as it showed the applicability for several uses if the starting POMs could be isolated again.

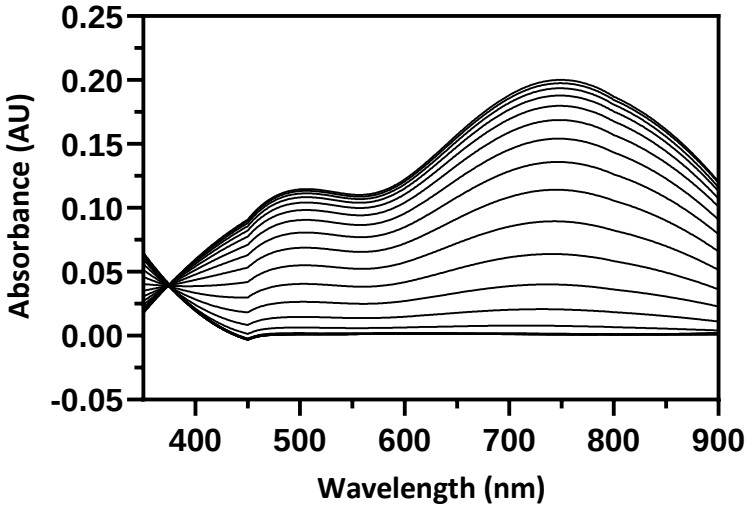

Figure 31: Scans taken for the first electron reduction of 2 mM Keggin in 0.2 M TBAPF6 electrolyte solution. The cathode (working electrode) was a platinum/ rhodium wire, and it was assumed that there was no change to the glassy carbon used for the CV scans. The anode was a platinum wire and the reference mercury, containing a saturated aqueous solution of mercury chloride. Reference and anode electrodes were separated in the reaction mixture by a porous fritted glass. Applying a potential of -0.57 V with the set up shown and discussed in Figure 27. Scans were taken every 10 minutes until the convergence point was reached; once achieved the potential was set to 0 V.

$$[PW12]^{3-} + e^{-} \rightarrow [PW12]^{4-}$$

Equation 5: showing the equation for the first electron reduction of the Keggin-{PW_{12}} POM; starting with an overall charge of 3^-.

The same set up as above was utilized for the metatungstate-{W_{12}} studies due to the success seen for the {PW_{12}}. This was relatively straight forward as the technique was developed whilst running the {PW_{12}} reactions. Divergent to the {PW_{12}} studies was the use of a 1:4 (v:v) water: DMF solvent mixture for the {W_{12}} species. Any potential complications cause by the presence of water and hence H_2 formation could be identified and was not observed. The baseline was seen to remain constant whilst the development of an

absorption band was observed at 725 nm characteristic of a POM reduction, shown in Figure 33, this shifted upon employing a more negative voltage to 650 nm.

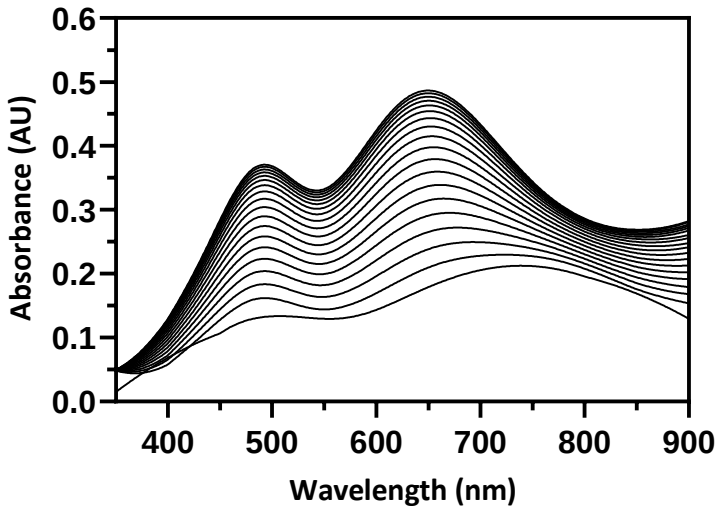

Figure 32: Scans from the second electron reduction of 2 mM Keggin in 0.2 M [TBA][PF_6] electrolyte solution. The cathode (working electrode) was a platinum/ rhodium wire, and it was assumed that there was no change to the glassy carbon used for the CV scans. The anode was a platinum wire and the reference mercury, containing a saturated aqueous solution of mercury chloride. Reference and anode electrodes were separated in the reaction mixture by a porous fritted glass. A potential of -1.12 V was applied, and scans taken every 10 minutes until the convergence point was reached, then the potential was reverted to -0.57 V and then 0 V to check the reversibility.

$$[PW12]^{4-} + e^{-} \rightarrow [PW12]^{5-}$$

Equation 6: The second electron reduction of the Keggin-{PW_{12}} POM starting with an overall charge of 4^-.

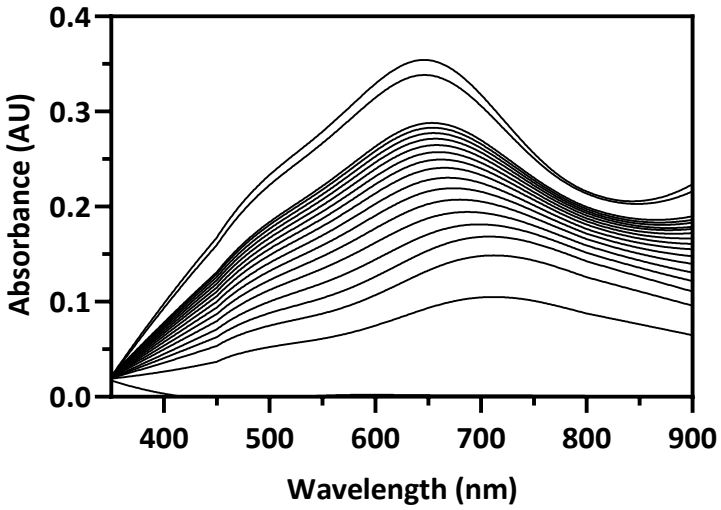

Figure 33: Spectro-electrochemistry of 2 mM Metatungstate in 1:4 water:DMF in 0.1 M $TBAPF_6$ electrolyte solution. The cathode (working electrode) was a platinum/ rhodium wire, and it was assumed that there was no change to the glassy carbon used for the CV scans. The anode was a platinum wire and the reference mercury, containing a saturated aqueous solution of mercury chloride. Reference and anode electrodes were separated in the reaction mixture by a porous fritted glass. A potential of -1.26 V was applied, and scans taken every 20 minutes until a point was reached where the scans converged, the voltage was then further decreased to -1.32 V when lines converged/ after a period of several hours, the voltage was reverted back to 0.0 V to check the reversibility.

$$[W12]^{6-} + e^{-} \rightarrow [W12]^{7-}$$

Equation 7: The first electron reduction of the metatungstate-{W_{12}} POM, starting with an overall charge of 6-.

2.3.2.4 Disulfide Substrates

To test the activity of the reduced POM species on varying strength disulfide bonds, two commercially available disulfides were used, Figure 34 and two synthesized peptide sequences. The IgG3 and AGT peptides were synthesized by Fmoc-SPPS (page 92), Figure 35 and Figure 37 respectively.

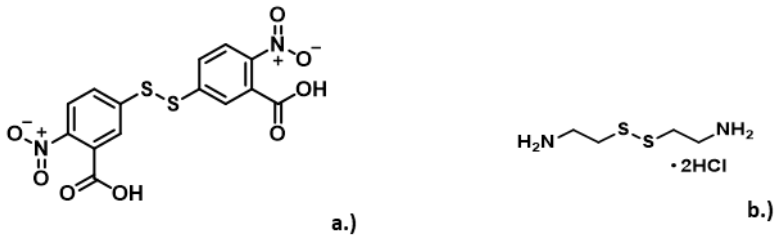

Figure 34: a) DTNB (**1**) the aromatic substrate, b) cystamine dihydrochloride, CD, (**2**).

These peptide sequences were taken from biologically relevant proteins: the AGT peptide represents residues from angiotensinogen (**5**); the IgG3 peptide (**4**) represents residues from an IgG3 antibody. The disulfide bond in the former protein modulates release of angiotensin which controls blood pressure. The disulfide in the IgG3 example links the heavy chains of the antibody. Single strands of the peptides were synthesized by hand using solid phase peptide synthesis (SPPS), the experimental for SPPS can be seen on page 92. Subsequently two strands were oxidized to form the relevant disulfide bond and yielding the planned peptide. Due to the homology of the sequence for the IgG3 dimer, this peptide could be oxidized to the dimer after synthesis and purification, through reverse-phase preparative HPLC, simply by dissolution in water and stirring in air for 48 hours. Several different methods to speed up the rate of oxidation were attempted such as adding an equivalent of iodine and a small volume of DMSO. While the DMSO was successful it did not increase the time scale of oxidation significantly. The addition of iodine did increase the rate of oxidation but also led to an increase in impurities, due to the higher isolated yield afforded by oxidation in air, this method was selected as the preferred approach. The same difficulties were encountered for the synthesis of the AGT peptide, however air oxidation took longer (a minimum of 14 days); therefore, the ratio of DMSO solvent was slightly increased and this led to a successful oxidation within 5 days.

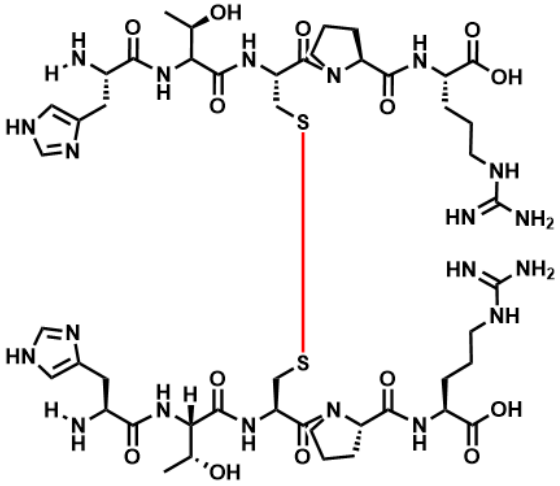

Figure 35: IgG3 peptide structure (**4**), the image shows the oxidized form as the S-S disulfide bond is present, both chains have the sequence: HTPCR, MS to indicate the oxidized peptide can be seen in the supporting information.

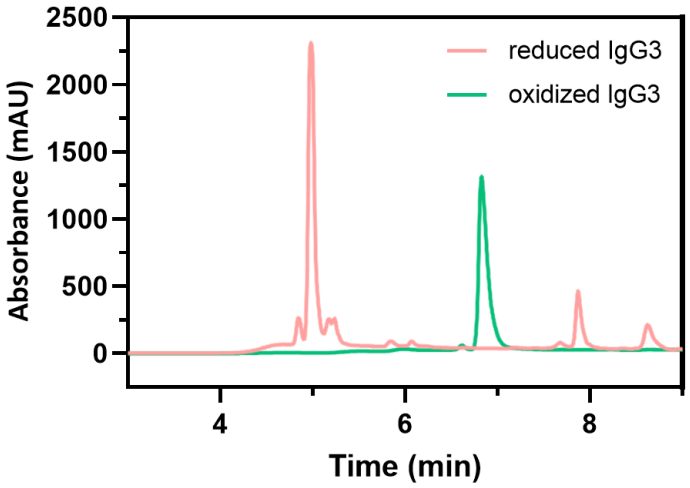

Figure 36: Analytical HPLC trace showing the shift for the reduced IgG3 peptide to the oxidized IgG3.

The analytical HPLC traces for the oxidized and purified peptides can be seen in Figure 36 for the IgG3 and Figure 38 for the AGT. Both figures also show the reduced chains and the shift associated, the extra peaks present in the reduced forms are impurities which are removed upon further purification once oxidised.

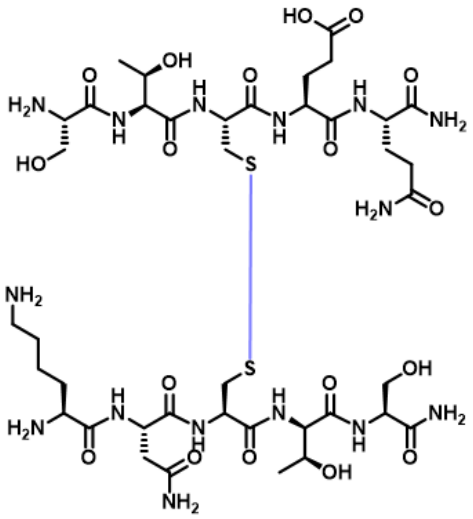

Figure 37: The AGT peptide used to represent the protein model. The sequences used for either chain was selected from the protein at the S-S bond being analysed. The peptide was synthesized via solid phase peptide synthesis and air oxidation.

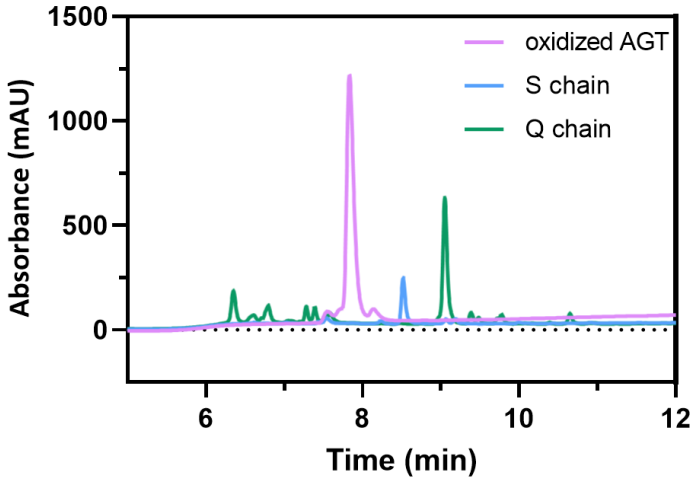

Figure 38: Analytical HPLC trace showing the formation of the oxidized AGT peptide from the two single strands named S and Q.

To identify electronic properties of the disulfides, CVs were taken of the two commercial substrates and the IgG3 peptide; as synthesis for this peptide was successful in a higher quantity, isolating (110 mg, 0.0899 mmol). The AGT peptide was characterized by HPLC and MS and used for several example experiments, see page 89. However, this model was not used for further experimental work, it is anticipated to be used in future investigations.

Comparisons of the CVs of the three-disulfide substrates indicated that, as predicted, the peptidic disulfide has the most negative redox potential, showing an irreversible reduction potential at -1.8 V, Figure 39. The lack of an oxidation peak indicates the irreversible nature as well as the decay of the peak upon cycling the CV. Due to fast decomposition of the peptide, repeated scans were not possible to study the reduction peak further. The scan taken of the peptide sample does shows two irreversible reduction events, however, the first at -0.6 V can be attributed to the presence of oxygen in the sample which dissipated with further degassing. The strength of the disulfide was anticipated due to the shielding effect of the surrounding amino acids and the differing strength of disulfide bonds in peptide structure[24].

Unsurprisingly, the CD (cystamine dichloride) molecule was only slightly more positive at -1.3 V due to it being an aliphatic molecule, Figure 41, the anticipated stronger disulfide of an aliphatic was also indicated by the DFT calculations introduced earlier. The CV of the DTNB

molecule looks far more complex but through literature and CV studies it was assumed with confidence that the first reduction peak correlates to the disulfide within the molecule being far more positive with a reduction potential of 0.2 V, Figure 40. This makes it the weakest disulfide substrates of those studied.[25] The relatively weak disulfide bond is a result of the strong electron withdrawing effects of the *para*-nitro substituted aromatic ring.

It is apparent that the reduction potential for the S-S bond cleavage of CD and the peptides (assuming AGT is similar to IgG3) is far more negative than for DTNB. Hence, a stronger reducing agent is required, which from Figure 28, can be seen to be the $\{W_{12}\}$.

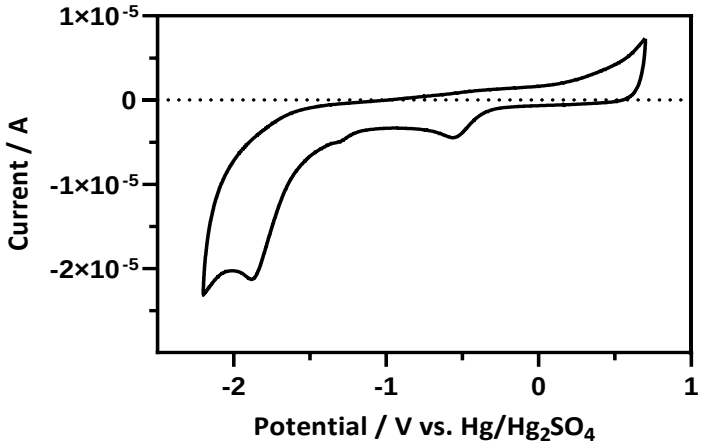

Figure 39: Shows the CV scan taken of 0.1 M IgG3 protein peptide model, dissolved in a dry DMF mixture with 0.1 M TBAPF6. The scan was swept positive to negative 1 V to -2.5 V and back, 2 cycles; displayed above is the second cycle. The reduction peak shown at -0.5 V is due to oxygen still being present in the solvent mixture due to not enough degassing. The 1st and only reduction of the peptide can be seen at -1.8 V.

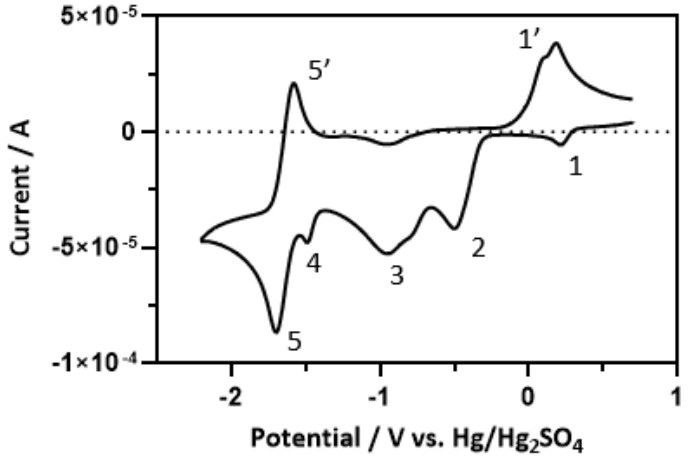

Figure 40: Shows the CV scan taken of 2 mM DTNB dissolved in dry DMF with 0.1 M $TBAPF_6$. The scan was swept from 0.8 V to -2.0 V and back, 2 cycles; displayed above is the second cycle.

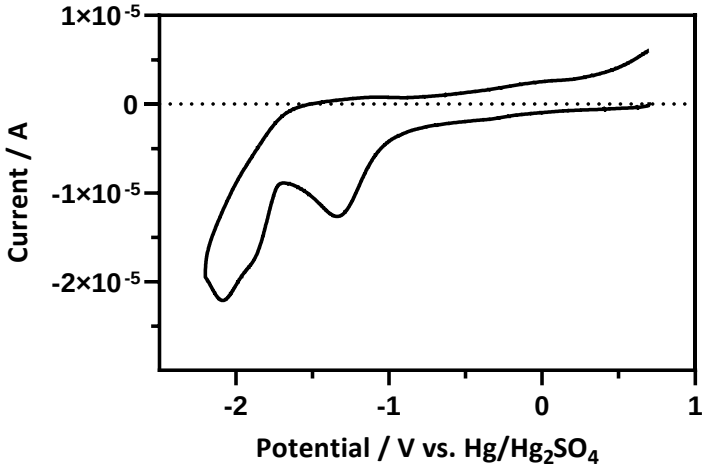

Figure 41: The CV scan taken of 1 mM **CD** dissolved in a 1:4 water: DMF mixture with 0.1 M $TBAPF_6$. The scan was swept from positive to negative 1 V to -2.5 V and back, 2 cycles; displayed above is the second cycle.

2.3.3 Solar Reductions

It is well known that POMs can be reduced through photo-excitations, causing a ligand to metal charge transfer (**LMCT**) and initiating the colour change from the colourless oxidized (d^0) state to the blue reduced (d^1) states.[3,26] The use of a solar-reactor, containing a 500 W mercury-xenon lamp (operating at 200 W) emitting strong UV and visible light, to reduce the POMs has several advantages: i) it is a clean reaction, no need to add chemicals or probes to the system and ii) reactions are relatively fast, several occurring under a minute. Due to easy access to a solar reactor, photo-reductions of the POMs were the first technique explored. Previous solvent screens showed the $\{PW_{12}\}$ to be more soluble than the $\{W_{12}\}$; DMF, which is a good electrolysis solution, with a wide potential window and routinely used for CVs and spectro-electrochemistry, was used for the photo-excitation experiments. The $\{W_{12}\}$ proved to be far less soluble compared to $\{PW_{12}\}$ in this solvent, after testing the solvent window using different mixtures it was concluded that a 1:4 water:DMF solvent mixture was optimal. This is rather unconventional as water has a small solvent window for electrolysis, however, we found that having a majority DMF system allowed for a large enough window whilst keeping the $\{W_{12}\}$, and $[TBA][PF_6]$, in solution throughout the experiments.

2.3.3.1 Solar Reduction Reactions

As the oxygen in the ambient atmosphere can re-oxidize the reduced POMs, a thoroughly inert system had to be set up for every reaction. Due to the lower LUMO of the Keggin-{PW_{12}} and less energy being required for the reduction of it, it proved to be more stable for a longer period even when exposed to small amounts of oxygen; the Metatungstate-{W_{12}} on the other hand is extremely sensitive to the presence of oxygen and was far less stable.

Solutions of the POM were degassed and placed under an argon atmosphere prior to placing them into the solar reactor, Figure 42; both POMs were tested simultaneously. The {PW_{12}} samples showed blue colouring to an obvious extent after 5 minutes. The {W_{12}} samples on the other hand, took a minimum of 3 to 4 hours to show an obvious blue colour.

It was concluded that the most effective way to add the substrate was as a solution due to the need for an inert atmosphere. The dissolved substrates were separately degassed and then added to the reduced POM *via* cannula. Adding 0.5 molar equivalents of DTNB to the Keggin-{PW_{12}} solution showed no noticeable change initially. An excess of DTNB was added and after 30 minutes a colour change was noticed, Figure 42. The colour change did not proceed to colourless but to a deep red solution.

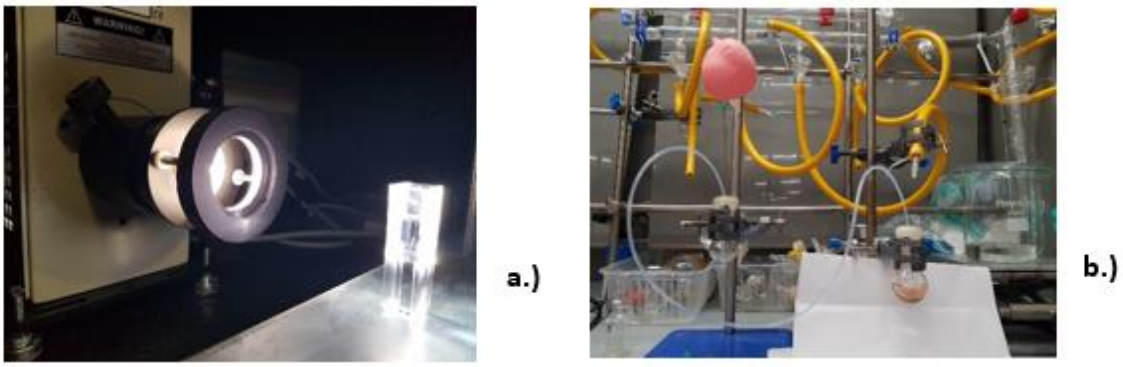

Figure 42: a.) illustrates the solar reactor shining on a sample, this is not a sample taken for the above-described reaction as it isn't in an inert atmosphere, however it shows a similar set-up used; b.) depicts the set-up of the dissolved substrate solution being cannulated to a reduced POM solution, the red colour is due to the DTNB reduction as mentioned above, hence showing a complete reaction.

DTNB does not absorb in the visible region however the distinctive absorption profile of its reduced form, 5-thio-2-nitrobenzoic acid (**TNB**), provides unambiguous spectroscopic confirmation of disulfide bond cleavage.[25] An example of the growth of the TNB peak can be

seen in Figure 48, at λ = 495 nm. Hence the addition of DTNB to reduced {PW_{12}} results in the formation of the oxidized product, TNB, and a dark red colour. The reaction was repeated several times with lower equivalents of the DTNB and longer residence time within the solar reactor, which proved successful.

In the case of the {W_{12}} POM several challenges were encountered. Due to the oxygen sensitivity of the POM, even adding a cannula to the sealed solution resulted in de-colouration, limiting the confidence of the reliability of this set-up. In addition, the colour resulting from solar irradiation never progressed passed a light blue, even after a 5-hour irradiation period, Figure 43.

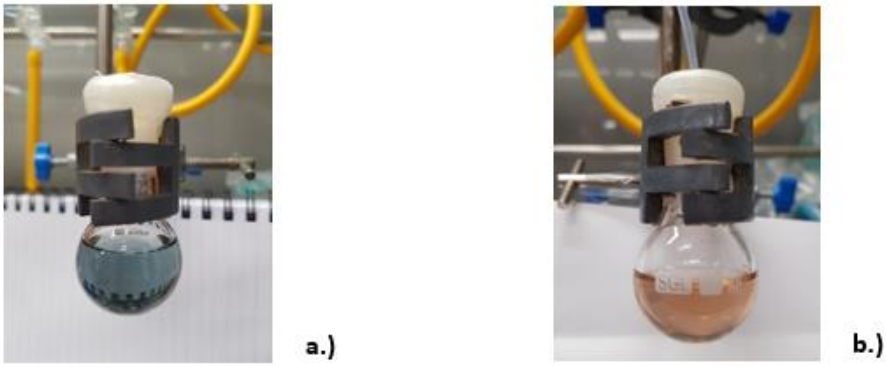

Figure 43: a.) the blue solution observed after long solar irradiation of the POM. The Metatungstate was never observed darker than depicted whilst the Keggin was observed to go opaque often and nearly black in colour due to the intensity; b.) the red solution observed after the cannular addition of DTNB solution.

These challenges were overcome by setting up the cannular system prior to irradiation. The system was degassed and placed under argon, with all reactants already prepared and placed into the solar reactor; but only the POM solution was placed in direct line of the solar beam. This led to a successful reaction and the same colour change was observed as previous however at a much faster rate than for the {PW_{12}}.

Due to extensive repetition of the experiment, an ATMOS-bag was set up to facilitate the handling of solutions and in an inert atmosphere starting from the preparation of solutions to ensure that no oxygen was present at any stage. The ATMOS-bag is simply a flexible, inflatable polyethylene chamber with built-in gloves that allows for a controlled and isolated environment within the fume hood. Another factor considered was the counter ion present on the Keggin-type-POM and hence both the $(NBu_4)_3[PW_{12}O_{40}]$ and the $H_3[PW_{12}O_{40}]$ types

were tested, Figure 44, however no observable difference was seen and the $H_3[PW_{12}O_{40}]$ type was used for further reactions.

Figure 44: Solutions of both the $(NBu_4)_3[PW_{12}O_{40}]$ (left 2 samples) and the $H_3[PW_{12}O_{40}]$ (right two samples) type Keggin with controls where no DTNB was added; to each 1 equivalent DTNB was added, and the reactions were done in the ATMOS-bag and reduced using solar-irradiation.

The same solar reactions were repeated with CD (**2**) as the substrate. In this case all solutions needed a 1:4 water:DMF mixture as the CD was also insoluble in pure DMF. As the techniques had been optimized for the POMs with DTNB, the same procedures were utilized for the CD regarding the set up and solar reactor timings.

As expected, a de-colourisation was only observed for the $\{W_{12}\}$. This added confidence in the initial predictions, which had stated that the $\{PW_{12}\}$ would not have enough potential energy to reduce the disulfide within the aliphatic molecules while the $\{W_{12}\}$ species could. No red colour was observed due to the CD not being a dye. Therefore, a clean blue to colourless reaction was observed for the $\{W_{12}\}$ reactions and no changes were observed for the $\{PW_{12}\}$; the final colour changes of each reaction can be seen in Figure 43. The Keggin-$\{PW_{12}\}$ solution for DTNB seems unchanged due to how dark the colour change is of the DTNB and some remaining reduced $\{PW_{12}\}$. The remaining blue colour observed in the $\{PW_{12}\}$ and DTNB reaction could be due to left over reduced $\{PW_{12}\}$ species. This indicated either the calculation was imprecise, and a large excess of POMs were used; or the POM was reduced to multiple electron reduction states and hence the POM species stays reduced even as it has lost electrons. The latter explanation seems reasonable as it is known that the first reduction process of the $\{W_{12}\}$ occurs at a much more negative potential, hence if the solar reactor can reduce the POM to this extent it potentially also has the ability to reduce the $\{PW_{12}\}$ species up to the 4^{th} reduction process or higher. This illustrates a large unknown

component of these experimental techniques, as characterization was done up to the first two reduction processes only, for each POM.

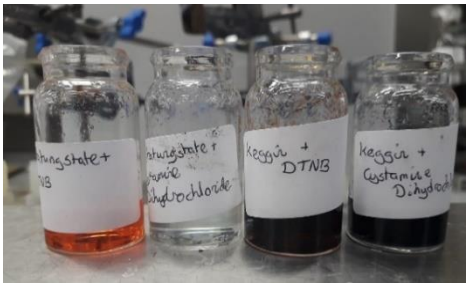

Figure 43: Solutions of POMs, $\{W_{12}\}$ (2 mM) to the left showing first with DTNB and second with CD in both cases 1 equivalent added; to the right shows the solutions containing Keggin, physically a dark red colour could be observed in the DTNB type reaction however it is difficult to see in the image and no change was observed with CD.

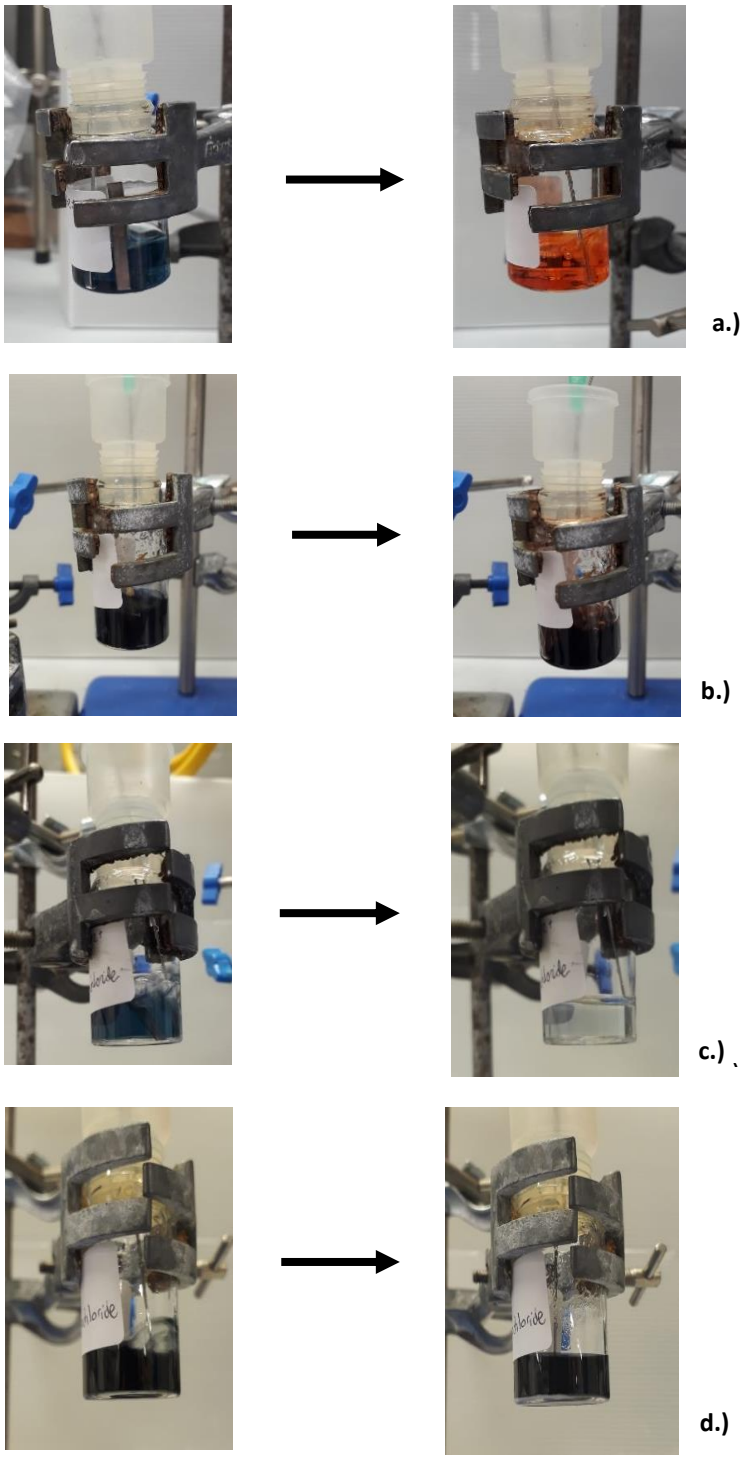

Figure 44: a.) Solar-reduced Metatungstate (2 mM) and DTNB addition, b.) Solar-reduced Keggin (2 mM) and DTNB addition, c.) Solar-reduced Metatungstate (2 mM) and CD addition, d.) Solar-reduced Keggin (2 mM) and CD addition.

2.3.4 Chemical Reductions

Following the solar-reductions, progress towards a system that allows for a faster reduction of the $\{W_{12}\}$ was sought. Chemical reduction was explored as a potential option. Several factors were of importance when choosing a reductant. The reductant was required to: a) be easily separable to the dissolved POM, b) have a potential strong enough to reduce the POM and c) leave only non-photon absorbing trace amounts.

The use of a magnesium (**Mg**) wire presented one of the best options. Mg has a standard reduction potential of -2.69 V making it strong enough to reduce both POMs. It was easily recoverable and simple to use in an inert atmosphere.

The POM solutions were placed under an inert atmosphere and degassed by bubbling argon through the solution for 15 minutes, prior to the addition of the magnesium wire. After optimisation it was concluded that for the reduction of the POM a 30-minute time period resulted in sufficient reduction. As the Mg has a significantly higher reduction potential compared with the $\{PW_{12}\}$ some unexpected results ensued, mainly the irreversible reduction of the POM. This was attributed to the Mg most likely reducing the $\{PW_{12}\}$ past the 3rd electron reduction. Hence for any $\{PW_{12}\}$ chemical reductions a shorter time frame was applied and the Mg was removed once a visible blue colour was formed. Results from the chemical reductions were used primarily to check the operation of the system for use with the $\{W_{12}\}$, as this was the more promising probe for peptidic disulfide bonds.

2.3.4.1 Chemical Reduction Reactions of the Keggin-type, $H_3[PW_{12}O_{40}].11H_2O$

The POM species was reduced as described using Mg ribbon. To attempt to remain consistent the Mg was weighed and the same concentrations of $\{PW_{12}\}$ were used. Initially the samples were left to reduce until a visible blue colour was observed. At this point the number of electrons reduced was not considered of paramount importance; as for the proof-of-principle it was merely required to show an accurate, measurable, and reliable process of re-oxidation of the POM species through the reduction of a disulfide.

Initially, it was expected that the UV-vis absorptions to decrease and then cease at differing absorbances depending on the concentration of disulfide added. However, after several

runs and repeats it was apparent that the samples always resulted in the re-oxidation of {PW_{12}} to an absorbance of 0 AU. Multiple repeat experiments were performed to attempt to find a pattern in the time the POM took to re-oxidize; Figure 45 shows an example of a run taken. From these results it was, however, deducible that no pattern could be found; in addition, the reproducibility of these runs was low as timings and initial absorbance values often differed.

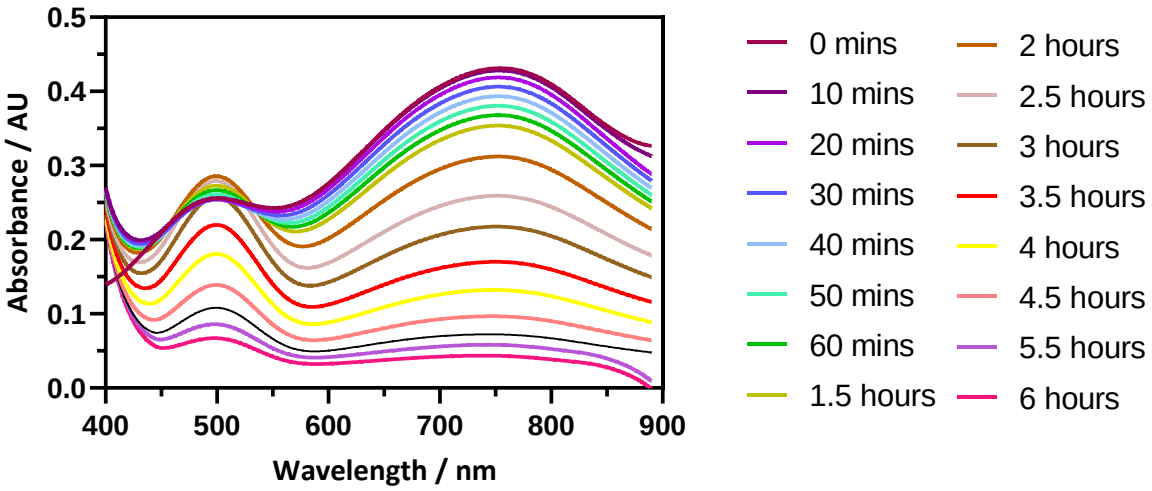

Figure 45: UV-Vis spectrum recorded over at intervals 5.5 hours of 1 mM {PW_{12}} in 3 mL solution of DMF. Reduction was achieved via the addition of a strip of Mg (~0.044 g). After the initial scan of the reduced species 1 mM DTNB was added

2.3.4.2 Absorption Spectroscopy using Mg ribbon as the reductant for the Keggin-type, $H_3[PW_{12}O_{40}].11H_2O$

To further understand the inconsistencies in our method, the reduction of the Keggin-{PW_{12}} POM was repeated using Mg ribbon as the reductant and the process monitored by UV-Vis absorption spectroscopy. The acquired data can be seen summarized in Figure 46.

The results of the timed reduction were surprising; when compared to the spectro-electrochemistry previously carried out, the second reduction is not observed; the characteristic peaks, previously at 494 nm and 693 nm are absent. Additionally, the maximum absorbance reached *via* spectro-electrochemistry was ~0.2 AU whereas with the Mg reduction technique above an absorbance of 1.3 AU was achieved, despite the chemical reduction being run at a lower concertation.

There is a strong possibility that the Mg is reducing the {PW_{12}} much further than the 2nd reduction. The reduction potential of Mg is -2.69 V,[27] which is far more negative than possibly all four reduction processes in the Keggin; hence an unknown number of electron reductions could be occurring. This makes the Mg an unsuitable reductant for this POM.

$Mg(OH)_2 + 2e^-$	⇌	$Mg + 2 OH^-$	-2.690	[27]

Equation 8: Showing the reduction potential of Mg.

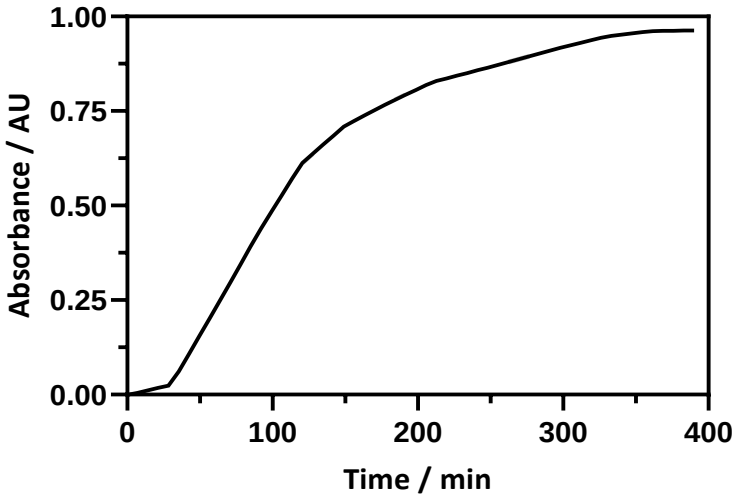

Figure 46: Spectrum showing the time against absorbance of the reduction of 1 mM {PW_{12}}-Keggin at 750nm using magnesium ribbon (~0.045g). The curve levels off indicating complete reduction of the species.

2.3.4.3 Reduced PW12: $H_3(PW_{12}O_{40})$ POM reactions with CD

A sample of the Keggin-{PW_{12}} species was tested with 1 molar equivalent of CD, Figure 47. Despite theoretical data hypothesizing this reaction should not work it was found to progress at a similar rate to the other reactions where DTNB was the disulfide added. Again within 5 hours a significant absorbance decrease is observed.

The success of the reaction could potentially be explained due to an electrostatic interaction between the {PW_{12}} and the charged groups situated on the CD. This hypothesis was verified *via* a reaction with reduced {PW_{12}} and the addition of a sample of diethyl disulfide in

excess, left under argon, to see whether a colour change occurred. After 1 day hardly any visible colour change was observed, and the reaction was terminated. This seems to suggest that charged moieties on CD could promote a favourable interaction with the {PW_{12}} that facilitates electron transfer. To confirm this more experimental studies are required.

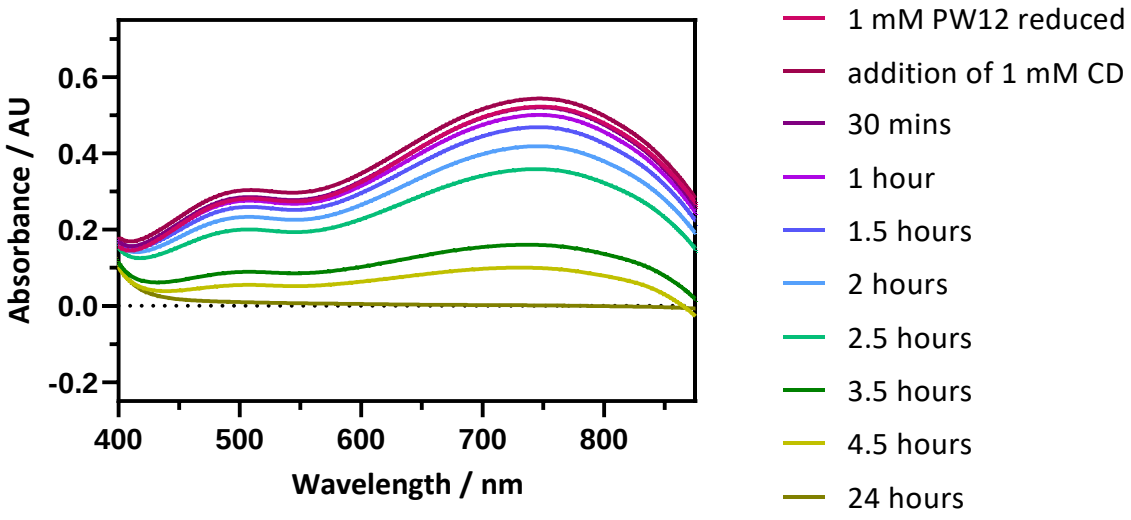

Figure 47: UV-Vis spectrum recorded over at intervals ~4.5 hours of 1 mM {PW_{12}}-Keggin in 3 mL solution of DMF, and a little H_2O for the solubility of the CD. Reduction was achieved via the addition of a strip of Mg (~0.044 g). After the initial scan of the reduced species 1 mM CD was added and consistent measurements taken.

2.3.4.4 Chemical Reduction of Metatungstate: $Na_6[W_{12}O_{39}].2H_2O$ {W_{12}}

As experiments with {PW_{12}} were primarily used as proof-of-principle, we now turned our attention towards the development of techniques to reduce {W_{12}}. The experimental techniques where kept the same as for the {PW_{12}}. Solution mixtures of 1:4 H_2O: DMF were used, and solutions thoroughly degassed with argon prior to UV readings being taken.

Initially the solutions were exposed to the Mg ribbon until an obvious blue colour was observed, the disulfide substrate was subsequently added, and the oxidation of the POM was monitored. All Metatungstate-{W_{12}} samples had a concentration of 1 mM and the amount of Mg by weight was kept at as consistent as possible.

Initially, an excess concentration of the disulfide substrate was used; CD, even with a 2:1 ratio of disulfide substrate to POM there were immediate disparities with the predicted absorbances, as an increase was observed over time, Figure 48.

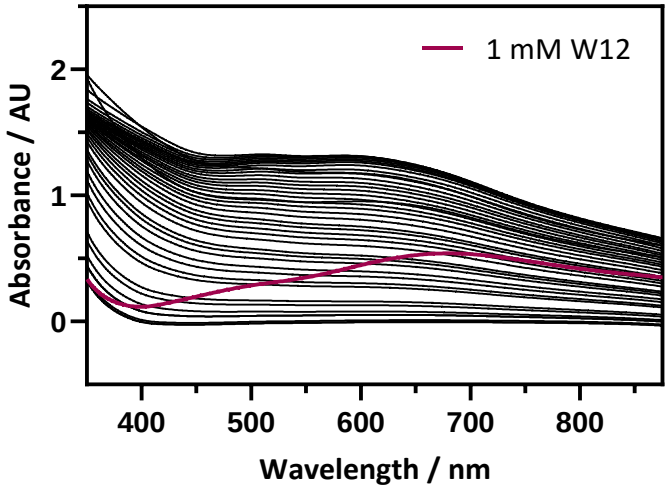

Figure 48: UV-Vis spectrum collected following the oxidation of the 1 mM {W_{12}} POM species (purple line) upon the addition of 2 mM CD (black lines) to a 3.5 mL solution of 1:4 H_2O:DMF. The full run took approximately 3 hours with each reading being taken every 5 minutes. Upon the addition of CD the absorbance increases initially before then decreasing.

Although the time scale to completion seemed to remain consistent, the initial increase in absorption indicates that a secondary process is occurring in addition to the re-oxidation of the POM and subsequent reduction of the disulfide. The same process was observed when experiments were run with a 1:1 equivalent ratio.

As shown in Figure 49, this increase in absorbance does not occur with an excess of {W_{12}} compared to CD. Reinforcing the assumption that there is a secondary process occurring. Conceivably, with the thiyl radicals that are formed, and as the CD molecules are in excess, the possibility that radical reactions and stabilization are occurring is plausible, especially as an electrostatic interaction could be occurring between CD molecules.

Given the above, it was decided to continue with lower concentrations of the disulfide substrate. From analysis of further measurements with lower CD concentrations, no observable pattern could be determined. Apart from the tendency that the lower the disulfide concentration the more time taken to reach 0 AU. However, a further discrepancy was soon realized after repeated experiments of differing concentrations; the starting absorbance values of the POM all differ despite similar reduction times and weights of Mg ribbon. This not only indicates that a clear comparison is not possible but more importantly that differing levels and concentrations of electrons potentially are being reduced (i.e., 1, 2

or more electrons per POM) as it is unknown where the possible electron reductions lie on a UV-vis spectrum.

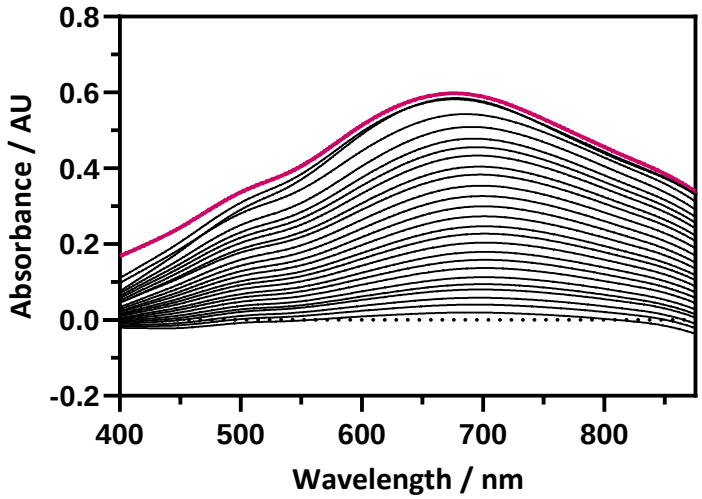

Figure 49: UV-Vis spectrum showing the oxidation of 1 mM {W_{12}} (red line) upon the addition of 0.5 mM CD to a 3.5 mL solution of 1:4 H_2O:DMF. The full run took roughly 2 hours, readings taken every 5 minutes.

2.3.4.5 Absorption Spectroscopy using Mg as the reductant of Metatungstate:

$Na_6[W_{12}O_{39}].2H_2O$

Due to the differences in starting absorption observed the spectro-chemical analysis was repeated with Mg as the reductant for the {W_{12}} POM species, Figure 50. Following this study, it was decided to target a starting absorbance of 2 AU. This appeared to be a convergence point of the reduction of the POM concentrations and hence possibly indicating a good absorbance to give a standard reduction. Re-iterations were undertaken of the three concentrations of the disulfide substrate, using the new starting standard absorbance as close to 2 AU as possible, shown in the following section.

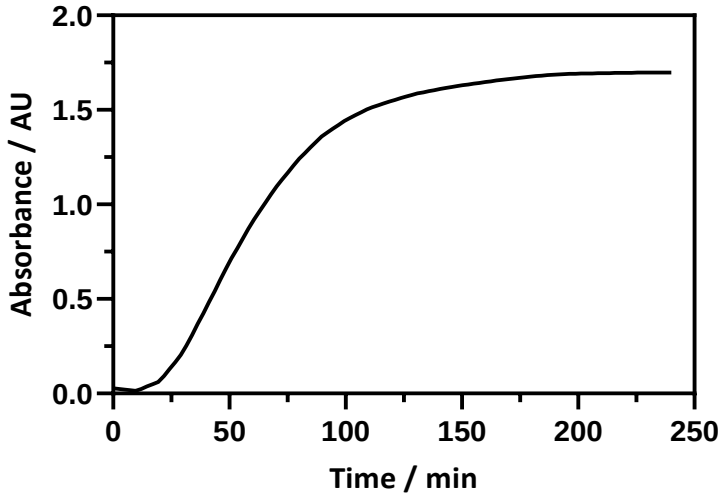

Figure 50: Graph showing the absorbance against time of the reduction of Metatungstate $\{W_{12}\}$ by Mg ribbon at 675 nm.

2.3.4.6 Reduction Reactions of Metatungstate: $Na_6[W_{12}O_{39}].{}_2H_2O$:

Reactions were undertaken using $\{W_{12}\}$ as previously described. Due to the variation in disulfide concentration a slight difference between the scans was anticipated. However, this was not observed. In fact, timings were extremely similar, often taking between 2 and 5 hours. The hypothesis was made that oxygen could be leaching into the system despite thorough degassing prior to the reaction and ensuring that the solution is under argon. As the reaction is kept under argon and is degassed there are limited ways oxygen could be entering the system; one possibility was through the removal of the magnesium and subsequently the substrate addition as the setup was only briefly degassed again after addition of substrate or removal of Mg. Despite cleaning the Mg thoroughly before addition, it is also possible that oxygen could be adsorbing onto the metal surface or present in between the powder particles of a substrate, and it only took a small volume of oxygen entering the system for it to make a marked difference and affect the results.

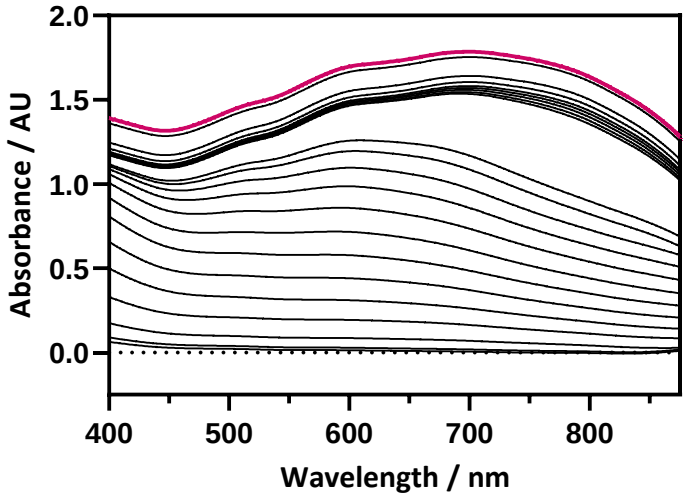

Figure 51: UV-Vis spectrum showing the oxidation of 1 mM $\{W_{12}\}$ (purple line) upon the addition of 0.5 mM CD to a 3.5 mL solution of 1:4 H_2O:DMF. The full run took approximately 5 hours, readings were taken every 10 minutes.

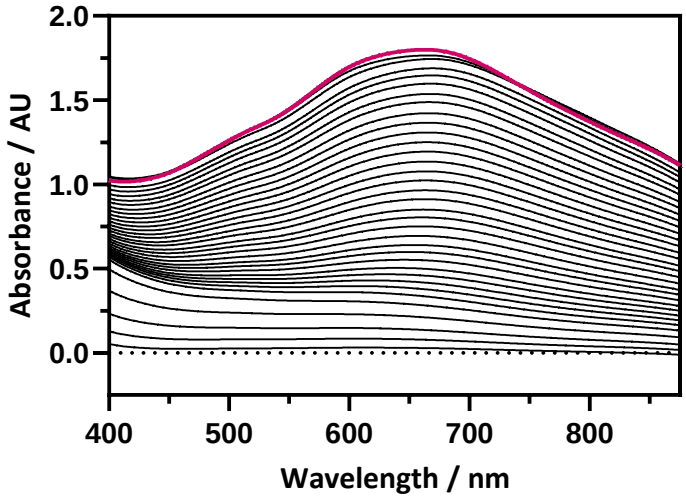

Figure 52: UV-Vis spectrum showing the oxidation of 1 mM $\{W_{12}\}$ (purple line) upon the addition of 0.25 mM CD to a 3.5 mL solution of 1:4 H_2O:DMF. The full run took roughly 5 hours, scans taken every 10 minutes.

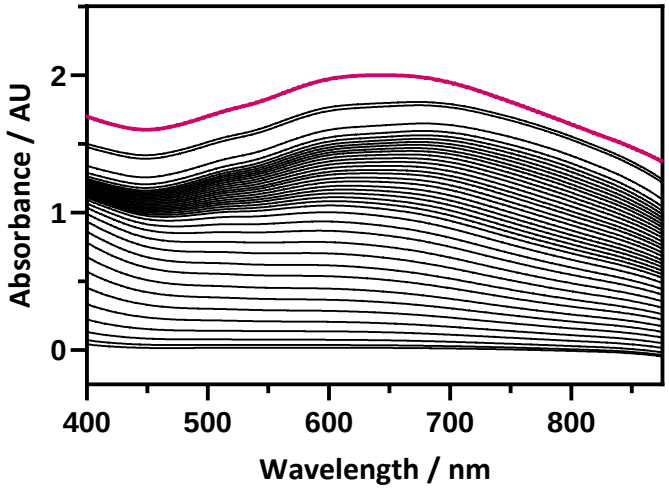

Figure 53: UV-Vis spectrum showing the oxidation of 1 mM $\{W_{12}\}$ (purple line) upon the addition of 0.125 mM CD to a 3.5 mL solution of 1:4 H_2O:DMF. The full run took roughly 6 hours, readings taken every 10 minutes.

Hence the setup was altered slightly and as well as degassing before reduction, the solution mixture was degassed after the addition of the Mg and placed under vacuum for a minimum of 30 minutes, followed by bubbling argon again, in hope of ensuring a completely inert environment. The data was then repeated, Figure 54.

At first these results seemed promising as a slight time trend could be seen; double the concentration of CD (0.5 mM compared to 0.25 mM) showed half the time required for the full re-oxidation of the $\{W_{12}\}$ to be reached (roughly 2 hours and 5 hours respectively), starting at roughly the same absorbance. However, further repeats of the reaction showed that the results were not reproducible. In addition after every reduction a solid blue substance could be seen at the bottom of the cuvettes; this lead to the assumption that the Mg was reacting with the POM in some unknown way, this theory was reinforced by the Mg ribbon always having a blue coating when removed from the POM solutions which after exposure to air turned white indicating that some of the POM was adhered to the surface of the Mg and therefore taken out of solution, thus changing the concentration.

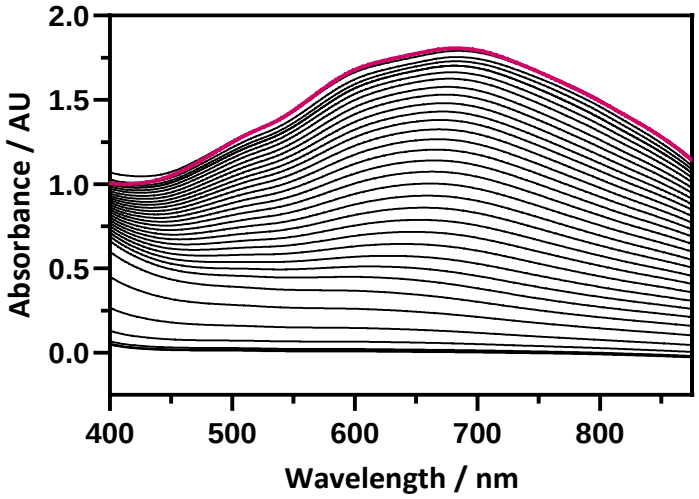

Figure 54: UV-Vis spectrum showing the oxidation of 1 mM {W_{12}} (purple line) upon the addition of 0.25 mM CD to a 3.5 mL solution of 1:4 H2O:DMF. The full run took roughly 5 hours and 22 minutes, readings taken every 10 minutes.

Additionally, it was realized that to find the extinction coefficient it was also necessary to change the concentration to lower the starting absorbance and hence after many trials a concentration of 0.6 mM was set as standard as it gave a starting absorbance below 1 AU. Another factor to consider was the agitation of the solution; so far, due to the small amount of volume (3.5 mL), it was considered that convection/diffusion sufficient to mix the solution allowing for all the POM to interact with the Mg surface; however, as the POM was seemingly coating the magnesium, mixing the solution could reduce this effect and allow for more uniform reduction.

Consequently, samples were taken while stirring the solution. Firstly, the reduction of the POM with Mg was monitored when stirring and for a period after removing the Mg, was saturation was reached. Figure 55 shows the increase in absorption as the POM sample is being reduced with Mg ribbon while the sample is stirred.

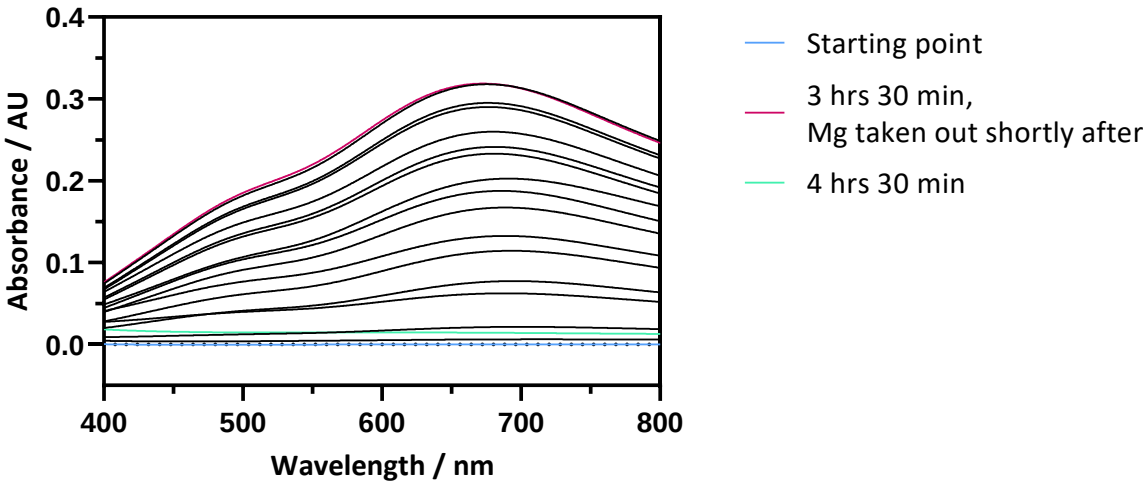

Figure 55: UV-Vis absorption plot indicating the increase in absorption as the POM sample is being reduced via Mg and constant stirring; Mg = 0.04311 g, pH 7 and 0.6 mM Metatungstate in a solution mixture of 1:4 H_2O:DMF. After the Mg ribbon is taken out the absorbance can be seen to decrease again quickly.

Two identical samples under the same conditions were reduced in unison and yet roughly ab hour difference was observed in the time taken to reach the max absorption point; this point was taken when an absorbance stayed at the same value over a 15 to 30-minute period. At this point the Mg was taken out and re-oxidation was monitored while continuing stirring. Although at first glance both samples show a similar pattern over the same time-frame, it is apparent that very different times were required to reach saturation. Additionally, the time-frame of the agitated sample is decreased compared to non-stirred samples, especially the re-oxidation, which indicates perhaps the agitation is increasing the kinetics of the oxygen reaction with the reduced POM. Repeats were taken in parallel with non-stirred samples and again the stirred samples, although quicker to reduce, were also quicker to re-oxidize.

This led to an investigation of the technique and re-evaluation of the process used. Prior literature[5] describes a possible destabilization of the POM under reduced condition in alkali media and hence a potential solution could be to acidify the mixture. Another obvious issue was the Mg as a reductant due to the very strong reduction potential it possesses and hence the unknown electron reduction process which could take place. A major factor to consider was the likely oxygen leakage into the system; through the addition of substrates and taking out of the Mg, as well as via the lid of the cuvettes and the solvent system as DMF strongly

absorbs water and is very difficult to degas. Hence to tackle these problems some changes had to be made in the experimental setup.

2.3.4.7 Altering the Chemical Reductant Species

An alternative reductant, cobaltocene, Figure 56, was chosen as the first electron reduction potential for the metatungstate-{W_{12}} POM lies at -1.25V and hence, we sought after a reductant whose reduction potential was only slightly more negative (-1.33 V) and would therefore have the potential to reduce all first electrons in the species.

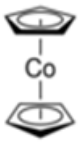

$Co(C_5H_5)_2^+ + e^- \rightleftharpoons Co(C_5H_5)_2$	−1.33V

Figure 56: Showing the structure of cobaltocene and the half equation of the reduction of the molecule with the reduction potential shown in volts.

As the cobaltocene is extremely oxygen sensitive the preparation had to be moved into a glovebox as in the fume hood it wasn't possible to eliminate oxygen entry. The solvent system was changed to methanol (MeOH) as it was easier to degas and more commonly used in the glovebox, in addition all substrates were soluble. Although initially preparing the cobaltocene in the glove box *via* making a stock solution, then subsequently moving outside of the glovebox and working on the Schlenk line the cobaltocene immediately appeared to reduce. This could be seen by the solution changing from a dark purple to a dark brown colour. This process was repeated several times with no success and so the whole process was moved into the glove box. This led to the successful reduction of the metatungstate-{W12}, producing a blue colour. However, after several minutes a precipitate was formed which led to the belief that the new cobaltocene species formed then underwent a cation exchange with the sodium cations surrounding the {W_{12}} species.

Re-oxidation of the sample was assumed, possibly due to the pH of the methanol mixture being too alkali, as the literature states that some reduced species of the POM have been

seen to be unstable in alkali solutions[5]. Hence possibly explaining the instability of the POM and the observed re-oxidation. Therefore, some degassed acetic acid was added. Additionally, the characteristic UV-Vis profile of the reduction of the POMs was not observed, likely due to the gradual development of the precipitate. In a final attempt to use cobaltocene a mixture of acetonitrile (MeCN) and water was used to attempt to keep all reagents soluble, however, this was met with little success. Due to the cation exchange (deduced by the precipitation) and the oxygen sensitivity, it was concluded that an alternative reductant must be employed.

Additionally, Mg ribbon reduction in the methanol 2.5% acetic acid mixture was attempted within the glove box, but the rate of re-oxidation appeared to be sped up turning colourless within minutes and the metal started decaying due to the interaction with the acid; hence this was also not viable option.

2.3.4.8 Attempted reactions with the AGT peptide

Although challenges were encountered identifying a reliable technique of reduction for POMs, the $\{W_{12}\}$ was trialled against the peptide AGT model, using the Mg reduction method. Despite this approach not being reliable, it was theorised that it may give an indication of a positive reduction if the re-oxidation of the POM occurred at a rate faster or comparable to the controls. The peptide model represents the section of the angiotensinogen protein carrying the redox switch (Cys-18 and Cys-138) and was synthesised *via* solid-phase peptide synthesis, purified using HPLC and characterised via MS, Figure 37. Oxidation of these residues causes a conformational shift to expose the tail end of the AGT protein to facilitate cleavage of the peptide angiotensin I, causing hypertension after conversion to angiotensin II.

As discussed, the DFT calculations run by our collaborators suggested that the mono reduced $\{W_{12}\}$ POM has a strong enough reduction potential to reduce disulfides even within a peptide model. This is reinforced and demonstrated through physical experiments and the data seen in Figure 57. The reduction of the $\{W_{12}\}$ and consequent addition of 1 equivalent of the AGT peptide resulted in the expected decolourisation of the solution; the UV-Vis scans were recorded over a 2-hour period after the addition of the peptide.

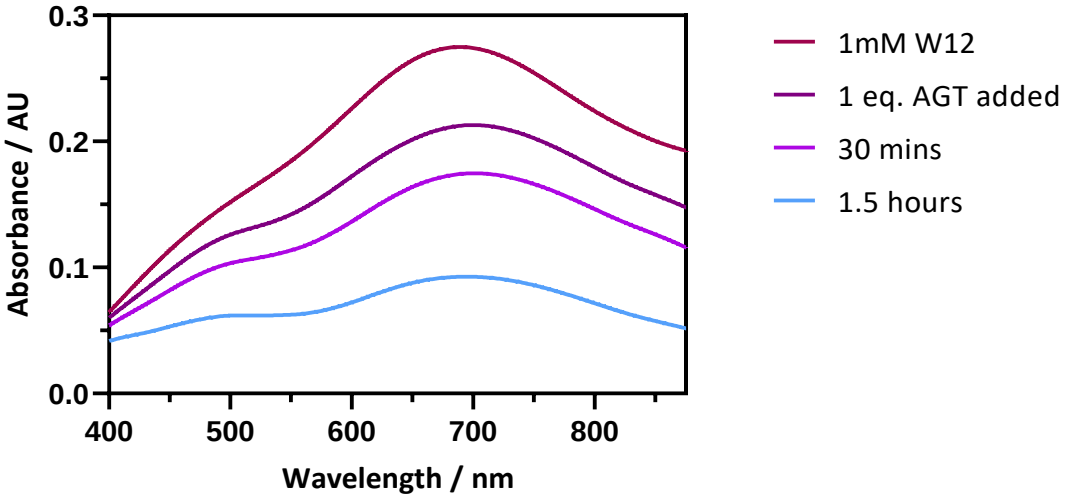

Figure 57: UV-Vis spectrum recorded over at intervals 1.5 hours of 1 mM Metatungstate in 3 mL solution of 1:4 water:DMF. Reduction was achieved via the addition of a strip of Mg (0.044 g). After the initial scan of the reduced specie 1 eq. AGT peptide was added and a measurement taken 15 minutes later.

2.4 Conclusions

Molecular dynamics simulations were employed to assess the viability of POMs as reducing agents for the cleavage of the disulfide bonds present in the DTNB and CD molecules, which was subsequently confirmed experimentally. This is the first time that a POM has been shown to be capable of disulfide bond cleavage.

The synthesis and full characterization of two POMs has been outlined as well as of two peptides. Additionally, we have demonstrated several different techniques for the reduction of the POMs. UV-Vis characterization and profiles were performed using electrolysis to demonstrate the characteristic IVCT band profiles formed by each POM. The samples were irradiated using the solar reactor containing a 500 W mercury-xenon lamp (operating at 200 W) emitting strong UV and visible light, and the reduced species subsequently trialed with disulfide substrates. This study indicated potential; however, addition of substrate and reduction of the POMs was challenging especially when attempting to maintain an inert atmosphere. Moreover, it is suspected that a reduction state lower than the two electron states was achieved, especially for $\{PW_{12}\}$, leading to an uncharacterized reduced species. Hence, we decided to move onto using chemical reduction; this presented an easy separation technique and the choice of a specific reduction potential of the reductant. Mg was used for these reductions and showed great promise. After performing these reactions and attempting further characterization using Mg, it was concluded that the system was not inert enough and the studies mainly showed re-oxidation through dioxygen leakage. Again, the reduction point of Mg was much lower than the $\{PW_{12}\}$ species and likely lead to reduction levels past the third electron.

Overall, the oxygen leakage into our systems was the most significant challenge along with the inaccurate reduction of the POMs to an unknown reduction point. This led to the conclusion that electrolysis would allow for the cleanest and most accurate form of reduction.

2.5 Experimental

2.5.1 Peptide Synthesis

Protected amino acids were purchased from Fluoro-chem and VWR chemicals, ChemMatrix resin from Sigma Aldich and Oxyma Pure (Ethyl cyano(hydroxyamino)acetate) from Fluoro-Chem. Solvents were supplied by SDS and trifluoroacetic acid by Sigma-Aldrich. Other chemicals were acquired from Sigma-Aldrich and were of the highest purity commercially available.

General Coupling Procedure: Peptides were obtained by Fmoc solid-phase synthesis in a 200-µmol scale on Rink Amide-ChemMatrix resin using Fmoc-L-amino acids carrying acid-labile sidechain protection. Fmoc (9-fluorenylmethoxycarbonyl) was deprotected with 20 % piperidine in DMF (dimethylformamide) (2 x 5 min). The resin was washed with DMF (5 x 30 sec) and DCM (dichloromethane) (5 x 30 sec) between synthetic steps. For peptide elongation the protected amino acid (4 eq.) was activated using DIC (diisopropylcarbodimide) (4 eq.) and Oxyma Pure (4 eq.) in DMF.

Determining loading: After deprotection both piperidine/DMF solutions were collected and 10–50 µL (depending on resin amount and loading) was diluted to 10 mL 20% piperidine/DMF. The absorbance of the fulvene-piperidine adduct (ε = 7800 M^{-1} cm^{-1}) was measured at 301 nm (using 10 % piperidine/DMF as the blank) and the loading calculated (Abs = εcl). If Abs > 1.0 the solution was further diluted, and the measurement repeated.

Final N-terminal deprotection: When the peptide was fully assembled, the N-terminal Fmoc group was removed by treatment with 20% piperidine/DMF (2 x 5 min). The resin was washed with DMF (10 x) and CH_2Cl_2 (10 x) and then dried *in vacuo*.

Cleavage: Peptides were cleaved with concomitant removal of the side-chain protecting groups, using TFA (trifluoroacetic acid), H_2O, thioanisole, TIS (triisopropylsilane) (85:5:5:5). After cleavage the solution was evaporated applying a stream of N_2. The residue was washed with diethyl ether and subsequently centrifuged. The cleaved peptides were then dissolved in H_2O with 0.1 % TFA and freeze-dried.

Work-up: The combined solutions were concentrated under a stream of nitrogen. The residue was dissolved in water containing 0.1 % TFA, filtered and purified by preparative HPLC and analysed by LC-MS and ESI mass spectrometry. Alternatively, the cleavage solution is transferred to a 50 mL falcon tube and evaporated under a stream of N_2 to 2-4 mL. Diethyl ether (approx. 30 mL) is added to precipitate the peptide and the solution centrifuged. The supernatant is discarded, and the pellet dissolved in 0.1 % TFA water/MeCN for HPLC purification.

Oxidation: The oxidation of thiols to obtain disulfide bridges was performed under air. A 100 µM solution of each peptide was prepared in H_2O or in a mixture of DMSO/H_2O (1:3) and stirred at 25 ^oC for 48 hours. The reaction was monitored by HPLC and MS.

2.5.2 POM Synthesis

2.5.2.1 Keggin-type POM Synthesis - $H_3[PW_{12}O_{40}].xH2O$ {PW_{12}}:

$Na_2WO_4.2H_2O$ (32.4 g) and $Na_2PO_4.2H_2O$ (16.2 g) were dissolved in 52 mL water at 80 ^oC over 30 mins. 6 M HCl (32 mL) was added dropwise over 5 mins, forming a white ppt. that then dissolved. The resultant solution was left at reflux (100 ^oC) for ~20 hrs, giving rise to a white ppt. The ppt. was filtered, washed with H_2O (3 x 15 mL) and dried under vacuum. The product was recrystallised from hot water yielding a white crystalline solid. Yield: 5.82 g, 0.002 mol. ^{31}P NMR (161 MHz, D_2O) δ(ppm): -15.27 (P). IR (cm^{-1}) ν max: 3475 (O-H), 1071 (P-O), 971 (W=O), 903 (W-O-W), 757 (W-O-W). TGA: H_2O, 6.56%.

2.5.2.2 Metatungstate Synthesis - $Na_6[W_{12}O_{39}].xH_2O$ {W_{12}}:

$Na_2WO_4.2H_2O$ dissolved in stirred 6 M HCl (6 mL) and left stirring for 4 hrs. The resultant yellow ppt. was isolated then washed with 0.1 M HCl (2 x 10 mL) and water (3 x 10 mL) before being dried under vacuum. The yellow ppt. was dissolved in 25 mL water with $Na_2WO_4.2H_2O$ (0.42 g) and left under reflux at 100 ^oC for 3 hrs. Solid impurities were isolated and the remaining solution extracted under reduced pressure, leaving a white ppt. that was washed with isopropanol (3 x 20 mL) and left to dry, resulting in a white crystalline solid. Yield: 1.00 g. IR (cm^{-1}) ν max: 3358 (O-H), 931 (W=O), 867 (W-O-W), 730 (W-O-W).

2.5.3 General POM Reduction Procedures

2.5.3.1 Solar-reduction Processes

The solar-reduction reactions were carried out using the solar reactor which contains a 36 W high energy UV lamp comprising of four 9 W bulbs. Samples were prepared in a fumehood, usually to 1 mM concentration in 5 mL solvent. The solutions were degassed and placed under Argon prior to placing in front of the UV beam. The samples were placed the same distance from the light source. Samples were reduced until an obvious blue colour was observed, 10 minutes was sufficient for the Keggin-type, however, the metatungstate-{W_{12}} version required up to 5 hours of exposure for a clearly visible blue colour; indicating reduction. Samples then either had substrates added via cannula transfer or by placing into an ATMOS-bag and solid addition of substrates.

2.5.3.2 Electrochemical Reduction

The electrochemical device was constituted of a pyrex glass container, containing a magnetic stirrer bar. The cathode (working electrode) was a high surface area carbon mesh. The anode was a platinum strip, situated behind a frit in electrolyte solution and the reference silver, behind a frit containing a saturated aqueous solution of silver nitrate. The measurements were performed on an AutoLab PGSTAT10.

Prior to electrochemical reduction the dissolved dioxygen was eliminated by bubbling nitrogen into the solution, and in later modifications freeze thaw drying. The substrates were dissolved in DMF for the Keggin and a 1:4, water:DMF mixture for the metatungstate initially; and 0.1M TBAPF6 used as a supporting electrolyte. The cell was continuously purged with nitrogen to provide an inert atmosphere. The working potential was set according to previous results in CVs taken; at -0.57V and -1.12V for Keggin {W_{12}} and -1.32 V for metatungstate {W_{12}}. Once bulk electrolysis had been performed on the solutions and the current output stabilised, the samples were poured via canular transfer into inert atmosphere quartz cuvettes.

The control sample contained the same volume used for the reaction mixtures and placed under the exact same conditions; in every case a background run was taken of only the electrolyte solution.

Changes made to technique and solvent mixtures are described above.

The spectrometer used was a Perkin Elmer, Lamda16 UVvis spectrometer.

2.5.3.3 Chemical Reduction

In order to reduce the metatungstate chemical reduction was employed. The same solvent system was used as for electrochemical reduction, namely a 1:4 water:DMF mixture. Before chemical reduction any dissolved dioxygen was removed by bubbling argon through the solution mixture. A strip of magnesium was used as the reductant; this was added post dioxygen removal. The magnesium was left in the reaction solution for 30 minutes, until the required blue solution was observed and then removed under argon prior to any UV-vis scans being taken.

Scans were taken of the background, solvent system, the starting reduced POM solution and at time intervals after addition of substrates.

The spectrometers used were a Perkin Elmer Lamda16 UV-vis spectrometer and a near infra-red Agilent Cary 5000 spectrometer.

2.5.3.4 DFT Calculation Procedures

All the calculations were carried out by collaborators at Universitat Rovira i Virgli and performed at the B3LYP level using LANL2DZ basis set for the W atoms and 6-31G(d,p) for the remaining atoms. Solvent effects were taken into account in the geometry optimisations by using the IEF-PCM continuum solvent model as implemented in Gaussian 09. More specific knowledge can sadly not be provided herein as the work was carried out wholly but the team at Universitat Rovira i Virgli.

2.6 References

1 E. P Papaconstantinou, M. T. Pope, *Inorg. Chem.*, 1967, **6**, 1147–1152.

2 V. De Waele, O. Poizat, M. Fagnoni, A. Bagno and D. Ravelli, *ACS Catal.*, 2016, **6**, 7174–7182.

3 G. M. Varga, E. Papaconstantinou and M. T. Pope, *Inorg. Chem.*, 1970, **9**, 662–667.

4 C. Streb, *Dalton. Trans.*, 2012, **41**, 1651–1659.

5 J. P. Launay, *J. Inorg. Nucl. Chem.*, 1976, **38**, 807–816.

6 C. Zhang, W. Bu, D. Ni, C. Zuo, C. Cheng, Q. Li, L. Zhang, Z. Wang and J. Shi, *J. Am. Chem. Soc.*, 2016, **138**, 8156–8164.

7 U. Kortz, M. T. Pope, *Encyclopedia of Inorg. and Bioinorg. Chem.*, Wiley: Hoboken, NJ, 2012, 1-14.

8 Q. Han, C. He, M. Zhao, B. Qi, J. Niu and C. Duan, *J. Am. Chem. Soc.*, 2013, **135**, 10186–10189.

9 H. N. Miras, J. Yan, D. L. Long and L. Cronin, *Chem. Soc. Rev.*, 2012, **41**, 7403–7430.

10 X. B. Han, Z. M. Zhang, T. Zhang, Y. G. Li, W. Lin, W. You, Z. M. Su and E. B. Wang, *J. Am. Chem. Soc.*, 2014, **136**, 5359–5366.

11 B. Hasenknopf, *Front. Biosci.*, 2005, **10**, 275–287.

12 S. Omwoma, C. T. Gore, J. Y, C. Hu and Y. Song, *Coord. Chem. Rev.*, 2015, **286**, 17–29.

13 Z. Kang, C. H. A. Tsang, Z. Zhang, M. Zhang, N. B. Wong, J. A. Zapien, Y. Shan and S. T. Lee, *J. Am. Chem. Soc.*, 2007, **129**, 5326–5327.

14 M. D. Symes and L. Cronin, *Nat. Chem.*, 2013, **5**, 403–409.

15 S. G. Sarafianos, U. Kortz, M. T. Pope and M. J. Modak, *Reactions*, 1996, **626**, 619–626.

16 J. T. Rhule, C. L. Hill, D. A. Judd and R. F. Schinazi, *Chem. Rev.*, 2002, **98**, 327–358.

17 D. A. Judd, J. H. Nettles, N. Nevins, J. P. Snyder, D. C. Liotta, J. Tang, J. Ermolieff, R. F. Schinazi and C. L. Hill, *J. Am. Chem. Soc.*, 2001, **123**, 886–897.

18 Q. Wu, J. Wang, L. Zhang, A. Hong and J. Ren, *Angew. Chemie - Int. Ed.*, 2005, **44**, 4048–4052.

19 H. Yanagie, A. Ogata, S. Mitsui, T. Hisa, T. Yamase and M. Eriguchi, *Biomed. Pharmacother.*, 2006, **60**, 349–352.

20 H. Sun, N. Gao, J. Ren and X. Qu, *Chem. Mater.*, 2015, **27**, 7573–7576.

21 G. R. S. Hartig, T. T. Tran and M. L. Smythe, *Protein Sci.*, 2005, **14**, 474–482.

22 M. Ammam, *J. Mater. Chem. A*, 2013, **1**, 6291–6312.

23 R. F. W. Randall, D. Lyon, P. Domaille, *Inorg. Synth.*, 1998, **32**, 242–268.

24 M. L. Smythe, *Comprehensive Medicinal Chemistry III*, ed. S. Chackalamannil and D. Rotella and S. E. Ward, Elsevier, 2017, pp. 157–170.

25 M. Scampicchio, N. Lawrence, A. Arecchi and S. Mannino, *Electroanalysis*, 2007, **19**, 2437–2443.

26 J. J. Walsh, A. M. Bond, R. J. Forster and T. E. Keyes, *Coord. Chem. Rev.*, 2016, **306**, 217–234.

27 D. R. Lide, *CRC Handbook of Chemistry and Physics (87th ed.)*, ed. D. R. Lide, CRC Press, 2006, pg 1172-1180.

CHAPTER THREE: EMPLOYING TWO REDUCED POM SPECIES FOR DISULFIDE BOND REDUCTION

3.1 Introduction

Sulfhydryl compounds play a vital role in biochemistry due to their diverse functionality, enhanced nucleophilicity and low redox potential; giving them the intrinsic ability to act both as an oxidizing and reducing agent through thiyl radical formation.[1–3] The canonical amino acid cysteine (Cys), carrying a thiol moiety as a side chain functional group, mediates the activity and stabilizes the structure of many proteins across the bacterial and eukaryotic proteomes. The formation of a disulfide bond between Cys residues within a polypeptide chain determines protein stability and functionality.[4–9] The efficient and controlled formation of structural disulfide bridges is essential for the maintenance of protein integrity and function; dysregulation of bridging disulfides is a key marker and precursor for the development of a number of life-threatening diseases including Creutzfeldt-Jakob disease (CJD), amyotrophic lateral sclerosis (ALS) and pre-eclampsia, all having the common forerunner of oxidative stress, which causes protein misfolding.[10–16]

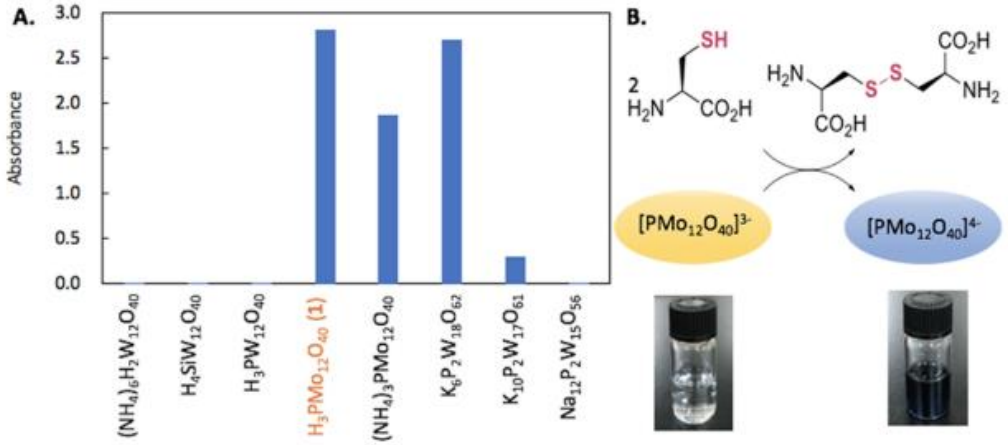

Figure 58: Absorbance of separate solutions of eight different POMs (10 mg/mL, 100 µL) and L-Cys (10 mg/mL, 500 µL) in water (after 2 hrs). Image taken from: H. Konno, H. Yasumiishi, R. Aoki, I. Nitanai and S. Yano, ACS Comb. Sci., 2020, 22(12) 745-749.[17]

Hence developing techniques to quantify the redox state of biologically relevant thiol/disulfides is highly important.

Recent studies by Yano *et al.* have employed polyoxometalate clusters to facilitate the oxidation of reduced biological thiols to form disulfide bonds, demonstrated by a characteristic deep-blue hue of the consequent POM reduction.[17] Within their work eight different POMs were screened for their ability to oxidize substrates coupled with a colour change. A colour change was only observed with the α-Keggin type and Wells-Dawson-type POMs, the former displaying a more intense deep blue and hence was subsequently used. Although this work demonstrates the prospective ability of POMs to interact with biological thiols, achieving a performance comparable to classic thiol oxidation reagents (dimethyl sulfoxide, iodine and silyl chloride-sulfoxide), the potential of POMs to act as redox probes for biological disulfides is unexplored.[18,19]

Evidently, POMs formed of transition metal oxide clusters (WO_4^-, Mo_z^-, VO_x^-, Nb_y^-), provide the building blocks for a highly active redox probes, where attainment of a desired redox profile is possible through synthetic design. The intrinsic self-adaptive electronic structure, intense d-d electronic transitions and intervalence charge transfer processes that are responsible for the distinctive deep-blue colour, and strong UV-Visible absorbance profile, of reduced POMs highlights their applicability as colorimetric redox probes.

Clearly, there is potential to use the colorimetric properties of POMs for detection. The feasibility of the design and application of two tungsten(W)-based POMs to provide a point-of-care, one-pot method to probe the redox state of oxidized biological disulfides is still unclear and yet to be explored. To the best of our knowledge there are no examples of the use of (W)-based POMs as disulfide reduction agents with the aim of reinvigorating the time-consuming testing procedure currently prevalent throughout the field, thus simplifying early diagnosis of time critical diseases.

3.2 Aims

As a proof of concept for this approach, two distinct polyoxoanions, **$[PW_{12}O_{40}]^{3-}$** {**PW_{12}**} and **$[H_3W_{12}O_{40}]^{5-}$** {**W_{12}**}, have been explored for use as redox probes by a combination of detailed theoretical, electrochemical, and spectroscopic analyses. Unlike existing analytical methods such as the classical Ellman's test (which quantify the reduced thiol), we show that this approach is suitable for the direct interrogation and quantification of disulfide bonds in a range of model substrates and propose that this technique shows great future promise for developing new assays to determine protein redox states.

Herein is explored the use of electrolysis for the accurate reduction of the POMs. The modification of the POM structure and solvent system used is described and following the full advancement of the technique, the successful S-S bond reduction of a synthesized peptide model is demonstrated.

3.3 Results and Discussion

3.3.1 Modifications to the $\{W_{12}\}$ POM Structure

Based on the results presented in Chapter 2, it was concluded that the cleanest and most efficient way to reduce the $\{W_{12}\}$ was *via* bulk electrolysis. Initially, this was abandoned due to difficulty reducing the POM in an inert atmosphere. However, due to the challenges presented by chemical- and photo-reduction methods it was decided to revisit electro-reduction techniques. The main draw was the ability to target a specific electron reduction process at a time.

The first step was to find a solvent system to use for the reduction processes. MeOH was not applicable as its solvent window is too small. DMF is applicable but due to the difficulty in lowering its oxygen content was also not suitable. Acetonitrile (MeCN) presented a preferable electrolysis solvent due to its solvent window and ease to degas. However, the **Na_6**$[H_3W_{12}O_{40}]$ {**W_{12}**} does not dissolve in MeCN. A cation exchange was performed to isolate the **TBA_6**$[H_2W_{12}O_{40}]$ {**$W_{12}.2$**}, metatungstate, a more soluble species of the POM.

The cyclic voltammogram taken of the newly formed $TBA_6[H_2W_{12}O_{40}]$ $\{W_{12}.2\}$ species shows one large reversible reduction at -1.5 V and one smaller reversible reduction at -1.1 V. As there was no access to ^{183}W NMR and as the metatungstate contains no internal templating ion the structure was determined through CV; confirming the formation of the $\{W_{12}.2\}$ species when compared to literature[20] and found to be coherent. Hence, the newly formed POM was used.

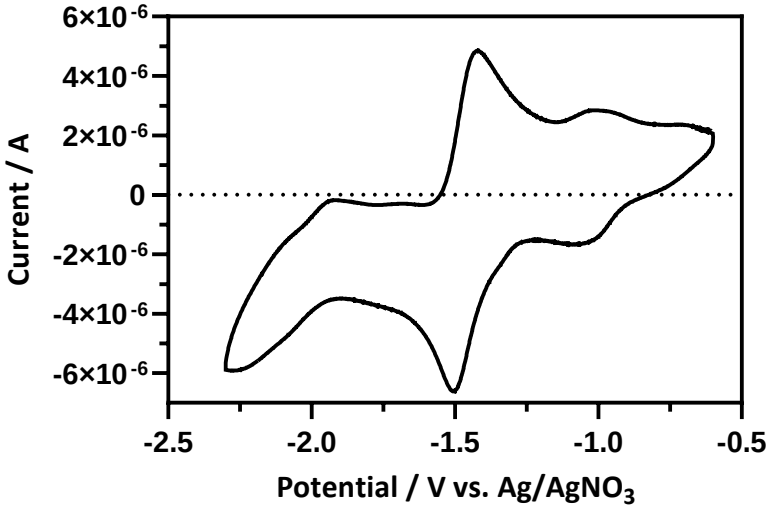

Figure 59: CV taken of 0.5 mM $TBA_6[H_2W_{12}O_{40}]$ in 0.1 M $[TBA][PF_6]$ electrolyte solution in MeCN. A glassy carbon working electrode was used, the counter electrode was platinum and an internal silver / silver nitrate reference electrode was used.

The next step was the bulk reduction of the $\{W_{12}.2\}$ species. For this a carbon working electrode was used with a large surface area, a small mesh platinum counter electrode was separated to the reduction solution *via* a frit containing the electrolyte solution and an internal reference was used ($Ag/AgNO_3$). The bulk electrolysis was run at -1.8 V as this point was past the first redox process which would ensure complete reduction of the species. Despite the presence of a minor reduction peak in the CV (Figure 59) prior to the process at -1.5 V, it was assumed that the major reduction peak indicated the real reduction of the 1st electron of the POM. The minor peak was also seen in the literature but ignored due to the fact that it is not a full electron reduction, however it was not elaborated as to what causes the formation of this minor peak.[20] Once the reduction was completed, which could be observed by the plateauing of the current, Figure 60, 3.5 mL of the blue solution (reduced POM solution) was transferred inside the glove box to a cuvette and taken to be tested on the UV-vis spectrometer, Figure 61.

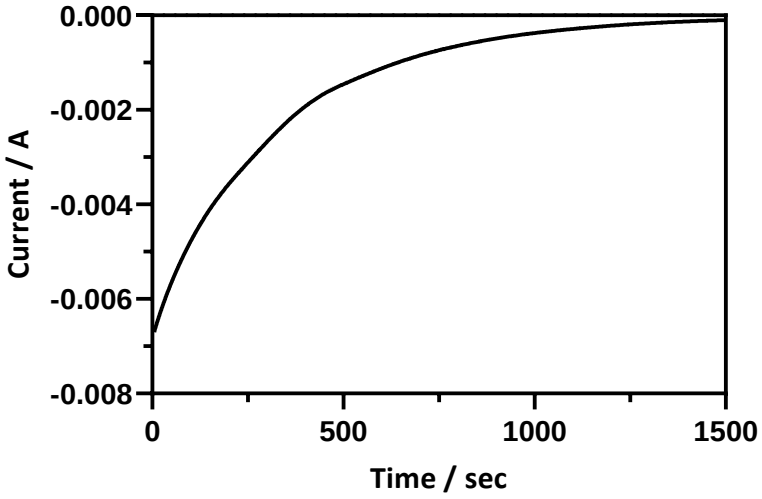

Figure 60: Showing the time vs current of the bulk reduction of 1 mM $TBA_6[H_2W_{12}O_{40}]$, $\{W_{12}.2\}$. Initial potential applied was -1.8 V, the total Q passed = -2.149 C and then end current = $-8.4647e^5$ A.

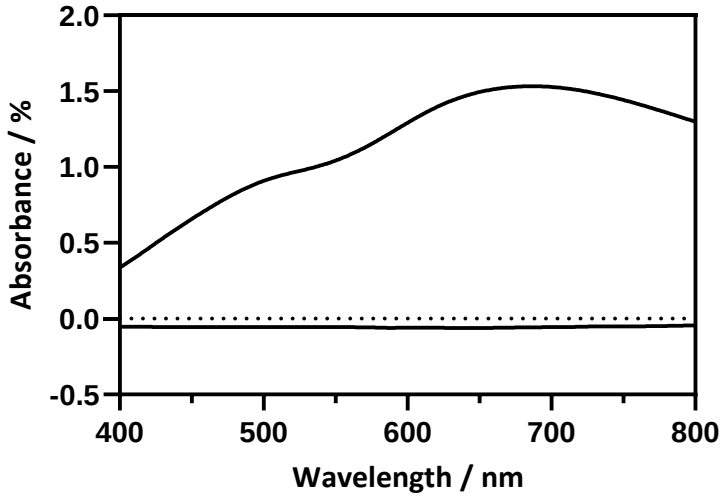

Figure 61: UV-vis spectrum of 1 mM $TBA_6[H_2W_{12}O_{40}]$ after full reduction at -1.8 V in the glove box.

A primary aim of this work was to find the extinction coefficient of our POMs and hence an absorbance below 1 AU was required. As 1 mM $\{W_{12}.2\}$ gave a much too high absorbance the solution was redone and diluted, this again showed a similarly large absorbance and was therefore diluted by half again and measured again at a concentration of 0.25 mM. However, through this exploration a few factors did not seem to correlate.

From the Beer Lambert Law, the maximum absorbance should decrease proportionally to the decrease in concentration; this was not observed. In addition, when using the end current values and calculating the number of electrons it did not correlate to the expected value of one electron, Equation 9.

$$Q = nfcv$$

Q = total charge reached C

n = the number of electrons

f = Faraday's constant taken to be 96485 C/ mol^{-1}

c = concentration in mol/ L^{-1}

v = the volume in L

Equation 9: The equation used to calculate the number of electrons reduced in a solution of POM.

Following Equation 9, as example using the values gained from the reduction in Figure 60; a value of 2.228 electrons was calculated. The further reductions carried out at differing concentrations also showed values of electrons either below 1 or above 2. Hence, it was concluded that the sample of POM must not be uniform and differing electron reductions are present. To make sense of these values a CV was run prior and post a bulk reduction; this would help to determine the stability of the POM. The first CV was the same as Figure 59, demonstrating the starting POM. However, after the reduction Figure 62 was achieved. Clearly the two aforementioned figures do not depict the same POM species. After consulting the literature, it was concluded that the difference in species is due to an interconversion between the $TBA_6[\mathbf{H_2}W_{12}O_{40}]$ and $TBA_5[\mathbf{H_3}W_{12}O_{40}]$ species. Himeno *et al.* describe this phenomenon proceeding upon the addition of a stoichiometric amount of H^+ leading to the internal protonation of the $[H_2W_{12}O_{40}]^{6-}$ species.[21]

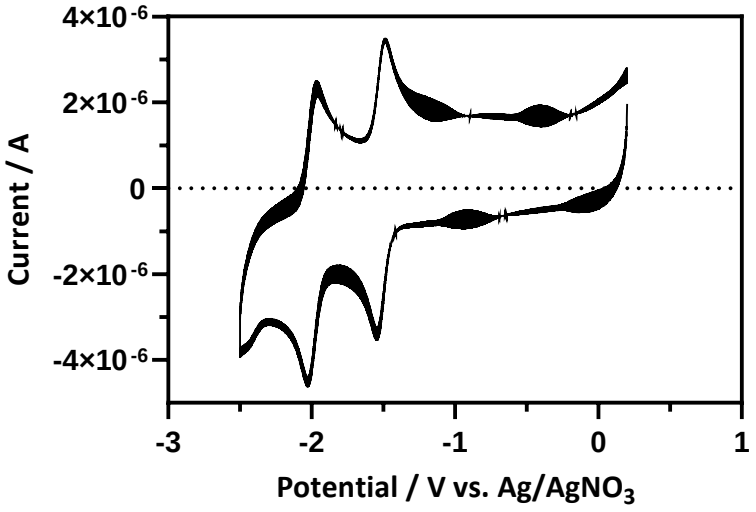

Figure 62: CV spectrum taken after a bulk reduction of the $TBA_6[H_2W_{12}O_{40}]$, {W_{12}.2}. Showing two reversible reduction peaks at -1.5 V and just over -2.0 V, scan taken from 0.2 to -2.5 V in 0.1 M [TBA][PF_6]electrolyte solution.

The occurrence of this interconversion between the dihydride and trihydride metatungstate species explained some of the inconsistent results observed, such as extra electron reductions, as any trihydride species would have differing redox potentials which could be partially achieved when applying a potential of -1.8 V. Therefore, it was necessary to convert the sample of POM solely into one of the species. Due to the clear electron reductions visible in the CVs of the trihydride metatungstate, $TBA_5[H_3W_{12}O_{40}]$, it was decided to form a new batch of this material to use for further reactions, from here on labelled {**W_{12}.3**}.

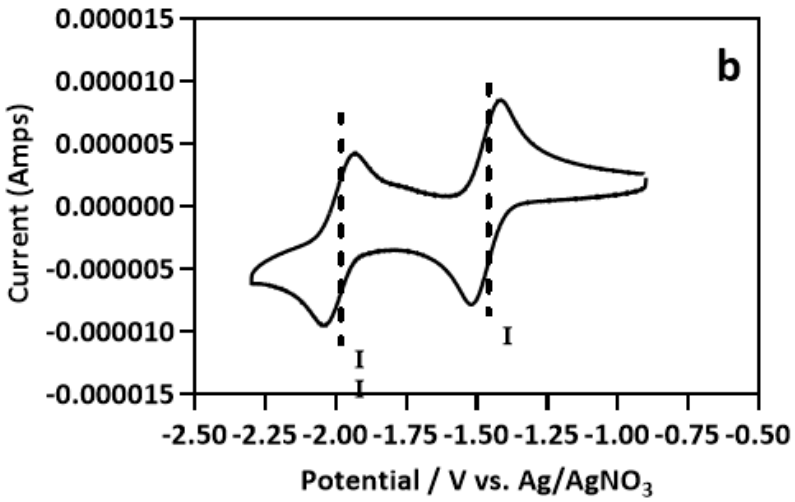

Figure 63: CV spectrum of the 1 mM $TBA_5[H_3W_{12}O_{40}]$, {W_{12}.3}. Showing two reversible reduction peaks at -1.5 V and just over -2.0 V taken in DMSO with 0.1 M $TBAPF_6$ electrolyte using a glassy carbon working electrode, platinum counter electrode and a $Ag/AgNO_3$ reference electrode.

After synthesizing the trihydride metatungstate {W_{12}.3}, the solvent was reconsidered. This is due to MeCN having a solvent window cutting off close to -2.5 V, near to the second reduction peak of the POM at approximately -2.0 V. This is in addition to there potentially being a high level of oxygen remaining in the solvent. Most importantly another factor to consider was that the peptide is not soluble in MeCN. Hence it was decided to move to a solvent system more ideal for both POM and peptide. As the combination of the two was the next step of the project. Dimethyl sulfoxide (DMSO) was chosen and dried prior to placing it into the glove box; it has a solvent window which can go down to -2.9 V and all substituents were soluble in the solvent. As mentioned in the introduction, DMSO can be used to oxidise two Cys molecules to Cystine or even under acidic conditions to form dimethyl sulfide as another product.[22] However due to the speed of the disulfide reduction reactions this was not anticipated to be a problem.

The CV of the Keggin type was also retaken under the same conditions as the new {W_{12}.3} POM, Figure 64.

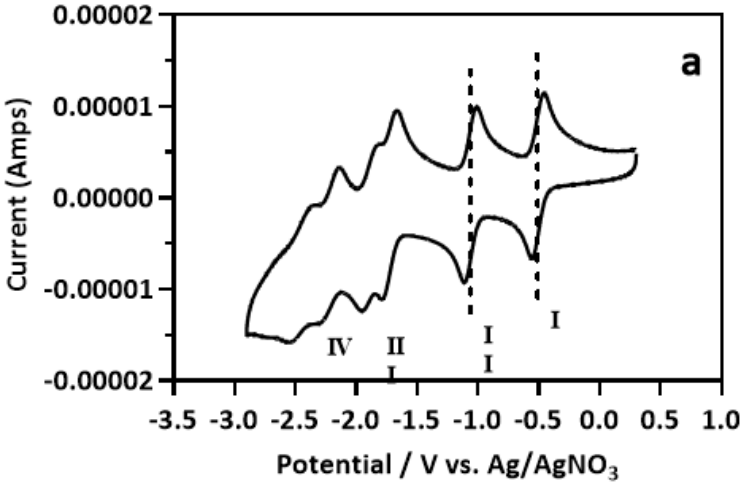

Figure 64: CV spectrum of the 1 mM $H_3[PW_{12}O_{40}].11H_2O$. Showing four reversible reduction peaks, the first to of interest are displayed at -0.5 V and just over -1.1 V taken in DMSO with 0.1 M $TBAPF_6$ electrolyte using a glassy carbon working electrode, platinum counter electrode and a $Ag/AgNO_3$ reference electrode.

3.3.1.1 POM electron counting

Due to some inconsistencies with the electron count using the data gained from bulk electrolysis it was decided to further study the reduction peaks of interest for the POMs. The number of electrons transferred in each electrochemical process can be determined

through the implementation of standard electrochemical techniques and manipulation of specific electrochemical equations. Cyclic voltammograms of the POM species characterized in this report revealed a diffusion controlled current response, detailed by the conventional 'duck shaped' profile, which obey the Randles-Sevcik equation.

$$i_p = 0.4463nFAC\left(\frac{nF\nu D}{RT}\right)^{\frac{1}{2}}$$ **Equation 10**

Equation 10: The Randles-Sevick equation describes the effect of scan rate, ν, on the observes peak current, ip, measured through a cyclic voltammetry of a redox event where, in a reversible process, a linear relationship of ip vs $\nu^{1/2}$ is observed.

$$i = \frac{nFAc^0\sqrt{D}}{\sqrt{\pi t}}$$

Where:

i = current (A)

i_p = peak current (A)

n = number of electrons passed per molecule reduced/oxidized

F = Faraday constant = 96485 (C/mol)

A = electrode surface area (cm^2)

C = concentration of analyte (mol/cm^3)

c^0 = initial concentration of analyte (mol/cm^3)

ν = scan rate (V/s)

D = diffusion coefficient (cm^2/s)

R = gas constant (J/K . mol)

T = Temperature (K)

t = time (s)

Equation 11: The Cottrell equation describe change in electric current, i, passed at an electrode surface as a function of time, t, when a given potential is applied where, for a reversible process, a linear relationship of i vs $t^{-\frac{1}{2}}$ is observed.

The common terms shared by the Randles-Sevcik and Cottrell equations, especially $CD^{\frac{1}{2}}$, provide the opportunity to isolate the term 'n' using simultaneous equations afforded by the implementation of chronoamperometry, to simplify the Cottrell equation.

$$i = \frac{nFAc^0\sqrt{D}}{\sqrt{\pi t}} \quad \rightarrow \quad i = m.\frac{1}{\sqrt{t}}$$ **Equation 12**

Where m = the gradient of the Cottrell plot

$$m = \frac{nFAc^0\sqrt{D}}{\sqrt{\pi}} \quad \rightarrow \quad CD^{\frac{1}{2}} = \frac{m\sqrt{\pi}}{nFA}$$ **Equation 13**

The term $CD^{\frac{1}{2}}$ can then be substituted into the Randles-Sevcik equation 10,

$$i_p = 0.4463nFAC\left(\frac{nF\nu D}{RT}\right)^{\frac{1}{2}} \quad \rightarrow \quad i_p = 0.4463nFA\left(\frac{nF\nu}{RT}\right)^{\frac{1}{2}}.\frac{m\sqrt{\pi}}{nFA}$$ **Equation 14**

All remaining variables in the Randles-Sevcik equation can be obtained through collection of a cyclic voltammogram of a given redox process at a given scan rate, within the viable region of the Randles-Sevcik equation.

This process was used to calculate the number of electrons in the first redox process of each POM characterized in this report, resulting in the conclusion that all POM redox processes described herein, are single electron processes.

This data was collected through a joint effort with Rory McNulty (PhD student at the University of Nottingham).

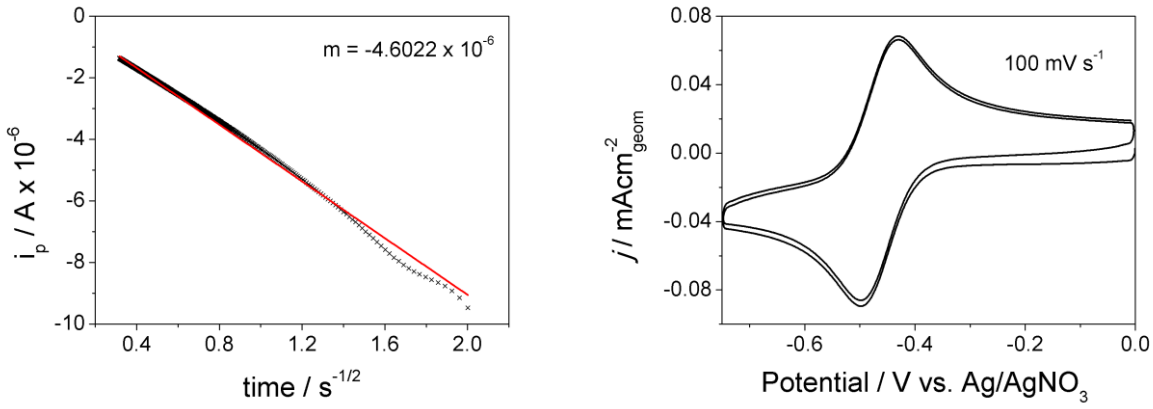

	i_p / A
n = 1	7.160×10^{-6}
n = 2	1.012×10^{-5}
n = 3	1.240×10^{-5}
Observed	6.320×10^{-6}

Figure 65: Cottrell plot and cyclic voltammogram of the 1st redox process of a $H_3[PW_{12}O_{40}]$, $\{PW_{12}\}$ POM.

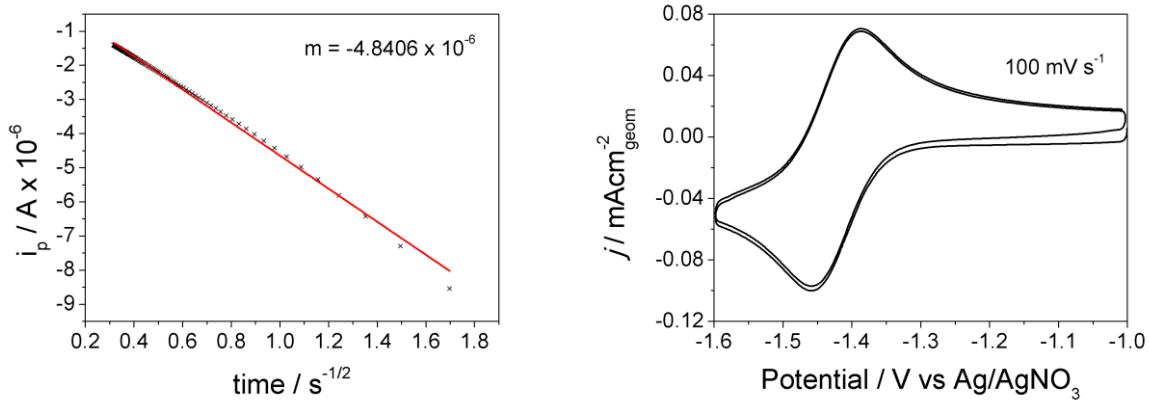

	i_p / A
n = 1	7.570×10^{-6}
n = 2	1.070×10^{-5}
n = 3	1.311×10^{-5}
Observed	7.080×10^{-6}

Figure 66: Cottrell plot and cyclic voltammogram of the 1st redox process of a $TBA_5[H_3W_{12}O_{40}]$, $\{W_{12}.3\}$ POM.

3.3.1.2 Spectro-electro chemical analysis of {W_{12}.3}

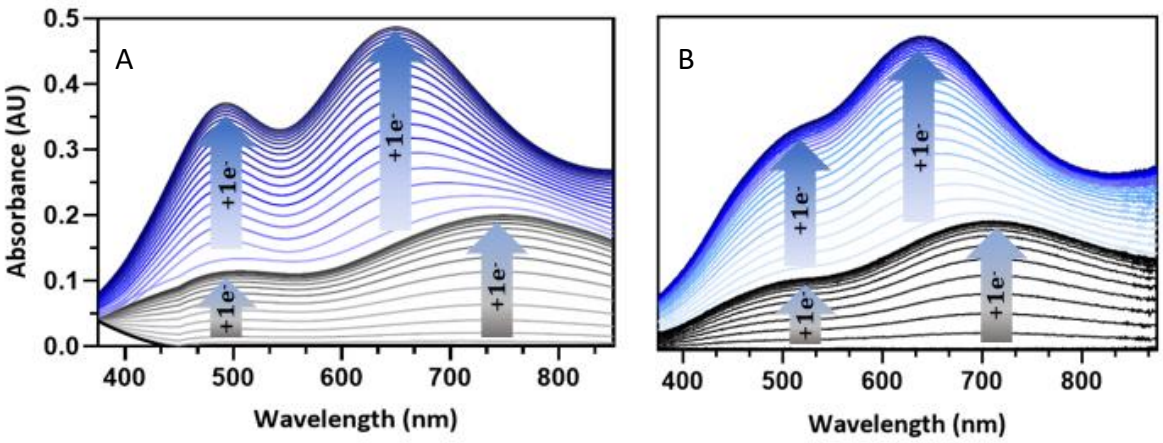

Figure 67: Spectro-electrochemical spectra of A) a Keggin-type POM: $H_3[PW_{12}O_{40}]$ and B) a metatungstate-type POM: $TBA_5[H_3W_{12}O_{40}]$. A three-electrode configuration consisting of a 3mm glassy carbon working electrode, a platinum counter electrode and a Hg reference electrode was employed to singly reduce the species by holding a potential of A) -0.57 V and B) -1.7 V until convergence was reached. A further single electron reduction was then carried out by applying a potential of A) -1.12 V and B) -2.4.

Due to the differing characteristics observed within the {W12.3}, compared to the {W12}, the electro-spectroscopy was repeated prior to progressing. Figure 67 shows the comparison between the two UV-vis profiles gained through the controlled electro-chemical reduction of the POMs. The new {W_{12}.3} species shows more defined characteristics than the {W_{12}}, although still not as defined as displayed by the {PW_{12}} profile. Here for both a shift can be seen in the wavelength and absorbance for the second electron reduction.

3.3.1.3 Extinction Coefficients

From all the reduction data collected and different techniques attempted, it was concluded that the data gained from the spectro-electro chemical set up was the most reliable and reproducible and therefore used for calculating the extinction coefficients from the POM.

Literature showed that few attempts had been made to deduce the extinction coefficients of POMs.[23] Comparing the few literature figures with the data extrapolated from the UV-vis plots indicated strong similarities.

Determinations of the extinction coefficient for polyoxometalates were carried out under argon using solutions ca. 1.52 mM {W_{12}.3} and 2 mM {PW_{12}}. Measurements were made carefully at the extinction maxima of the anion at each electron reduction: (λ_{max}) at 750 nm*

and 693 nm for the {PW_{12}} (first and second electron reductions) respectively and at 712 nm and 642 nm for the {W_{12}.3} (first and second electron reductions respectively). Reductions were carried out as described above in a 0.1 M [TBA][PF_6] electrolyte solution in DMSO.

PW12: $H_3[PW_{12}O_{40}]$				
Concentration (mM)	1st electron reduction		2nd electron reduction	
	Peak 1: 506 nm	Peak 2: 750 nm	Peak 1: 494 nm	Peak 2: 693 nm
	0.11470	0.20011	0.37050	0.24953
2.00	Extinction Coefficient (ε)		Extinction Coefficient (ε)	
	1.1470	2.0011	3.7050	2.4953
	x 10^3 $M^{-1}cm^{-1}$	x 10^3 $M^{-1}cm^{-1}$	x 10^3 $M^{-1}cm^{-1}$	x 10^3 $M^{-1}cm^{-1}$
W12.3: $TBA_5[H_3W_{12}O_{40}]$				
Concentration (mM)	1st electron reduction		2nd electron reduction	
	Peak 1: 508 nm	Peak 2: 712 nm	Peak 1: 533 nm	Peak 2: 642 nm
	0.10370	0.19315	0.34441	0.47075
1.52	Extinction Coefficient (ε)		Extinction Coefficient (ε)	
	1.3645	1.9315	3.4441	4.7075
	x 10^3 $M^{-1}cm^{-1}$	x 10^3 $M^{-1}cm^{-1}$	x 10^3 $M^{-1}cm^{-1}$	x 10^3 $M^{-1}cm^{-1}$

Table 1: Showing the concentrations and absorbance maximum at each peak for the first and second electron reductions for the {PW_{12}} and the {W_{12}.3} POMs. Extinction coefficients calculated using the Beer-Lambert equation.

As described in the introduction DTNB is also a molecule commonly used for the detection of disulfides, hence it presents a good comparison to the studied POMs. Usually, DTNB concentrations are excess over the thiol, causing DTNB to become partially consumed and TNB formed in a stoichiometric amount of a mixed disulfide. Studies performed by *Reiner et al*. on the molar absorption coefficients of DTNB under varying temperatures deduced that at 25 ^oC the maximal absorbance for the TNB molecule was found at 409 nm and produced a molar absorption coefficient of 14.250 x 10^3 $M^{-1}cm^{-1}$.[24] The highest molar absorption coefficient collected was from the doubly reduced {W_{12}.3} species at 642 nm at 4.708 x 10^3 $M^{-1}cm^{-1}$. This data indicates that the TNB molecule absorbs much more strongly than either POM tested. Which indicates a lower concentration of TNB would be required for testing.

*It is known that the efficiency of the silicone detectors become less accurate above 700 nm, meaning there may be a small level of uncertainty attached to the results.

However, the POMs have the advantage of reducing intact disulfide bonds (i.e., direct quantification of disulfides) and still allow for a measurable emittance of light in low concentrations.

3.3.2 Electro-Reduced POM Reactions with Disulfides

Having made several integral changes such as the solvent, the {W_{12}.3} POM and the technique of reduction; it was decided to proceed to the reduction of the DTNB and IgG3 molecules. The new reduction technique gave greater confidence in the achievement of the specific targeted electron reduction as electrolysis allowed for the controlled targeting of reduction points, hence giving more confidence to our data and in using the precious peptide substrate.

The reactions were trialled using the DTNB substrate to finalize the technique prior to using the IgG3 substrate. Having carried out the spectro-electro chemistry profiles for the first two reduction processes of both POMs, it was easy to identify whether the correct reduction had been achieved.

After initial trial and error to understand and correct the bulk electrolysis technique, it was decided to move a UV-Vis set up into the glove box to minimize oxygen leakage when taking the cuvette outside of the glovebox to the UV-vis machine. A three-electrode bulk electrolysis system was employed, using a carbon mesh for the working electrode, the counter electrode was platinum but situated behind a glass frit in electrolyte solution and a silver / silver nitrate (**Ag/AgNO$_3$**) reference electrode, also behind a glass frit.

The experiments were initiated with the doubly reduced Keggin-{PW_{12}} species as the absorption profile was so distinct. From previous experiments a large absorption from the reduced DTNB was expected making it a good indicator that the reduction process was successfully working. As previously stated, although DTNB does not absorb in the visible region, the distinctive absorption profile of its reduced form, 5-thio-2-nitrobenzoic acid (TNB), provides unambiguous spectroscopic confirmation of disulfide bond cleavage.[25]

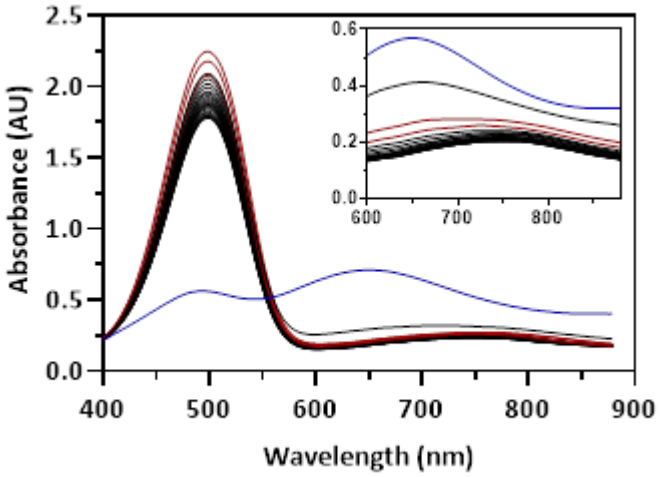

Figure 68: UV-Vis spectrum following the doubly reduced 0.125 mM Keggin species (blue) once 1 eq, DTNB was added.

The addition of DTNB to a solution of doubly reduced $\{PW_{12}\}$ results in the instantaneous formation of a strong absorption peak at 498 nm, characteristic of the oxidized product, TNB. This is paired with a simultaneous reduction in the intensity of the $\{PW_{12}\}$ absorbance maxima, Figure 68. Although this experiment confirmed the cleavage of the disulfide bond in DTNB, complete quenching of the $\{PW_{12}\}$ absorbance was not achieved. After 75 minutes, the absorbance plateaued at a maximum of 750 nm indicative of the singly reduced $\{PW_{12}\}$ cluster.

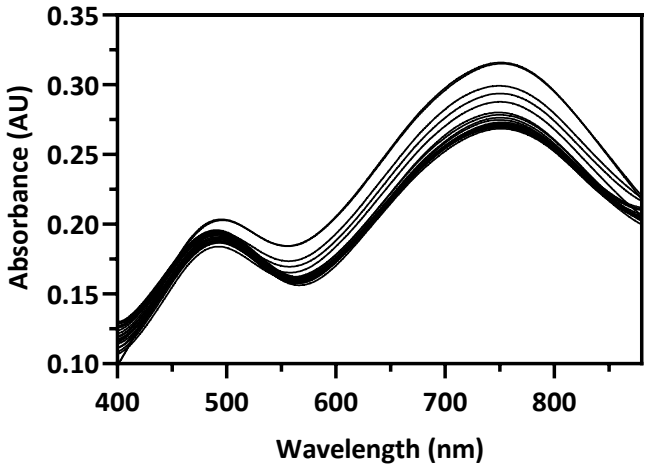

Figure 69: UV-Vis spectrum following the singly reduced 0.125 mM Keggin species after the addition of 1 eq, DTNB.

This suggests that the singly reduced cluster has insufficient reductive strength to facilitate the cleavage of the disulfide bond in DTNB. Shown in Figure 69 above is the scan taken for the singly reduced {PW_{12}} species which depicts little to no reaction with the DTNB species indicating the assumption that the strength of the first electron reduction is insufficient in breaking the disulfide bond, reinforced by the absence of the TNB peak. The slight decrease in absorbance observed in the spectrum is likely due to oxygen leakage either into the cuvette from the surroundings or from oxygen already present within the DMSO solvent (despite degassing), however the decrease observed is comparable to the control samples run and therefore can be dismissed as not part of the re-oxidation reaction due to disulfide reduction.

Conversely, it was expected that for the {W_{12}.3} cluster, both the singly and doubly reduced states are sufficiently strong reducing agents to cleave the DTNB disulfide bond, with a faster rate of reduction. This was verified with the doubly reduced species having re-oxidation rate of less than 15 seconds.

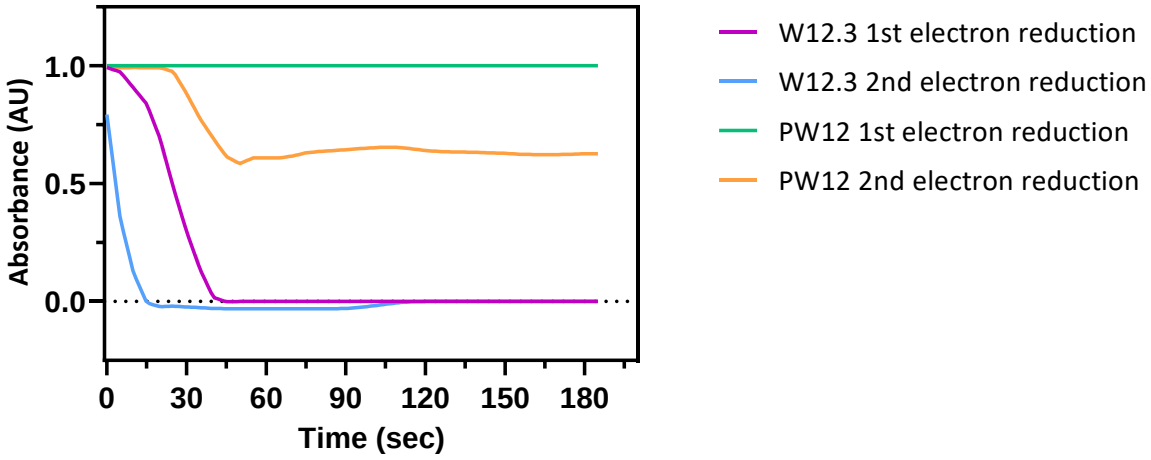

Figure 70: Showing the reactions of both POMs and each electron reduction for the first 185 seconds of the reaction with DTNB. Due to set up and starting the instruments about 2 mins are unaccounted for on the graph, each measurement taken once started is 5 seconds apart. All the POMs were measured at a concentration of 0.125 mM and 1 eq DTNB added.

From Figure 70, only the {W_{12}.3} species manage to achieve complete reduction of the DTNB sample within the first 185 seconds, and overall. The singly reduced {W_{12}.3} species required more time than the doubly reduced species as expected. Additionally, the first reduction

process of the {PW_{12}} shows no reaction; whilst the doubly reduced species of {PW_{12}} shows an initial reduction and then plateau.

To determine the applicability of this technique to biologically relevant systems, a simple peptide model containing a fragment of the IgG3 antibody was synthesized through solid-phase peptide synthesis.[26] This peptide represents a section of the antibody that contains multiple disulfide bonds connecting the two heavy chains of the structure.[27,28] More detail on the structure and biological activity of the IgG3 antibody is given in the introduction, page 37. Neither the oxidized (*i.e.,* disulfide containing) form of IgG3 or its reduced thiol-containing derivative exhibit absorption in the visible region of the electromagnetic spectrum. The ability of each POM to cleave the disulfide bond in IgG3 was carried out using the techniques established with the {PW_{12}} species and the DTNB.

As indicated in the graph above, DTNB reactions with the {W_{12}.3} species progressed almost immediately, the reactions with IgG3 as predicted progressed slightly slower. Analogous to the DTNB system, although the doubly reduced {PW_{12}} cluster proved a powerful enough reducing agent to cleave the disulfide bond in the IgG3 peptide, the singly reduced species possessed insufficient reductive power, highlighted by the absorbance plateau with a λ_{max} indicative of the singly reduced {PW_{12}} species, Figure 71.

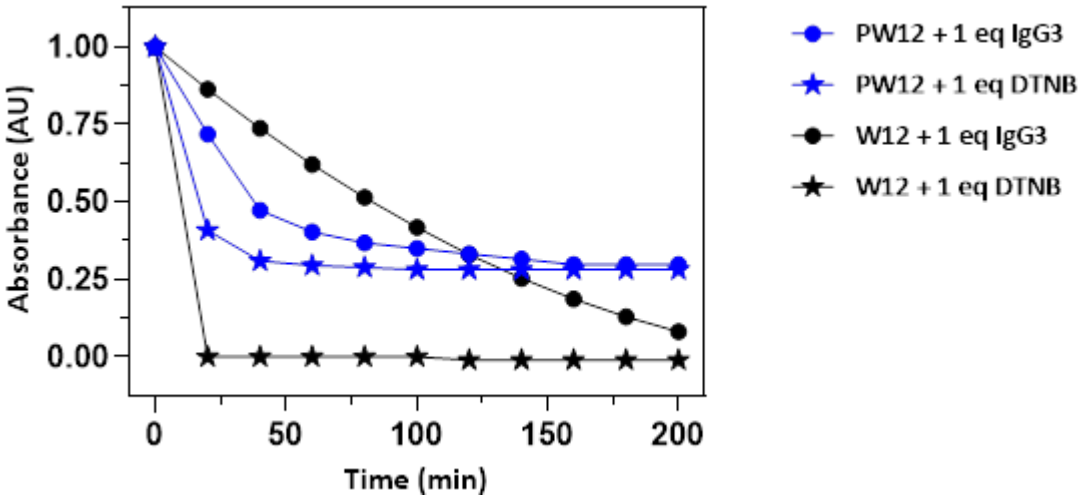

Figure 71: A concentration of 0.125 mM was used for each POM and then reduced to the 2-electron reduction, then 1 eq of DTNB or IgG3 was added.

Both the singly and doubly reduced {W_{12}.3} clusters are shown to be strong enough reducing agents to cleave the IgG3 disulfide bond, reaching full absorbance extinction over the full duration of measurements taken. Although the DFT calculations for the {W_{12}} and cyclic voltammetry confirm that the doubly reduced {W_{12}.3} cluster has the highest occupied molecular orbital, and therefore largest thermodynamic driving force of disulfide reduction, the rate of re-oxidation of this cluster in the presence of IgG3 is slower than the equivalent rate for the doubly reduced {PW_{12}} cluster. An important aspect to note was that the absorbance profile of the doubly reduced {PW_{12}} species with IgG3 changes shape, furthermore the profile decreases over the point of stabilisation and then increases, Figure 72. This indicates some sort of interaction with the POM, it has been reported and discovered through other work that certain peptide sequences can interact in an ionic fashion with POMs.[29] This could also be the reason for the faster initial re-oxidation of the {PW_{12}} species.

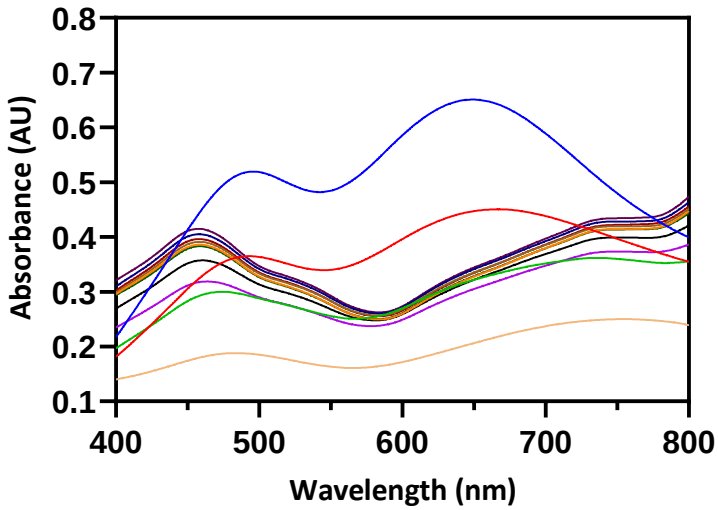

Figure 72: Showing the interaction between 0.125 mM {PW_{12}} and 1 eq. IgG3.

3.4 Conclusion

In conclusion, we have demonstrated the reduction of two POM species to accurate potentials using cyclic voltammetry, utilizing a bulk electrolysis set up. The system underwent numerous improvements, modulations to the POM were undertaken to make it more soluble as well as identifying further electron reductions. The method was moved into a glove box to allow for a completely inert environment and the solvent, and its preparation procedure, was changed to again limit the addition of oxygen.

The method shown herein differs from typical disulfide detection due to the POMs ability to detect the intact, oxidised disulfide bond. Standard methods quantify the amount of disulfide bonds in a sample through the reduction and subsequent detection of the thiols through a multi-step system. Through the detect quantification of disulfides, which this project works towards, many time-consuming steps can be avoided.

Following the optimization of the reduction technique we explored the ability of the two POMs to reduce disulfides. The $\{PW_{12}\}$ structure showed capability to reduce the disulfide in both the DTNB and IgG3 models, however the re-oxidation of the POM never reached competition as there was only a regression in absorbance observed and a shift in the IVCT bands to the profile in line with the first electron reduction of the POM. This indicated that the first electron reduction is not at a strong enough potential to participate in reduction of the disulfides and therefore remain on the POM. Additionally, we surprisingly observed a faster initial decrease in absorbance of the two-electron reduced $\{PW_{12}\}$ than the $\{W_{12}.3\}$ following the addition of the IgG3 peptide model. It was hypothesized that this phenomenon could be due to an electrostatic interaction between the $\{PW_{12}\}$ POM and the peptide, however this theory requires further analysis.

Overall, the $\{W_{12}.3\}$ POM species showed promise as a colorimetric redox agent as it showed stability and redox reversibility as well as efficient reduction of the disulfide in all substrates tested. Further studies are required to allow quantification of the disulfide bonds broken.

Future work is likely to consist of testing the POM species with more complex peptide models and proteins; identifying the ability to reduce only those disulfide bonds exposed to

the bulk solvent or also those buried within a folded structure. Quantification of intact disulfides could theoretically be monitored providing the consistent re-oxidation rate of the POM. The set-up would also require slight optimization as there was indication that some POM adheres to the electrode therefore altering the concentrations used.

3.5 Experimental

3.5.1 Peptide Synthesis

CHAPTER 2: section 2.5.1.

3.5.2 POM Synthesis

3.5.2.1 Keggin-type POM Synthesis - $H3[PW_{12}O_{40}].xH_2O$ $\{PW_{12}\}$:

CHAPTER 2: section 2.5.2.1.

3.5.2.2 Metatungstate Synthesis - $Na_6[W_{12}O_{39}].xH_2O$ $\{W_{12}\}$:

CHAPTER 2: section 2.5.2.2.

3.5.2.3 Synthesis of α-$TBA_5[H_3W_{12}O_{40}]$ $\{W_{12}.3\}$:

The POM was prepared as described in previous methods.[30] To 250 mL water was added Sodium Metatungstate (14.94 g, 5.0 mmol: 0.02 M) with vigorous stirring. The pH was carefully adjusted from ~5.1 to 2.0 using a pH meter and dilute aqueous hydrobromic acid.

The mixture was transferred to a separating funnel and shaken for 3 mins with 150 mL DCM containing 5 equivalents TBA.Br (8.086 g, 25 mmol: 0.2M solution).

The organic layer was removed and dried over magnesium sulphate, gravity filtered, and the volume reduced to ~20 mL. Diethyl ether diffusion was set up for 2 days at -20 ^{o}C. The precipitate was collected and washed with ethanol and ether.

The white powder was characterized through cyclic voltammetry, Figure 45.

3.5.3 Electrochemical Reduction Technique

CHAPTER 2: section 2.5.3.2.

3.6 References

1 I. Dalle-Donne and R. Rossi, *J. Chromatogr. B Anal. Technol. Biomed. Life Sci.*, 2009, **877**, 3271–3273.

2 L. B. Poole, *Free Radic. Biol. Med.*, 2015, **80**, 148–157.

3 C. E. Hand and J. F. Honek, *J. Nat. Prod.*, 2005, **68**, 293–308.

4 A. Tangerman, *J. Chromatogr. B Anal. Technol. Biomed. Life Sci.*, 2009, **877**, 3366–3377.

5 H. Østergaard, C. Tachibana and J. R. Winther, *J. Cell Biol.*, 2004, **166**, 337–345.

6 M. Depuydt, J. Messens and J. F. Collet, *Antioxidants Redox Signal.*, 2011, **15**, 49–66.

7 G. Bulaj, *Biotechnol. Adv.*, 2005, **23**, 87–92.

8 J. R. Winther and C. Thorpe, *Biochim. Biophys. Acta - Gen. Subj.*, 2014, **1840**, 838–846.

9 W. J. Wedemeyer, E. Welker, M. Narayan and H. A. Scheraga, *Biochemistry*, 2000, **39**, 7032.

10 V. I. Pérez, A. Pierce, E. M. de Waal, W. F. Ward, A. Bokov, A. Chaudhuri and A. Richardson, *Methods Enzymol.*, 2010, **473**, 161–177.

11 R. Rossi, D. Giustarini, G. Colombo, A. Milzani and I. Dalle-Donne, *J. Chromatogr. B Anal. Technol. Biomed. Life Sci.*, 2009, **877**, 3467–3474.

12 K. Dasuri, L. Zhang and J. N. Keller, *Free Radic. Biol. Med.*, 2013, **62**, 170–185.

13 J. W. Naskalski and G. Bartosz, *Adv. Clin. Chem.*, 2000, **35**, 161–253.

14 S. Parakh and J. D. Atkin, *Front. Cell Dev. Biol.*, 2015, **3**, 1–11.

15 H. D. Mistry, L. A. McCallum, L. O. Kurlak, I. A. Greenwood, F. B. Pipkin and R. M. Tribe, *Hypertension*, 2011, **58**, 497–504.

16 M. T. Islam, *Neurol. Res.*, 2017, **39**, 73–82.

17 H. Konno, H. Yasumiishi, R. Aoki, I. Nitanai and S. Yano, *ACS Comb. Sci.*, 2020, **22**, 745–749.

18 T. J. Wallace, *J. Am. Chem. Soc.*, 1964, **86**, 2018–2021.

19 K. Akaji, T. Tatsumi, M. Yoshida, T. Kimura, Y. Fujiwara and Y. Kiso, *J. Am. Chem. Soc.*, 1992, **114**, 4137–4143.

20 S. Himeno, K. Nakajima and K. Eda, *Polyhedron*, 2010, **29**, 2595–2599.

21 C. R. Sprangers, J. K. Marmon and D. C. Duncan, *Inorg. Chem.*, 2006, **45**, 9628–9630.

22 D. J. Kieber, K. Mopper, in *Biogeochemistry of Marine Dissolved Organic Matter*, ed. D. A. Hansell and C. A. Carlson, Academic Press, Elsevier, Amsterdam, 2002, pp. 455–507.

23 J. P. Launay, *J. Inorg. Nucl. Chem.*, 1976, **38**, 807–816.

24 E. Reiner, P. Eyer, F. Worek, D. Kiderlen, G. Sinko, A. Stuglin, V. Simeon-Rudolf, *Anal. Biochem.*, 2003, **312**, 224–227.

25 M. Scampicchio, N. Lawrence, A. Arecchi and S. Mannino, *Electroanalysis*, 2007, **19**, 2437-2443.

26 J. Stewart, *J. Macromol. Sci. Part A - Chem.*, 1977, **10**, 259–288.

27 G. Vidarsson, T. Rispens, in *Antibody Fc: Chapter 9. Human IgG Subclasses*, ed. M. E. Ackerman and F. Nimmerjahn, Academic Press, Boston, 2014, pp. 159–177.

28 T. Damelang, S. J. Rogerson, S. J. Kent and A. W. Chung, *Trends Immunol.*, 2019, **40**, 197–211.

29 K. Stroobants, E. Moelants, H. G. T. Ly, P. Proost, K. Bartik and T. N. Parac-Vogt, *Chem. - A Eur. J.*, 2013, **19**, 2848–2858.

30 J. Lei, J. J. Yang, T. Liu, R. M. Yuan, D. R. Deng, M. Sen Zheng, J. J. Chen, L. Cronin and Q. F. Dong, *Chem. - A Eur. J.*, 2019, **25**, 11432–11436.

CHAPTER FOUR: DEVELOPMENT OF BISPHOSPHONATE HYBRID POMS

4.1 Introduction

As discussed, POMs can be functionalised with inorganic and organic ligands. Where inorganic hybridisation (more accurately known as transition metal substituted POMs) involves the addition of a hetero-transition metal or f-block elements. These are usually introduced to the structures *via* a 1 pot synthesis or through coupling with a lacunary species, where the vacant pocket forms an available site for the cationic metal species to bind. This type of hybridisation has been presented for some bioactive POM studies such as proposed by Qu *et al.* where the group utilised the ability of a Nickel (**Ni**) to attach to a histidine (His) sequence.[1] Due to the broad range of cationic species available a large variety of structures are accessible. The precedent of His groups binding to metal ions is utilised for His-tag protein purification procedures.[2] Here a recombinant protein is expressed with a 6 x His or poly-His-tag fused to its N- or C- terminus. These expressed His-tagged proteins can then be purified and detected easily due to the His affinity to certain metal ions, including nickel, cobalt, and copper. Qu *et al.* produce two Wells-Dawson, $\{P_2W_{18}\}$, POM structures with Ni and Co substituted into the POMs and proceed to demonstrate the chelating affinity towards amyloid β-peptides (Aβ), Figure 73.

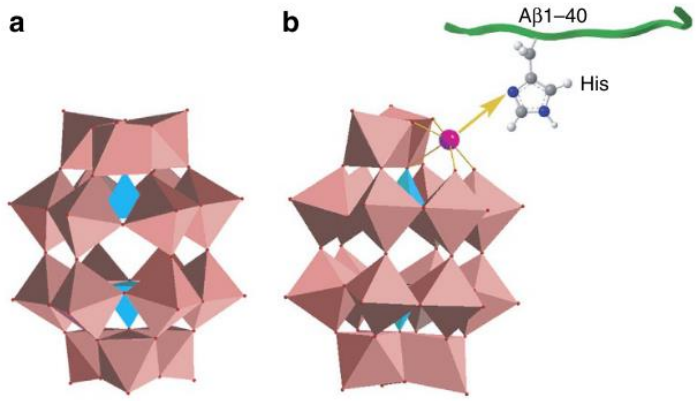

Figure 73: Schematic reproduced from N. Gao, H. Sun, K. Dong, J. Ren, T. Duan, C. Xu and X. Qu, Nat. Commun., 2014, 5, 1–9:[1] Structures of POM and POMds. a) Wells-Dawson structure, b) Wells-Dawson POMds with defined histidine-chelating metals (e.g. Nic, Co, Cu, Fe and Mn). The PO_4 and WO_6 polyhedra are shown in blue and light pink, respectively, the histidine-chelating metal is shown as a purple ball. The O, C, N and H atoms are shown as red, grey, dark blue and white balls, respectively.

The focus in this chapter lies in organic functionalisation of POMs involving the coupling of organic moieties to inorganic clusters. The functionalisation of organic linkers and molecules can work in a synergistic effect to enhance activity of the POM. The linker systems play a crucial role in the reaction to hybridise the POM to the organic molecule. Not only has the type of linker been shown to impart the POM with properties but it has also been demonstrated to alter the electronic properties of POMs based on the linker's own electronic effects. Previous studies by Odobel *et al.* identified the comparison and investigation of electrochemical differences between siloxane and phosphonate linkers to POMs.[3,4] These studies are interesting as the linkers are at the forefront used for $\{P_2W_{18}\}$ organ-functionalisation reactions. When compared to the parent, $\{P_2W_{18}\}$, the siloxane groups were shown to cause a negative shift in the first two redox processes and the reverse was found for the phosphonate hybrid. This shift is due to the inductive electron donating characteristics of the siloxane group and the electron withdrawing effects of the phosphates. These slight difference are of interest in a biological sense as it has been theorised that the movement through cells and effect on cells is due to the electrochemical characteristics of POMs.[5]

Typically, five main categories for the functionalisation of POMs are used, summarised in a review by Newton *et al.*[6] One of the most common methods is the use of tripodal alcohols (1,1,1-tris(hydroxymethyl)alkanes), which has been demonstrated effective for a large variety of POMs. This method is especially common for Anderson-Evans hybrids and has been shown to be used for biofunctinonalisation,[5,7,8] additionally the majority are formed exclusively from polyoxo-molybdates.

The focus in this study was on the functionalisation of the Wells-Dawson structure, *via* the first lacunary structure, $\{W_{17}\}$. Despite a large variety of functionalisation methods available there are few that form a single available post functionalisation site. Additionally, many use a toxic linker system such as organo-tin or organo-germanium. The most ubiquitously used linker for the single post functionalisation of a $\{P_2W_{18}\}$ are organotin hybrids.[6] Tin is classed as extremely toxic biologically, additionally it is a scarce element with an abundance of 2 ppm within the earth's crust.[9] Hence finding an alternative linker system which provides one attachment site for organo-molecules is advantageous.

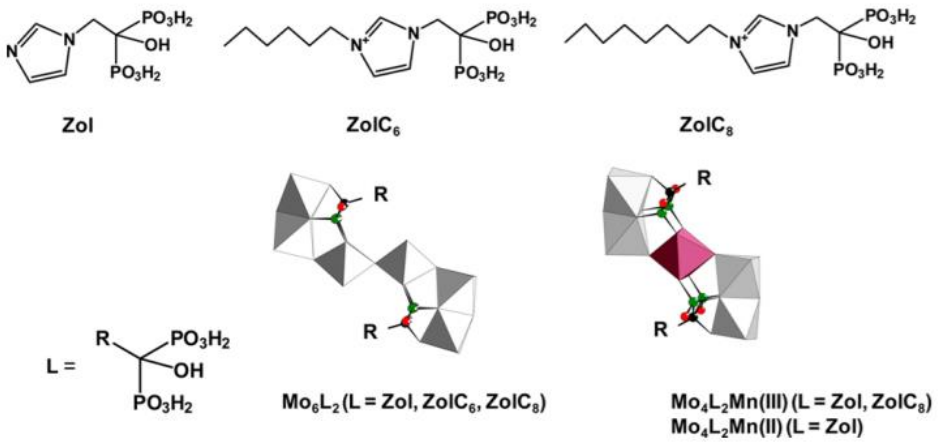

Figure 74: Schematic structures of biologically active diphosphonate hybrid-POMs. Gray polyhedral = MoO6, purple polyhedron = MnO6, green spheres = P, black spheres = C, red spheres = O. Reproduced from A. Boulmier, X. Feng, O. Oms, P. Mialane, E. Rivière, C. J. Shin, J. Yao, T. Kubo, T. Furuta, E. Oldfield and A. Dolbecq, Inorg. Chem., 2017, 56, 7558–7565 with permission from American Chemical Society. [11]

Despite considerable research undertaken by several groups on POM-bisphosphonate (POM-BP) hybrid structures the use of BP molecules as linkers and their effects on POM properties as ligands is relatively unexplored. These molecules have been of interest in the last few decades due to their activity to treat bone resorption diseases, additionally they show potent activity against some parasitic protozoa and tumour cells.[10] These biologically active species having the general formula $H_2O_3PC(OH)(R)PO_3H_2$ and similarly to the phosphonate ions these species display the same number of -OH ligands bound to the phosphorus. These hydroxyl groups increase the affinity towards bone mineral with R typically determining the drug efficacy, conversely the hydroxyl groups can be used similarly as phosphonates to enable them to act as linkers or ligands in a similar fashion. The Dolbecq group investigated the antitumour activity of a series of POM-bisphosphonate complexes.[10,11] They demonstrated the importance of the R group through its modulation, for example, the primary nitrogen containing alendronate (Ale, R = $(CH_2)_3NH_2$) is 100-1000 times less active than zoledronate (Zol, R = $(H_2(C_3H_3N_2))$), which has a heterocyclic amine at position R.[12] Additionally the group incorporated an Mn centre, synthesising an Mn(III)-containing POM $[(Mo^{VI}{}_2O_6)_2(Zol)_2Mn]^{5-}$, this POM also showed activity towards breast cancer cells. The demonstrated POM-BP complexes are not classical POM-based structures, and the most studied compounds exhibit the general formulas M_6L_2 and M_4L_2X (M = $\{MoO_6\}$, $\{WO_6\}$, $\{VO_6\}$; L = BP and X = $Mn^{II/III}$, Fe^{III}), Figure 74. This work demonstrated that the

structure of these ligands can be manipulated to enhance the anti-cancer activity of these POM-BP hybrids.

Further studies have investigated the addition of bisphosphonates to larger POM structures, forming more open POM architectures with extended coordination capabilities compared to the monophosphate [PO_4^{3-}] ions which usually are encapsulated into the POM shell.[13] The polyanion [$(P_2O_7)_4W^{VI}_{12}O_{36}]^{16-}$ ($W^{VI}_{12}POP_4$) (POP=pyrophosphate), is recognised as the first example of a poly-tungstate diphosphate hybrid; this structure was shown to have a dodecameric structure with a 'saddle-shaped' {W12} architecture, and is capped by four diphosphonate groups (POP angle = 123.7°). Later Himeno *et al.* reported a 17-tungsto(VI)diphosphate [$(P_2O_7)W^{VI}_{17}O_{51}]^{4-}$ ($W^{VI}_{17}POP$), this had an open '*inkpot-shaped*' structure and was comprised of a {$(P_2O_7)W^{VI}_{16}O_{50}$} fragment (POP angle = 132.11°) capped by a {$W^{VI}O_5$} square pyramid.[14]

Hybrid-POM complexes incorporating BP ligands have been shown to impart potent synergistic effects with applications in medicine, such as anti-tumour properties. As described above several groups have shown extensive work on POM segments and the effects combined with BP molecules, as well as in depth studies on the synthesis, structure, and bonding of BPs to some larger intact POMs. However, to the best of our knowledge the effects of the BP structure on the electronic properties of a hybrid POM structure remains unclear. There appears to be no literature on the use of these ligands to alter the electronic properties of redox rich Wells-Dawson POMs and simultaneously be modified to act as linkers.

4.2 Aim

This chapter focuses on the development of new POM-BP hybrids. Lacunary Wells-Dawson clusters were hybridised with commercial BP molecules. Literature precedent describes some of the biological advantages of BP functionalised POM clusters[11] as well as the synergistic effects which can be displayed from ligands to the POM structure.[3,15] Within this chapter three novel $\{P_2W_{18}\}$ hybrid POMs are synthesised through the functionalisation with 3 different diphosphonate ligands: i) methylenediphosphonate (**MDP**), ii) imidodiphosphonate (**IDP**) and iii) pyrophosphate (**PP**), Figure 75. The similarity in the ligands will differ only through the modulation of the atom between the phosphorus atoms, this allows for some variety to assess slight changes in the properties on the hybrid POMs. These structures are synthesised with the possibility of forming linker systems for further biological functionalisation therefore the retention and enhancement of certain POM properties such as photo- and electro-activity is important. Herein will be described the synthesis of each hybrid, the structural characterisation, the observed electronic effects exhibited on the POM and their photo-oxidative properties will be tested.

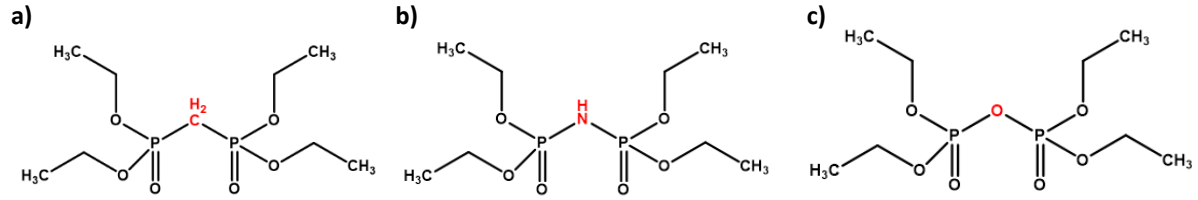

Figure 75: showing the structures of a) methylenediphosphonate (MDP), b) imidodiphosphonate (IDP) and c) pyrophosphate (PP).

This work was done as a collaboration between Dr Sharad Amin and I. Data was collected both independently and together. Sharad initiated this project and I joined with the start of the development of synthesis methods for the hybrid POMs due to the promise the ligands showed as linkers for biological functionalisation. Any data generated by Dr Amin alone has been acknowledged in the text.

4.3 Results and Discussion

4.3.1 Synthesis and Characterisation

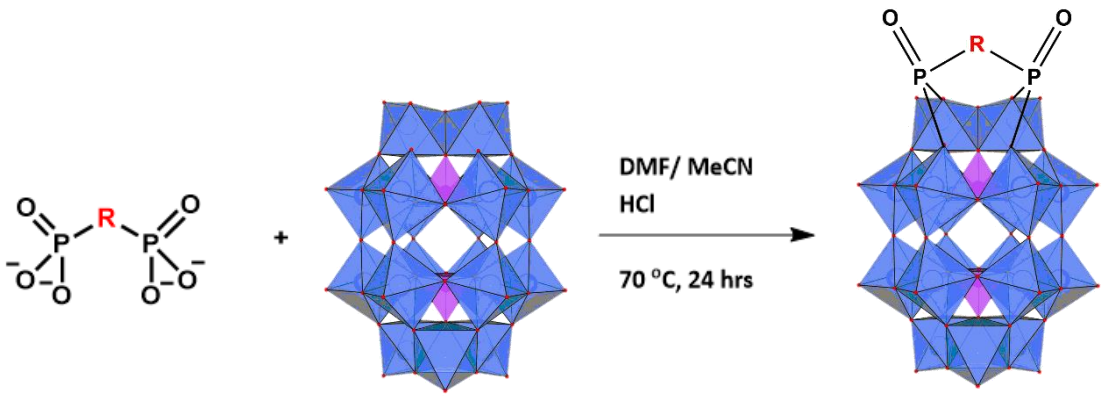

Figure 76: Hybridisation reaction of a lacunary WD $\{W_{17}\}$ and BP to form $\{W_{17}DP\}$ hybrid molecules where X=CH_2, NH and O. Molecule colour code: blue polyhedral = $\{WO_6\}$, purple polyhedral = $\{PO_4\}$, red spheres = O.

The synthesis of all three hybrids was undertaken in the presence of DMF or MeCN with a catalytic amount of HCl, Figure 76. This was based on a previously known method for producing K^+ salts of hybrid structures. The simplest strategy was applied when using the MDP ligand. Due to its robust nature a commonly used one pot method was employed to yield the pure MDP-POM hybrid cluster as a light-yellow powder (61 %). The PP and IDP ligands are only commercially available as tetra-sodium salts, this is due to the hydrolytic instability of the acidic ligands. This required the development of a strategy which circumvents possible ligand hydrolysis and basic degradation of the POM. Thus the POM and ligands were acidified separately for 5 mins at 40 °C, resulting in sufficient protonation of the molecules prior to mixing both solutions /suspensions together and heating to 70 °C. Both yielded as light green powders (15 % and 20 % isolated yield, respectively). To avoid acid catalysed hydrolysis of the ligand a catalytic amount of acid was used. These hybrid-POM molecules will now be named as **{W_{17}MDP}, {W_{17}IDP}** and **{W_{17}PP}.**

An aim for the project was to use a BP ligand as an attachment site for biofunctionalization of POMs; therefore, the structure of the ligands and the effects on the POM had to be fully explored. This was started with a full characterisation of the hybrids and further analysis to understand the effects of these ligands and the stability of the hybrid structures.

4.3.1.1 NMR and MS studies

Due to the lack of non-exchangeable protons on the hybrid clusters, the main analytical tool to confirm hybridisation was ^{31}P NMR. Three peaks are observed for each hybrid. These correspond to: one peak for the phosphorus on the symmetrical ligands used and two peaks for the internal phosphates of the POM. These two typical POM peaks (associated to the mono-lacunary Wells-Dawson POM, **{W_{17}},** phosphorus environments) can be seen to shift closer together (squeeze), a classic sign within POMs of hybridisation occurring, and caused through the electronic contribution effects of the ligands.

A direct correlation can be inferred between the relative position of the phosphorus peaks of the ligands and the electronic contribution of the central heteroatom of the ligand. Due to the size and electronegativity of the POM it exhibits an overall electron-withdrawing nature on the ligand, resulting in a downfield shift. This is even observed for methylene despite a slight inductive electron donating effect.

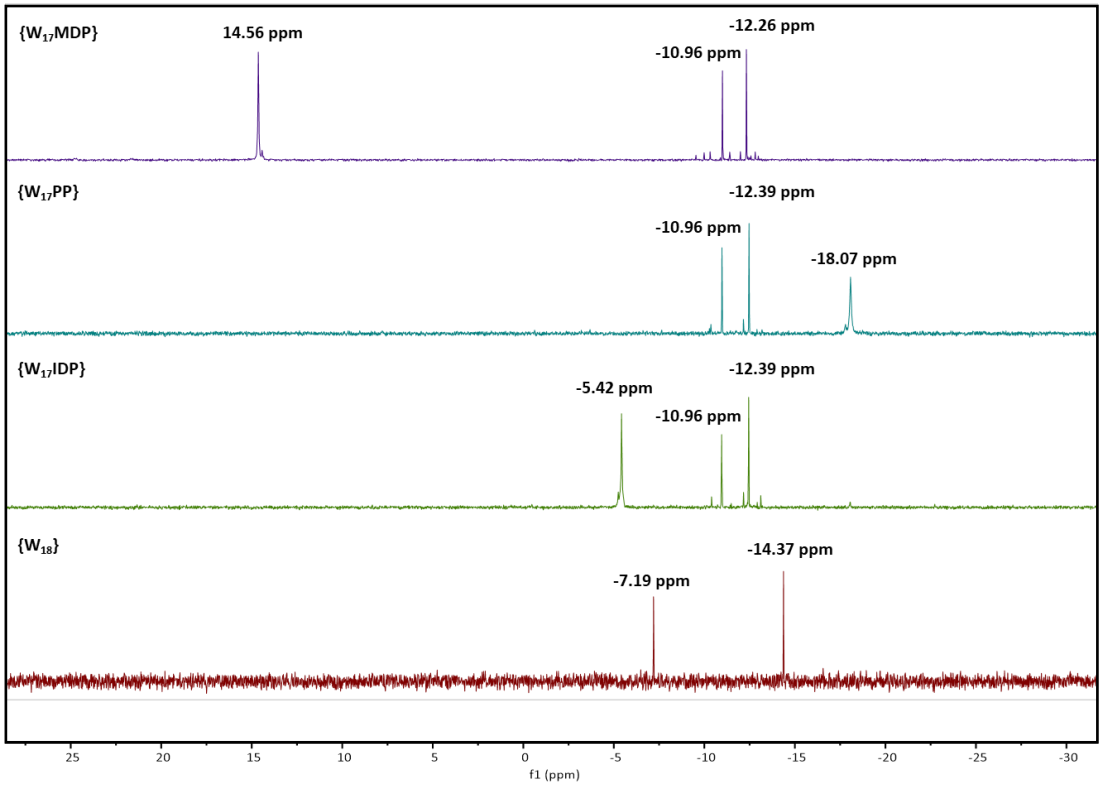

Figure 77: ^{31}P NMR comparisons of the three hybrid BP-POMs and the original $\{P_2W_{18}\}$ POM.

Considering the peak associated to the ligand signals; the MDP in {W_{17}MDP} is significantly shifted down-field at 14.56 ppm with respect to the ligand environments of {W_{17}IDP} and {W_{17}PP}. The shifts related to the ligands of {W_{17}IDP} and {W_{17}PP} are observed further up-field at -5.42 ppm and -18.07 ppm respectively. When comparing {W_{17}MDP} to the {W_{17}PP} and {W_{17}IDP}, the ligand peaks of the latter two are seen to be significantly more shielded. This trend is attributed to the electron-donating associated with the inductive effects of the central N and O atoms, who's lone pairs allow for extensive orbital mixing. The two lone pairs located on the PP oxygen results in a higher degree of shielding of the ligands phosphorus compared to the MDP and IDP, Figure 77.

A similar trend can be observed for the internal POM phosphates of the hybrids. As the bottom phosphate is located further from the ligands, they are most shielded as less affected by the ligand species. The degree of induction is greatest for the {W_{17}PP}, hence the peak is most shielded and the least for the {W_{17}MDP}. However, for the upper phosphate located closer to the ligand, the trend stands for {W_{17}IDP} and {W_{17}PP} but is seen to be the opposite and found most upfield for the {W_{17}MDP}.

{W_{17}MDP}			
Assignment	**z**	**m/z (calc.)**	**m/z (obs.)**
$\{Na_3(C_2NH_8)[W_{17}P_2O_{61}(P_2CH_2O_2)]\}$	2-	2192.86	2192.98
$\{Na_2(C_2NH_8)_2[W_{17}P_2O_{61}(P_2CH_2O_2)]\}$	2-	2204.40	2204.48
$\{HNa(C_2NH_8)_2[W_{17}P_2O_{61}(P_2CH_2O_2)]\}$	2-	2193.41	2193.47
$\{H_2K(C_2H_8N)[W_{17}P_2O_{61}(P_2CH_2O_2)]\}$	2-	2178.86	2178.97
$\{H_3(C_2H_8N)[W_{17}P_2O_{61}(P_2CH_2O_2)H_2O\}$	2-	2168.89	2168.97
$\{H_3(C_2H_8N)[W_{17}P_2O_{61}(P_2CH_2O_2)](H_2O)_2\}$	2-	2177.90	2177.99
$\{H_3(C_2H_8N)[W_{17}P_2O_{61}(P_2CH_2O_2)](H_2O)_3\}$	2-	2186.90	2186.98
$\{(C_2H_8N)H_3[W_{17}P_2O_{61}(P_2CH_2O_2)](H_2O)_4\}$	2-	2195.91	2195.98
$\{(C_2H_8N)Na_2H_4[W_{17}P_2O_{61}]\}$	3-	1419.60	1419.64
$\{Na_3H_3(C_2H_8N)[W_{17}P_2O_{61}]\}$	3-	1426.93	1426.98

Table 1: Mass spectrum peaks corresponding to {W_{17}MDP}$^{n-}$.

To further verify the hybridisation the molecules were also characterised by ESI-MS. Table 1 to Table 3 show the subsequent assigned peaks. The most intense peak in the sigmoid for each hybrid is observed for a 2^- charged species at: m/z = 2186.98 for $\{W_{17}MDP\}$ assigned to $H_3(C_2H_8N)\{W_{17}MDP\}^{2-}$ $3(H_2O)$, where three protons and a dimethylammonium cation (**DMA^+**) are coordinated to the cluster; m/z = 2170.96 corresponding to $HNa_3\{W_{17}IDP\}^{2-}$ and m/z = 2160.93 $H_3(C_2H_8N)\{W_{17}PP\}^{2-}$.

$\{W_{17}IDP\}$			
Assignment	**z**	**m/z (calc.)**	**m/z (obs.)**
$\{H_4[W_{17}P_2O_{61}(P_2O_2NH)]\}$	2-	2137.86	2137.96
$\{H_3Na[W_{17}P_2O_{61}(P_2O_2NH)]\}$	2-	2148.85	2148.85
$\{H_2Na_2[W_{17}P_2O_{61}(P_2O_2NH)]\}$	2-	2193.41	2193.47
$\{HNa_3[W_{17}P_2O_{61}(P_2O_2NH)]\}$	2-	2170.83	2170.96
$\{H_3[W_{17}P_2O_{61}(P_2O_2NH)\}$	3-	1424.90	1424.95
$\{H_3Na_4[W_{17}P_2O_{61}]\}$	3-	1419.24	1419.28

Table 2: Mass spectrum peaks corresponding to $\{W_{17}IDP\}^{n-}$.

$\{W_{17}PP\}$			
Assignment	**z**	**m/z (calc.)**	**m/z (obs.)**
$\{H_4[W_{17}P_2O_{61}(P_2O_3)]\}$	2-	2138.35	2138.46
$\{H_3Na[W_{17}P_2O_{61}(P_2O_3)]\}$	2-	2249.34	2149.45
$\{H_3K[W_{17}P_2O_{61}(P_2O_3)]\}$	2-	2157.33	2157.46
$\{H_3(C_2H_8N)[W_{17}P_2O_{61}(P_2O_3)]\}$	2-	2160.88	2160.93
$\{H_3(C_2H_8N)[W_{17}P_2O_{61}(P_2O_3)]H_2O\}$	2-	2169.88	2169.92
$\{H_4[W_{17}P_2O_{61}(P_2O_3)](H_2O)\}$	2-	2147.35	2147.44
$\{H_7[W_{17}P_2O_{61}](H_2O)\}$	3-	1395.93	1395.93

Table 3: Mass spectrum peaks corresponding to $\{W_{17}PP\}^{n-}$.

MS data was run and analysed by Dr Sharad Amin.

4.3.1.2 Cyclic Voltammetry Studies

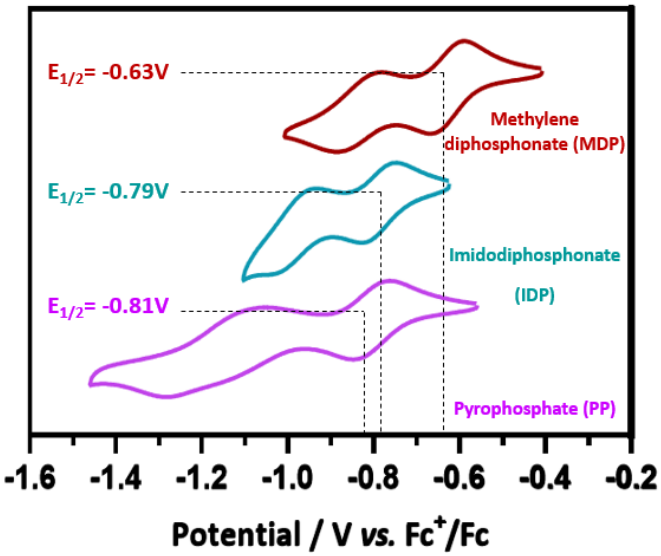

Figure 78: CV graphs for all BP-hybrid structures vs Fc+/Fc redox couple. The 1st redox potential is shown for each molecule.

Cyclic voltammetry was used to further explain the effects of the observed ligand electronic properties with that of the hybrid structures by identifying the relative reduction potentials. All CVs were performed under an argon atmosphere in anhydrous DMF with 0.1 M [TBA][PF_6] as the supporting electrolyte. As previously used a three-electrode setup was used with a glassy carbon working electrode, Pt wire was the counter electrode, throughout a Ag wire was used as a pseudo-reference and Ferrocenium/Ferrocene (Fc^+/Fc) redox couple added at the end as the external reference, Figure 78.

Each ligand exhibits differing electronegativities and number of lone pairs due to the each having a different central atom. Therefore, each hybrid is exposed to different electronic induction effects. Therefore, it is expected that the ligands differing electronic characteristics affect the redox properties of the POM in differing ways. All three hybrids exhibit two quasi-reversible processes. All are seen to have shifted positively with respect to their parent anion {P_2W_{18}} ($E_{1/2}$=- 1.168 V Fc^+ /Fc).

This positive shift can be attributed to the electron-withdrawing nature of the phosphonates, resulting in reduced electron density on the metal centres. This lowers the LUMO energy.[3,15,16] {W_{17}MDP} displayed the most positive redox process ($E_{1/2}$= -0.63 V),

followed by {W_{17}IDP} ($E_{1/2}$= - 0.79 V) and {W_{17}PP} ($E_{1/2}$= -0.81 V). Again, this trend can be understood by considering the induction effects presented by central heteroatom of the BP ligand.

The two lone pairs on the central oxygen atom of the PP ligand impart additional electron-density onto the POM via the phosphonates. Due to this electron density contribution coupled with the orbital mixing, the POM cluster has a reduced ability to accept electrons from outside the structure. Resulting in a more negative reduction potential, making the addition of an electron more difficult and requiring more energy. Similarly, the + 20 mV positive shift of the first redox potential of {W_{17}IDP}, compared to {W_{17}PP}, can be explained by the nitrogen atom within the IDP molecule only having 1 lone pair of electrons. There is a minimal amount of electron donating behaviour within the {W_{17}MDP}, this causes the observed positive shift of + 160 mV and + 180 mV of the redox process with respect to {W_{17}IDP} and {W_{17}PP}.

These trends agree with the previously observed trends in the ^{31}P NMR. In the NMR the {W_{17}PP} hybrid exhibited an very obvious up-field shift explained by the electron-donating behaviour of the ligand whilst the {W_{17}MDP} was observed the most down-field due to its weaker inductive behaviour. Therefore, theoretically {W_{17}MDP} is the most readily reduced due to the more positive reduction potentials displayed.

4.3.1.3 UV-Vis Characterisation

As discussed in the introduction and previous chapters the excitation of a LMCT within a POM between O to M results in the rich photochemical properties exhibited by POMs.[17] The LMCT results in the formation of a short-lived charge separated state. Here an electron is excited from a spin-paired, doubly occupied bonding orbital (the HOMO) to an empty antibonding orbital (the LUMO). Causing the formation of radical centre at the oxo-ligand. This oxo-radical has been seen taking part in a range of oxidation and hydrogen abstraction reactions.[18,19]

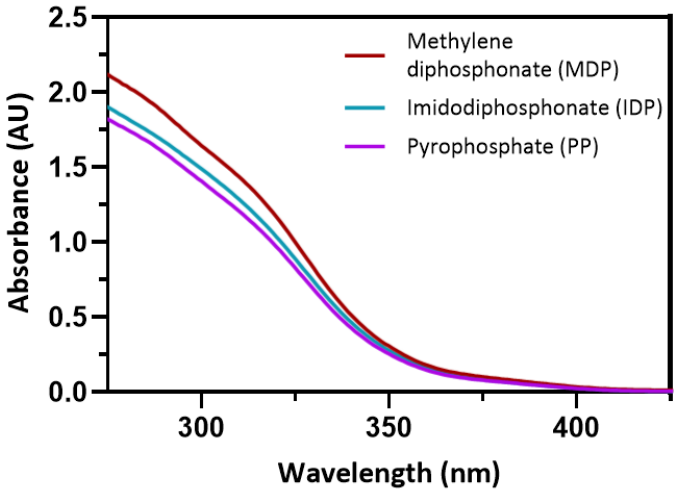

Figure 79: UV-Vis spectrum of 5 x 10^{-5} mM {W_{17}MDP} (red), {W_{17}IDP} (green) and {W_{17}PP} (purple).

Typically POM photo-activations are limited to the UV region of the spectrum. However, it has been demonstrated that through organo-functionalisation, effectively modulating the HOMO-LUMO levels of the molecule, the excitation can be pushed towards visible wavelengths. Due to the obviously and commonly unique absorption bands exhibited alterations to the POM exhibited post-functionalisation can be investigated using UV-Vis spectroscopy. However, these polynuclear clusters display particularly broad LMCT absorption bands due to the complexity of their structure. This can cause difficulty in the identification of discreet changes in the absorption properties. As expected, minor variations can be seen when comparing the three synthesised BP-hybrid POMs. {W_{17}MDP} demonstrated a more intense absorption band, Figure 79.

4.3.2 Photo-reduction Experiments

In 2017 it was found by Newton *et al.* that the frontier LUMO orbitals of a POM could be engineered to photo-activate (using the POM for catalysis) based on the electronic effects imparted by the ligand onto the POM.[3] The group displayed the correlation between the magnitude of the electron withdrawing effects of the phosphonate ligand to the photocatalytic degradation of indigo blue dye. These studies were considered, and it was decided to similarly explore the photoactivity of the BP hybrid POMs *vs* the parent anion $\{P_2W_{18}\}$ as it was more stable than the $\{W_{17}\}$ species.

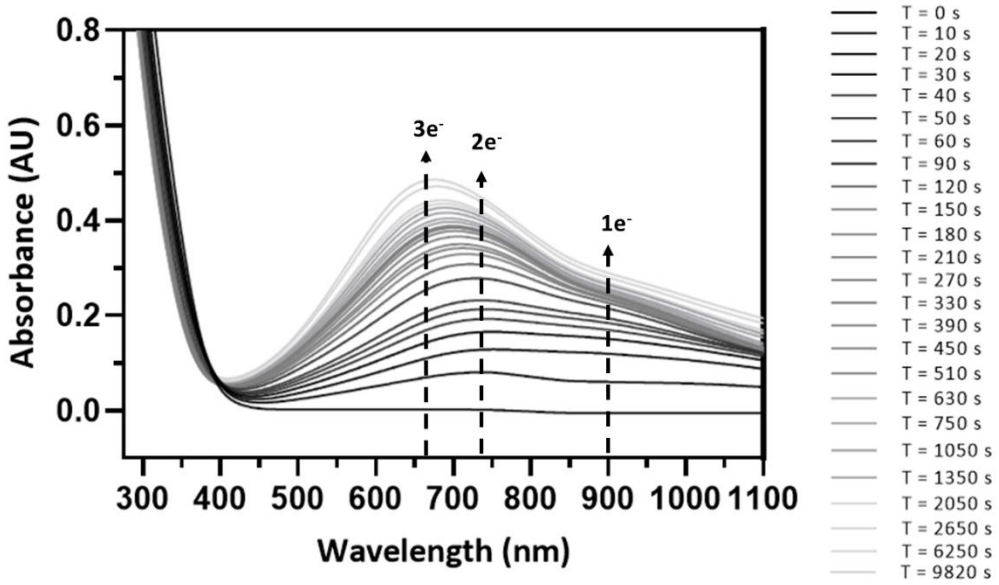

Figure 80: Photoreduction of $\{P_2W_{18}\}$ using UV-vis light.

The hybrid-POM structures were dissolved in DMF and irradiated. This triggered the LMCT, resulting in a d^1 electron located on the W centre and a short-lived charge separated state, where an oxo-radical is formed. Due to the presence of DMF this acted as the sacrificial electron donor and quenched the oxo-radical formed. As described before this results in a trapped d^1 electron resulting in the reduced POM state. This results in the 'heteropolyblue' due to the IVCT process. Prolonged irradiation is expected to result in increasing concentrations of the electron reduced species, this would be reflected in the increase in the absorption band which can be monitored using UV-Vis spectroscopy. The growth of new

absorption bands indicates the formation of multiple electrons reduced species of the POM, each reduction state corresponding to a unique IVCT band.[20,21]

The samples were irradiated using the solar reactor containing a 500 W mercury-xenon lamp (operating at 200 W) emitting strong UV and visible light. Additional experiments were run with a 395 nm cut-off filter (where all lower wavelengths are filtered out), to determine the photoactivity of the clusters with visible light. The study was done under an inert atmosphere to avoid any reoxidation of the reduced species by atmospheric oxygen. The reoxidation was studies by measuring the regression of the absorption band every 2 mins for approx. 1.5 hours with the solution exposed to dioxygen in the atmosphere.

Due to comparison the initial investigation was conducted with the parent analogue $\{P_2W_{18}\}$, by irradiating with UV-Vis light in DMF, Figure 80. Within 10 sec an instant reduction to the second electron species was observed, shown by the shift in the peak of the absorption band. The corresponding IVCT bands located for the 1e- and 2e- at 902 nm and 732 nm respectively. These reduced states become saturated upon 90 s and 330 s of irradiation. The 3rd electron reduction gradually appears at 664 nm and appears to dominate the spectral absorbance after 60 s saturating at 9820 s. The saturation of the bands indicated all POM species in the solution having reached that electron reduction state.

Irradiating the $\{P_2W_{18}\}$ species with visible light (using the filter at 395 nm) showed a negligible absorption peak even after 5 hours. This indicated that the $\{P_2W_{18}\}$ species is not photoactive under-visible light. It is likely that due to a large energy gap between the HOMO and LUMO, the visible light did not have sufficient energy to photoexcite an electron.

The irradiation of $\{W_{17}MDP\}$ with UV-Vis light, again showed a rapid initial growth of the 1e- and 2e- absorption bands at 691 nm and 873 nm respectively. These peaks appeared within the first 10 seconds similarly to the $\{P_2W_{18}\}$. The absorption peak identifying the 3rd electron reduced POM species again grows after 60 seconds at 652 nm, Figure 81 a). The procedure was repeated using the 395 nm cut-off filter, Figure 81 b) displays the relevant photo-reduction profile. Hence, $\{W_{17}MDP\}$ does exhibit significant visible light photoactivity, contrariwise to the parent analogue. Comparing the saturation point of the IVCT bands for

the 1e- reduced state of {W_{17}MDP} using a) UV-Vis light and b) visible light demonstrated that using visible light a lower absorbance is achieved at equivalent time frames. Interestingly, for the visible light reduced experiments a slight shift in peaks can be observed indicating the growth of the 2e- reduced species at 691 nm after 2100 s. Comparing this to the non-existent activity in the {P_2W_{18}}, a significantly greater photoactivity in the visible regime is observed. This photoactivation fits well with observation made by Newton *et al.*[3] The {W_{17}IDP} similarly showed growth of the 1e- and 2e- reduced species at 855 nm and 693 nm respectively within 10 s; saturating at 30 s and 90 s respectively, Figure 82. After 90 s the emergence of the 3e- species at 655 nm dominates the spectrum. This was followed by the visible-light photo-irradiation studies. Again, the absorbance was far lower. The emergence of 1e- and 2e- absorbance profiles were observed at a similar rate at 880 nm and 753 nm and saturating at 8340 s, Figure 82 b).

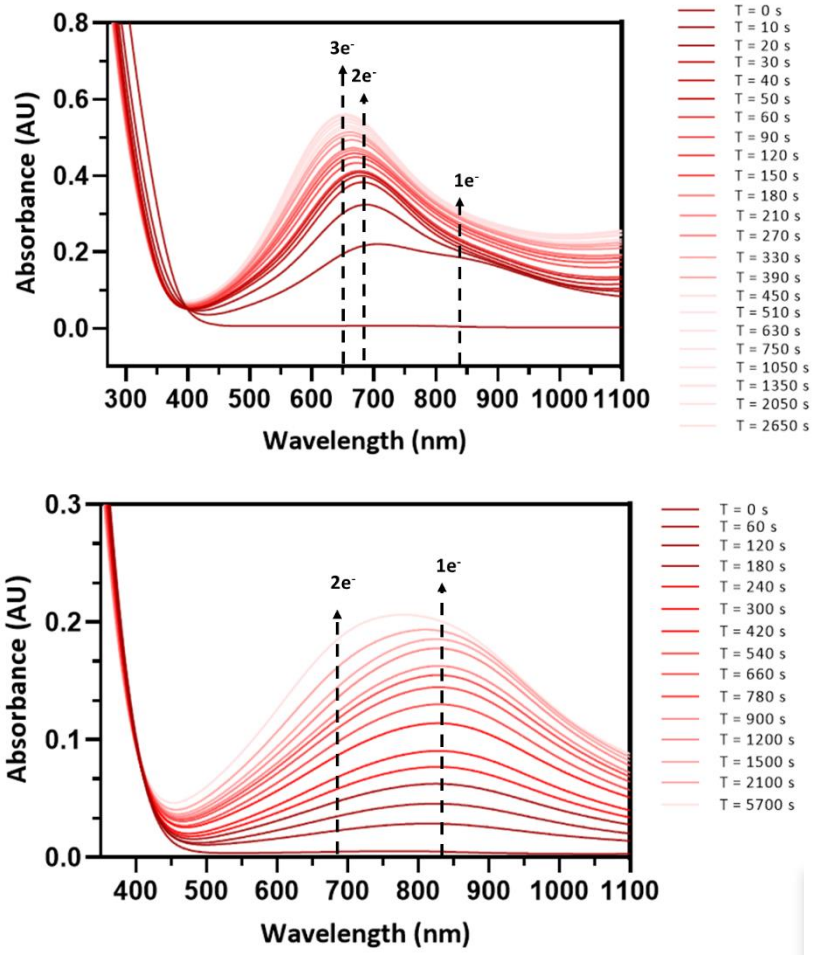

Figure 81: Photoreduction of {W_{17}MDP} using a) UV-vis and b) visible light.

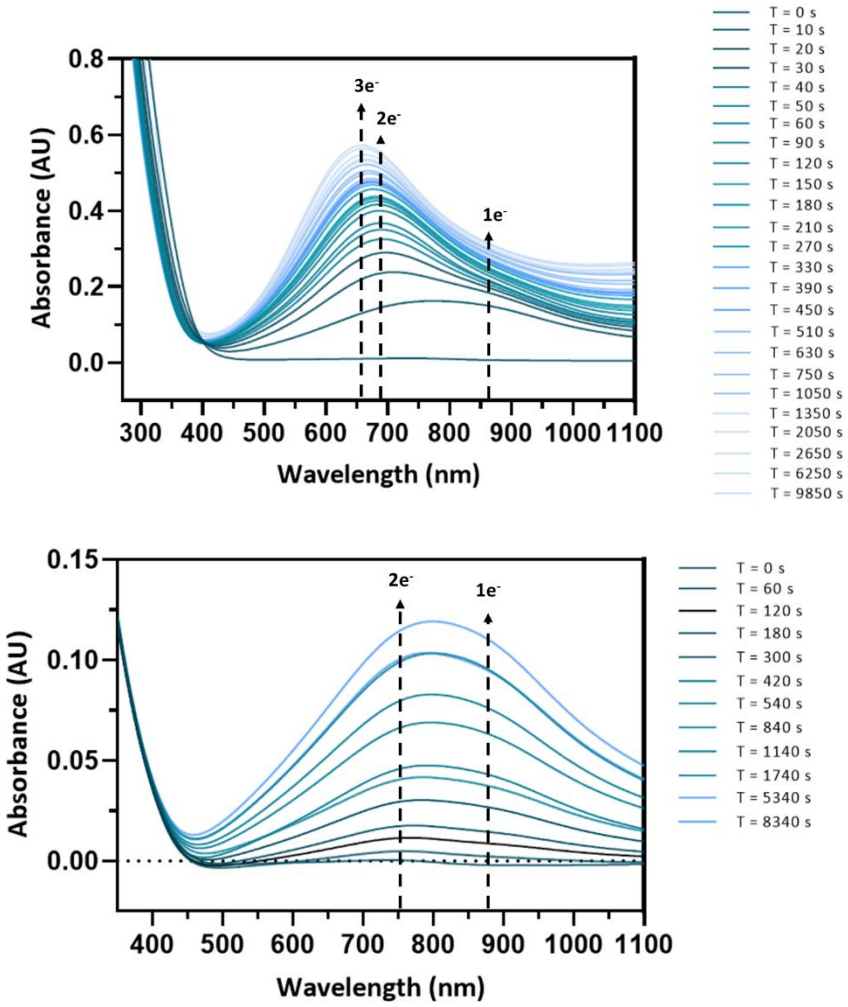

Figure 82: Photoreduction of {W_{17}IDP} using a) UV-vis and b) visible light.

Finally, {W_{17}PP}, Figure 83, was investigated. Under UV-Vis irradiation, within the initial 10 s the growth of the 1e- and 2e- reduced species was observed at 861 nm and 695 nm, saturating in 30 s and 90 s, respectively. After 60 secs the spectrum is dominated by the growth of the 3e- species, located at 649 nm. The visible-light photo irradiation study showed a shift in the 1e- and 2e- absorption profiles to 880 nm and 753 nm. Compared to the to other hybrids the growth of the 2e- species was less defined. This was anticipated based on the more negative reduction potential observed in Figure 78. Therefore, the rate of reduction was expected to be slower for this hybrid.

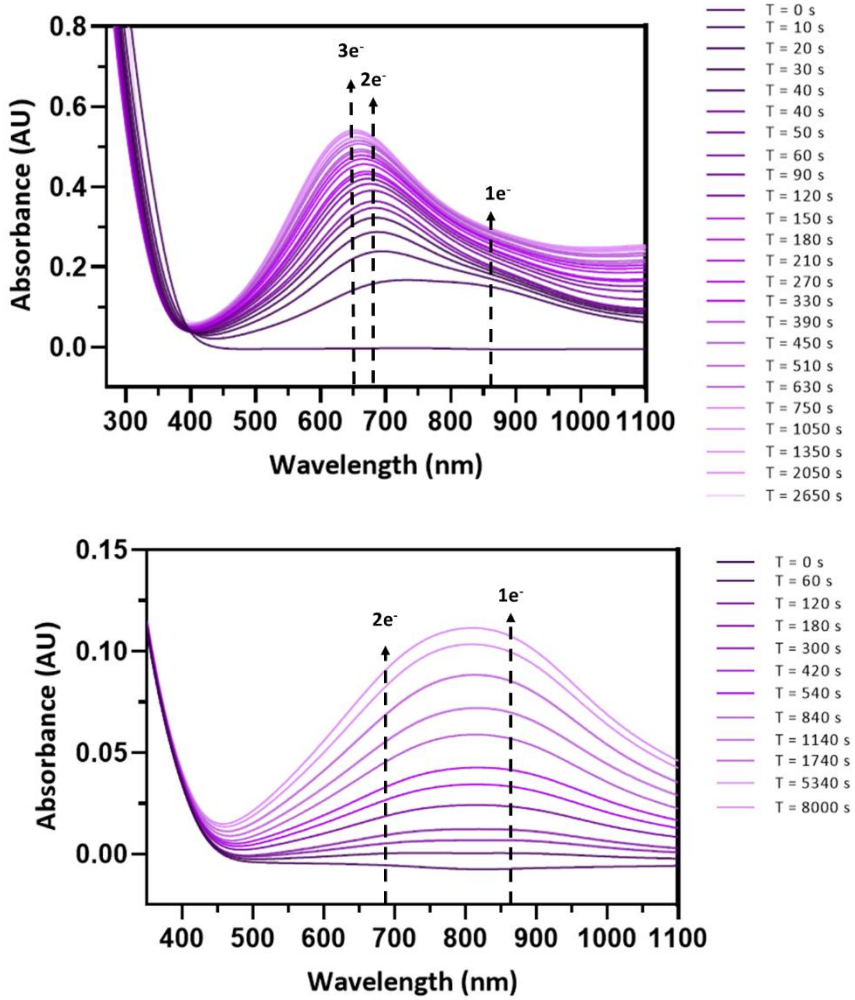

Figure 83: Photoreduction of {W_{17}PP} using a) UV-vis and b) visible light.

A direct comparison was down by using the maximum saturation point of each hybrid's electron reduction and converting it into an absorption percentage and shown against time, Figure 85. The data used was taken from the UV-vis studies for the 2e- and 3e- species, Figure 84. The visible light experiments were used for comparison of the 1e- species as these displayed more plots overall whereas in the UV-Vis experiments the 1e- reduced species is dampened after 10 s. A trend in the photoexcitation of the hybrid: {W_{17}MDP} >{W_{17}IDP} > {W_{17}PP} > {P_2W_{18}}, can be seen; deduced from the rate at which the species reach 100 % absorbance. This trend correlates well with the reduction potentials seen in the CV graphs, where the {W_{17}MDP} is reduced at a more positive potential, followed by {W_{17}IDP} and {W_{17}PP} closely. Therefore, the reduction of the {W_{17}MDP} species is anticipated to be faster, than the other two hybrids as less energy is required, resulting in the predictably better photoactivity than the parent analogue {P_2W_{18}}.

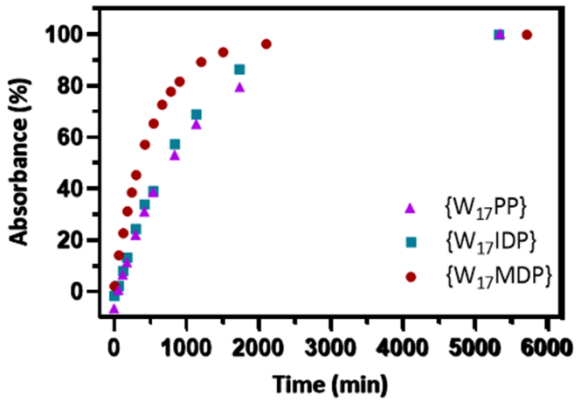

Figure 84: Graph showing the absorbance % against time for the rate of growth of the absorbance peaks under visible light irradiation for the 1e- reduced species.

The data extrapolated from the visible-light experiment, Figure 85, shows a slightly greater rate of reduction for {W_{17}IDP} than the {W_{17}PP}, which differs from the UV-Vis data gained. As both species displayed similar reduction potentials they were expected to act likewise. Again, the relative rates of reduction are influenced on the electron-donating behaviour and hence reduction potentials, i.e. {W_{17}PP} has the most electron-donating character, most negative reduction potential and slowest reduction rate. This was also observed most obviously under the visible light environment.

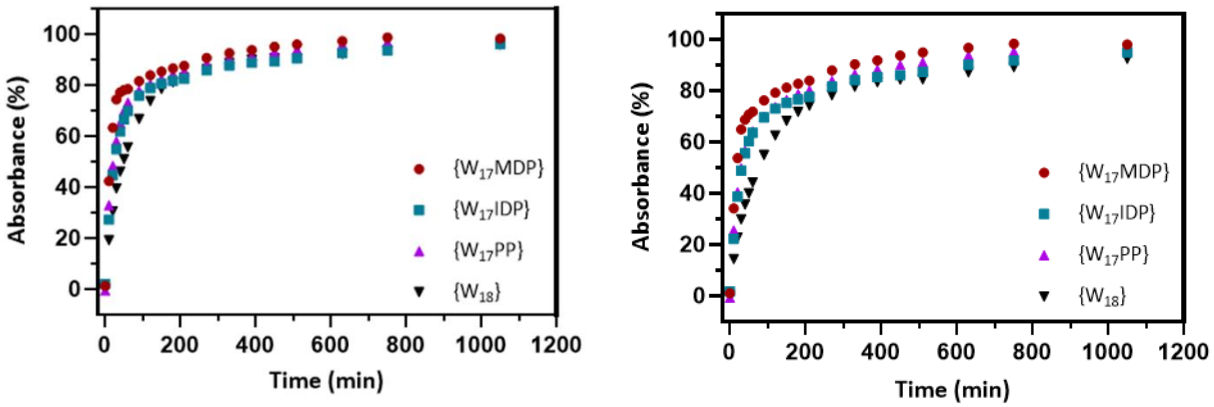

Figure 85: Graphs showing the absorbance % against time for the rate of growth of the absorbance peaks under UV-vis irradiation for a) 3e- and b) 2 e- .

Re-oxidation of the hybrids was then briefly explored. This would ascertain whether these species could be used as aerobic photocatalysts where rapid regeneration is crucial. Upon the saturation of the reduced states POM, identified by the absorption staying the same, the solutions were left to re-oxidise in the presence of atmospheric oxygen, Figure 86.

The graphs demonstrate an inverse trend in the re-oxidation of the POM, where the more readily reduced {W_{17}MDP} possesses the slowest reoxidation rate.

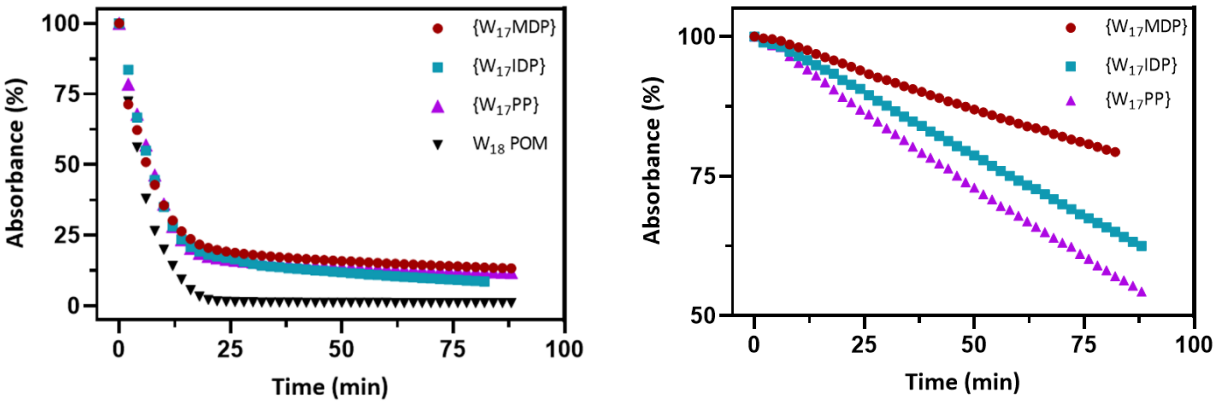

Figure 86: Absorbance vs time plots for the reoxidation of a) 3e- and b) 1e- {W_{17}DP} reduced species.

4.4 Conclusion

In summary, a new class of bisphosphonate hybrid polyoxometalates was synthesised. The characterisation of the clusters was achieved *via* NMR and MS. These ligands hybridised to the POM cluster stoichiometrically. Electronic properties were probed through UV-vis spectroscopy and CV studies. These techniques found that all hybrids were redox-active and displayed a positive shift in the first redox process with respect to parent anion $\{P_2W_{18}\}$.

The $\{W_{17}MDP\}$ possessed the most positive reduction and hence lowest LUMO, indicating that it would be more readily reduced. Conversely the oxygen in the PP ligand in $\{W_{17}PP\}$ possessing two lone pairs contributed the most electron density to the POM cluster and therefore led to the most negative reduction potential and therefore highest LUMO.

Based on the electronic characteristics the photoreduction properties were compared under UV-Vis and Vis regimes. All hybrids displayed superior rates of photo reduction compared to $\{P_2W_{18}\}$ under UV-Vis irradiation. $\{W_{17}MDP\}$ possessed the highest rate of reduction under UV-Vis and visible light irradiation. $\{W_{17}IDP\}$ and $\{W_{17}PP\}$ exhibited similar photo reduction rates which corroborates the experimentally acquired reduction potentials. Conversely, $\{W_{17}MDP\}$ was the slowest to oxidise, most likely due to having the most stable LUMO energy of the three. All three hybrids did show recovery to the ground state through oxidation with atmospheric oxygen.

4.5 Experimental

4.5.1 POM Synthesis

4.5.1.1 Synthesis of Wells-Dawson - α,β-$K_6[P_2W_{18}O_{62}]$ - $\{P_2W_{18}\}$

$Na_2WO_4.2H_2O$ (100 g, 0.303 mol) was dissolved in deionised water (117 ml) and stirred for 10 mins. To the colourless solution, 4M HCl (83 ml, 0.33 mol) was added to the solution dropwise, forming a white precipitate that dissolved with further stirring. 4M H_3PO_4 (83 ml, 0.33 mol) was then added drop wise to form a pale-yellow solution. The mixture was heated at reflux (100 °C) for 24 h. The bright yellow solution was then cooled to room temperature, followed by addition of KCl (50 g, 0.67 mol) to form a chalky-yellow precipitate. The solution was stirred for 10 mins and filtered using a glass porous frit. The crude product was then recrystallized using minimum amount of hot water to yield $\{P_2W_{18}\}$ (78 g, 96%, 0.0170 mol)* as yellow crystals. ^{31}P NMR (162 MHz, $CDCl_3$) δ -13.02 ppm. ATR-IR cm^{-1}: 1086, 952, 930, 899, 734.

4.5.1.2 Synthesis of Lacunary Wells-Dawson - α-$K_{10}[P_2W_{17}O_{61}]$ – $\{W_{17}\}$

$K_6[P_2W_{18}O_{62}]$ (40 g, 5.75 mmol) was dissolved in deionised water (100 ml). $KHCO_3$ (10 g, 0.1 mol) was then added to the reaction mixture and stirred overnight, forming a milky white precipitate. The precipitate was filtered and washed with deionised water and acetone. The crude was recrystallized from minimum amount of hot water to form $K_{10}[P_2W_{17}O_{61}]$ (32.99 g ,91 %, 7.24 mmol) as white powder crystals. ^{31}P NMR (162 MHz, $CDCl_3$) δ -7.19, -14.37. ATR-IR cm^{-1}: 3540, 3442 (O-H, b), 1080, 1048, 1013, 935, 882, 796, 719.

*yield calculated according to P in the POM structures.

4.5.2 Hybrid Synthesis

4.5.2.1 Synthesis of {W_{17}MDP}

Methylenediphosphonic acid (15 mg, 0.056 mmol) was added to DMF (40 ml) followed by $K_{10}[P_2W_{17}O_{61}]$ (0.25 g, 0.055 mmol) and 12 M HCl was added (0.07 ml). The temperature was then raised to 70 ^oC and left to stir for 16 hrs. The solution was then cooled to r.t and centrifuged (8000 rpm, 5 mins) to remove the remaining solid. Diethyl ether was added (large excess - approx. 150 ml) to the solution until a white suspension was formed. The white suspension was then centrifuged, and the solvent was decanted off. The centrifuge tube with the remaining white solid was when attached to the vacuum, before the solid was redissolved in a minimum amount of MeCN. The suspension was centrifuged (8000rpm, 5 mins) and decanted off before adding an excess of diethyl ether (40 ml) to the solution. The white suspension was then centrifuged, and the solvent was decanted off. The centrifuge tube with the remain white solid was when attached to the vacuum and the solid dried, before being redissolved in a minimum amount of acetone. The suspension was centrifuged (8000rpm, 5 mins) and decanted off before adding an excess of diethyl ether (40 ml) to the solution. The centrifuge tube with the remaining white solid was when attached to the vacuum and dried to yield $K_6[P_2W_{17}O_{61}(P_2O_2CH_2)]$ as a grey solid (0.148 g, 61%, 3.28 x10^{-3} mmol). ^{1}H NMR (400 MHz, Acetonitrile-d_3) δ 1.99 (s, 2H). ^{31}P NMR (162 MHz, Acetonitrile-d_3) δ 14.64, -11.00, -12.32; ATR-IR (cm^{-1}): 3650 (w) 3201, 1630, 1445, 1070, 945, 905, 800, 600.

4.5.2.2 Synthesis of {W_{17}IDP}

Tetra-sodium imidodiphosphate (15 mg, 0.056 mmol) was added to DMF (20 ml) and 12M HCl (0.25 ml). The suspension was stirred at 35 ^oC for 2 mins. The temperature was then raised to 70 ^oC, $K_{10}[P_2W_{17}O_{61}]$ (0.25g, 0.055 mmol) was added to DMF (20 ml) and 12 M HCl (0.25 ml). The suspension was also stirred at 35 ^oC for 2 mins. The two suspension mixtures were then added together and stirred for a further 2 mins at 35 ^oC before raising the temperature to 75 ^oC and stirring for 16 hrs. The solution was then cooled to r.t and centrifuged (8000 rpm, 5 mins) to remove the remaining solid. The solution was then rotary evaporated to remove the excess solvent, and the solid redissolved in 2 ml MeCN. Diethyl ether was added (large excess - approx. 40 ml) to the solution until a white suspension was

formed. The white suspension was then centrifuged, and the solvent was decanted off. The centrifuge tube with the remaining white solid was when attached to the vacuum and dried, before being redissolved in a minimum amount of acetone (2 ml) and methanol (1 ml). The suspension was centrifuged (8000 rpm, 5 mins) and decanted off before adding an excess of diethyl ether (40 mL) until a precipitate was formed. The centrifuge tube with the remaining white solid was when attached to the vacuum and dried to yield $K_6[P_2W_{17}O_{61}(P_2O_2NH)]$ as a grey solid (0.0371 g, 15%, 8.23 x10^{-6} mol). ^{1}H NMR (400 MHz, Acetonitrile-d3) δ 3.45 (q, 1H); ^{31}P NMR (162 MHz, Acetonitrile-d3) δ -5.44, -10.96, - 12.44; ATR-IR (cm^{-1}): 3650, 3201, 2987, 1731, 1390, 1222, 1070, 945, 905, 800 ,555.

4.5.2.3 Synthesis of {W_{17}PP}

Tetrasodium pyrophosphate (15 mg, 0.056 mmol) was added to DMF (40 ml) followed by $K_{10}[P_2W_{17}O_{61}]$ (0.25 g, 0.055 mmol). The suspension was stirred at 40 ^{o}C for 10 mins. The temperature was then raised to 70 ^{o}C and left to stir for 16 hrs. The solution was then cooled to r.t and centrifuged (8000 rpm, 5 mins) to remove the remaining solid. Diethyl ether was added (large excess - approx. 150 ml) to the solution until a white suspension was formed. The white suspension was then centrifuged, and the solvent was decanted off. The centrifuge tube with the remain white solid was when attached to the vacuum and dried, before being redissolved in a minimum amount of MeCN. The suspension was centrifuged (8000 rpm, 5 mins) and decanted off before adding an excess of diethyl ether (40 ml) to the solution. The white suspension was then centrifuged, and the solvent was decanted off. The centrifuge tube with the remain white solid was when attached to the vacuum and dried, before being redissolved in a minimum amount of acetone. The suspension was centrifuged (8000 rpm, 5 mins) and decanted off before adding an excess of diethyl ether (40 ml) to the solution. The centrifuge tube with the remain white solid was when attached to the vacuum and dried to yield $K_6[P_2W_{17}O_{61}(P_2O_3)]$ as a grey solid (49.5 mg, 20%, 1.10 x10^{-5} mol). The solid was then sonicated for 10 mins in diethyl ether (30 ml). The solution was decanted off and the remaining solid was dried under vacuum to yield a grey solid. ^{31}P NMR (162 MHz, Acetonitrile-d3) δ -10.98, -12.47, -18.07ppm; ATR-IR (cm^{-1}): 3650, 3201, 1634, 1404, 1180, 1115, 937, 795, 660, 500, 480.

4.6 References

1 N. Gao, H. Sun, K. Dong, J. Ren, T. Duan, C. Xu and X. Qu, *Nat. Commun.*, 2014, **5**, 1–9.

2 A. Spriestersbach, J. Kubicek, F. Schäfer, H. Block and B. Maertens, *Methods Enzymol.*, 2015, **559**, 1–15.

3 J. M. Cameron, S. Fujimoto, K. Kastner, R. J. Wei, D. Robinson, V. Sans, G. N. Newton and H. H. Oshio, *Chem. Eur. J.*, 2017, **23**, 47–50.

4 M. Boujtita, J. Boixel, E. Blart, C. R. Mayer and F. Odobel, *Polyhedron*, 2008, **27**, 688–692.

5 A. Bijelic, M. Aureliano and A. Rompel, *Angew. Chemie*, 2019, **58**, 2980–2999.

6 A. J. Kibler, G. N. Newton, *Polyhedron*, 2018, **154**, 1–20.

7 D. L. Long, R. Tsunashima and L. Cronin, *Angew. Chem. Int. Ed.*, 2010, **49**, 1736–1758.

8 H. Soria-carrera, I. Franco-castillo, P. Romero, S. Martín, J. M. De Fuente, S. G. Mitchell and R. Martín-rapffln, *Angew. Chem. Int. Ed.*, 2021, **60**, 3449–3453.

9 X. Liu, S. Wang and C. Feng, *Chinese J. Chem.*, 2010, **28**, 2411–2415.

10 H. El Moll, W. Zhu, E. Oldfield, L. M. Rodriguez-Albelo, P. Mialane, J. Marrot, N. Vila, I. M. Mbomekallé, E. Rivière, C. Duboc, A. Dolbecq, *Inorg. Chem.*, 2012, **51**, 7921–7931.

11 A. Boulmier, X. Feng, O. Oms, P. Mialane, E. Rivière, C. J. Shin, J. Yao, T. Kubo, T. Furuta, E. Oldfield and A. Dolbecq, *Inorg. Chem.*, 2017, **56**, 7558–7565.

12 L. Widler, K. A. Jaeggi, M. Glatt, K. Müller, R. Bachmann, M. Bisping, A. R. Born, R. Cortesi, G. Guiglia, H. Jeker, R. Klein, U. Ramseier, J. Schmid, G. Schreiber, Y. Seltenmeyer and J. R. Green, *J. Med. Chem.*, 2002, **45**, 3721–3738.

13 A. Banerjee, B. S. Bassil, G. V. Röschenthaler and U. Kortz, *Chem. Soc. Rev.*, 2012, **41**, 7590–7604.

14 S. Himeno, T. Katsuta, M. Takamoto and M. Hashimoto, *Bull. Chem. Soc. Jpn.*, 2006, **79**, 100–105.

15 H. Cameron, J. M. Fujimoto, S. Wei, R. Newton, G. N. Oshio, *Dalton. Trans.*, 2018, **47**, 10590–10594.

16 S. Fujimoto, J. M. Cameron, R. J. Wei, K. Kastner, D. Robinson, V. Sans, G. N. Newton, H. Oshio, *Inorg. Chem.*, 2017, **56**, 12169–12177.

17 M. T. Pope, in *Polyoxometalate Molecular Science*, ed. M. Borrás-Almenar, J.J., Coronado, E., Müller, A., Pope, Springer Netherlands, 2003, pp. 3–31.

18 C. Streb, *Dalton. Trans.*, 2012, **41**, 1651–1659.

19 D. Ravelli, M. Fagnoni, T. Fukuyama, T. Nishikawa, I. Ryu, *ACS Catal.*, 2018, **8**, 701–713.

20 G. M. Varga, E. Papaconstantinou and M. T. Pope, *Inorg. Chem.*, 1970, **9**, 662–667.

21 D. Dimotikali and E. Papaconstantinou, *Inorg. Chim. Acta*, 1984, **87**, 177–180.

CHAPTER FIVE: DEVELOPMENT OF BISPHOSPHONATE PEPTIDE HYBRID POMS – CHAIN GROWTH AND CHARACTERISATION

5.1 Introduction

Over the last few decades, the characteristic diversity in the structures and properties of POMs has led to their emergence as promising biological agents. Purely inorganic POMs have been shown to exhibit toxic side effects and limited cell penetration due to their surface qualities, hence, the field of biologically active POMs has become focused on organically functionalised hybrid POMs. The introduction of organic moieties into the POM framework can change its surface, chemistry charge, polarity and redox properties. A wide range of organic substrates have been attached to POMs such as quinolones[1], 5-fluorouracil[2], bisphosphonates[3] and biomolecules[4]. The focus herein is based on the attachment of amino acids (AA). The interest to graft AAs onto POMs is due to their structural and chemical variety and biocompatibility. In addition, polypeptides are ubiquitous in nature and perform a myriad of essential roles within cellular biochemistry, protecting and transport in living organisms. It has been shown that short polypeptide chains can be used for targeting specific tissue.[57] Whilst POMs have been identified as possessing anti-tumour and anti-microbial properties, targeting POMs solely towards affected tissues still requires further investigation. The combination of POMs and peptides could potentially combine the properties of both entities, aiding in the efficacy and bio-specificity of the POMs.

A lot of interest has been shown in understanding the interaction between polyoxometalates and biomacromolecules such as proteins. These interactions are mainly attributed to electrostatic interactions and have been reported by several groups.[7,8] The high binding affinity of POMs to macromolecules creates an effective inhibitor to various biological processes such as DNA binding activities of oncogene Sox2[9] and amyloid β-peptide aggregation.[10] However, the structural complexity of POMs, and the conformational flexibility displayed by most biomacromolecules, as well as multiple interactions within the molecule makes the further understanding of these interactions a challenge. To circumvent these challenges and explore them further, covalently grafting biomolecules onto POM

clusters is a viable pathway to achieve controllable structures and identify biological functions of POMs.

The Mn-Anderson-POM archetype are one of the best studied systems due the ease of tris-functionalization (tris = tris(hydroxymethyl)amino-methane) leading to the exposure of an amino group for further modification. Multiple techniques have been employed for the functionalization of these structures. Liu *et al*. recently reported the self-assembly of a series of peptide-Anderson-peptide hybrids.[11] The group studied how the effects of the addition of functional peptide tails lead to possible electrostatic interaction (charged chains), hydrophobic interaction, π–π stacking (aromatic rings) as well as hydrogen bonding to Anderson clusters. For each hybrid, two identical peptide chains were symmetrically grafted onto one Anderson-type cluster, with TBA (tetrabutyl ammonium) being the counterions. Six Anderson-peptide hybrids with different chain lengths and architectures were studied to evaluate the contributions to their self-assembly behaviours. Additionally, the Cronin group separately demonstrated the incorporation of an Anderson-POM into a peptide chain.[12] This exhibited a novel approach to the incorporation of POMs into peptide chains via NHS ester activated precursors, Figure 87.

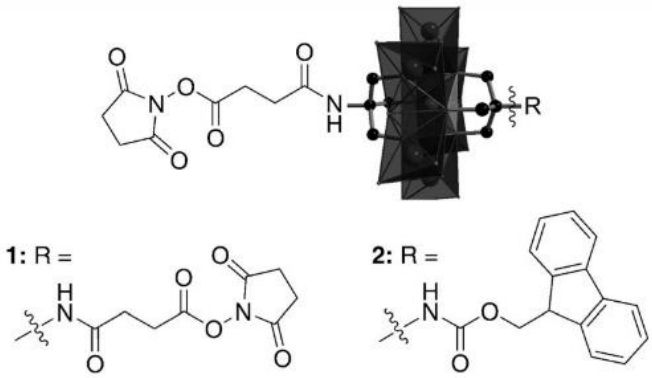

Figure 87: Schematic representation of the two Mn-Anderson precursors, used by Cronin et al, activated as NHS esters. Polyhedral/ball and stick representation of the Mn-Anderson $[MnMo_6O_{18}(O(CH_2)_3C)_2]^{3-}$ core; MnO6 and MoO6 are shown as light grey and black octahedra, respectively, and carbon atoms are depicted as black spheres; countercations were omitted for clarity. Image was taken from C. Yvon, A. J. Surman, M. Hutin, J. Alex, B. O. Smith, D.-L. Long and L. Cronin, Angew. Chemie, 2014, 126, 3404–3409.[12]

Carraro *et al*. demonstrated a novel approach to improve cancer cell recognition of a POM through the grafting of a bombesin analogue peptide forming bio-hybrid structures.[5] The group recognised the difficulty in achieving POM-peptide hybrid functionality due to POM-induced folding of the peptide, preventing availability towards biological targets.[13] They found that the introduction of a tailored spacer between the POM and peptide reduced on-

POM folding of the chains leading to higher availability of the receptor-binding region; shown by an increase in cytotoxicity towards cancer cells, Figure 88.

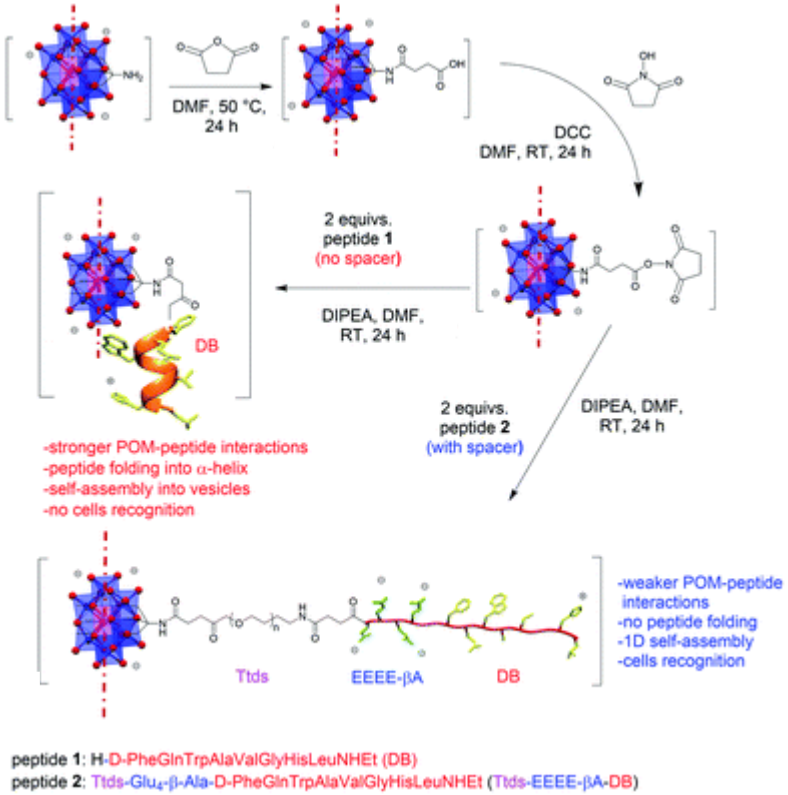

Figure 88: Reaction scheme to obtain POMs, demonstrating the differing impact of the spacer on the peptide secondary structure (evolving into α-helix for one and to random coil for the other). For graphical reasons, only one side of the bis-functionalized POM is shown. Countercations (TBA) are also omitted. DCC = N,N -dicyclohexylcarbodiimide: DIPEA = N,N -diisopropylethylamine. Taken from V. Tagliavini, C. Honisch, S. Serratì, A. Azzariti, M. Bonchio, P. Ruzza and M. Carraro, *RSC Adv.*, 2021, 11, 4952–4957.[5]

Another study of note undertaken by Mitchell *et al.* aimed to exploit the antimicrobial activities of POMs and certain peptides and combine the effect in their hybrid POM-polymers.[14] The group demonstrated the use of amino-functionalised Mn-Anderson-POMs as initiators for the on-POM ring opening polymerisation of amino acid *N*-carboxyanhydrides. Their work exhibited the POM-polymers antibacterial activity at low concentrations preventing biofilm growth. Their proof-of-principle study indicated a design route which can lead to the development of alternative antimicrobial hybrids to tackle biofilms that provide highly protective environments for pathogenic bacteria.

The studies discussed above show an insight into POM bio-functionalisation, of note is the predominant use of the Anderson type structure due to the ease of the addition of a tris group. A study undertaken by Liu *et al.* in 2005 demonstrated the impact of the POM

structure on the antitumoral activity. The polyoxovanadate (**POV**) and the hepta-polymolybdate (**PM-8**) displayed the most activity followed by a series of Anderson POMs, but Keggin and Wells-Dawson structures were shown to be the least active clusters.[15] Despite the lower antitumoral activity displayed by the Keggin and Wells-Dawson POM architectures they are still at the forefront of interest due to other properties exhibited. Firstly, through the functionalisation of these POMs, their reactivity has the potential to be increased and focused for selectivity, *via* correct peptide selection and a synergistic effect. Additionally, it has been demonstrated that the Wells-Dawson POM has the ability to cross the blood brain barrier (**BBB**), which can be rare for many types of medication.[10,16] Furthermore the use of Keggin and Wells-Dawson POMs has demonstrated promise as composites for photothermal therapy (**PTT**).[17] PTT is an emerging method for cancer treatment that converts light energy into heat using light-to-light transducers (or photosensitizing agents), leading to the thermal ablation of cancer cells, concluding in localised cell death.[18–20] Another property of note is the electrochemical characteristics displayed by the Keggin, Wells-Dawson and Molybdenum Blue POMs, which is far superior to other structures.[21,22] As well as exhibiting less negative reduction potentials the poly-oxotungstate version of the two structures have also demonstrated superior structural stability.[22]

Despite the variety of studies and advancement made within the bioactive POM society there is still scope for improvement and diversification. Not only on which POMs are used but also on the type of modification and application.

5.2 Aim

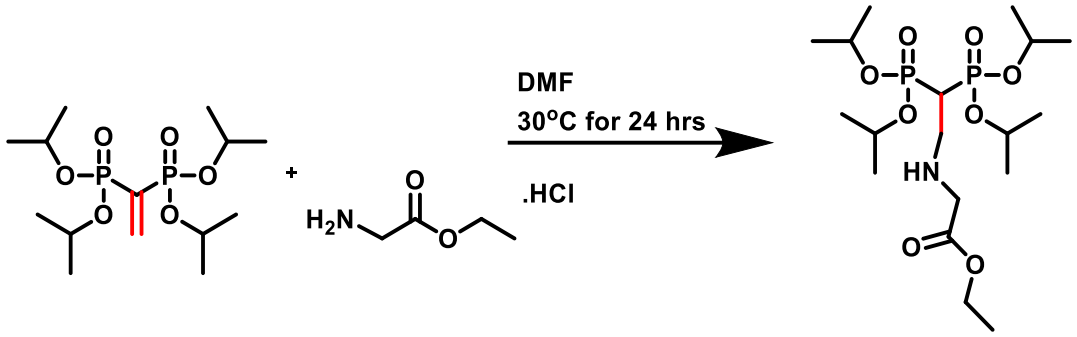

Scheme 1: Showing the route taken to attach the ligand to a protected glycine molecule.

Many examples of amino acid functionalised POM hybrids exist in literature[4,23–25]. However, there are few examples of the biofunctionalization of Wells-Dawson type POMs and to our knowledge no examples exist where a diphosphonate linker is used as the attachment site for a peptide chain.

In this chapter, the aim was to develop a diphosphonate-based synthesis route and explore the versatility of the new route for the functionalisation of a Wells-Dawson POM from a single attachment site with a peptide chain. The functionalisation with bio-macromolecules shows great promise as it has the potential to increase selectivity of the POM and mimic properties of the installed biological peptides. Herein is described the use of tetraisopropyl vinylidene diphosphonate (**TPVD**) as the linker system due to the ease of functionality and commercial availability; this was employed to couple to amino acid/peptide moieties either at an amine terminal end or a free thiol. Techniques are described for the on-resin and off-resin attachment of peptides to the ligand, and subsequent hybridisation to the POM.

5.3 Results and Discussion

5.3.1 Synthesis

The synthesis methodology of the diphosphonate-amino acid ligand complexes was adopted and modified from previously reported thiol-maleimide reactions which are commonplace within peptide functionalisation when using the free thiol of cysteine (**Cys**) as the targeted side chain.[26–28] Where commonly a free thiol is reacted with a maleimide species either functionalised to a peptide directly[28] or to the surfactant to add the bioactive material to.[29] The approach was inspired by the work of Klumpp *et al.*,[30] where successful Michael-addition of amino acid esters to N-heterocycles. These Michael additions in general are mild making them ideal for ligation coupling reactions to peptides.[31]

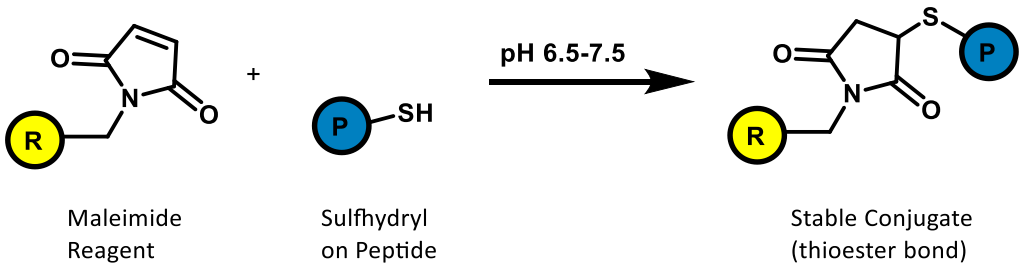

Scheme 2: Maleimide reaction scheme for chemical conjugation to a sulfhydryl. R typically represents a labelling reagent or one end of a crosslinker having the maleimide reactive group; P represents a protein or other molecule that contains the target functional group (i.e. sulfhydryl, -SH)

In this case the TPVD possesses a reactive vinyl group which is attached to electron withdrawing phosphonates. This allows nucleophilic addition reactions to occur readily with mild conditions. Free thiols can be incorporated into peptides, *via* the canonical amino acid, Cys, to attack the electrophilic vinylidene on the protected diphosphonate ligand, **Scheme 2**. Initially we attempted to attach the ligand to the POM prior to the reaction with the thiol, however, it was observed that upon the deprotection of the TPVD the very reactive vinylidene undergoes side reactions, hence the TPVD was thereafter first reacted with the peptide substrate prior to deprotection and hybridisation.

The reactions were attempted with an ester protected Cys as the nucleophilic reagent, due to the presence of the thiol. It was found that at low temperature of 35 ^{o}C, the Michael addition was successful with moderate conversion in 24 hrs, yielding a **Cys-DP** ligand (40 % yield), characterised by MS and ^{31}P NMR. Due to the effective addition of a thiol under mild

conditions, either neat or with minimal DMF it was decided to trial free amines found either at the terminal end of a peptide or in a side chain (e.g., Lys). These reactions also highlighted that amine Michael-addition reactions were also successful, demonstrated on the LGG peptide discussed below. However, the purification procedure for these compounds needs further development, as ligand impurities remained. The success of the amino acids was determined by the identification of correct masses in the MS. After successfully coupling the ligand, phosphonate-isopropyl ester and amine-Boc protecting groups were cleaved with TMSBr overnight at room temperature, and the TMS hydrolysed off the phosphonate with MeOH to generate the cysteine-diphosphonic acid ligand. Upon completion of the isopropyl deprotection the DCM and excess TMSBr was evaporated off on the Schlenk line. The product was dissolved in minimum amount MeOH and precipitated out with an excess of Acetone. The product was characterised by MS and ^{31}PNMR.

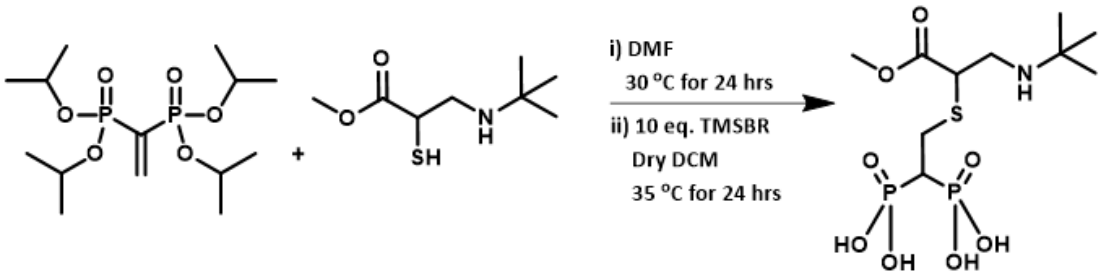

Scheme 3: Showing the reaction conditions for the Cys-TPVD reaction, yielding **Cys-DP**.

For all reactions mild conditions were employed and success was found using glycine (Gly), cysteine (Cys), phenylalanine (Phe), and leucine (Leu) within a tripeptide, among the small library trailed.

The next stage involved the hybridisation of Cys-DP with a lacunary Wells-Dawson {W_{17}} POM. By employing previously developed hybridisation methods, page 131, it was found that Cys-DP could successfully be coupled to the POM, yielding {W_{17}CysDP}. We characterised this structure *via* ^{31}P NMR, Figure 89. The difference in the NMR structures between the lacunary anion, the ligand and the hybrid POM are displayed in Figure 90.

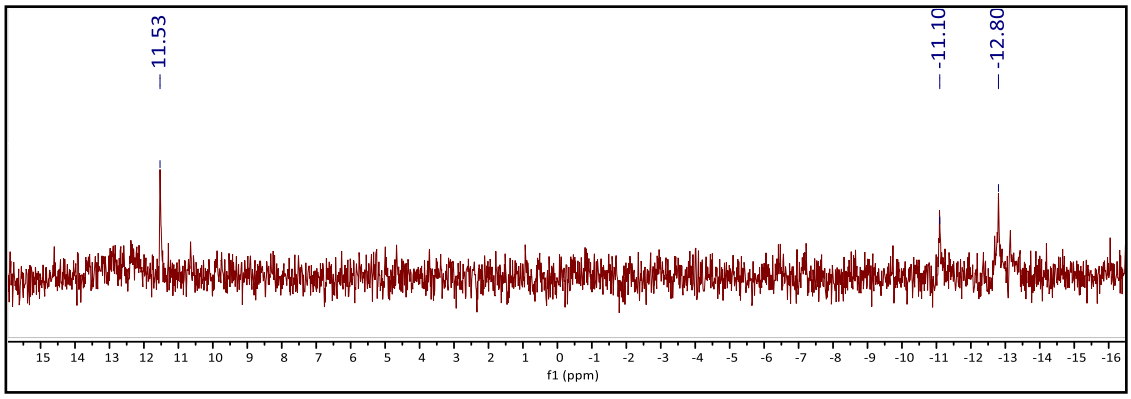

Figure 89: ^{31}P NMR of {W_{17}CysDP} in d-MeCN with labels signals.

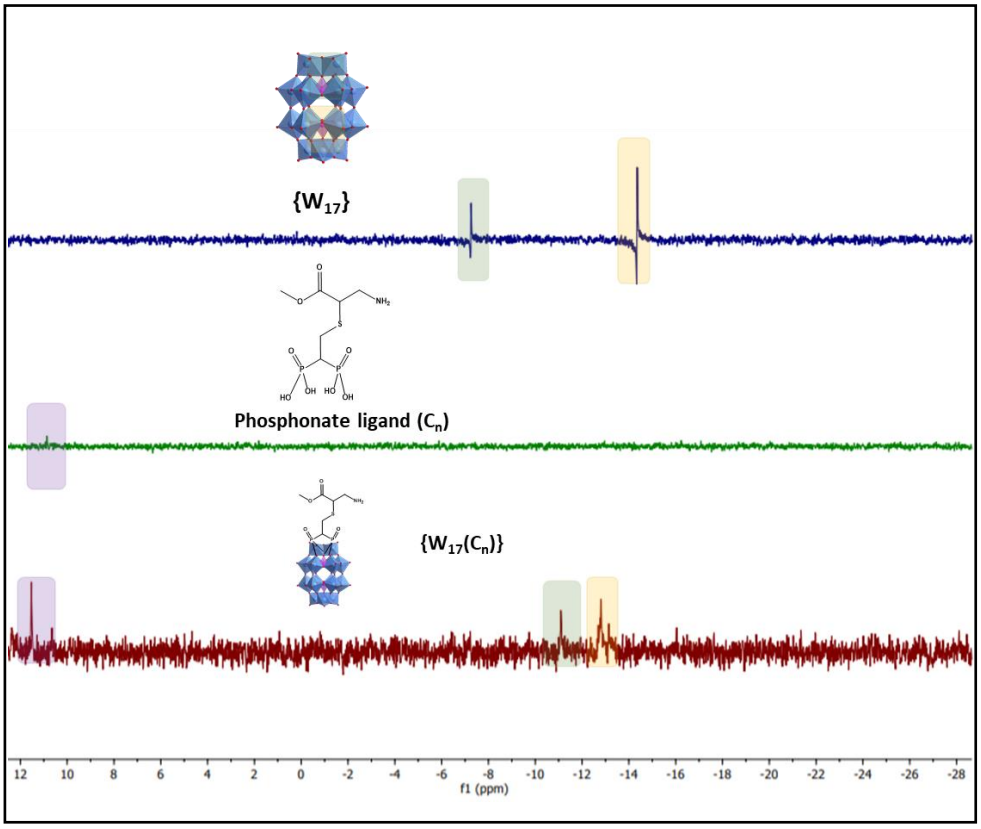

Figure 90: ^{31}PNMR's of the {W_{17}} POM, the Cys-DP and the hybrid formed.

5.3.2 Development of Peptide Chains

5.3.2.1 Tripeptide Diphosphonate Ligands and Hybrids

Due to the successful use of both an amine (page 162) and a thiol as the nucleophilic element this gave a large amount of flexibility to which tripeptide could be tested. It was decided to use Leu-Gly-Gly (H-**LGG**-OH) as this was commercially available, Figure 91. The sequence was ideal due to the presence of only one amine and no competing amines or thiols, three amino acids was considered appropriate as it indicated the viability of an extended chain.

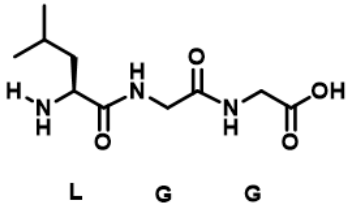

Figure 91: Displaying the structure of the LGG tripeptide.

The same synthesis procedure was undertaken as for the single amino acid ligands, with an excess of LGG peptide to TPVD as it was realised that an excess of TPVD was very difficult to separate out whereas peptides easily precipitated when adding diethyl ether. Hence moderately facile isolation of the protected LGG-DP ligand from the starting materials was achieved.

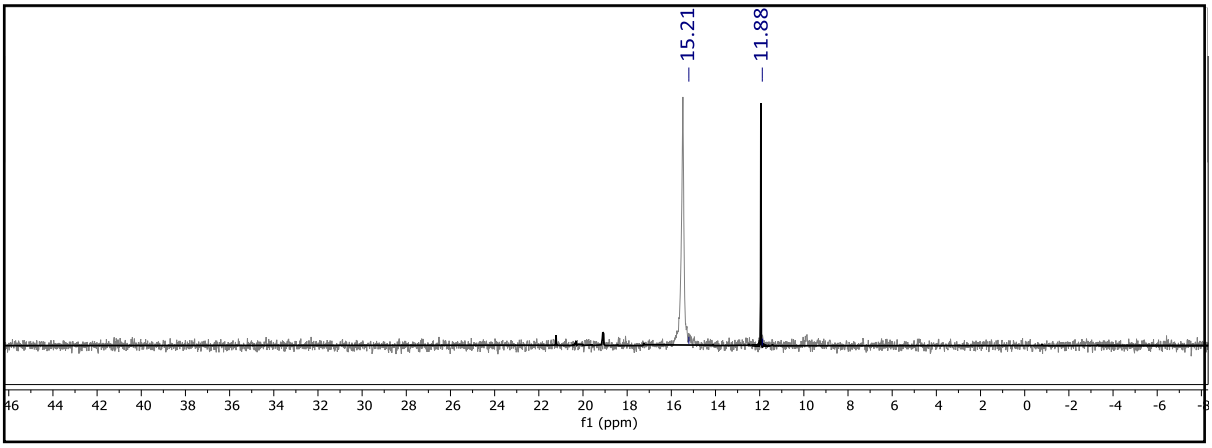

Figure 92: ^{31}PNMR of the LGG-DP at 15.21 ppm and the TPVD starting material 11.88 ppm. This clearly shows the shift of the ligand upon addition to the tripeptide, the ligand was also verified using MS.

As the peptide was deprotected only the TPVD required deprotection this progressed as described previously and the product LGG-DP was separated out through subsequent solvent washes. The newly formed ligand then underwent hybridisation with {W_{17}} to form the LGG-POM, Figure 93. It was found that the peptide-DP ligands were soluble in Diethyl ether while the POM hybrids were not and hence that was the last washing step to remove any unreacted ligand material. Standard hybridisation conditions were used with a small modification, the temperature was lowered to 50 ^{o}C due to concern of peptide structures degrading, this was less of a concern for tripeptides however this allowed us to establish suitable synthesis routes for larger subsequent peptides.

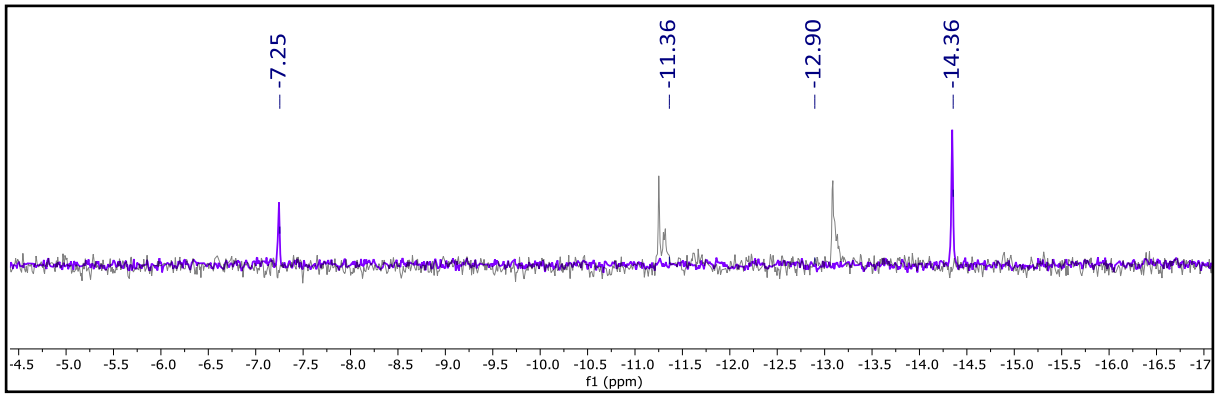

Figure 93: ^{31}PNMR showing the LGG-POM hybrid (grey) and the original {W_{17}} POM (purple), the NMR clearly shows the characteristic shift of the peaks when the POM is hybridised.

5.3.2.2 Hexapeptide Diphosphonate Ligand and Hybrid

It was then decided to advance to larger peptide sequences as the main interest was to see whether this method remained suitable for larger biomolecules. For ease it was decided to start the sequence with LGG, L being the attachment site for the TPVD again as it showed success. Then a tyrosine (Y) was introduced for easy detection on the HPLC, making characterisation and purification simpler. Finally, glycine and arginine (R) were added to the end, Figure 94, this is due to them beginning the start of the sequence for the HIV-TAT

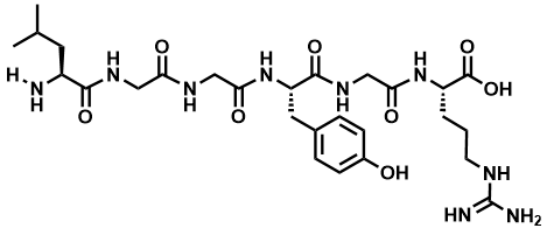

Figure 94: Depicts the structure of the LGGYGR free peptide: $C_{27}H_{43}N_9O_8$.

peptide, which is a commonly used cell penetrating peptide[6,32]. ESI-MS (MeCN) m/z (calculated, found): [L-H]- (621.68, 620.31).

Additionally, it was decided to attempt the attachment of the TPVD on resin, whereas before all peptides and amino acids had been free in solution. This approach was decided for ease of purification. Retaining the peptide on resin meant that it was possible to deprotect the final amine and keep all other side chains protected; due to the Fmoc deprotection od the amine and orthogonal conditions for the peptide cleavage. Furthermore, as the DP-LGGYGR- would remain on resin any unreacted TPVD could be removed *via* washing and unreacted peptides could easily be separated upon cleavage off the resin *via* HPLC purification.

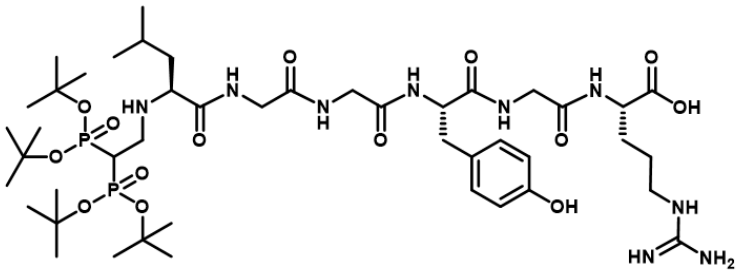

Figure 95: Depicts the structure of DP-LGGYGR: $C_{29}H_{45}N_9O_{10}P_2$.

As stated, the H-LGGYGR-NH peptide was synthesised *via* SPPS on rink amide resin. The final Fmoc deprotection was performed and the resin washed with DMF and then DCM. To the resin bound LGGYGR displaying a terminal amine was added 5 eq. of the TPVD with 1 mL DMF and the mixture was agitated at room temperature overnight. The mixture was tested through mini-cleaves to determine the successful coupling and then a full cleave was performed. A standard cleavage cocktail was used to deprotect all side chains and cleave the peptide off the resin. The peptide was purified through preparative HPLC and then isolated on a freeze-dryer.

TMSBr was used for the deprotection of the isopropyl protecting groups on the TPVD of the isolated peptide (LGGYGR-DP). The deprotection was performed as previously described, in inert conditions with 10 eq. TMSBr and 1 mL dry DCM. The reaction was stirred at 35 ^{o}C overnight. After reaction completion, the solvent had fully evaporated off and solid black

flakes were collected, the product was purified *via* preparative HPLC, Figure 96. ESI-MS (MeCN) m/z (calculated, found): [L-H]- (741.67, 740.20).

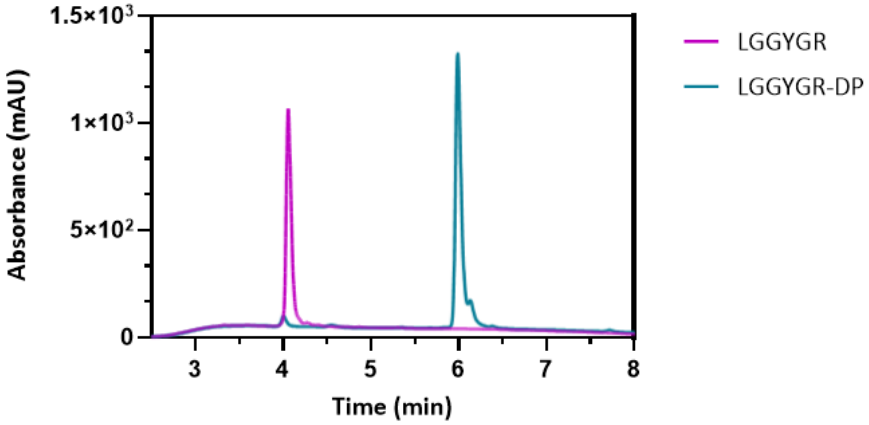

Figure 96: Analytical reverse phase HPLC traces of LGGYGR-DP (Green) and LGGYGR (Purple), preparative HPLC run at 2-95% B over 10 minutes 0.6 ml/min.

The isolated white diphosphonate peptide was then hybridised to the $\{W_{17}\}$ POM. A 1:1 equivalents of POM: LGGYGR-DP was added in 12.5 mL DMF and heated gently to 30 ^{o}C, followed by adding 14.3 µL concentrated HCl. After 5 minutes the mixture was heated to 50 ^{o}C and left overnight. Due to the small quantities of LGGYGR-DP (26 mg), the reaction was scaled down compared to standard POM hybridisations.

5.3.2.3 Characterization of the LGGYGR-POM hybrid

Due to the small quantity of LGGYGR-POM isolated only selected techniques could be performed on the hybrid. General characterisation was carried out ie, ^{31}PNMR, and ESI-MS. The obtained hybrid could not be completely purified due to limited time and material. However, the data shows proof of isolation of the hybrid material. The NMRs show the typical shift of peaks common to hybrid POM formation whilst the MS indicate peaks less than 1 m/z to the theoretically calculated, Figure 97, peaks were also broad due to multiple isotopic splitting of tungsten which also indicates POM-like character.

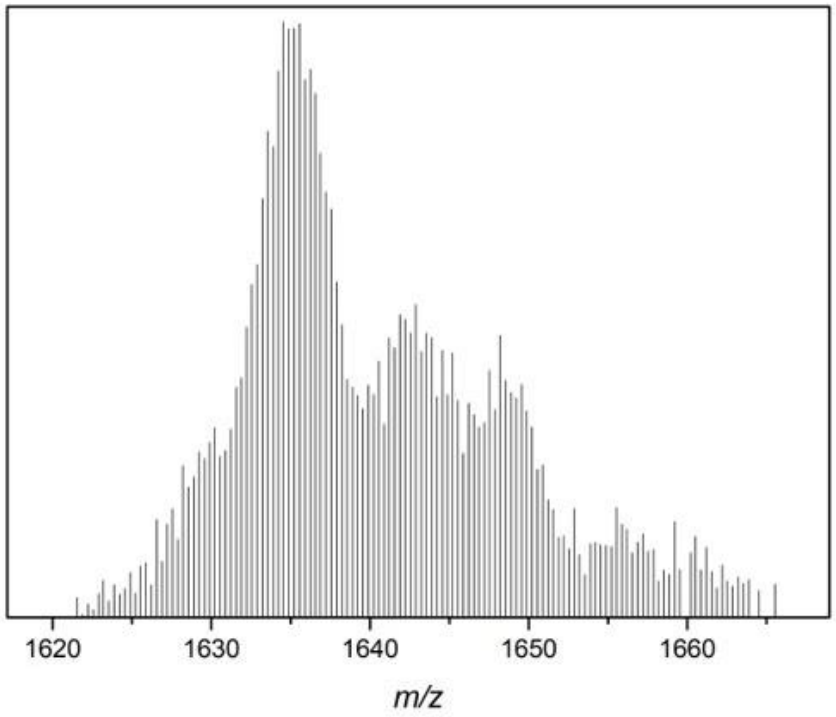

Figure 97: MS data showing the main peaks correlating to the Hybrid POM.

LGGYGR HYBRID	Z	m/z calc	m/z obs
$H_3(C_{29}H_{45}N_9O_{10}P_2)(W_{17}P_2O_{61})$	3-	1636.01039	1636.22
$H_2Na(C_{29}H_{45}N_9O_{10}P_2)(W_{17}P_2O_{61})$	3-	1643.33771	1643.214
$HNa_2(C_{29}H_{45}N_9O_{10}P_2)(W_{17}P_2O_{61})$	3-	1650.66502	1650.545
$Na_3(C_{29}H_{45}N_9O_{10}P_2)(W_{17}P_2O_{61})$	3-	1657.99234	1657.859
$H_2K(C_{29}H_{45}N_9O_{10}P_2)(W_{17}P_2O_{61})$	3-	1648.66235	1648.528

Table 1: The calculated and observed MS data of the POM, the peaks shown in Figure 98.

One of the putative mechanisms of antitumoral POMs, suggested originally by Yamase,[33] purports that the repetition of redox events between the POM and the cell components, likely members of the electron transport chain, interferes with ATP generation finally leading to apoptosis.

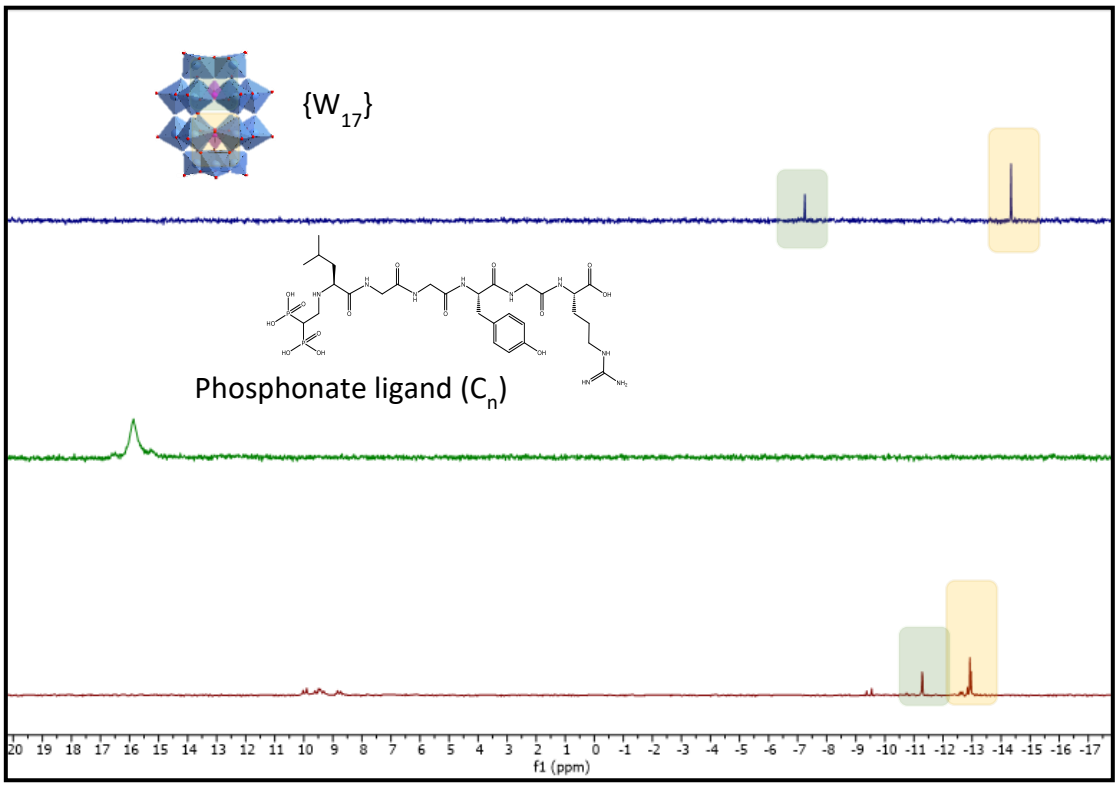

Figure 98: ^{31}PNMR depicting the LGGYGR-POM. The (W_{17}} POM is shown in blue and the LGGYGR-DP ligand is shown in green with the hybrid POM in red.

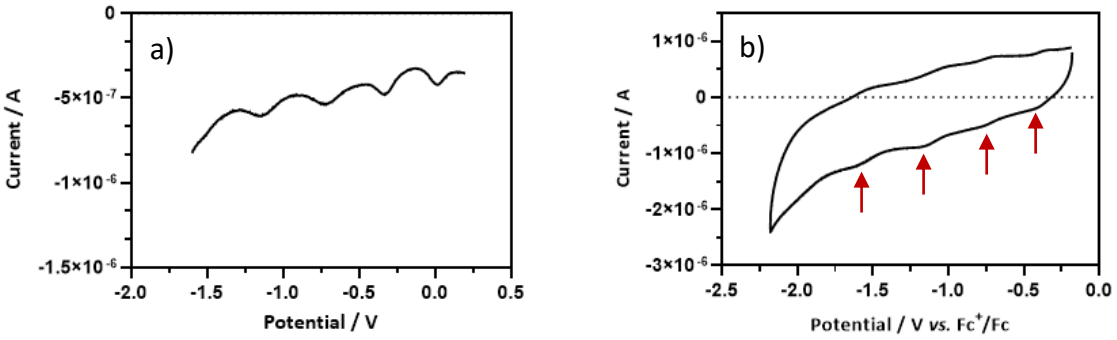

Figure 99: a) DPV and b) CV graphs of the Hybrid LGGYGR-W_{17} POM. Graphs of 0.1 mM LGGYGR hybrid POM, 0.1 M $TBAPF_6$ electrolyte solution in DMF, 0.1 mM of the LGGYGR-POM hybrid. A glassy carbon working electrode was used with a silver wire reference and platinum counter electrode; ferrocene was added as an external reference.

Hence the redox properties by POMs are important for their function as antitumoral agents. It was decided that cyclic voltammetry would be performed to determine whether some of the electronic properties of the POM were retained, Figure 99.

The CV shown in Figure 99 indicated the retention of reduction profiles of the POM. Four poorly resolved reductions are indicated at, -0.31 V, -0.70V, -1.17 V and -1.57 V, which can be seen far more easily in the DPV graph, Figure 99. The subtle peaks are due to high dilution of the sample owing to the small amount of material obtained. Despite this, the voltammograms show good evidence of retention of the redox processes of the POM. Especially when seen compared to Figure 100 depicting the P_2W_{18} POM. Comparing the two figures a similarity can be seen in the two reductions demonstrated by the $\{P_2W_{18}\}$ CV at -1.17 V and -1.35 V and the 3rd and 4th reductions of by the LGGYGR Hybrid at -1.17 V and -1.57 V.

Overall, a shift can be seen in the redox potentials of the POM to a more positive potential; this indicates that the hybrid species has a lower LUMO energy.

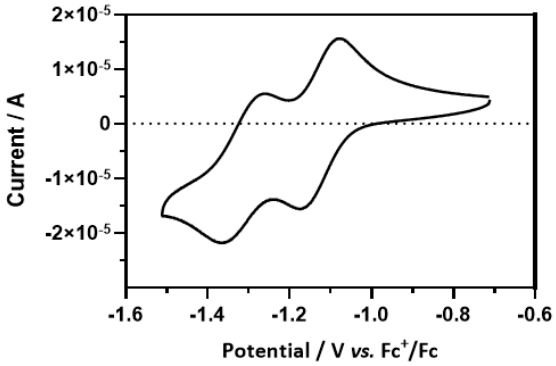

Figure 100: 1.4 mM P_2W_{18} POM in 0.1 M $TBAPF_6$ electrolyte solution in DMF, 0.1 mM of the LGGYGR-POM hybrid. A glassy carbon working electrode was used with a silver wire reference and platinum counter electrode; ferrocene was used as an external reference.

5.4 Conclusion

In summary, we have employed a new hybridization strategy to isolate a stable, new class of hybrid polyoxometalates based on the hybridisation of diphosphonate with Wells-Dawson POMs. The structures were characterised via NMR and MS. The electronic property of the hexapeptide hybrid was also probed by employing cyclic voltammetry. Based on the electrochemical results, it was determined that some of the redox-active properties of the original POM were retained. The hybrid POM displayed an overall positive shift with regards to the parent $\{P_2W_{18}\}$ anion.

Two different approaches are described regarding the functionalisation of the POM with amino acids and peptides. Above is demonstrated the addition of unprotected peptides off resin in free solution to the ligand and POM and conversely the addition of a protected peptide on resin. The two approaches show versatile biofunctionalization methods for the Wells-Dawson type POM, with one peptide chain. This displays a novel approach of grafting a single peptide chain to a Wells-Dawson POM under mild conditions. The progression from single amino acids to tripeptides to a hexapeptide was demonstrated with increased functionality with each step. The final hexapeptide also contains the starting sequence of the HIV-TAT peptide which has often been used in literature to add cell penetrating properties and increase specificity of substrates.

Overall, we have demonstrated that DP based molecules can be used as bio-linkers and ligands for lacunary Wells-Dawson POMs. Upon hybridisation, some of the redox properties are retained based on the combined electronic effects of the phosphonate and central hetero atom. DP molecules can, therefore, be used to graft ligand moieties such as bio molecules to the POM clusters and generate enhanced hybrid molecules with potential applications in medicine, drug delivery and antimicrobial activities.

5.5 Experimental

5.5.1 POM Synthesis

5.5.1.1 Synthesis of Wells-Dawson - α,β-$K_6[P_2W_{18}O_{62}]$ - $\{P_2W_{18}\}$

See section 4.5.1.1.

5.5.1.2 Synthesis of Lacunary Wells-Dawson - α- $K_{10}[P_2W_{17}O_{61}]$ – $\{W_{17}\}$

See section 4.5.1.2.

5.5.2 Peptide Ligand Synthesis

5.5.2.1 Synthesis of Cys-DP

N(tert-butoxycarbonyl)-L-cysteine methyl ester (428 mg, 2.26 mmol) was dried under vacuum for 30 mins before backfilling with argon, to this was added to tetraisopropyl vinylidenediphosphonate (184 mg, 0.516 mmol). To the mixture was added an DMF (1 mL) and stirred vigorously at 35 ^{o}C overnight. The mixture was centrifuged (8000rpm, 5 mins) and rotary evaporated before sonicating in diethyl ether. The protected product (400 mg, 0.676 mmol) was dried on a Schlenk line and the flask evacuated before backfilling with argon and keeping in an inert atmosphere. Dry dichloromethane (3mL) was added followed by Bromo trimethyl silane (0.828 g, 5.41 mmol). The mixture was stirred at 30 ^{o}C for 20 hrs. Upon completion the DCM and excess TMSBr was evaporated off on the Schlenk line. The product was dissolved in minimum amount MeOH and precipitated out with an excess of acetone. The product was collected as a white powder and dried under vacuum (0.292 g, 0.904 mmol, 40% yield). ^{31}P NMR (162 MHz, DMSO-d6) δ 17.45; ESI-MS (MeCN) m/z (calculated, found): [L-H]- (323.00, 321.99).

5.5.2.2 Synthesis of Gly-DP

Glycine ethyl ester hydrochloride (315 mg, 2.26 mmol) was used, and the same procedure followed as for the Cys-DP.

The product was collected as a white powder and dried under vacuum (0.182 g, 0.625 mmol, 27% yield). ^{31}P NMR (162 MHz, DMSO-d6) δ 14.76; ESI-MS (MeCN) m/z (calculated, found): [L-H]- (291.12, 290.02).

5.5.2.3 Synthesis of Phe-DP

L-Phenylalanine ethyl ester hydrochloride (519 mg, 2.26 mmol) was used, and the same procedure followed as for the Cys-DP.

The product was collected as a white powder and dried under vacuum (0.182 g, 0.625 mmol, 27% yield). ^{31}P NMR (162 MHz, DMSO-d6) δ 17.60; ESI-MS (MeCN) m/z (calculated, found): [L-H]- (549.58, 550.27).

5.5.2.4 Synthesis of Cys-DP hybrid-POM

$K_{10}[P_2W_{17}O_{61}]$ (0.25g, 0.055 mmol) was added to 40 mL DMF at 40 ^{o}C followed by the Cysteine ligand ($C_6H_{15}NO_8P_2S$, 0.03 g, 0.093 mmol). To the suspension was added conc. HCl (50 µL) and stirred for a further 5 mins. The mixture was then heated to 75 ^{o}C and stirred overnight. The solution was then cooled to r.t and centrifuged (8000 rpm, 5 mins) to remove the remaining solid. Diethyl ether was added (larger excess - approx. 150 ml) to the solution until a white suspension was formed. The white suspension was then centrifuged, and the solvent was decanted off. The centrifuge tube with the remain white solid was when attached to the vacuum and dried, before being redissolved in a minimum amount of MeCN. The suspension was centrifuged (8000 rpm, 5 mins) and decanted off before adding an excess of diethyl ether (40 mL) to the solution. The white suspension was then centrifuged, and the solvent was decanted off. The centrifuge tube with the remain white solid was when attached to the vacuum and the solid dried, before being redissolved in a minimum amount of acetone. The suspension was centrifuged (8000 rpm, 5 mins) and decanted off before adding an excess of diethyl ether (40 mL) to the solution. The centrifuge tube with the remain white solid was when attached to the vacuum and dried to yield $K_6[P_2W_{17}O_{61}(C_6H_{11}NO_8P_2S)]$ as a white solid (0.156 g, 0.033 mmol, 70 % yield). ^{31}P NMR (162 MHz, Acetonitrile-d3) δ 11.53, -11.10, -12.80.

5.5.2.5 Synthesis of Tripeptide-DP molecules: LGG-DP

Leu-Gly-Gly (0.303 g, 1.23 mmol) was dried under vacuum for 30 mins before backfilling with argon, to this was added to tetraisopropyl vinylidenediphosphonate (1.753 g, 4.92 mmol). To the mixture was added an DMF (2 mL) and stirred vigorously at 35 ^{o}C overnight. The mixture was centrifuged (8000rpm, 5 mins) and rotary evaporated. The protected product (0.808 g, 1.23 mmol) was dried on a Schlenk line and the flask evacuated before backfilling with argon and keeping in an inert atmosphere. Dry dichloromethane (3mL) was added followed by Bromo trimethyl silane (2.23 g, 0.0146 mol). The mixture was stirred at 30 ^{o}C for 20 hrs. Upon completion the DCM and excess TMSBr was evaporated off on the Schlenk line. The product was dissolved in minimum amount MeOH and precipitated out with an excess of acetone. The product was collected as a white powder and dried under vacuum (0.308 g, 0.0.711 mmol, 57.8% yield). ^{31}P NMR (162 MHz, DMSO-d6) δ 16.45; ESI-MS (MeCN) m/z (calculated, found): [L-H]- (433.29, 434.11).

5.5.2.6 Synthesis of Hexapeptide-DP molecules: LGGYGR-DP

The hexapeptide was prepared through SPPS as described in on rink amide resin. Due to the peptide not being cleaved off resin till after the addition of the tetraisopropyl vinylidenediphosphonate an estimate was used for the addition of substrates.

Arg (2.86 g, 4.41 mol) was initially loaded onto the resin, using the synthesiser, the peptide was weighed out as 4 eq. to the resin. This was followed by iterative peptide synthesis. The final deprotection of the terminal Fmoc on the Leu was administered prior to washing and collection of the resin. The resin was reswollen in DMF and then a large excess of the TPVD was added to the resin in a fritted syringe. The resin was left to shake for 24 hours until a mini-cleave showed the successful coupling to the terminal amine. The resin was washed with DMF (5 x 3mL) and DCM (10 x 3 mL) prior to addition of the cleavage cocktail; trifluoro acetic acid (85%), triisopropylsilane (5%), thioanisole (5%) and H_2O (5%), and left to shake for 2 hours. The cocktail solution was collected and rinsed with some TFA, the mixture was blown down using N_2 till less than 1 mL remained, upon which diethyl ether was added ~30 mL. A white precipitate crashed out and the mixture was centrifuged (4000 rpm, 15 mins).

The white precipitate collected was redissolved in 2 mL H_2O with 0.1% TFA and placed on the preparative HPLC for purification with a gradient of 20-95% B over 30 minutes. The separate fractions were frozen and placed on the freeze drier overnight. A white fluffy peptide of protected LGGYGR-DP was collected (75 mg, 0.073 mmol).

The protected product (75 mg, 0.073 mmol) was dried on a Schlenk line and the flask evacuated before backfilling with argon and keeping in an inert atmosphere. Dry dichloromethane (3 mL) was added followed by bromo-trimethyl silane (0.050 g, 0.0146 mol). The mixture was stirred at 30 ^oC for 20 hrs. Upon completion a dark brown flaky substance remained. This was again purified *via* preparative HPLC. A white solid was isolated of the deprotected LGGYGR-DP (26 mg, 0.0321 mmol, 44.0% yield). ESI-MS (MeCN) m/z (calculated, found): [L-H]- (741.67, 740.20).

5.5.3 Hybrid POM Synthesis

5.5.3.1 Synthesis of LGG-DP hybrid-POM

$K_{10}[P_2W_{17}O_{61}]$ (0.25g, 0.055 mmol) was added to 40 mL DMF at 40 ^oC followed by the LGG ligand ($C_{12}H_{25}N_3O_{10}P_2$, 0.033 g, 0.055 mmol). To the suspension was added conc. HCl (50 µL) and stirred for a further 5 mins. The mixture was then heated to 70 ^oC and stirred overnight. The solution was then cooled to r.t and centrifuged (8000 rpm, 5 mins) to remove the remaining solid. Diethyl ether was added (larger excess - approx. 150 ml) to the solution until a white suspension was formed. The white suspension was then centrifuged, and the solvent was decanted off. The centrifuge tube with the remain white solid was when attached to the vacuum and dried, before being redissolved in a minimum amount of MeCN. The suspension was centrifuged (8000 rpm, 5 mins) and decanted off before adding an excess of diethyl ether (40 mL) to the solution. The white suspension was then centrifuged, and the solvent was decanted off. The centrifuge tube with the remain white solid was when attached to the vacuum and dried, before being redissolved in a minimum amount of acetone. The suspension was centrifuged (8000 rpm, 5 mins) and decanted off before adding an excess of diethyl ether (40 mL) to the solution. The centrifuge tube with the remain white solid was when attached to the vacuum and dried to yield

$K_6[P_2W_{17}O_{61}(C_{12}H_{21}N_3O_{10}P_2)]$ as a white solid (0.156 g, 0.033 mmol, 70% yield). 31P NMR (162 MHz, Acetonitrile-d3) δ 11.53, -11.10, -12.80.

5.5.3.2 Synthesis of LGGYGR-DP hybrid-POM

$K_{10}[P_2W_{17}O_{61}]$ (0.25g, 0.055 mmol) was added to 40 mL DMF at 40 ^oC followed by the Cysteine ligand ($C_6H_{15}NO_8P_2S$, 0.03 g, 0.093 mmol). To the suspension was added conc. HCl (50 µL) and stirred for a further 5 mins. The mixture was then heated to 75 ^oC and stirred overnight. The solution was then cooled to r.t and centrifuged (8000 rpm, 5 mins) to remove the remaining solid. Diethyl ether was added (larger excess - approx. 150 ml) to the solution until a white suspension was formed. The white suspension was then centrifuged, and the solvent was decanted off. The centrifuge tube with the remain white solid was when attached to the vacuum and dried, before being redissolved in a minimum amount of MeCN. The suspension was centrifuged (8000 rpm, 5 mins) and decanted off before adding an excess of diethyl ether (40 mL) to the solution. The white suspension was then centrifuged, and the solvent was decanted off. The centrifuge tube with the remain white solid was when attached to the vacuum and dried, before being redissolved in a minimum amount of acetone. The suspension was centrifuged (8000 rpm, 5 mins) and decanted off before adding an excess of diethyl ether (40 mL) to the solution. The centrifuge tube with the remain white solid was when attached to the vacuum and dried to yield $K_6[P_2W_{17}O_{61}(C_6H_{11}NO_8P_2S)]$ as a white solid (0.156 g, 0.033 mmol, 70 % yield). ^{31}P NMR (162 MHz, Acetonitrile-d3) δ 11.53, -11.10, -12.80.

5.6 REFERENCES

1 C. Li, J. Lu, F. Tu, J. Chen and Y. Li, *Inorg. Chem. Commun.*, 2011, **14**, 1192–1195.

2 X. Liu, S. Wang and C. Feng, *Chinese J. Chem.*, 2010, **28**, 2411–2415.

3 H. El Moll, W. Zhu, E. Oldfield, L. M. Rodriguez-Albelo, P. Mialane, J. Marrot, N. Vila, I. M. Mbomekallé, E. Rivière, C. Duboc and A. Dolbecq, *Inorg. Chem.*, 2012, **51**, 7921–7931.

4 A. Bijelic, M. Aureliano and A. Rompel, *Angew. Chemie*, 2019, **58**, 2980–2999.

5 V. Tagliavini, C. Honisch, S. Serratì, A. Azzariti, M. Bonchio, P. Ruzza and M. Carraro, *RSC Adv.*, 2021, **11**, 4952–4957.

6 A. P. E. Vives, J. Schmidt, *Biochim. Biophys. Acta.*, 2008, **1786**, 126–138.

7 G. Zhang, B. Keita, C. T. Craescu, S. Miron, P. De Oliveira and L. Nadjo, *J. Phys. Chem. B*, 2007, **111**, 11253–11259.

8 L. Zheng, Z. Gu, Y. Ma, G. Zhang, J. Yao, B. Keita and L. Nadjo, *J. Biol. Inorg. Chem.*, 2010, **15**, 1079–1085.

9 K. Narasimhan, K. Micoine, E. Lacôte, S. Thorimbert, E. Cheung, B. Hasenknopf and R. Jauch, *Cell Regen.*, 2014, **3**, 1–7.

10 M. Li, C. Xu, L. Wu, J. Ren, E. Wang and X. Qu, *Small*, 2013, **9**, 3455–3461.

11 J. Luo, B. Zhang, C. Yvon, M. Hutin, S. Gerislioglu, C. Wesdemiotis, L. Cronin and T. Liu, *Eur. J. Inorg. Chem.*, 2019, **2019**, 380–386.

12 C. Yvon, A. J. Surman, M. Hutin, J. Alex, B. O. Smith, D.-L. Long and L. Cronin, *Angew. Chemie*, 2014, **126**, 3404–3409.

13 D. Ventura, A. Calderan, C. Honisch, S. Krol, S. Serratì, M. Bonchio, M. Carraro and P. Ruzza, *Pept. Sci.*, 2018, **110**, 1–11.

14 H. Soria-carrera, I. Franco-castillo, P. Romero, S. Martín, J. M. De Fuente, S. G. Mitchell and R. Martín-rapffln, *Angew. Chem. Int. Ed.*, 2021, **60**, 3449–3453.

15 Y. Liu, S. Tian, S. Liu and E. Wang, *Transit. Met. Chem.*, 2005, **30**, 113–117.

16 N. Gao, H. Sun, K. Dong, J. Ren, T. Duan, C. Xu and X. Qu, *Nat. Commun.*, 2014, **5**, 1–9.

17 G. Guedes, S. Wang, H. A. Santos and F. L. Sousa, *Eur. J. Inorg. Chem.*, 2020, **2020**, 2121–2132.

18 W. Tang, W. Fan, Z. Wang, W. Zhang, S. Zhou, Y. Liu, Z. Yang, E. Shao, G. Zhang, O. Jacobson, L. Shan, R. Tian, S. Cheng, L. Lin, Y. Dai, Z. Shen, G. Niu, J. Xie and X. Chen, *ACS Nano*, 2018, **12**, 12269–12283.

19 C. Zhang, W. Bu, D. Ni, C. Zuo, C. Cheng, Q. Li, L. Zhang, Z. Wang and J. Shi, *J. Am. Chem. Soc.*, 2016, **138**, 8156–8164.

20 G. Guedes, S. Wang, F. Fontana, P. Figueiredo, J. Lindén, A. Correia, R. J. B. Pinto, S. Hietala, F. L. Sousa and H. A. Santos, *Adv. Mater.*, 2021, **33**, 1-10.

21 J. Y. Zhang, Z. H. Chang, X. L. Wang, X. Wang and H. Y. Lin, *New J. Chem.*, 2021, **45**, 3328–3334.

22 D. Wang, L. Liu, J. Jiang, L. Chen and J. Zhao, *Nanoscale*, 2020, **12**, 5705–5718.

23 Y. Yao, Q. Zhang, P. Liu, L. Yu, L. Huang, S. Z. Zeng, L. Liu, X. Zeng, J. Zou, *RSC. Adv.* 2018, **8**, 1857-1865.

24 Y. Ji, Y. Fang, P. Han, M. Li, Q. Chen and Q. Han, *Inorg. Chem. Commun.*, 2017, **86**, 22–25.

25 J. S. S. Xue, A. Chai, Z. Cai, Y. Wei, C. Xiang, W. Bian, *Dalton. Trans.*, 2008, 4770–4775.

26 L. Martínez-Jothar, S. Doulkeridou, R. M. Schiffelers, J. Sastre Torano, S. Oliveira, C. F. van Nostrum and W. E. Hennink, *J. Control. Release*, 2018, **282**, 101–109.

27 O. Boutureira and G. J. L. Bernardes, *Chem. Rev.*, 2015, **115**, 2174–2195.

28 M. Lahnsteiner, A. Kastner, J. Mayr, A. Roller, B. K. Keppler and C. R. Kowol, *Chem. - A Eur. J.*, 2020, **26**, 15867–15870.

29 B. T. Houseman, E. S. Gawalt and M. Mrksich, *Langmuir*, 2003, **19**, 1522–1531.

30 S. H. Kennedy and D. A. Klumpp, *J. Org. Chem.*, 2017, **82**, 10219–10225.

31 A. M. Freedy, M. J. Matos, O. Boutureira, F. Corzana, A. Guerreiro, P. Akkapeddi, V. J. Somovilla, T. Rodrigues, K. Nicholls, B. Xie, G. Jiménez-Osés, K. M. Brindle, A. A. Neves and G. J. L. Bernardes, *J. Am. Chem. Soc.*, 2017, **139**, 18365–18375.

32 S. G. Sarafianos, U. Kortz, M. T. Pope and M. J. Modak, *Reactions*, 1996, **626**, 619–626.

33 A. Ogata, H. Yanagie, E. Ishikawa, Y. Morishita, S. Mitsui, A. Yamashita, K. Hasumi, S. Takamoto, T. Yamase and M. Eriguchi, *Br. J. Cancer*, 2008, **98**, 399–409.